Tensile High Strain Rate Behavior of AZ31B Magnesium Alloy Sheet

by

Dan Hasenpouth

A thesis
presented to the University of Waterloo
in fulfilment of the
thesis requirement for the degree of
Master of Applied Science
in
Mechanical Engineering

Waterloo, Ontario, Canada, 2010

I hereby declare that I am the sole author of this thesis. This is a true copy of the thesis, including any required final revisions, as accepted by my examiners.

I understand that my thesis may be made electronically available to the public.

ABSTRACT

In an effort to improve the fuel efficiency of automobiles, car designers are investigating new materials to reduce the overall vehicle weight. Magnesium alloys are good candidates to achieve that weight reduction due in part to their low density and high specific strength. To support their introduction into vehicle body structures, the dynamic behavior of magnesium alloys must be determined to assess their performance during a crash event. In this work, the tensile high strain rate behavior of AZ31B magnesium alloy sheets was characterized. Two different temper conditions were considered: AZ31B-O (fully annealed) and AZ31B-H24 (partially hardened). Three different sheet thicknesses were considered for the O temper condition, 1.0, 1.6 and 2.5 mm, while the H24 temper was 1.6 mm in thickness. The sheet condition of the magnesium alloys implies an in-plane anisotropy induced by the rolling process. Therefore, both the rolling and transverse directions were investigated in the current research.

In order to characterize the constitutive behaviour of AZ31B-O and AZ31B-H24 magnesium alloy sheets, tensile tests were performed over a large range of strain rates. Quasi-static experiments were performed at nominal strain rates of $0.003s^{-1}$, $0.1s^{-1}$ and $1s^{-1}$ using a servohydraulic tensile machine. Intermediate strain rate experiments were performed at $30s^{-1}$ and $100s^{-1}$ using an instrumented falling weight impact (IFWI) apparatus, and high strain rate experimental data at $500s^{-1}$, $1000s^{-1}$ and $1500s^{-1}$ was collected using a tensile split Hopkinson bar (TSHB) apparatus. Elevated temperature experiments (up to 300°C) were also performed at high strain rates using a radiative furnace mounted on the TSHB apparatus.

The tensile experiments show a significant strain rate sensitivity of the constitutive behavior of both the O and H24 temper conditions. The two tempers exhibit an average increase of stress level of 60-65 MPa over the range of strain rates considered. As the strain rate increases, the strain rate sensitivity of both tempers also increases. The strain rate has a different effect on the ductility of the two material conditions. The ductility of AZ31B-O is significantly improved under high strain rate deformations, whereas the AZ31B-H24 exhibits similar ductility at low and high strain rates.

Both material conditions presented a strong in-plane anisotropy, with an average stress level in the transverse direction higher than in the rolling direction by 15 MPa and 35 MPa for the O and H24 tempers, respectively.

The thermal sensitivity for both tempers at high strain rates was obtained. The two material conditions exhibit a clear thermal softening. From room temperature to 250°C, the loss in strength at 5% plastic strain was found to be 55 MPa and 125 MPa for the AZ31B-O and AZ31B-H24 materials, respectively.

The thickness of the AZ31B-O sheets has a mild effect on the measured constitutive behavior. The flow stress increases with increasing thickness. An average difference of 10-15 MPa was seen between the flow stress of the 1.0mm and 2.5mm sheets. However, similar strain rate sensitivity was seen for the three thicknesses.

The experimental data was fit to three constitutive models: the Johnson-Cook model, its modified version with a Cowper-Symonds strain rate sensitivity formulation, and the Zerilli-Armstrong model. The three models were evaluated by numerical simulation of the TSHB experiment under various testing conditions. It was found that the Zerilli-Armstrong model was the most accurate in predicting the flow stress of the different material conditions. However, finite element models incorporating the three constitutive fits failed to predict necking in the specimen.

ACKNOWLEDGEMENTS

I would like to thank my supervisor, Professor Michael Worswick for giving me the opportunity to complete a Master's degree as part of his research group, and for his knowledge, guidance and support during my graduate studies. I also would like to thank the NSERC Magnesium Strategic Research Network (MagNET), which supported this research. I would like to thank Professor Warren Poole, along with the other theme leaders, who created MagNET and made it an active and interactive research network across Canada.

I would like to thank Alex Bardelcik and Chris Salisbury who initiated me into fine art of handling the Hopkinson bars and the Drop Tower, and helped me countless times with my research. I also would like to thank my office companions and people from our research group, Dariush, Jon, Reza, Usman, Dr. Farzin, Kamyar, Ryan, Sooky and Jose for making it enjoyable to come in everyday. A special thank to Dariush with whom I shared many things, including wonders on life and magnesium, as well as traveling experiences around Canada and Europe.

I am grateful to many laboratory technicians, including Richard Gordon for his help on the Drop Tower, Andy Barber and Jason Benninger for their advice, and of course Tom Gawel for the precious help and solutions he provided for the Hopkinson bars. I also would like to thank the administrative staff of the Mechanical Engineering Department, especially Laurie Wilfong and Connie Slaughter who helped me many times with administrative duties. Thank you also to Debbie Burgess from UBC for her kindness and her logistic skills to organize high quality workshops in Vancouver.

Finally, I would like to thank my family in France. I don't think this work would have been possible without your support and understanding. Thank you to my Mom, my Dad, my sister Orane and my brother David. Merci pour votre amour et votre soutien tout au long de cette aventure. Je suis fier de faire partie de cette famille, et j'espère que ce sentiment est réciproque.

Thank you. Merci.

To my mother and father

TABLE OF CONTENTS

LIST OF FIGURES

LIST OF TABLES

1 INTRODUCTION

Automotive manufacturers are looking for ways to reduce the overall weight of vehicles to improve their fuel efficiency, as well as their performances. More than 60% of vehicle weight is due to the use of steel or cast iron in the body structure [1]. Currently in North America, aluminum alloys represent 8% of the vehicle weight while use of magnesium alloys is quite low with a contribution to the overall vehicle weight of only 0.3% [1]. However, due to their low density and high specific strength, magnesium alloys are very good candidates to produce lightweight vehicles. The United States Automotive Materials Partnership (USAMP) [1] estimates that vehicle weight can be reduced by 290 lbs (131 kg) using magnesium alloys instead of steel or aluminum alloys. Prior to the introduction of magnesium alloys in automotive body structures, their performance during crash events must be known. Deformation under a wide range of strain rates occurs during a car crash, with locally high strain rate deformation within crash regions of the vehicle. Furthermore, finite element simulations are widely used in the design processes to reduce the cost associated with safety evaluation of structures. Good constitutive models should thus be available to accurately predict the behavior of a vehicle during a crash event for example. Therefore, it is important to study and be able to predict the high strain rate behaviour of magnesium alloys to support their introduction into vehicle body structures.

Nowadays, AZ31 is the most common commercial magnesium alloy available in sheet form. Rolled sheet offers a variety of technical and commercial advantages over cast products. Indeed, forming processes, such as stamping, are faster than die casting, thereby reducing the production cost of a stamped part. Unfortunately, due to their crystallographic structure and as-rolled texture, magnesium alloys exhibit low ductility at room temperature and strong anisotropy in their constitutive behavior. Therefore, elevated temperature stamping is needed to produce magnesium alloy parts, which increases their production cost. Improvements in magnesium alloy sheet are thus needed and the research interest on this activity has greatly increased in the past few years [2]. Large research programs, such as the NSERC Magnesium Strategic Research Network (MagNET), have been created to study several aspects of

magnesium sheets, such as: alloy improvements, solidification and casting properties, thermo-mechanical processing, formability and high rate deformation, and joining properties of magnesium sheets. The current research is a part of the NSERC MagNET within the formability and high rate deformation theme.

The goal of the present research is to determine the high strain rate tensile behavior of AZ31B magnesium alloy sheets. Uniaxial tensile experiments were performed on work-hardened AZ31B-H24 and annealed AZ31B-O sheets. Three thicknesses of AZ31B-O were studied to characterize the effect of thickness on its constitutive behavior. A large range of strain rate was considered, from quasi-static experiments (at $0.003s^{-1}$) to high strain rates (up to $1500s^{-1}$). The low strain rate experiments ($0.003s^{-1}$ – $1s^{-1}$) were performed on a classical servohydraulic tensile machine. Intermediate rate experiments ($30s^{-1}$ – $100s^{-1}$) were performed on an instrumented falling weight impact apparatus, while the high strain rate tests ($500s^{-1}$ – $1500s^{-1}$) were performed using a tensile split Hopkinson bar.

Parameters of three constitutive models were fit to the experimental data. The models considered were the Johnson-Cook model [3,4], its modified version with a Cowper-Symonds [5] strain rate formulation, and the Zerilli-Armstrong model [6-8]. These three constitutive models are available in commercial finite element codes, such as LS-DYNA [9] which was used to simulate the constitutive behaviour of AZ31B-O during the tensile split Hopkinson bar experiments.

The remainder of this chapter presents a review of the literature pertinent to this research. This includes: a review of the characteristics and properties of magnesium alloys, especially in their sheet form; a brief review of material behaviour under high strain rate deformation, focusing on AZ31; a discussion on the development and different configurations of the split Hopkinson bar; and, a review of the Johnson-Cook and Zerilli-Armstrong constitutive models.

1.1 Magnesium Alloy Sheets

Among all elements, magnesium (Mg) is considered to be the 4th most abundant element in the Earth, following iron, oxygen and silicon [2]. Albeit largely available on Earth, magnesium has a limited usage in industry. As illustrated by Figure 1.1, magnesium is primarily used as an alloying component for aluminum alloys, 30% is used for die casting of magnesium alloys, and only 1% is used for wrought products such as magnesium sheet. Among commercially available magnesium alloys used in sheet production, AZ31 is the most common [10].

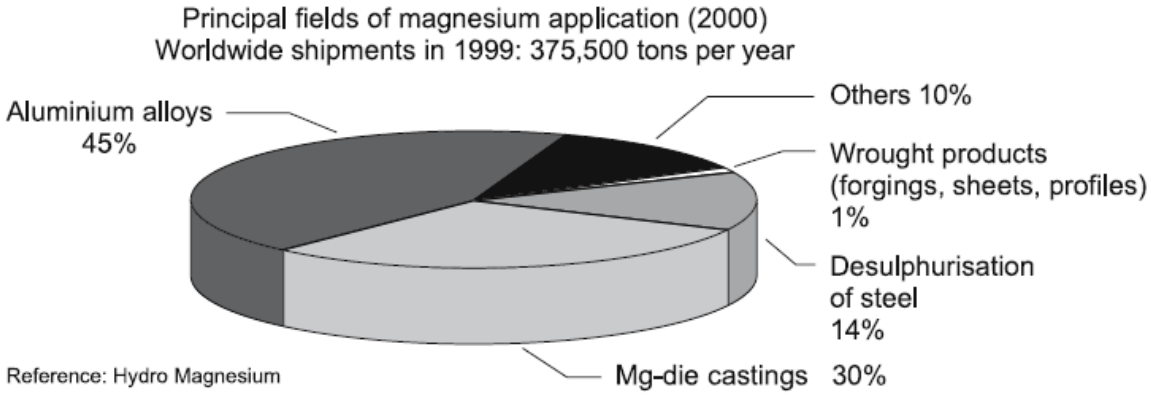

Figure 1.1: Principal fields of magnesium application [10]

The main reason for the low usage of magnesium alloy sheet is that they exhibit poor formability at room temperature [1,2,10]. However, their ductility is greatly increased at temperatures above 200°C. Therefore they can be formed, but the elevated temperature forming process increases the production cost. Several attempts to use magnesium sheet in vehicle body structures have been made, such as the ultralight magnesium body prototype developed by Allard in 1952 (Figure 1.2) with a total weight of only 64 kg [10]. But the low cost and good formability of steel forced magnesium alloys to step aside for the last 50 years. With increasing environmental concern, magnesium alloys have again became of interest to the automotive industry. Magnesium alloy sheet also presents tensile properties similar to conventional aluminum alloy sheet used for car body applications, as illustrated in Figure 1.3 [10].

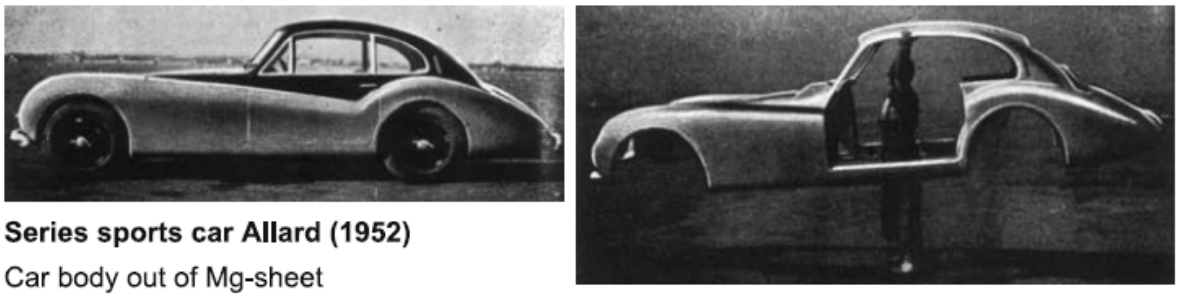

Series sports car Allard (1952)

Car body out of Mg-sheet
(thickness: 1.3 to 2.0 mm); Global weight (incl. doors and bonnet): 64 kg

Figure 1.2: Car body developed by Allard in 1952 and made of magnesium sheet [10]

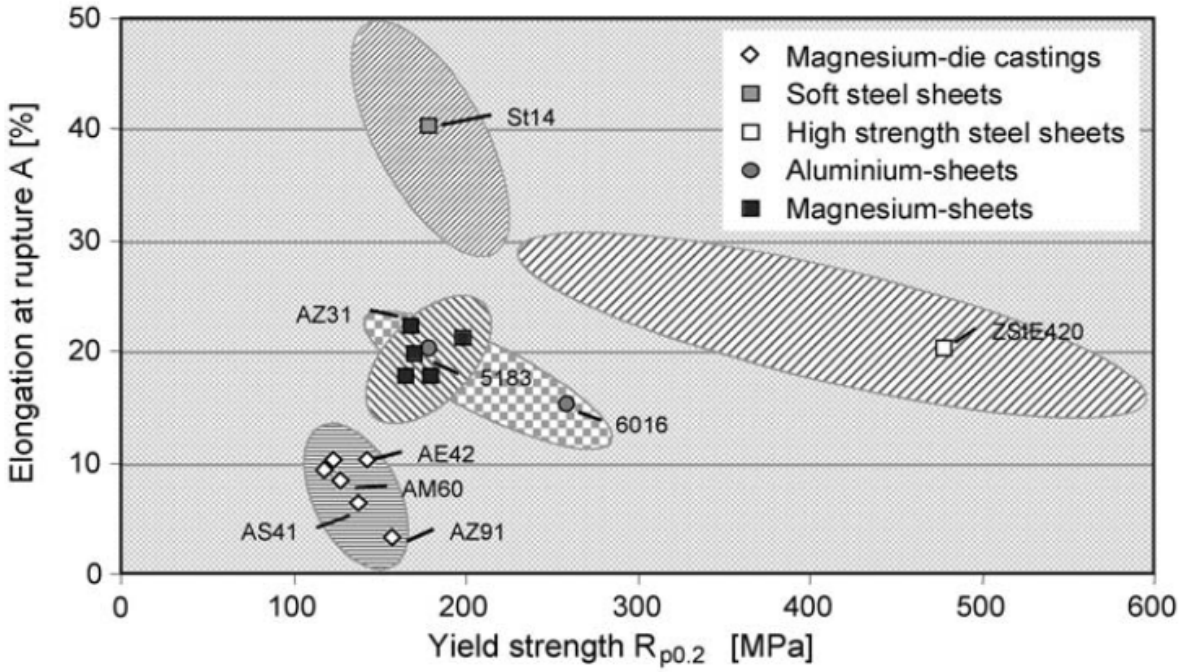

Figure 1.3: Mechanical properties of different materials for car body construction [10]

Magnesium alloys have a hexagonal close-packed (HCP) crystal structure with a c/a ratio of approximately 1.62 [11]. Therefore, only a limited number of slip systems are available to accommodate plastic deformation. According to the von Mises-Taylor criterion [11,12], at least five independent slip systems are needed to accommodate the arbitrary homogeneous deformation of polycrystalline materials. At room temperature, magnesium alloys have only four independent slip systems, and the remaining deformation is accommodated by twinning [12-14]. The different slip systems in HCP materials are illustrated in Figure 1.4. At elevated

temperatures, additional slip systems become active, providing sufficient independent systems to fulfill the von Mises-Taylor criterion [12-14]. This explains the clear improvement of ductility at elevated temperatures.

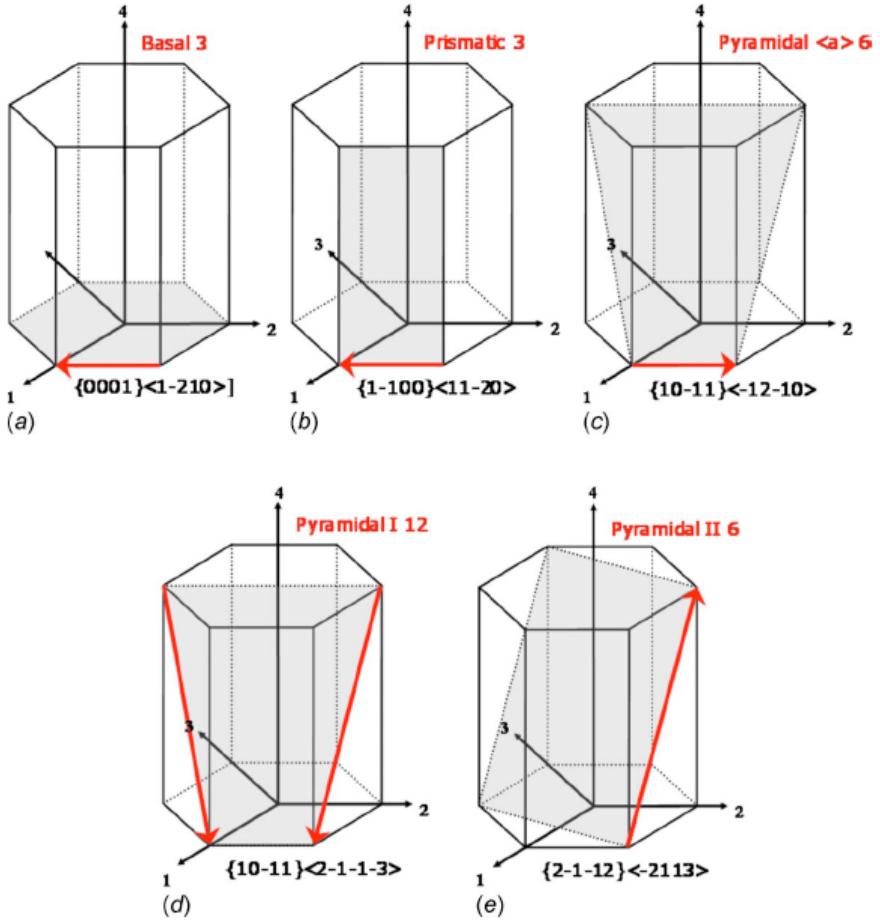

Figure 1.4: Main deformation mechanisms in magnesium crystals active at room temperature (a,b and c) and thermally activated (d and e) [15]

As few slip systems are available to accommodate deformation, the constitutive behaviour of magnesium alloys is strongly dependent on the orientation of their grains, known as their texture [16-18]. The texture evolution of magnesium depends on the deformation applied to the material. Thus, rolled material will have a different texture from extruded or cast parts [16-18]. Rolled magnesium alloy sheets show a strong basal texture, which means that the c-axis of the grains are mainly oriented parallel to the normal direction of the sheet, as illustrated in Figure 1.5.

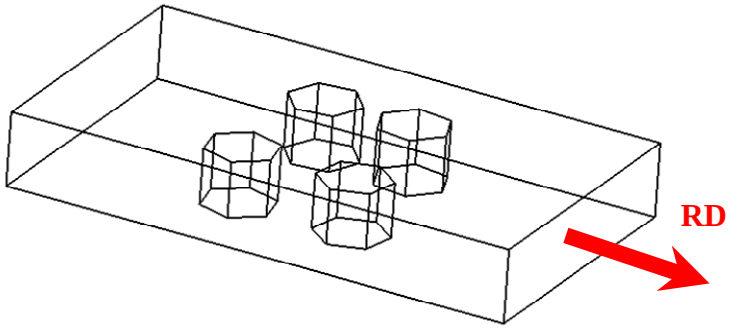

Figure 1.5: Schematic of grain orientation in rolled magnesium alloy sheet

This preferred grain orientation in magnesium alloy sheets creates a strong asymmetry in the constitutive behavior between in-plane tension and compression. Lou *et al.* [12] performed in-plane cyclic loading on AZ31B sheet. Their results can be seen in Figure 1.6, where (a) is a cyclic loading starting with compression, and (b) is a cyclic loading starting with tension. The strong tension-compression asymmetry can clearly be seen in the figure. The tensile part shows a "concave-down" curvature, whereas compression has a "concave-up" curvature. The shape of the compressive part is due to the onset of twinning occurring. One can notice that the tension behavior is different if it occurs after compression or not. Tension following compression shows an "S-shape" in the flow curve that is caused by a detwining process [12]. There is also an asymmetry in the yield strength with a lower value in compression than in tension.

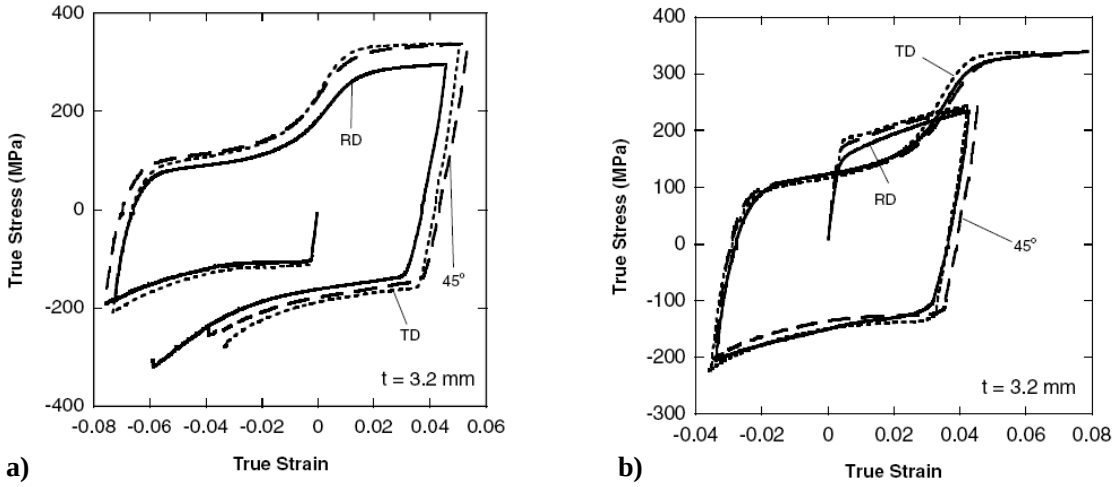

Figure 1.6: Cyclic loading on AZ31B sheet [12]

In addition to the asymmetric tension-compression behavior, Figure 1.6 also shows a strong anisotropy in the sheet plane; once again this is due to the preferred grain orientations induced by the rolling process [12].

Therefore, the constitutive behavior of AZ31 can only be determined after a given forming process which corresponds to a particular texture of the material.

1.2 High Strain Rate Material Behavior

Most materials exhibit a different constitutive behavior under various strain rate deformations. The strain rate sensitivity has been studied for an important number of materials, not limited to metals, such as ceramics [19], polymers [20], concrete [21], or muscle tissue [22], for example. For most metals, the flow stress has been shown to be linearly dependent on the logarithm of the strain rate, at least for certain ranges of strain rates. In fact, three ranges are generally accepted with three different log-linear relationships defined by different mechanisms governing the plastic flow [23]. These three regions can be seen in Figure 1.7 for En3B Steel [24].

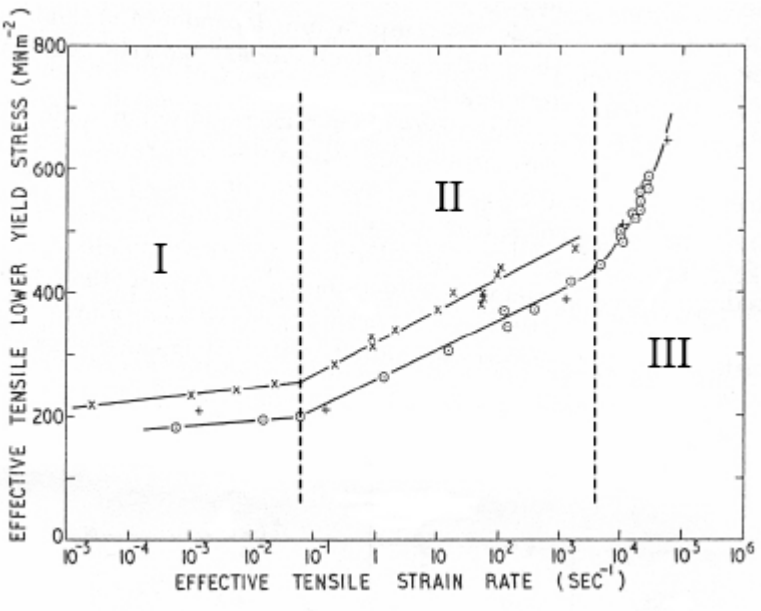

Figure 1.7: Effective tensile stress as a function of strain rate for En3B Steel [24]

Region I is governed by long-range obstacles to dislocation motion [24,25]. In region II, the deformation is controlled by thermally activated dislocation motion, while regions III is believed to be governed by drag mechanisms and relativistic effects [23]. Follensbee and Weertman [26] showed that dislocation drag effects are not rate controlling at strain rates below $10^4 s^{-1}$; therefore thermally activated dislocation motion can be considered as the governing mechanism over the range of strain rates considered in the current research ($0.003 s^{-1}$ – $1500 s^{-1}$).

1.2.1 Thermally Activated Dislocation Motion

During plastic deformations, dislocations moves through the lattice. They continuously encounter obstacles that make their motion more difficult. These obstacles can be solute atoms, vacancies, grain boundaries, precipitates, or even other dislocations [23]. Energy is needed to overcome these obstacles, and it can be provided either by an increase in the applied stress or by random thermal fluctuations. Figure 1.8 shows a schematic of the stress required to overcome short-range obstacles as a function of temperature. As seen in the figure, thermal energy only can be sufficient to overcome these shot-range obstacles. However, there are long-range obstacles that only depend on the structure of the material and can not be overcome by thermal energy. The flow stress can therefore be decomposed into thermal and athermal components [23]:

$$\sigma = \sigma_G(structure) + \sigma^*(T, \dot{\varepsilon}, structure) \tag{1.1}$$

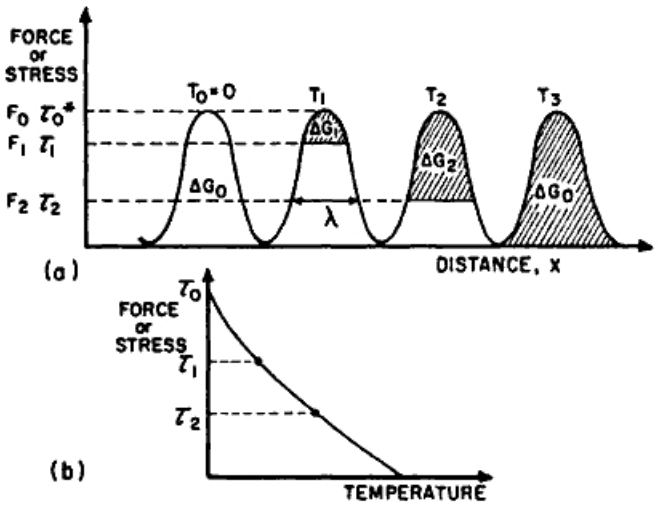

Figure 1.8: (a) Overcoming of barriers by thermal energy; (b) stress required to overcome obstacle as a function of temperature [23]

Based on statistical considerations for dislocations to overcome obstacles, the average strain rate can be described by an Arrhenius equation, presented in Equation (1.2) [23], where $\dot{\varepsilon}_0$ is a material constant, k is the Boltzmann constant, T is the absolute temperature and ΔG is the amount of energy provided by thermal fluctuations to overcome the obstacle.

$$\dot{\varepsilon} = \dot{\varepsilon}_0 \exp\left(-\frac{\Delta G}{k T}\right) \tag{1.2}$$

This equation can be transformed to express ΔG as a function of the temperature and the strain rate, as seen in Equation (1.3). This equation is very important since it shows that the short-range energy barrier is reduced as the temperature increases, but is increased by increasing strain rate. Therefore, increasing temperature tends to soften the material, whereas increasing strain rate strengthens it.

$$\Delta G = k T \ln\left(\frac{\dot{\varepsilon}_0}{\dot{\varepsilon}}\right) \tag{1.3}$$

Lindholm and Yeakley [27] expressed the thermal energy ΔG as a function of stress in a linear relationship and deduced a constitutive model exclusively based on thermal activation presented in Equation (1.4), where ΔG_0 is the activation energy at 0 K and V is the activation volume. In most cases, σ_G and V are taken to be functions of strain only [27].

$$\sigma = \sigma_G + \frac{\Delta G_0}{V} + \frac{kT}{V} \ln\left(\frac{\dot{\varepsilon}_0}{\dot{\varepsilon}}\right) \tag{1.4}$$

In this equation, there is a logarithmic dependence of the flow stress on the strain rate, which agrees with what can be seen in regions I and II of Figure 1.7.

1.2.2 High Strain Rate Properties of Magnesium Alloys

Most of the previous work on magnesium alloys has been focused on quasi-static deformation to understand the effect of temperature and texture on their mechanical response. However, some dynamic experiments have been carried on magnesium alloys, mostly on extruded and cast material, and predominantly in compression.

Dominant deformation mechanisms at different strain rates have been studied for magnesium alloys. Ishikawa *et al.* [28,29] performed some compression tests on cast AZ31 and AZ91

materials; and showed that deformation is mainly driven by dislocation creep for strain rates lower than $0.1s^{-1}$, whereas at higher strain rates the dominant mechanisms are dislocation glide and twinning, even at elevated temperatures. Tan *et al.* [30] confirmed these results and provided tensile experiments for strain rate up to $10s^{-1}$. They conclude that tensile deformations are mainly controlled by dislocation glides, and not also by twinning as for compression.

Tan *et al.* [30] also showed that twinning in compression is still present at high strain rate and elevated temperatures, whereas quasi-static deformations at the same temperatures are mainly governed by dislocation glide. This results in different shapes of the true stress-strain curves, as seen in Figure 1.9. One can also notice in the figure that under quasi static conditions, there is a clear change of behavior between 473 K and 523 K data, which is explained by the existence of a critical number of twins that controls deformations during the S-shape region of the curve [30].

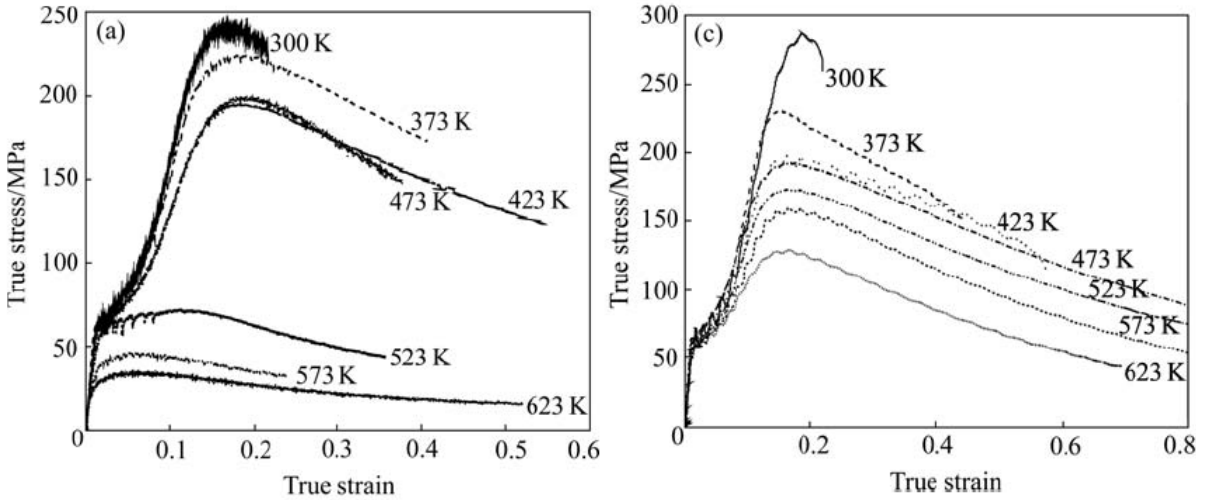

Figure 1.9: Compressive true stress-strain curves at different temperatures and at strain rates of $10^{-3}s^{-1}$ (a) and $10s^{-1}$ (c) [30]

Li *et al.* [31] and Mukai *et al.* [32] investigated the effect of grain size on the dynamic behavior of extruded magnesium alloys ZK60 and WE43, respectively. Mukai *et al.* [32] performed tensile experiments, while Li *et al.* [31] performed compressive tests. In both cases, they observed an improvement of the ductility at high strain rate as the average grain size is reduced, as seen in Figure 1.10. Li *et al.* [31] also showed that at high strain rate, the

compressive ductility improves as the strain rate increases, as illustrated in Figure 1.11. This result is also confirmed by El-Magd and Abouridouane [33] for extruded AZ80.

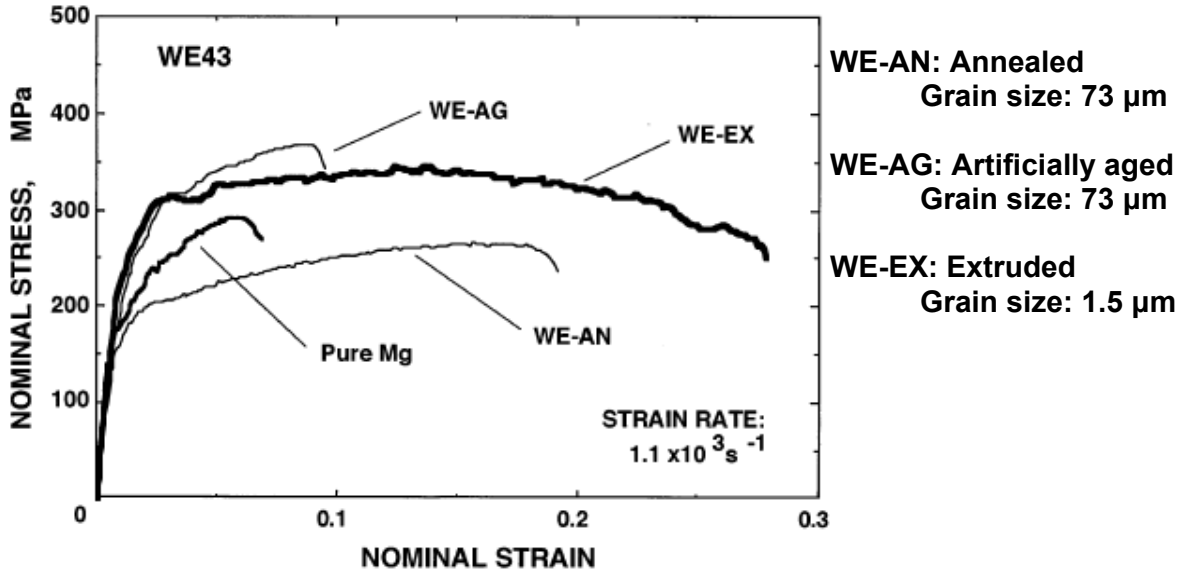

Figure 1.10: Effect of grain size on the ductility at high strain rate of WE43 magnesium alloy [32]. (The present author added the legend on the right.)

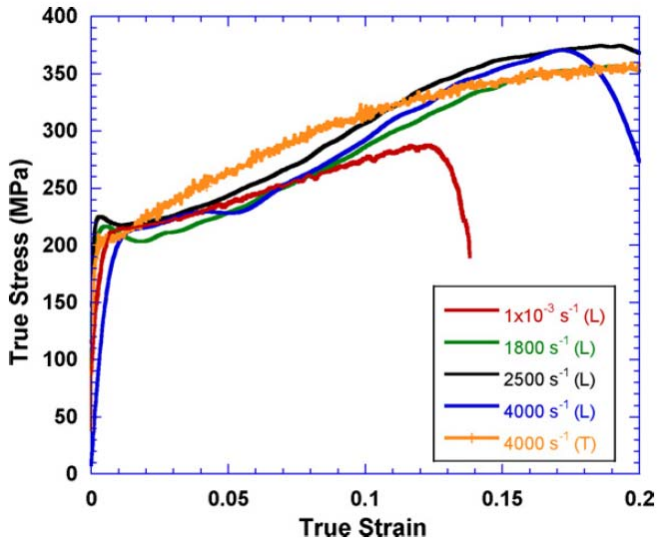

Figure 1.11: True stress vs. true strain for ZK60 processed by ECAP and tested in compression at different strain rates [31]

All of the previously cited work was done on cast and extruded materials, very few studies have been made on rolled materials at high strain rate. Tucker *et al.* [34] performed compressive experiments on 19.05 mm thick AZ31B-H24 plate in different directions and at high strain rates. They showed that in addition to a strong anisotropy of the material, the strain rate sensitivity is also anisotropic, as seen in Figure 1.12. They also reported that as the strain rate increases, the strain to failure increases for compression tests in the normal direction, whereas it slightly decreases for the rolling and transverse directions [34].

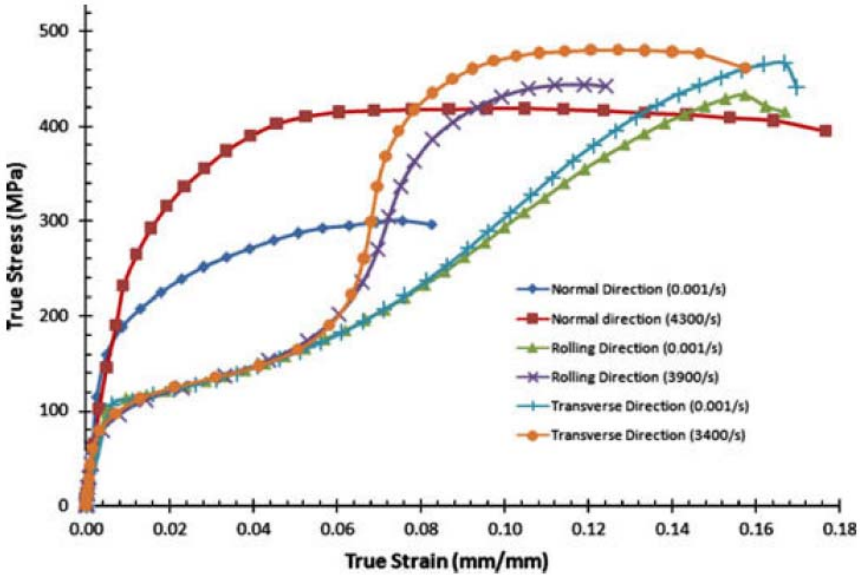

Figure 1.12: Compressive true stress-strain curves of AZ31B-H24 showing the anisotropic effect on the strain rate dependence [34]

Ulacia *et al.* [35] investigated the dynamic behavior of AZ31B-O sheets and its microstructural evolution. They performed low and high strain rate tests ($10^{-3}s^{-1}$ and $10^{3}s^{-1}$) in both tension and compression and at different temperatures. Tensile tests were performed on a 1mm thick material, whereas compression samples were machined from 3mm thick material. They showed that even at high temperature (up to 400°C), the material has a clear anisotropy, as well as a strong tension-compression asymmetry, as seen in Figure 1.13; whereas at quasi-static rates, tensile and compressive behaviors are similar for temperatures higher than 200°C [35]. They explained this behavior based on the activation of non-basal slip systems rather than twinning when the temperature increases at quasi-static rates, whereas twinning remains as

more easily activated than non-basal slip systems under elevated temperature at high strain rate conditions [35].

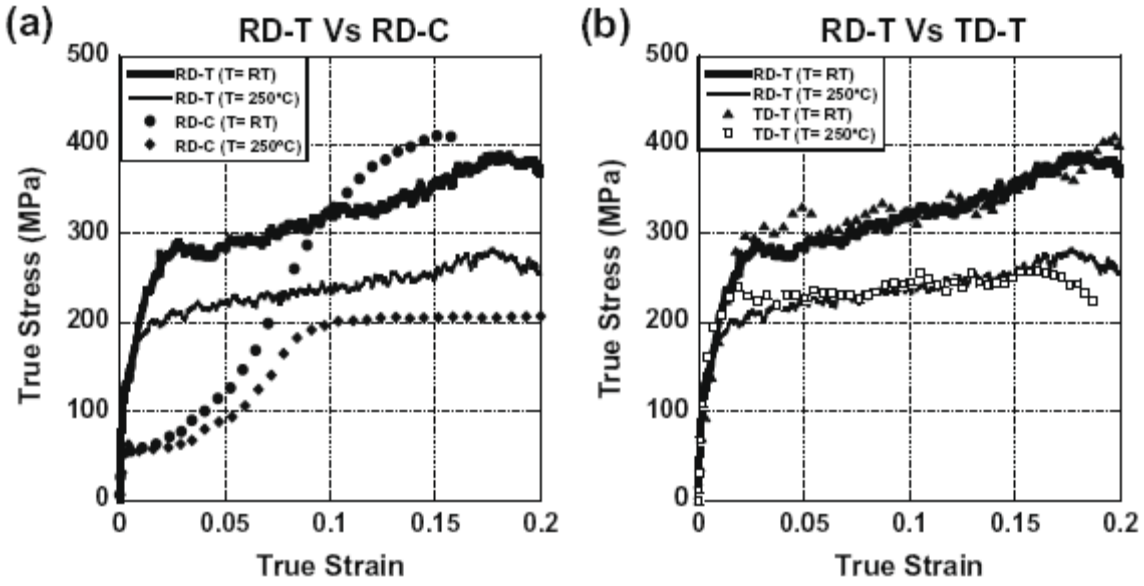

Figure 1.13: True stress-strain curves of AZ31B-O at $10^3 s^{-1}$ and different temperatures for in-plane tension-compression in the RD (a) and in-plane tension in the RD and the TD (b) [35]

1.3 The Split Hopkinson Bar

1.3.1 Creation of the Apparatus

In 1914, Hopkinson [36] developed an apparatus to study the pressure pulse produced by the impact of a bullet or by a detonation. His apparatus consisted of a round bar, a small pellet and a ballistic pendulum. A schematic of this apparatus is given in Figure 1.14. The explosive and the pellet are placed at each end of the bar. The pellet is made of the same material and has the same cross section as the bar, and is initially in contact with it. During the experiment, the explosive (A) creates a compressive pulse that propagates along the bar (B). When the pulse reaches the pellet (C), a portion of it enters the pellet, causing the pellet to fly away from the bar and to trap a part of the momentum generated by the detonation. The momentum of the

pellet was measured by a ballistic pendulum (D). Hopkinson used pellets of different sizes to measure the pressure-time relationship of the compressive pulse generated by the detonation.

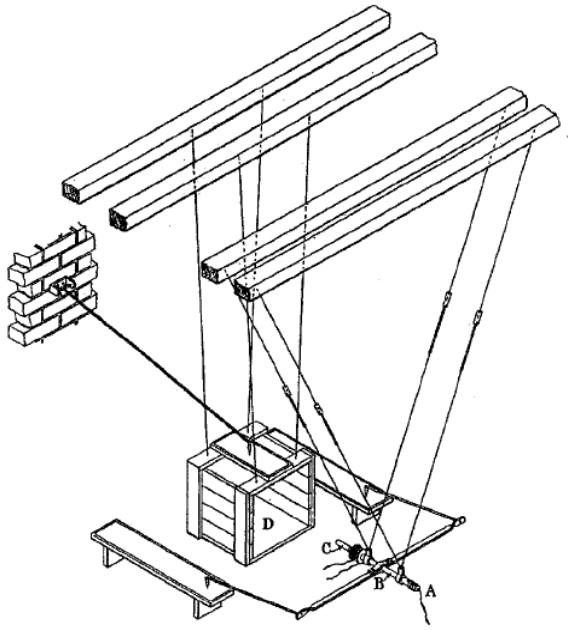

Figure 1.14: Apparatus developed by Hopkinson in 1914 [36]

In 1949, Kolsky [37] modified this experiment and introduced the split Hopkinson pressure bar (SHB) apparatus, and used it to determine the dynamic behaviour of several materials (polythene, rubber, PMMA, copper and lead) [37]. Kolsky initially design the SHB for compressive experiments. It comprises two bars of similar material and cross section. The material that is tested is placed between the two bars. Kolsky determined the stress-strain response of the material by analysing the transmission of a compressive pulse through the tested material. He used explosives to create a compressive pulse and measured the stress waves in each bar using condensor microphone. By assuming that the bars remain elastic, he could directly relate the stress waves to the displacement of the bars. Nowadays, the pulse is created by a striker bar propelled by a gas gun; and the pulse propagation through the bars is recorded by strain gauges.

The SHB comprises three bars with similar characteristics: a striker, an incident bar and a transmitted bar. During a test, the striker impacts the end of the incident bar, creating a stress pulse that propagates in the bar. When it reaches the specimen, a part of the pulse is transmitted

to the transmitted bar through the specimen, and the remainder is reflected back into the incident bar. The duration of the loading pulse is controlled by the length of the striker since the end of the pulse corresponds to the reflection of the elastic wave in the striker reaching the interface striker-incident bar. Therefore the distance that this wave travels is approximately equal to two times the striker length. A schematic of a compressive SHB can be seen in Figure 1.15, as well as a diagram illustrating the pulse propagation in the different parts of the apparatus.

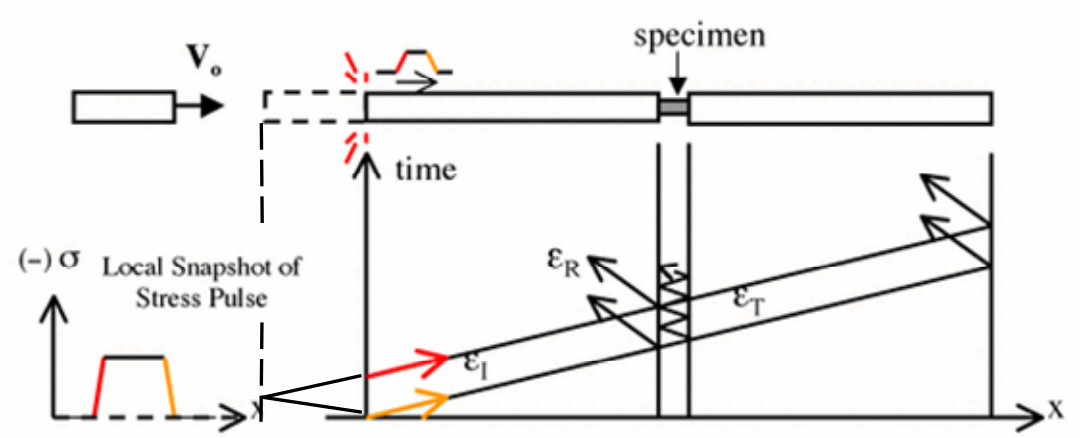

Figure 1.15: Schematic of a CSHB and propagation of elastic waves in the bars

To fully understand the principle of the split Hopkinson bar, stress and strain waves propagation in the bar must be understood, as well as their possible application to determine the constitutive behaviour of the tested material.

1.3.2 Elastic Waves in a Cylindrical Bar:

The Hopkinson bar theory is based on elastic waves propagating in a cylindrical bar. The striker hits the bar and creates a longitudinal wave in the incident bar [23]. A cylindrical bar is a bounded medium, so boundary conditions will be taken into account, i.e. only the axial stress is non-zero. The following analysis neglects any strains or inertia along the direction transverse to the bar. Such assumptions of the split Hopkinson bar analysis are discussed later in Section 1.3.4. The following derivations are taken from the text book by Meyers [23].

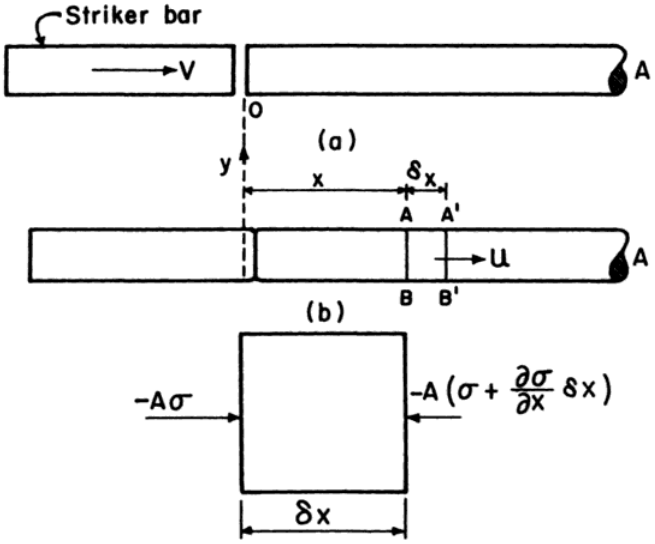

Figure 1.16: Propagation of wave in bar produced by impact of the striker (q) prior to impact and (b) after impact [23].

Considering two sections AB and A'B' at the front of the wave at time t, as seen in Figure 1.16, Newton's second law applied to AA'BB' can be seen in Equation (1.5), where A is the cross section of the bar, ρ is its density, σ_x is the axial stress in the bar and u_x is the particle axial displacement.

$$-\left[A\sigma_x - A\left(\sigma_x + \frac{\partial \sigma_x}{\partial x}\right)\delta x\right] = A\rho\,\delta x \frac{\partial^2 u_x}{\partial t^2} \tag{1.5}$$

Equation (1.5) can then be reduced to:

$$\frac{\partial \sigma_x}{\partial x} = \rho \frac{\partial^2 u_x}{\partial t^2} \tag{1.6}$$

Considering that the material of the bar is isotropic and only the axial stress is non-zero, the axial stress can be expressed using the one-dimensional Hooke's law as:

$$\sigma_x = E\,\varepsilon_x = E\frac{\partial u_x}{\partial x} \tag{1.7}$$

Using Equation (1.7), Equation (1.6) can be expressed in term of displacement as:

$$E\frac{\partial^2 u_x}{\partial x^2} = \rho \frac{\partial^2 u_x}{\partial t^2} \tag{1.8}$$

Equation (1.8) is a wave propagation equation for the displacement field in the case of longitudinal waves in a cylindrical bar. This wave propagates at a velocity of:

$$C_0 = \sqrt{\frac{E}{\rho}} \tag{1.9}$$

A similar wave propagation equation can be obtained for the axial strain in the bar by taking the derivative of Equation (1.8) with respect to x:

$$E\frac{\partial^2}{\partial x^2}\left(\frac{\partial u_x}{\partial x}\right) = \rho\frac{\partial^2}{\partial t^2}\left(\frac{\partial u_x}{\partial x}\right) \quad \Leftrightarrow \quad E\frac{\partial^2 \varepsilon_x}{\partial x^2} = \rho\frac{\partial \varepsilon_x}{\partial t^2} \tag{1.10}$$

Using Hooke's law, the wave propagation equation for the axial stress is easily obtained from Equation (1.10):

$$E\frac{\partial^2 \sigma_x}{\partial x^2} = \rho\frac{\partial \sigma_x}{\partial t^2} \tag{1.11}$$

This analysis shows that during a split Hopkinson bar test, both the axial strain and stress are propagating in the bar at the same velocity C_0.

Furthermore, the particle velocity V_p can be related to the amount of stress or strain due to the conservation of momentum. When the striker hits the incident bar, it creates a change in momentum:

$$\begin{aligned} F\,dt &= d(mV_p) \\ \sigma_x A dt &= \rho A dx V_p \\ \sigma_x &= \rho\frac{dx}{dt}V_p \\ \sigma_x &= \rho C_0 V_p \end{aligned} \tag{1.12}$$

Using Hooke's law and the expression of the wave velocity C_0, the particles velocity can be simply expressed as:

$$V_p = C_0 \varepsilon_x \tag{1.13}$$

1.3.3 Application to the Hopkinson Bar Apparatus

Even if elastic waves only occur in the incident and transmitter bars during a split Hopkinson bar experiment (the specimen does yield), elastic wave theory can be used to determine the constitutive response of the specimen.

In the following analysis, all material properties or dimensions related to the bars are noted with the subscript *0*, and no subscript is used for the sample properties, dimensions, stress and strain values.

The interfaces between the sample and the bars are studied to determine the stress and strain of the specimen. These interfaces can be seen in detail in Figure 1.17, where ρ_0 is the, E_0 is the Young's modulus, and A_0 is the cross-section of the bars, A is the cross section of the specimen, and L is its initial gauge length.

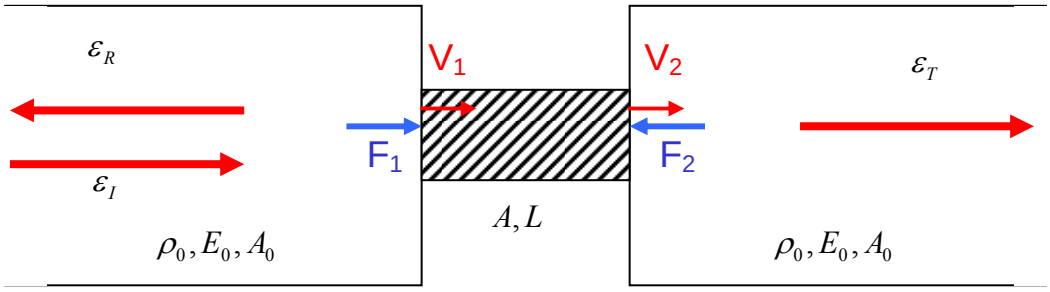

Figure 1.17: Interface velocities and forces during a split Hopkinson bar test

Based on Equation (1.13), the particle velocities at each interface are given by Equation (1.14), where ε_I, ε_R and ε_T are respectively the incident, reflected and transmitted strain waves at the end of the bars.

$$\begin{cases} V_1 = C_0(\varepsilon_I - \varepsilon_R) \\ V_2 = C_0\varepsilon_T \end{cases} \qquad where \;\; C_0 = \sqrt{\frac{E_0}{\rho_0}} \tag{1.14}$$

The strain rate of the sample is defined by $\dot{\varepsilon} = \frac{\partial \varepsilon}{\partial t} = \frac{V_1 - V_2}{L}$, and can thus be related to the elastic waves in the bars using Equation (1.14):

$$\dot{\varepsilon} = \frac{C_0}{L}(\varepsilon_I - \varepsilon_R - \varepsilon_T) \tag{1.15}$$

At each interface, the forces applied to the specimen are respectively:

$$\begin{cases} F_1 = A_0\sigma_{0I} = E_0A_0(\varepsilon_I + \varepsilon_R) \\ F_2 = A_0\sigma_{0T} = E_0A_0\varepsilon_T \end{cases} \tag{1.16}$$

If the specimen is at equilibrium, those forces are equal: $F_1=F_2=F$. A relation between the different strain waves at the end of the bars can be deduced using Equation (1.16) and the equilibrium assumption:

$$\varepsilon_T = \varepsilon_I + \varepsilon_R \tag{1.17}$$

Using this relation in Equation (1.15) gives a simplified form of the sample strain rate:

$$\dot{\varepsilon} = -\frac{2C_0}{L}\varepsilon_R \tag{1.18}$$

Finally, the equilibrium condition along the sample gives the expression of the uniform stress in the specimen:

$$\sigma = \frac{F}{A} = E_0 \frac{A_0}{A}\varepsilon_T \tag{1.19}$$

Equations (1.18) and (1.19) express the strain rate and stress history of the sample as a function of the strain history at the end of the bars. The strain of the sample is obtained by integration of the strain rate.

To summarize the previous analysis, the specimen stress, strain and strain rate histories can be calculating using the set of equations presented in Equation (1.20).

$$\begin{cases} \sigma(t) = E_0 \dfrac{A_0}{A}\varepsilon_T(t) \\ \dot{\varepsilon}(t) = -\dfrac{2}{L}\sqrt{\dfrac{E_0}{\rho_0}}\varepsilon_R(t) \\ \varepsilon(t) = -\dfrac{2}{L}\sqrt{\dfrac{E_0}{\rho_0}}\int_0^t \varepsilon_R(t)dt \end{cases} \tag{1.20}$$

1.3.4 Assumptions and Limitations of the Hopkinson Bar Analysis

Throughout the previous analysis, several assumptions were made and must be validated to be used for a split Hopkinson bar test. First, the specimen was assumed to be at equilibrium during the experiment. However, wave propagation through the specimen must also be considered since the load is applied to only one end of the specimen. Davies and Hunter [38] estimated that π reverberations of the stress wave in the specimen are needed to reach a uniform stress state. The "ring-up time" t_e before equilibrium was estimated by Equation (1.21)

[38,39], where ρ_s is the specimen density, L_s is its gauge length, and $d\sigma/d\varepsilon$ is the slope of the true stress-strain curve of the material tested.

$$t_e = \sqrt{\frac{\pi^2 \rho_s L_s^2}{\frac{d\sigma}{d\varepsilon}}} \tag{1.21}$$

As this ring-up time is necessary prior to being able to analyze the experimental data, it becomes very difficult to determine the elastic behavior of the specimen and its yield strength. Several techniques have been used to reduce the ring-up time. One of them is to reduce the size of the specimen, as its length is proportional to the ring-up time [23]. Another method is to increase the rise time of the incident pulse. This is done by using a "pulse shaper", which consists in placing a soft metal shim between the incident bar and the striker [23].

Another assumption made during the split Hopkinson bar analysis is that the waves were only propagating in one direction. During an actual impact between the striker and the incident bar, several types of waves, such as spherical or surface waves, are generated and propagate at different velocities in every direction [23]. Pochhammer and Chree [40,41] calculated the solution to elastic wave propagation in an infinitely long cylinder, and proved that the longitudinal stress varies across the section of the bar. Davies [42] applied their solution to the SHB and found that the stress across the section of the bar was uniform after 10 diameters distance along the length of the bar [42]. Therefore, if the incident bar is long enough, the stress wave can be considered as a 1D wave, as described in Section 1.3.2.

Furthermore, the analysis presented in Section 1.3.3 refers to incident, reflected and transmitted strain waves at the bar-specimen interface. Due to the superposition of the incident and reflected waves, it is impossible to measure them independently at this interface. Therefore, strain gages are used at different locations on the bars to measure the strain histories. The direct use of these strain histories implied that stress and strain waves propagate without distortion along the bars. Davies [43] showed that the propagation velocity of an elastic wave is a function of the ratio between the radius R of the bar and the wavelength λ of the wave. As the incident pulse can be expressed as a sum of several waves with different wavelength using its Fourier series, the overall shape of the pulse will be distorted as it

propagates in the bar. However, the propagation velocity is equal to the sound velocity in the bar for $R/\lambda<<1$ [43]. Salisbury [44] used a spectral analysis on AA6061-T6 bars and found that no dispersion or attenuation correction was needed. The current research uses split Hopkinson bars with characteristics similar to those used by Salisbury [44], therefore the same assumption was made.

1.3.5 Tensile Split Hopkinson Bar

The previous SHB analysis was given for compressive tests, but the SHB principle can be applied to different loading states, including compression, tension, torsion [23], and even complex loading tests such as three-points bending [45]. The compressive split Hopkinson bar (CSHB) is the most used configuration due to its setup simplicity. The second most used is the tensile split Hopkinson bar (TSHB), but there are several challenges that are the subject of constant improvement, such as the quality of the incident tensile pulse generation and the gripping of the specimen [23].

There are two approaches to generate a tensile load: using a modified version of a CSHB to generate tension in the specimen; or directly generating a tensile pulse in the incident bar. The first method was investigated by Lindholm *et al.* [46], who used a CSHB apparatus with a hat-shaped specimen to generate tension, as seen in Figure 1.18. One advantage of this configuration is that it doesn't need external components to attach the specimen, such as threads, screw or glue. Therefore, it avoids possible wave dispersion associated with mechanical gripping of the specimen.

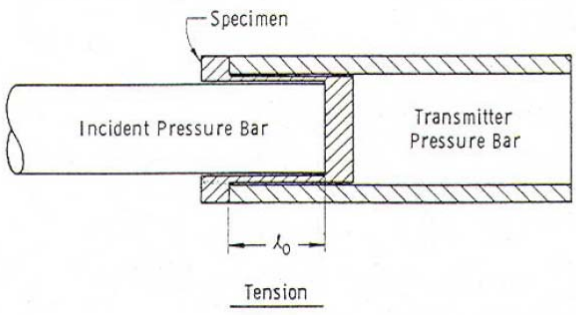

Figure 1.18: TSHB setup used by Lindholm [46]

A second method using a CSHB setup was proposed by Nicholas [47]. He used a cylindrical specimen threaded into the ends of the bar. He included a tight-fit collar between the two bars and over the specimen, as seen in Figure 1.19. The collar was made of a similar material to the bars to avoid any reflections created by a difference in material impedance. When the compressive pulse reaches the specimen region, ideally the whole pulse travels through the collar and is transmitted to the other bar. When it reaches the end of the transmitted bar, the pulse reflects entirely as a tensile wave. On the way back, the pulse loads only the specimen in tension since the collar is not attached to the either of the bars. This method requires a very precise assembly, and many reflections and interactions can occur and affect the experimental data [47,48].

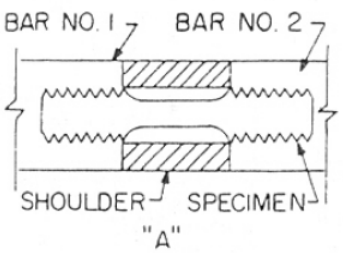

Figure 1.19: TSHB setup used by Nicholas [47]

Due to their specimen geometries, those two configurations can't be applied to thin materials such as metal sheets. Mouro [49] proposed a CSHB configuration to test metal sheet in tension. Mouro [49] used a configuration similar to the one proposed by Lindholm [46], but adapted to metal sheets. A view of his setup and the specimen used can be seen in Figure 1.20.

a) 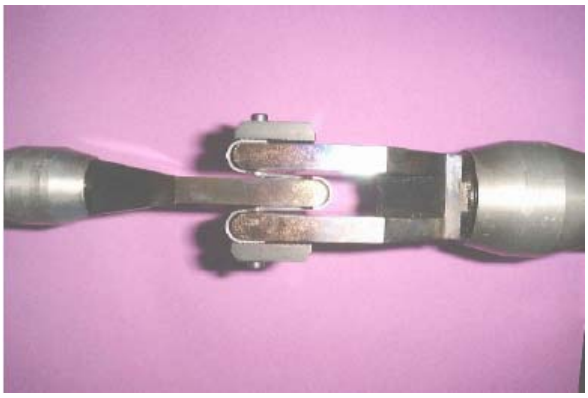 b) 

Figure 1.20: Details of the TSHB setup (a) and the tensile specimen (b) used by Mouro [49]

Haugou *et al.* [50] proposed another CSHB configuration to provide indirect tensile load on the specimen. His method is similar to the one proposed by Nicholas [47] and used the reflection of the pulse in the second (transmitter) bar to load the samples in tension. To reduce the dispersion caused by this method and the important transition of geometry associated with the collar (Figure 1.19), he fixed the specimen on the outside of the bar, as seen in Figure 1.21. Four specimens are attached to the setup using an epoxy adhesive.

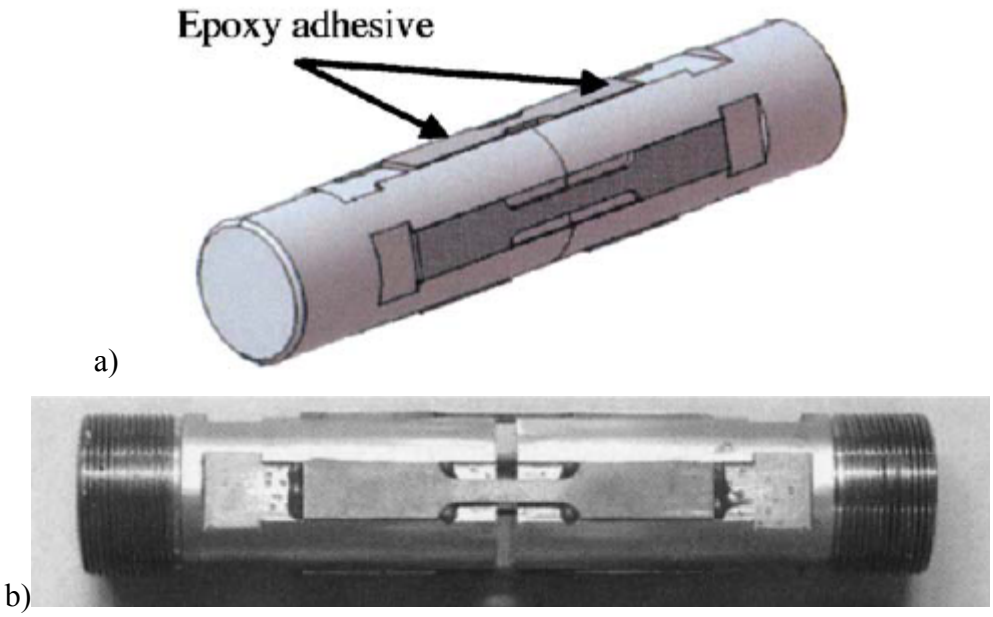

Figure 1.21: (a) Schematic and (b) picture of the TSHB setup for sheet used by Haugou [50]

Another widely used approach is to directly generate a tensile pulse in the incident bar using a hollow striker that travels over the incident bar and impact an end cap threaded at the end of the bar. This method is more complex to set up, as the striker and the gas gun surround the incident bar, as seen in Figure 1.22.

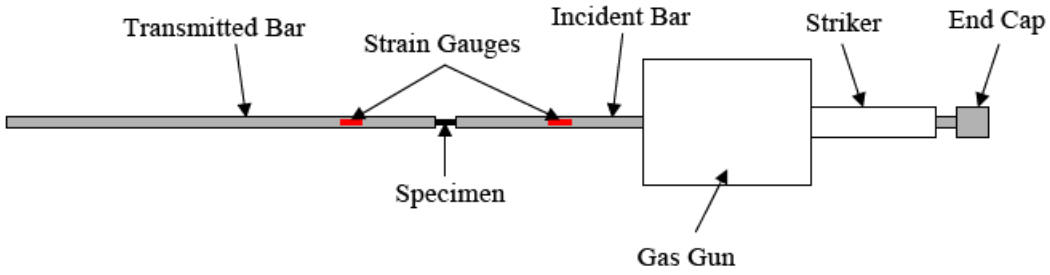

Figure 1.22: Schematic of a directly loaded TSHB

Several techniques were used to fasten the specimen in the grips. LeBlanc and Lassila [51] used a wedge-type grip, while Kang *et al.* [52] and Huh *et al.* [53] used slots machined at the end of the bars and fastened the specimen using screw. A similar technique was used by Smerd *et al.* [54], Bardelcik *et al.* [55], Thompson *et al.* [56] and Winkler *et al.* [57] to characterize the high strain rate tensile properties of sheets of aluminum alloys, boron steel, dual phase steels and high-strength steels, respectively. However, this last technique implied a set of bar for each material thickness, as the specimen should perfectly fit in it to provide a good clamping pressure. A picture of the gripping technique used by Huh *et al.* [53] can be seen in Figure 1.23. In more recent techniques, such as the one used by Verleysen and Degrieck [58], the specimen is glued in the slot to avoid any distortion created by the screws.

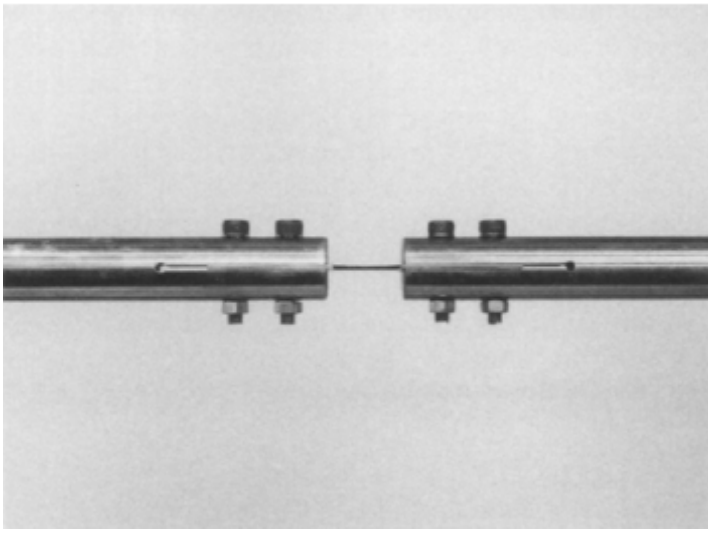

Figure 1.23: TSHB setup for metal sheets used by Huh [53]

Staab and Gilat [59], and Gilat *et al.* [60] used a so-called "direct-tension split Hopkinson bar" technique to create the loading pulse. For this technique, a clamp is used in the middle of the incident bar. The end part of the bar is then loaded in tension, the energy being stored in the bar by the clamp. When the clamp is released, a tensile wave propagates from the clamp position in the two half of the bar; their magnitude is then equal to half of the initial energy stored. A schematic of this configuration and the wave propagation of the different waves in the bar can be seen in Figure 1.24. This technique presents many advantages, the striker is not needed anymore, and thus, there is no distortion of the incident pulse induced by the impact or the lack of geometry match between the striker and the incident bar, as seen in Figure 1.25 where the

incident wave is almost perfectly square. Furthermore, the duration of the loading is controlled by the position of clamp on the bar and not by the length of the striker. And finally, the magnitude of the incident wave can be precisely controlled by the amount of stored load applied initially.

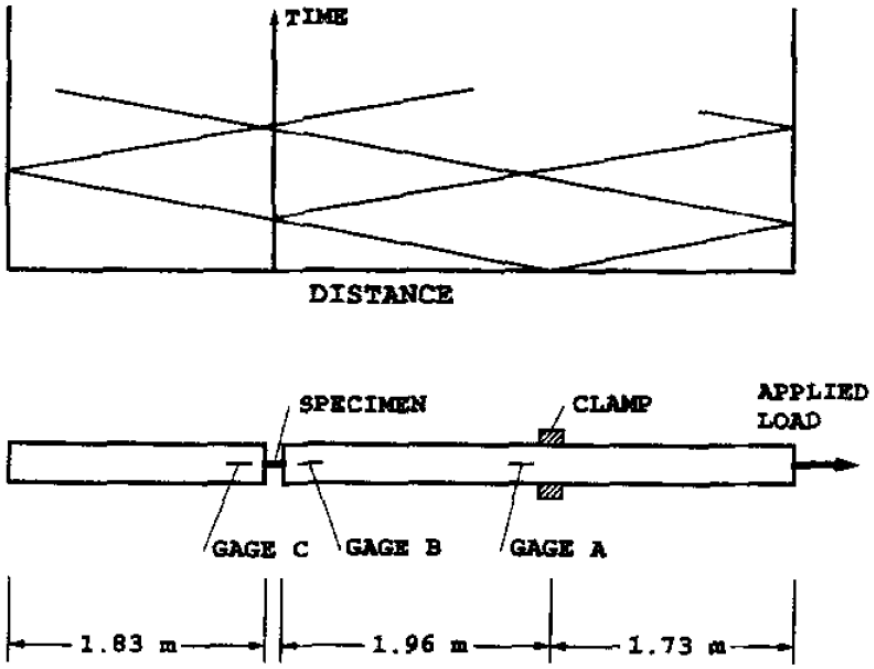

Figure 1.24: Schematic and wave propagation diagram of the direct-tension split Hopkinson bar [59]

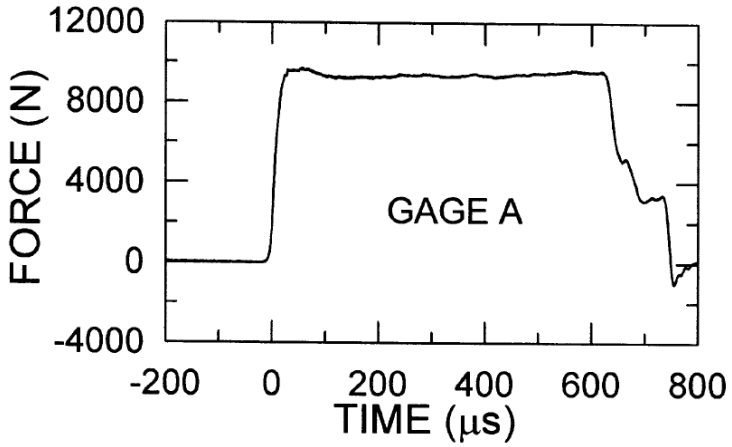

Figure 1.25: Incident wave created by the direct-tension split Hopkinson bar technique [60]

1.4 Constitutive Models

Numerical modeling is a very important tool in the analysis of many industrial processes and impact events, such as vehicle crashworthiness. In order to improve the accuracy of numerical simulations, good material models are essential to represent the material's constitutive response. Two of the most commonly used models for high strain rate deformation are the Johnson-Cook [3,4] and Zerilli-Armstrong models [6-8]. They are widely used because of their simplicity, which is essential to save computational resources large-scale in simulations, such as car crash simulations. These two models take into account the effect of strain rate and temperature on the constitutive behavior of the material, and can be used over a wide range of temperature and strain rate. Therefore they were adopted in the current research and are presented in this section.

1.4.1 Johnson-Cook

The Johnson-Cook model was introduced by Johnson and Cook [3,4] in 1983. This is an empirical model that accounts for the effect of strain, strain rate and temperature on the flow stress. The mathematical formulation of this model can be seen in Equation (1.22).

$$\sigma = \left(A + B\,\varepsilon_p^{n}\right)\left(1 + C\ln\dot{\varepsilon}^{*}\right)\left(1 - T^{*m}\right) \tag{1.22}$$

In Equation (1.22), σ is the true stress, ε_p is the effective plastic strain, $\dot{\varepsilon}$ is the plastic strain rate, and T^* is a form of homologous temperature, defined in Equation (1.23). A, B, n, C and m are material constants that should be determined experimentally. $\dot{\varepsilon}^*$ is a dimensionless strain rate defined in Equation (1.24), where $\dot{\varepsilon}_0$ is a reference strain rate that allows a dimensionless expression in the natural logarithm, and permits different time units in finite element simulations without modifying the other material constants.

$$T^{*} = \frac{T - T_{ref}}{T_{melt} - T_{ref}} \tag{1.23}$$

$$\dot{\varepsilon}^{*} = \frac{\dot{\varepsilon}}{\dot{\varepsilon}_0} \tag{1.24}$$

The Johnson-Cook model is based on a power-law hardening relationship in the term relating true stress to effective plastic strain (the first term in Equation (1.22)) and the material

parameters A, B and n. The power-law relationship is then scaled by the second and third terms of the model to take into account the increase of flow stress as the strain rate increases, and its decrease as the temperature increases. Material parameter C controls the logarithmic strain rate sensitivity, and m describes the exponential thermal softening.

When Johnson and Cook evaluated their model [3,4], they predicted the deformed shape of cylindrical samples after Taylor impact experiments, which consists of the impact of a cylindrical sample against a hardened anvil. The end of the cylinder deforms plastically in a mushroom shape. A very wide range of strain rate deformations is involved in this experiment, therefore correctly predicting the mushrooming of the cylinder assess the quality of the model over this very large range of strain rates. They considered three different materials: Armco iron, 4340 steel and Oxygen-free high conductivity (OFHC) copper. Numerical predictions were in very good agreement with the experiments for Armco iron and 4340 steel. However, the OFHC copper simulations were not as good as the other two materials, even if the prediction was still acceptable [3].

As presented in Section 1.2, the log-linear strain rate dependency considered in this model is only reliable for strain rates lower than $10^4 s^{-1}$. As seen in Figure 1.7, a dramatic increase in strain rate sensitivity can occur for strain rates higher than $10^4 s^{-1}$. To model this behavior, many modified versions of the Johnson-Cook model have been formulated. Kang *et al.* [52] modified the strain rate expression of the model to include a second order logarithmic strain rate dependency. The constitutive model formulation is given in Equation (1.25). Kang *et al.* [52]performed tensile experiments on different sheet steels at strain rates from $10^{-3} s^{-1}$ to $5000 s^{-1}$ and found a closer correlation between experimental and numerical results using this modified form of the Johnson-Cook model.

$$\sigma = \left(A + B\,\varepsilon_p^n\right)\left(1 + C_1 \ln \dot{\varepsilon}^* + C_2 \left[\ln \dot{\varepsilon}^*\right]^2\right)\left(1 - T^{*m}\right) \tag{1.25}$$

Another widely used expression for the strain rate dependency of materials was introduced by Cowper and Symonds [5] to model the high strain rate behaviour of mild steel, and is presented in Equation (1.26), where σ_0 is the static true stress, and C and p are material constants.

$$\sigma = \sigma_0 \left(1 + \left[\frac{\dot{\varepsilon}}{C} \right]^{\frac{1}{p}} \right) \tag{1.26}$$

The modified Johnson-Cook model with the Cowper-Symonds formulation is given by Equation (1.27). The Cowper-Symonds model considers a power-law for the strain rate dependency to capture the increase in the strain rate sensitivity as the strain rate increases.

$$\sigma = \left(A + B\,\varepsilon_p^n \right) \left(1 + \left[\frac{\dot{\varepsilon}}{C} \right]^{\frac{1}{p}} \right) \left(1 - T^{*m} \right) \tag{1.27}$$

Schwer [61] compared numerical simulations performed on A36 steel using the classical Johnson-Cook model and its modified version with the Cowper-Symonds strain rate dependency. A clear improvement in the results was seen using the Cowper-Symonds model, particularly for strain rates higher than $10^3 s^{-1}$ [61].

1.4.2 Zerilli-Armstrong

Zerilli and Armstrong [6-8] developed a physically-based constitutive model, considering thermally activated dislocation motions in metals. Zerilli and Armstrong originally identified that dislocation interactions are different in BCC and FCC metals; thus, they developed two different formulations depending on the crystal structure of the metal [6-8]. Their model takes into account the strain, strain rate, temperature and grain size effects in an additive form. The general formulation of the model is defined by Equation (1.28), where $\sigma_{athermal}$ and $\sigma_{thermal}$ are respectively the thermally independent and dependent terms; and l is the average grain size of the material.

$$\sigma = \sigma_{athermal} + \sigma_{thermal} + k\,l^{-1/2} \tag{1.28}$$

Zerilli and Armstrong [6-8] concluded that overcoming Peierls-Nabarro barriers, associated with dislocation motions, was the principal thermal activation mechanism for BCC metals, whereas dislocation interactions, and thus density, was the controlling mechanism for FCC metals [6-8,62].

They proposed thus two formulations for their model, given by Equation (1.29) for BCC metals, and Equation (1.30) for FCC metals.

BCC: $$\sigma = \sigma_G + C_1 \exp\left(-C_3 T + C_4 T \ln \dot{\varepsilon}\right) + C_5 \varepsilon^n + k l^{-1/2} \tag{1.29}$$

FCC: $$\sigma = \sigma_G + C_2 \varepsilon^{1/2} \exp\left(-C_3 T + C_4 T \ln \dot{\varepsilon}\right) + k l^{-1/2} \tag{1.30}$$

In these models, σ_G, C_1, C_2, C_3, C_4, C_5, n, k and l are material constants that should be determined experimentally. As seen in Equations (1.29) and (1.30), the Zerilli-Armstrong model considers the work-hardening rate to be independent of temperature for BCC metals, and that the yield stress is not affected by the temperature for FCC metals.

Zerilli and Armstrong [7] predicted the shape of cylindrical samples of OFHC copper and Armco iron deformed by Taylor-impact experiments. They compared the predicted shapes with the experimental data provided by Johnson and Cook [3,4] and obtained closer predictions, especially for the OFHC copper, as seen in Figure 1.26.

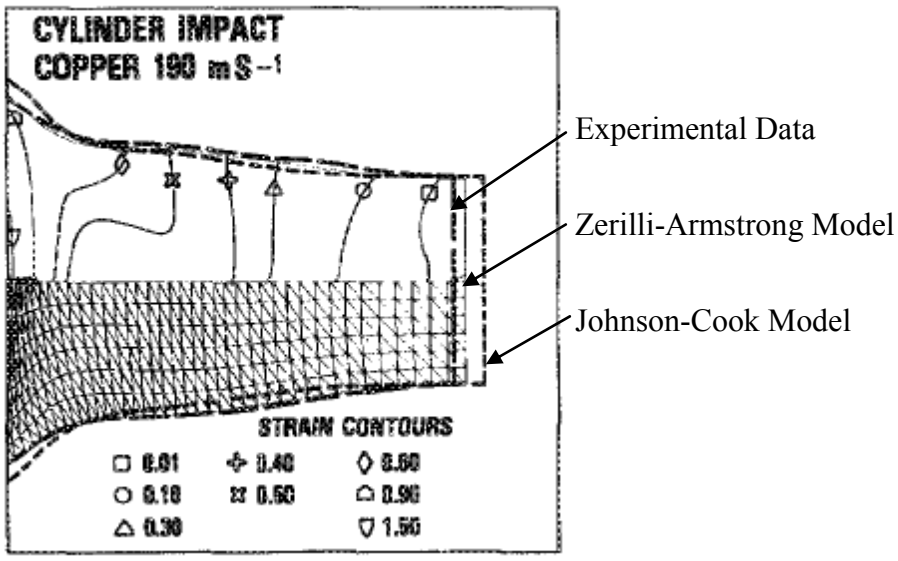

Figure 1.26: Numerical predictions and experimental shape of deformed cylinder of OFHC copper after Taylor-Impact experiments [7]. The present author added the labels and arrows

In 1991, Goldthorpe [63] showed that BCC metals present a change in work-hardening rate, mainly caused by adiabatic heating during large deformations at high strain rate. Goldthorpe proposed then a modified version of the BCC Zerilli-Armstrong model, given by Equation (1.31), where C_6 is a material constant, and $\mu(T)$ is the shear modulus at the temperature T. The ratio of the shear modulus at the testing temperature and at room temperature is assumed to be a function of temperature and can be modeled by a second order polynomial function [63].

$$\sigma = \sigma_G + k\,l^{-1/2} + C_1 \exp\left(-C_3 T + C_4 T \ln\dot{\varepsilon}\right) + \left(C_5 \varepsilon^n + C_6\right)\frac{\mu(T)}{\mu(293)} \tag{1.31}$$

When Zerilli and Armstrong originally presented their model [7], they stated that the BCC formulation was incomplete, since it doesn't account for deformation by twinning, which can be important in BCC metals at high strain rate [7]. Therefore, they modified the Hall-Petch term in their model by Equation (1.32) [64], where N_T is the average number of twins per grain.

$$\sigma_{athermal} = \sigma_G + k\,l^{-1/2}\left[\left(N_T + 1\right)^{1/2} - 1\right] \tag{1.32}$$

Holt *et al.* [65] used the Zerilli Armstrong model to predict the deformation of titanium during Taylor-impact experiments. Even if titanium as a HCP crystallographic structure, it shows a behavior close to BCC materials [65]. As twinning deformation is important in HCP metals, they used the modification of the Hall-Petch term, seen in Equation (1.32), but they also included a threshold stress value σ_{twin} to account for twinning or not. They predicted the deform shapes of titanium Taylor-impact cylindrical specimens and reported a significant improvement in the predicted shape [65].

Zerilli and Armstrong [66] introduced then a constitutive relation for HCP metals, based on a combination of their previous models for BCC and FCC materials. The HCP version of the Zerilli-Armstrong model is given by Equation (1.33).

$$\text{HCP:} \qquad \sigma = \sigma_G + k\,l^{-1/2} + B\exp\left(-\beta_0 T + \beta_1 T \ln\dot{\varepsilon}\right) + A\varepsilon^{1/2}\exp\left(-\alpha_0 T + \alpha_1 T \ln\dot{\varepsilon}\right) \tag{1.33}$$

Once again, Zerilli and Armstrong [66] used predicted shape of Taylor-impact cylindrical specimens to validate their models. They compared experimental and numerical results for Ti-6Al-4V titanium alloy and HY-100 steel; and got very good predictions for both alloys.

1.5 Current Research

Prior to the current research, high strain rate testing on magnesium alloys was mainly performed on extruded and cast materials. Moreover, most of the studies on magnesium alloys at high strain rates were performed in compression. Dynamic experiments on AZ31B-O magnesium alloy sheet were only performed in tension at $1000s^{-1}$ [35], and were used to characterize the texture evolution of the sheet under various temperatures at high strain rates. Therefore, one focus of the present research will be to fully characterize the constitutive behavior of AZ31B-O sheet over a wide range of strain rates, from quasi-static to high strain rates.

Furthermore, the dynamic behavior of AZ31B-H24 has only been investigated in compression for plate material [34]. To the author's knowledge, no tensile characterization of this material condition has been made under high strain rate conditions to date. Thus, another focus of the present research will be to perform tensile experiments at high strain rates for AZ31B-H24 sheet.

The primary effort in this research, then, is to characterize AZ31B in the O and H24 tempers over a very wide range of strain rates from 0.003 s^{-1} to 1500 s^{-1}. In addition, constitutive fits using three commonly used high strain rate material models, the Johnson-Cook model, its modified version with a Cowper-Symonds formulation, and the Zerilli-Armstrong model, are undertaken. Finally, validation of the constitutive fits is performed by finite element simulations of the actual experiments using these constitutive models.

The balance of this thesis is organized as follows. The experimental configurations and the data analysis procedures used for the current research are described in Chapter 2 and Chapter 3, respectively. Experimental results for the different materials are discussed in detail in

Chapter 4, followed by the constitutive fit results presented in Chapter 5. Numerical simulations of the tensile split Hopkinson bar experiments are given in Chapter 6. Finally, Chapter 7 and 8 present conclusions from the current work and provide recommendations for future work.

2 EXPERIMENTAL METHODS

The strain rate sensitivity of AZ31B-H24 and AZ31B-O magnesium alloy sheets was studied by performing quasi-static and high rate uniaxial tensile experiments. Three different thicknesses were considered for the O-Temper condition and one available for the H24 condition was tested. Thermal softening was also studied by performing high strain rate experiments at elevated temperature.

2.1 Materials and Experimental Conditions

Two different conditions of the AZ31B magnesium alloy were characterized as part of the current research. AZ31B-H24 is a cold rolled and partially annealed material, and AZ31B-O is a hot rolled and fully annealed material. The chemical composition of AZ31B magnesium alloy can be seen in Table 2.1

Three different nominal sheet thicknesses were tested for the AZ31B-O material: 1 mm, 1.6 mm and 2.5 mm; while the H24 material was 1.6 mm in thickness. Tensile tests were performed in both the rolling direction (RD) and the transverse direction (TD) of each magnesium alloy sheet.

Table 2.1: Chemical composition of AZ31B magnesium alloy

Material	*Nominal Composition wt.%*								
	Al	Zn	Mn	Ca	Cu	Fe	Ni	Si	Mg
AZ31B	2.5 - 3.5	0.6 - 1.4	0.2 - 1.0	< 0.04	< 0.05	< 0.005	< 0.005	< 0.05	Balance

To characterize the strain rate sensitivity of each material, uniaxial tensile experiments were performed over a large range of strain rates, from $0.003s^{-1}$ to $1500s^{-1}$. Elevated temperature experiments at high strain rate, i.e. from 150°C to 300°C and at nominal strain rates from $500s^{-1}$ to $1500s^{-1}$, were also performed to determine the thermal softening of the materials. Elevated temperature experiments were only considered for the H24 and O material with a thickness of 1.6mm.

A complete test matrix can be seen in Table 2.2 for room temperature (RT) experiments and in Table 2.3 for high temperature tests. At least three good tests were carried out at each condition to ensure measurement repeatability. A total of 150 room temperature experiments and 60 high temperature experiments were performed.

Table 2.2: Matrix of experiments performed at room temperature

MATERIAL		NOMINAL STRAIN RATE (s^{-1})							
		0.003	0.1	1	30	100	500	1000	1500
AZ31B-H24	RD	X			X	X	X	X	X
1.6 mm	TD	X			X	X	X	X	X
AZ31B-O	RD	X	X		X		X	X	X
1 mm	TD	X	X		X		X	X	X
AZ31B-O	RD	X	X	X	X	X	X	X	X
1.6 mm	TD	X	X	X	X	X	X	X	X
AZ31B-O	RD	X	X		X		X	X	
2.5 mm	TD	X	X		X		X	X	

Table 2.3: Matrix of experiments performed at high temperature

MATERIAL		NOMINAL STRAIN RATE (1/s)								
		500			1000			1500		
		150°C	250°C	300°C	150°C	250°C	300°C	150°C	250°C	300°C
AZ31B-H24	RD				X		X	X		X
1.6 mm	TD				X		X	X		X
AZ31B-O	RD	X	X		X	X		X	X	
1.6 mm	TD	X	X		X	X		X	X	

2.2 Specimen Geometry

To avoid any geometrical effect from one test to another, the same sample geometry was used for all of the different strain rate conditions. A schematic of the "miniature dog-bone" specimen that was used can be seen in Figure 2.1. This geometry has been developed by Smerd *et al.* [54] to perform high-rate tests on aluminum alloy AA5754. This geometry has a gauge length of 12.5 mm which is small enough to ensure dynamic equilibrium during high-rate experiments. Furthermore, at quasi-static rate ($0.003s^{-1}$), this geometry matches the behaviour

obtained with ASTM samples up to the ultimate tensile strength (UTS) for various materials such as aluminum [54,67] and advanced high strength steels [55-57,68]. This correspondence was confirmed in the current work for magnesium alloys, as seen in Figure 2.2 for the two magnesium alloys AZ31B-H24 and AZ31B-O. The data for the 25mm ASTM sample and the current dog-bone samples agrees well up to the onset of necking (UTS) for both the O and H24 tempers.

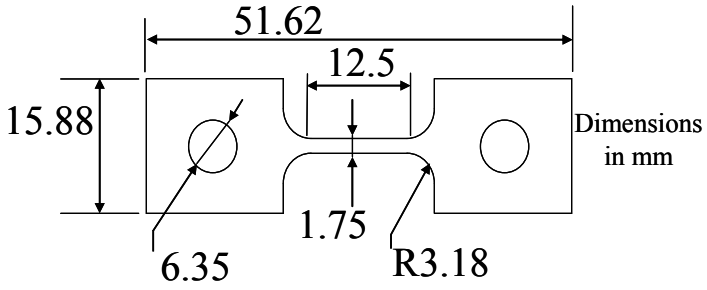

Figure 2.1: Specimen geometry (not to scale)

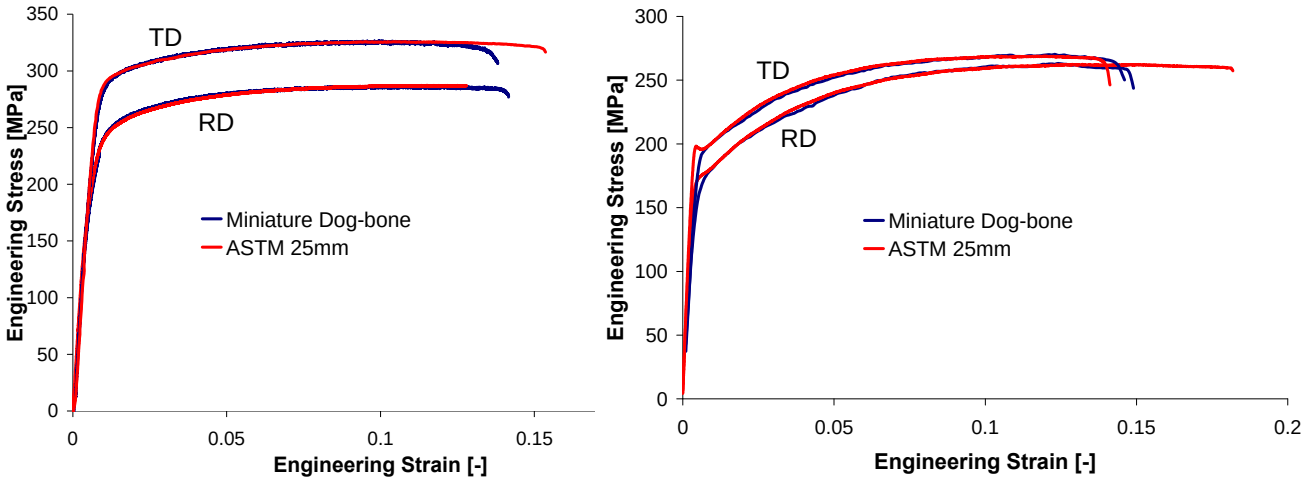

Figure 2.2: Miniature dog-bone vs. ASTM specimen for AZ31B-H24 (a) and AZ31B-O (b) at quasi-static strain rate

2.3 Low Rate Experiments

Low strain rate experiments were performed using a servo-hydraulic INSTRON 1331 tensile testing device. The load cell used on this apparatus has a capacity of 25 kN. Specimen displacement was measured using a ±5 mm extensometer manufactured by INSTRON. The

specimens were mounted in a pair of grips designed to match the thickness of the tested material. The experimental set up can be seen in Figure 2.3. This assembly was mounted in the INSTRON using vee-grips to align the specimen with respect to the loading axis of the apparatus, which reduces the likelihood that bending loading will be applied to the specimen.

The cross-head velocity was set to 0.375 mm/s, 1.25 mm/s and 12.5 mm/s to obtain nominal strain rates of $0.003s^{-1}$, $0.1s^{-1}$ and $1s^{-1}$, respectively.

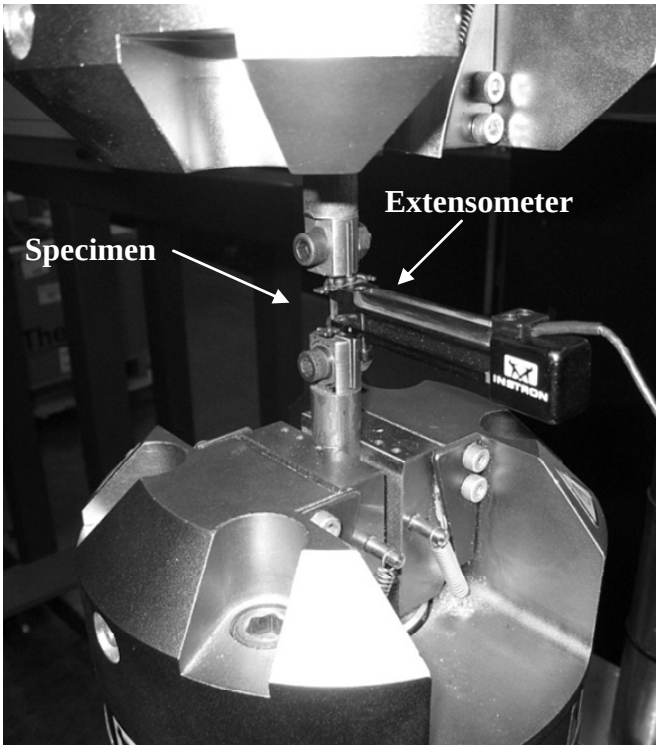

Figure 2.3:Quasi-static experimental setup

2.4 Intermediate Rate Experiments

2.4.1 Experimental Method

Intermediate strain rates were achieved using an IMATEK Instrumented Falling Weight Impactor (IFWI). The apparatus and a schematic of the specimen region can be seen in Figure 2.4.

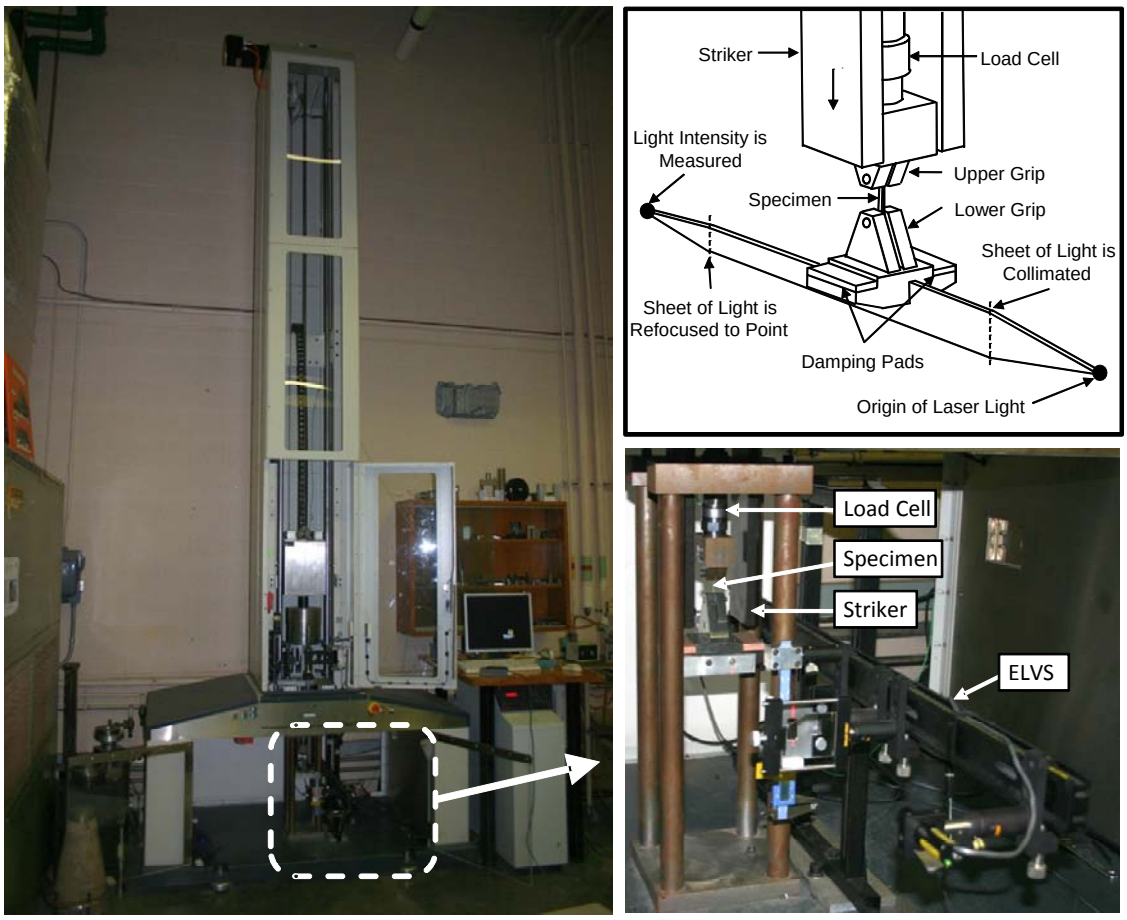

Figure 2.4: IFWI apparatus and a schematic showing the specimen region

At the beginning of the experiment, the specimen is fastened between the upper and lower grip. The upper grip is fixed and the lower grip hangs freely from the specimen. A striker falls from a predetermined height and impacts the lower grip, which loads the specimen in tension. The impact of the striker can create significant ringing in the force signal. RTV silicon pads are placed on the lower grip to damp the impact and thus reduce the oscillations in the load signal, as illustrated in Figure 2.5. However this also increases the rise time before achieving a constant strain rate, as seen in Figure 2.6.

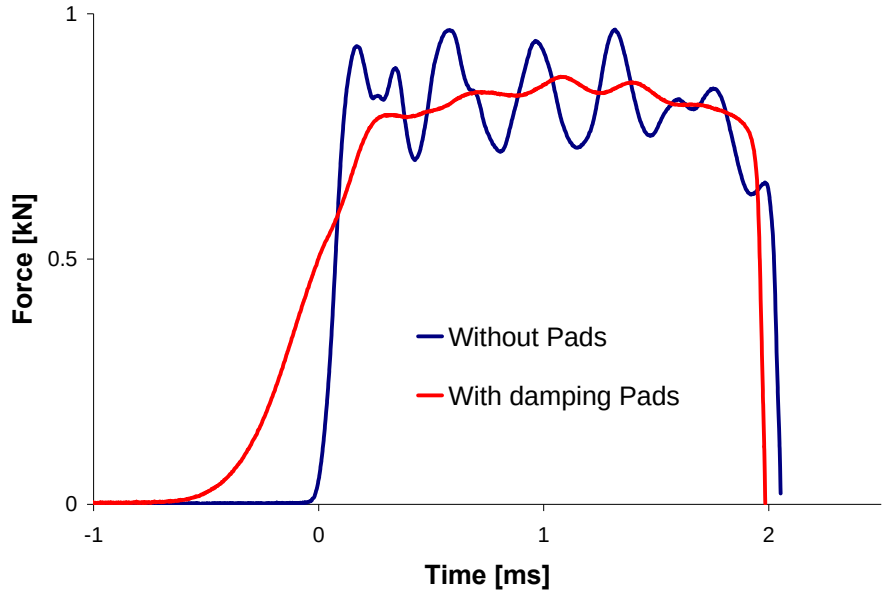

Figure 2.5: Effect of damping pads on the force vs. time for AZ31B-H24

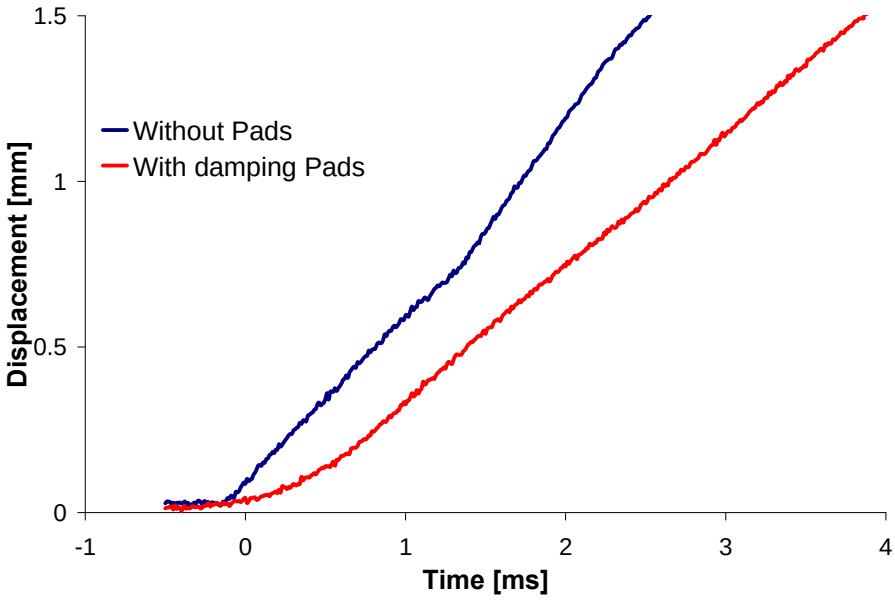

Figure 2.6: Effect of damping pads on the displacement vs. time for AZ31B-H24

The load is measured using a KISTLER 9500A4 ±30kN piezoelectric load cell at a sampling rate of 200 kHz. The load cell is located directly above the upper grip.

The lower grip is made of titanium alloy Ti-6Al-4V which is strong enough to withstand repeated impacts without deforming plastically. The lower grip has a mass of 1.54 kg which preloads the sample to 3.45 MPa for the 2.5 mm thick specimens to 8.63 MPa for the 1 mm thick specimens due to the weight of the grip.

The elongation of the specimen is measured by an Enhanced Laser Velocity System (ELVS). A schematic of the ELVS can be seen in Figure 2.4. The ELVS system is composed of a laser that emits a diverging sheet of light. This sheet is then collimated by a plano-cylindrical lens to make it parallel. A rectangular aperture ensures that the sheet has a fixed width of 25.4 mm. The sheet is then refocused to a point by a convex lens and the intensity of the light is measured by a high-speed PIN photodetector. The sheet of light is set so that it is partially blocked by the lower grip at the beginning of the test. As the deformation occurs, the lower grip moves downward and blocks more light, reducing then the intensity of light received by the photodetector. The output voltage of the photodetector is then acquired and converted to displacement after a calibration process. Over the range of the specimen deformation (< 3 mm), there is a linear relationship between the output voltage of the photodetector and the displacement of the lower grip, as seen in the calibration curve in Figure 2.7. The ELVS has a sampling rate of 200 kHz and a sensitivity of ±0.01 mm.

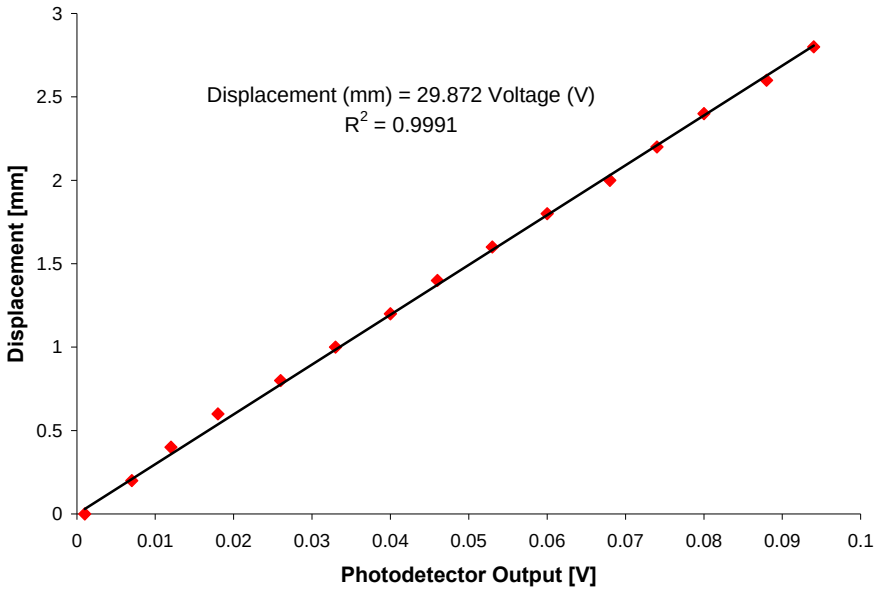

Figure 2.7: Calibration curve of the ELVS

2.4.2 Temperature Rise

During each experiment, heat is generated from plastic work. The temperature rise in the sample is then given by Equation (2.1). Typically 85% to 95% of the plastic work is converted into heat [69-71]. An average value of 90% was used in the current research, which can be expressed as $\beta = 0.9$ in Equation (2.1).

$$\Delta T = \beta \frac{1}{\rho C} \int \sigma_T d\varepsilon_p \tag{2.1}$$

Depending on the speed of the deformation, this heating is dissipated to the surrounding apparatus through conduction or to the air through convection.

For the quasi-static experiments, the heat generated by the plastic deformations is quickly dissipated and the deformation is considered to be isothermal. On the other hand, high strain rate deformations are considered as adiabatic [69], i.e. none of the heat generated by the plastic deformation has time to be dissipated by conduction or convection over the short duration of the experiment.

During intermediate strain rate experiments, the heat generated by the plastic deformations is only partially dissipated. The duration of an IFWI experiment is less than 10 ms, so only dissipation by conduction was assumed. Considering a one-dimension model, the heat distribution is given by Equation (2.2), where k is the thermal conductivity constant (equal to 76.9 $W \cdot m^{-1} \cdot K^{-1}$ for AZ31B at room temperature [72]), ρ is the density, C is the heat capacity, and x represents the position along the gauge length; the grips being considered at x = 0 mm and x = 12.5 mm.

$$\rho C \Delta T = \beta \int \sigma_T d\varepsilon_p + k \frac{\partial^2 T}{\partial x^2} \Delta t \tag{2.2}$$

To calculate the temperature distribution in the sample during the tests, the specimen gauge length was discretized into 30 evenly distributed points. A finite difference solution from Equation (2.2) was then solved. The grips are considered as large heat sink, so their temperatures are assumed to be constant and equal to the room temperature (RT). This is modeled by the boundary conditions presented in Equation (2.3).

$$\begin{cases} T_{x=0\,mm} = T_{room} \\ T_{x=12.5\,mm} = T_{room} \end{cases} \tag{2.3}$$

For each node j and time step i, the transient temperature was calculated using Equation (2.4).

$$T_{i+1,j} = T_{i,j} + \frac{1}{\rho C}\left[\beta \int_{\varepsilon_i}^{\varepsilon_{i+1}} \sigma_T d\varepsilon_{pl} + k\frac{T_{i+1,j+1} - 2T_{i+1,j} + T_{i+1,j-1}}{(\Delta x)^2}(t_{i+1} - t_i)\right] \tag{2.4}$$

For calculation purposes, a power law was used to describe the flow stress and the strain rate was considered to be constant during the test. These assumptions are described by Equation (2.5), where A, B and n are material constants.

$$\sigma_T = A + B\,\varepsilon_{pl}^n = A + B(\dot{\varepsilon}\,t)^n \tag{2.5}$$

The plastic work can then be approximated by Equation (2.6).

$$\int_{\varepsilon_i}^{\varepsilon_{i+1}} \sigma_T d\varepsilon_{pl} = \int_{t_i}^{t_{i+1}} \left[A + B(\dot{\varepsilon}\,t)^n\right]\dot{\varepsilon}\,dt = A\dot{\varepsilon}(t_{i+1} - t_i) + \frac{B}{n+1}\dot{\varepsilon}^{n+1}\left(t_{i+1}^{n+1} - t_i^{n+1}\right) \tag{2.6}$$

Each curve was fitted independently using a nonlinear regression algorithm in the statistical analysis software MYSTAT. An example of the fitting can be seen in Figure 2.8 where the experimental flow stress for AZ31B-O at $30s^{-1}$ in the rolling direction of the 1.6 mm thick sheet was fitted.

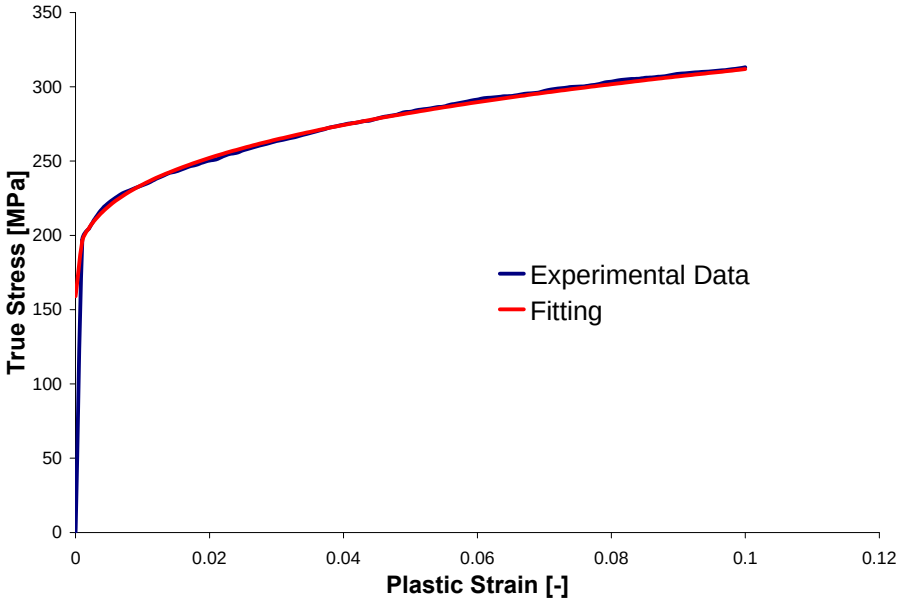

Figure 2.8: Power law fitting for AZ31B-O at $30s^{-1}$ in the rolling direction.

Figure 2.9 shows the temperature distribution calculated for deformation up the UTS, respectively at strain rates of $30s^{-1}$ and $0.003s^{-1}$. A clear temperature rise can be seen at $30s^{-1}$; whereas the isothermal state at $0.003s^{-1}$ is confirmed by the temperature distribution calculation.

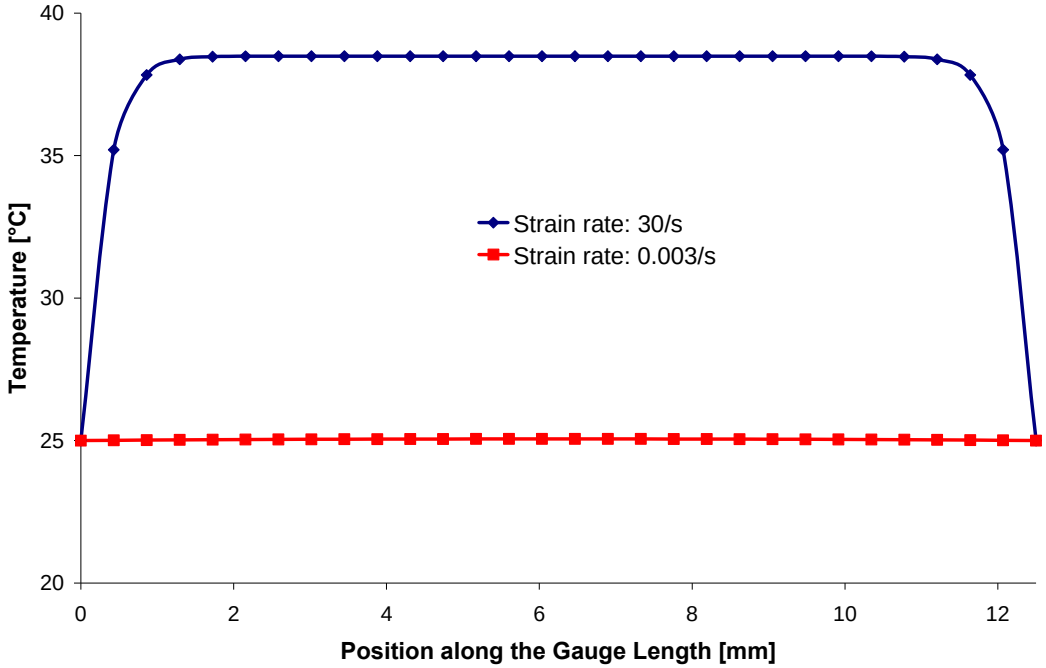

Figure 2.9: Temperature distribution in the gauge length at $30s^{-1}$ and $0.003s^{-1}$.

Using the average temperature rise in the gauge length, the percentage β_{eq} of plastic work that contributes to the temperature rise can be calculated using Equation (2.7).

$$\rho C \Delta T = \beta_{eq} \int \sigma_T d\varepsilon_p \tag{2.7}$$

Figure 2.10 shows the evolution of β_{eq} as deformations occur for experiments at $100s^{-1}$ and $30s^{-1}$. At strain rate of $30s^{-1}$, β_{eq} varies from 0.822 to 0.837 with an average of 0.829; and at $100s^{-1}$, β_{eq} varies from 0.834 to 0.839 with an average of 0.836. Therefore, for constitutive fitting purposes, a value of 0.83 was considered to estimate the temperature rise during all the IFWI experiments.

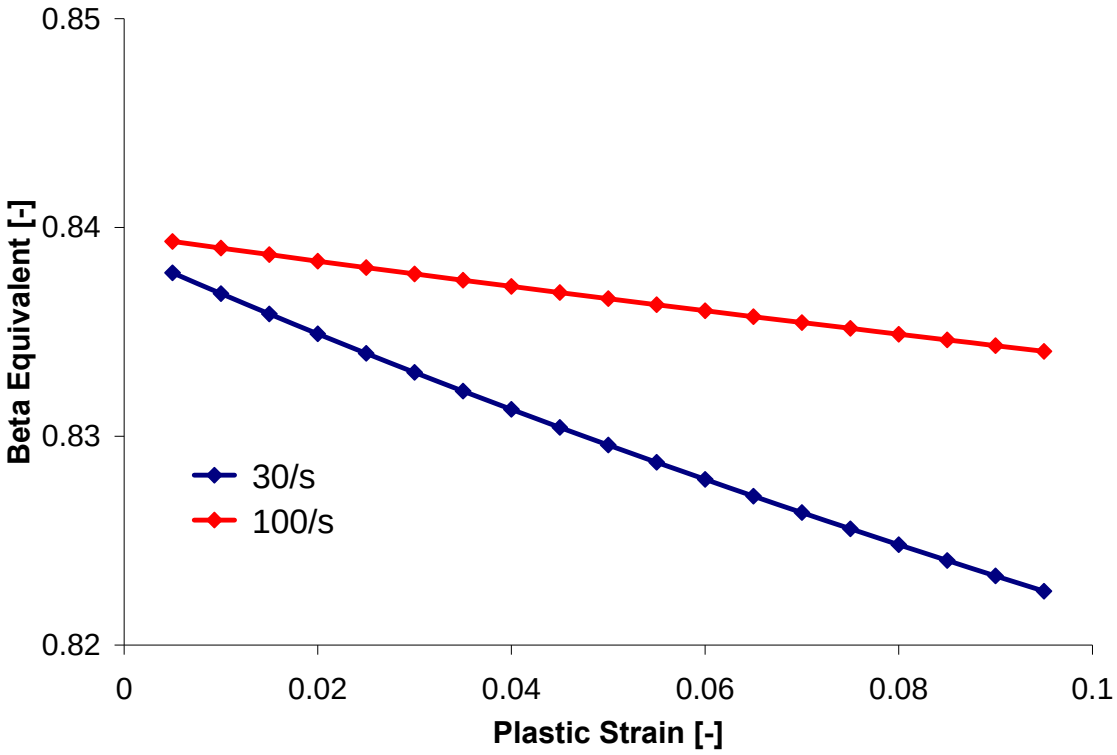

Figure 2.10: Beta Equivalent vs. Plastic Strain for deformations at $30s^{-1}$ and $100s^{-1}$

2.5 High Rate Experiments

2.5.1 Experimental Method

High strain rate experiments were performed using a Tensile Split Hopkinson Bar (TSHB). A schematic of the apparatus is presented in Figure 2.11. As seen in the figure, the TSHB is comprised of a striker tube, an incident bar and a transmitted bar. Upon impacting the end cap, the striker creates an elastic tensile wave in the incident bar. As the incident wave reaches the end of the bar, a portion is reflected, with the remainder being transmitted through the sample into the transmitted bar [73]. The three strain-time histories of the elastic waves are recorded with strain gauges on each bar. A complete description of the principle of the TSHB and the stress-strain calculation can be seen in Section 1.3.

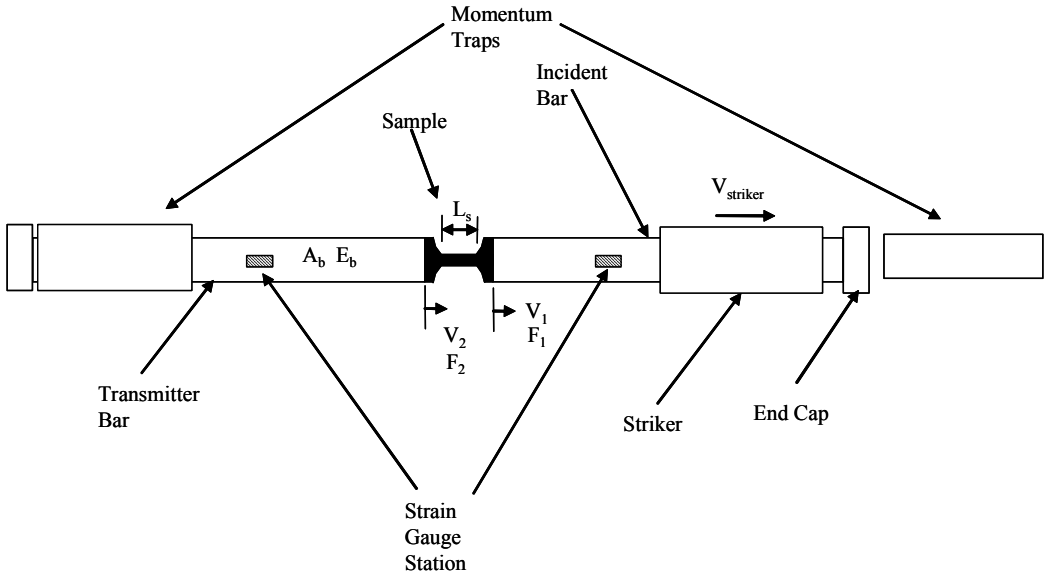

Figure 2.11: Schematic of the TSHB

The incident bar, transmitted bar, end cap and striker are made of aluminum alloy 6061-T6. In the gripping region, slots are machined at the end of each bar to hold the specimen. Steel screws are then used to clamp the specimen and provide enough friction to prevent the specimen from slipping during the test.

Strain histories on the incident and transmitted bars are recorded using foil strain gauges. Two gauges were used on each bar. The gauges were placed on opposite sides of the bar to cancel any bending stresses within the bar. For each strain measurement, a half Wheatstone bridge configuration was used, as seen in Figure 2.12. Gauges and resistors of nominal resistance equal to 120 Ω and 1000 Ω were used on the incident and the transmitted bars, respectively.

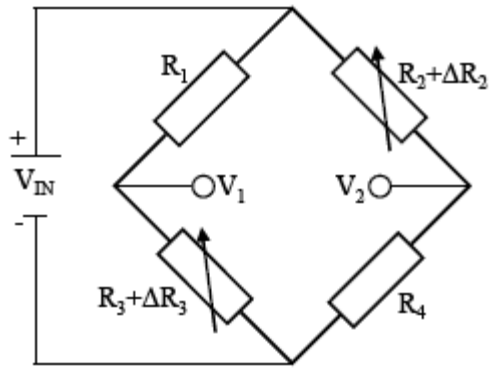

Figure 2.12: Half Wheatstone Bridge configuration

The Wheatstone bridge is excited by a 10V DC input voltage. The output signal is amplified by a VISHAY 2210B Signal Conditioning Amplifier with an amplifier gain G_0 = 300 and frequency response of 120 kHz. Input and output voltages of the Wheatstone bridge are related by Equation (2.8) [74].

$$E = G_0 \left(V_1 - V_2\right) = G_0 \frac{R_2 R_3 - R_1 R_4}{\left(R_2 + R_4\right)\left(R_1 + R_3\right)} V_{in} \tag{2.8}$$

For the two strain gauges R_2 and R_3, the strain can be related to the resistance by Equation (2.9), where *GF* is the gauge factor, and R_0 is the original resistance.

$$R = R_0\left(1 + GF\,\varepsilon\right) \tag{2.9}$$

As the two resistors and the two gauges have the same initial resistance R_0, Equation (2.8) can be simplified into Equation (2.10), which leads to the relation between the strain and the measured voltage presented in Equation (2.11).

$$E = G_0 \frac{GF\,\varepsilon}{2 + GF\,\varepsilon} V_{in} \tag{2.10}$$

$$\varepsilon = \frac{2E}{GF\left(G_0 V_{in} - E\right)} \tag{2.11}$$

Because of the tolerances on the resistors and the variations of the resistance of the strain gauges with temperature and small deformations, a balancing circuit is required so that at zero strain $R_2 R_3 = R_1 R_4$. This allows the use of the previous calculations to determine the strain histories of the bars. A detailed description of the balancing circuit can be found in the thesis by Salisbury [44].

2.5.2 Elevated Temperature Experiments

High strain rate tests at elevated temperature were performed using a radiative furnace mounted on the TSHB. As seen in Figure 2.13, the furnace comprises four 1000 W quartz heating lamps. Inside the heating chamber, highly-polished aluminum plates are used to reflect heat and light towards the specimen. Highly-polished aluminum tubes are also used to protect the end of the Hopkinson bars and thus reduce their temperature rise.

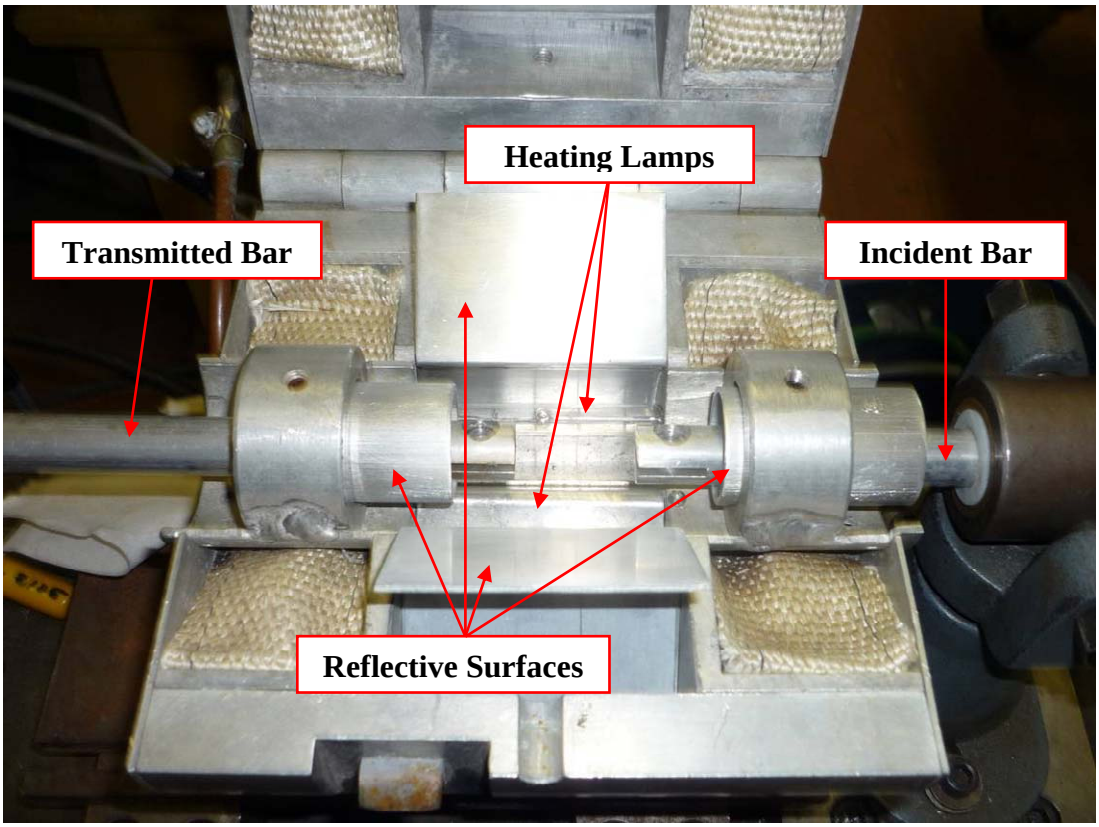

Figure 2.13: Radiative furnace

To estimate the time needed to heat the specimen at the right temperature, a thermocouple was attached to the center of the specimen. The temperature history was then recorded by a data acquisition module Omega OMB-DAQ-55. An additional K-type thermocouple was attached to the transmitted bar to assess the temperature rise of the bar just outside the furnace. It was found that the temperature of the bar was within 20°C of room temperature when the specimen was heated to 250°C.

The time needed to heat the specimen depends on its material. For example, Figure 2.14 shows the temperature history of 1.6 mm thick AZ31B-O and AZ31B-H24 specimens. It was found that for the O-temper material, 150°C was reached in 22 seconds; and 250°C in 121 seconds, whereas the H24 material reached 150°C in 8 seconds, 250°C in 57 seconds and 300°C in 123 seconds. The heating time difference between the two materials is due to their surface finishing. The O-temper material presented a near polished surface, whereas the H24 condition

has a blackened surface, which absorbs more radiative energy. The two different materials can be seen in Figure 2.15.

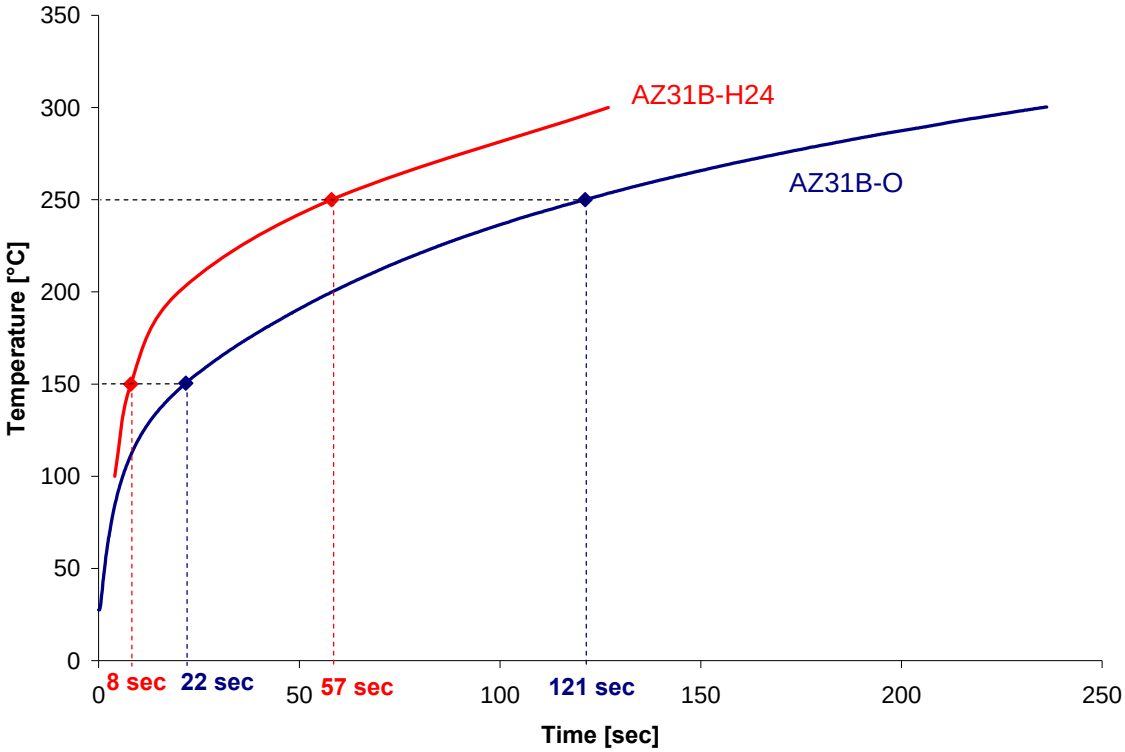

Figure 2.14: Temperature history of 1.6 mm thick AZ31B-O specimen

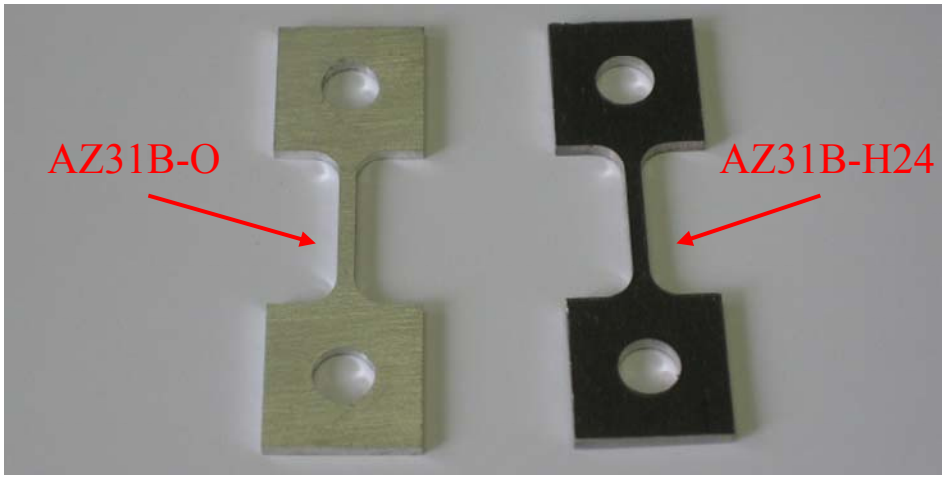

Figure 2.15: AZ31B-O and AZ31B-H24 specimen

For each elevated temperature test, the striker was fired as soon as the correct heating time was reached. Immediately before firing, the two Wheatstone bridges are balanced to compensate any effect of the bar temperature on the strain gauges.

3 PROCESSING OF EXPERIMENTAL DATA

Raw data was recorded from three different apparatus depending on the nominal strain rate considered. Each experimental technique needs its own processing procedure to extract the flow stress, i.e. true stress as a function of plastic strain, strain rate and temperature during each test. All these testing conditions and results are needed for constitutive modelling and fitting purposes. This section presents the procedure used to analyse the raw data for each apparatus.

3.1 Low Rates

Low strain rate experiments, from $0.003s^{-1}$ to $1s^{-1}$, were performed using a servo-hydraulic INSTRON 1331 tensile testing device. The embedded software records the load and the displacement from the extensometer. For a given specimen geometry, it automatically converts load and displacement into engineering stress and engineering strain, then graphically determines the apparent Young's modulus, the yield stress and the ultimate tensile strength.

From the measured engineering stress (σ_{eng}) and engineering strain (ε_{eng}), true stress and true strain were calculated using Equation (1.22).

$$\begin{cases} \varepsilon_{True} = \ln(1+\varepsilon_{eng}) \\ \sigma_{True} = \sigma_{eng}(1+\varepsilon_{eng}) \end{cases} \tag{3.1}$$

This equation is based on the assumption of volume constancy in the gauge length of the sample and is valid up to the onset of necking.

The plastic strain was then determined by subtracting the elastic strain component from the true strain using Equation (3.2), where E is the Young's modulus of the material.

$$\varepsilon_p = \varepsilon_T - \frac{\sigma_T}{E} \tag{3.2}$$

For each test, the Young's modulus could not be measured accurately since strain gages were not used to capture small strains. An "apparent modulus" was thus calculated and used in Equation (3.2). For low strain rate, the apparent Young's modulus varies from 35 GPa to 43 GPa, which is very close to the value of 45 GPa commonly measured for AZ31 [72].

The elastic part of the engineering stress-strain data is of little interest for the current research since the deformation doesn't occur at a constant strain rate at the beginning of the experiments, even at the lowest strain rate, as seen in Figure 3.1.

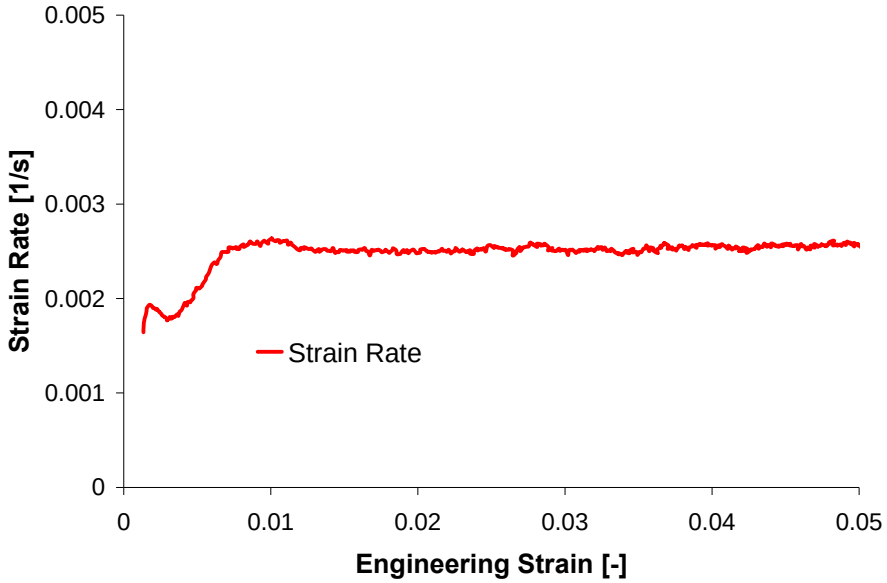

Figure 3.1: Strain rate vs. engineering strain for quasi-static experiments

For constitutive fitting purposes, the measured flow stress must be used only for uniform deformation occurring at constant strain rate. Those conditions reduce the range of strain over which the flow stress should be calculated. Indeed after the ultimate tensile stress (UTS), necking occurs so the deformation is no longer uniform. Furthermore, constant strain rate is not instantly reached: there is a rise time at the beginning of each test. For quasi-static experiments, the rise time is very short and occurs only during the elastic deformation of the specimen. Thus, all the stress-strain data prior to the UTS can then be used for the low strain rate experiments.

3.2 Intermediate Rates

Intermediate strain rate experiments ($30s^{-1}$ and $100s^{-1}$) were performed using an instrumented falling weight impactor (IFWI) apparatus. The specimen load was measured by a load cell, and the specimen elongation was measured by an enhanced laser velocity system (ELVS). The measured raw data are the force and the output voltage of the ELVS.

Using the specimen geometry, the engineering stress can easily be deduced from the force data using Equation (3.3), where A_0 is the initial cross-section of the tested sample.

$$\sigma_{eng} = \frac{F}{A_0} \tag{3.3}$$

There is a linear relationship between the output voltage of the ELVS and the specimen elongation. To determine the linear coefficient that should be used, a calibration of the ELVS is performed before each set of experiments. The calibration consists of progressively blocking the ELVS sheet of light by a plate fixed to a calliper. This method provides an accuracy of 0.1 mm, which corresponds to a strain of 0.008 for the specimen geometry used in the current research. A simple linear regression is then used to get the calibration coefficient. Figure 2.7 shows an example of the linear relationship between the output voltage of the ELVS and the elongation.

Once the ELVS calibration is done, the engineering strain can be calculated using Equation (3.4), where K is the calibration coefficient, V_{ELVS} is the measured ELVS voltage, V_0 is the initial ELVS voltage, and L_0 is the gauge length of the specimen.

$$\varepsilon_{eng} = \frac{K \cdot \left(V_{ELVS} - V_0\right)}{L_0} \tag{3.4}$$

The same procedure as the one used for the low rate experiments is then used to calculate the flow stress.

For intermediate rate experiments, there is a significant variability in the apparent Young's modulus, from 15 GPa to 35 GPa. Fortunately this variation of Young's modulus has been confirmed as a testing artifact by Thompson [68], and has no effect on the flow stress calculation. This is shown for the current data in Figure 3.2, where three tests performed on the same samples under identical conditions have different initial slopes in the engineering stress-strain data, but have similar behavior once the elastic part has been removed to calculate the flow stress.

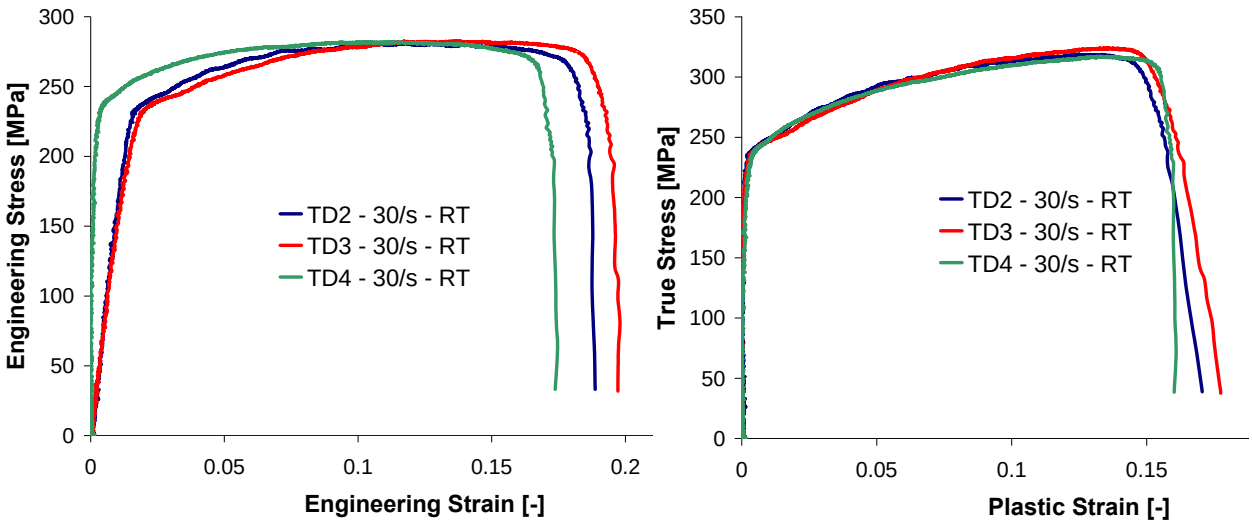

(a) (b)

Figure 3.2: Engineering stress-strain curves (a) with different apparent Young's modulus and their corresponding flow stress (b).

During the IFWI experiments, the striker impacts rubber pads that reduce the ringing on the data; however this increases the time needed to reach a constant strain rate. Figure 3.3 shows the strain history during IFWI tests at $30s^{-1}$ and $100s^{-1}$. The strain rate is considered as constant after 4% and 6% elongation for the $30s^{-1}$ and $100s^{-1}$ experiments respectively, as seen in Figure 3.5.

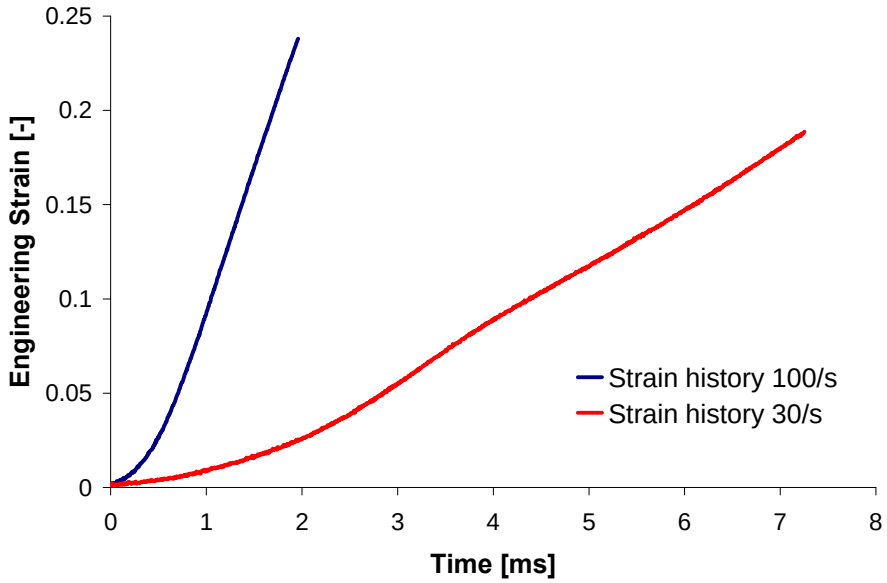

Figure 3.3: Engineering strain vs. time for experiments at 100/s and 30/s

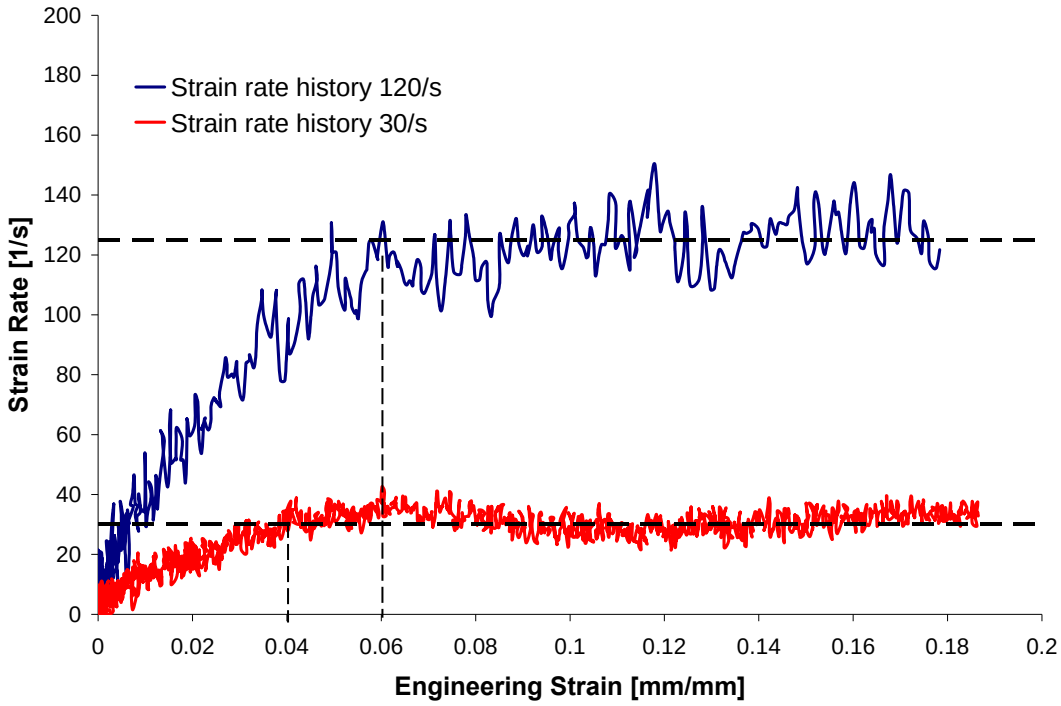

Figure 3.4: Strain rate vs. engineering strain for experiments at 100/s and 30/s

3.3 High Rates

High strain rate experiments (from $500s^{-1}$ to $1500s^{-1}$) were performed using a tensile split Hopkinson bar (TSHB) apparatus. The testing outputs are voltage histories of the two Wheatstone bridges used to measure the strains on the incident and transmitted bars. A software developed at the University of Waterloo by Salisbury [44] was used to convert the strain histories of the bars into the stress and strain of the specimen. The software uses the theory presented in Section 1.3.3, as well as some computational algorithms that are fully described in the thesis by Salisbury [44].

Once again, the flow stress was calculated using the apparent Young's modulus of the engineering stress-strain curve. As for the intermediate strain rate experiments, constant strain rate is not achieved instantly. The rise time is imposed by the geometry and the material used for the striker and the bars [23] and is independent of the nominal strain rate of the test, as seen in Figure 3.5. The rise time was found to be 45μs, which corresponds to a strain value of

respectively 1.4%, 2.2% and 3.7% for experiments at nominal strain rate of $500s^{-1}$, $1000s^{-1}$ and $1500s^{-1}$. Thus the usual range of data for constitutive fitting purposes was limited by the rise time of each test (to ensure constant strain rate) and the onset of necking (UTS).

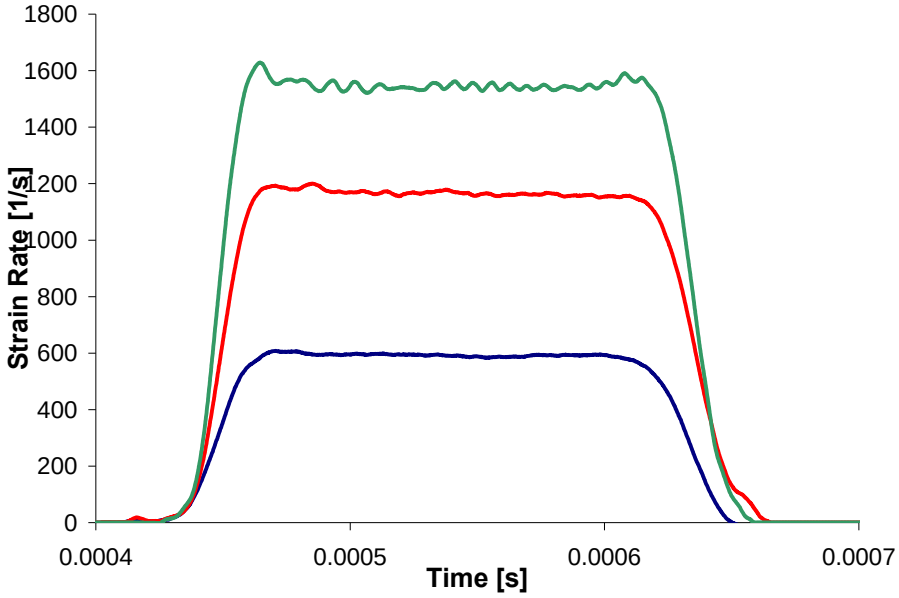

Figure 3.5: Strain rate vs. time for tests at nominal strain rates of 500 s^{-1}, 1000 s^{-1} and 1500 s^{-1}

4 EXPERIMENTAL RESULTS

In this chapter, the experimental results for the different materials and thicknesses are discussed. The effects of strain rate, temperature, orientation of the tensile direction and thickness on the constitutive behaviour of AZ31B are presented for the H24 condition, followed by the O-temper results. The first part of this chapter also presents the actual strain rate measured for each testing condition.

4.1 Nominal and Actual Strain Rate

For each experiment, the strain rate was measured based on the time history of the strain in the gauge length. Therefore, there can be a difference between the nominal strain rate and the actual one.

For the quasi-static experiments, the strain rate was imposed by the cross-head velocity, and the strain was measured by an extensometer to avoid measuring any elastic deformation outside of the gauge length of the specimen.

During the intermediate rate tests, the strain rate is controlled by the initial drop height of the impactor. This height can be approximated using the simple formula presented in Equation (1.22), where L_0 is the gauge length of the specimen, and g is the standard gravitational acceleration. However, the silicon pads used to damp the impact reduces the strain rate obtained. A higher initial height, given in Table 4.1, was then set to compensate from the damping of the impact. There is thus a small difference between the nominal and actual strain rate during each test.

$$h = \frac{\left(L_0 \, \dot{\varepsilon}\right)^2}{2\,g} \tag{4.1}$$

For high strain rate experiments, the strain rate is imposed by the striker velocity, which is controlled by the pressure in the gas gun. The different pressures used for the current research are given in Table 4.1. These pressures overestimate the nominal strain rate, but the order of magnitude of the actual strain rate remains very close to the nominal one.

The average measured strain rates and their corresponding nominal strain rates are presented in Table 4.1.

Table 4.1: Nominal and average measured strain rates

Nominal strain rate [1/s]	Average measured strain rate [1/s]	Testing parameter
Instron		
0.003	0.0025	
0.1	0.08	
1	0.8	
Drop Tower		*Initial Height*
30	30	0.01 m
100	120	0.1 m
200	185	0.25 m
Hopkinson Bar		*Gas gun pressure*
500	580	6.2 psi
1000	1175	17 psi
1500	1665	32.2 psi

For clarity in presenting the results, only the nominal strain rate will be used to refer to the testing conditions. One should thus refer to Table 4.1 to know what the actual testing condition was. Of course, all the various constitutive calculations and curve fits were performed using the actual strain rate for each experiment.

4.2 AZ31B-H24

The strain rate effect on the constitutive behavior of AZ31B-H24 can be seen in Figure 4.1 and Figure 4.2, where the flow curves at different strain rates are plotted for the rolling direction (RD) and the transverse direction (TD), respectively. A comparison between the two directions is also given in Figure 4.3 for five selected strain rates, covering the whole range of strain rate tested.

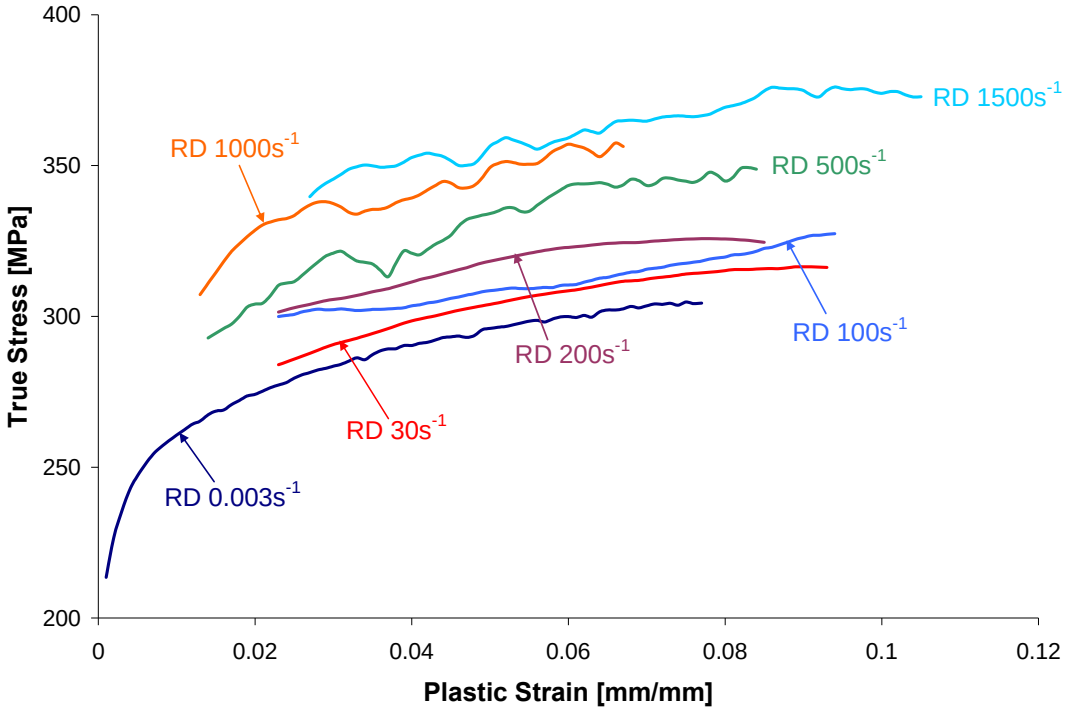

Figure 4.1: Flow curves of AZ31B-H24 in the RD at room temperature

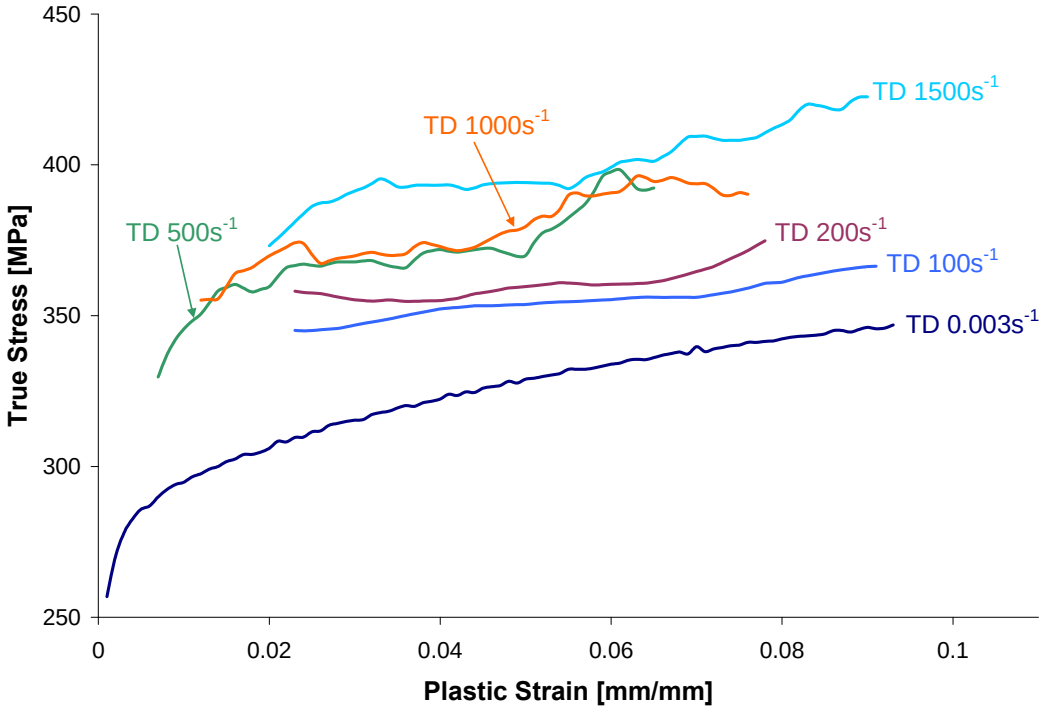

Figure 4.2: Flow curves of AZ31B-H24 in the TD at room temperature

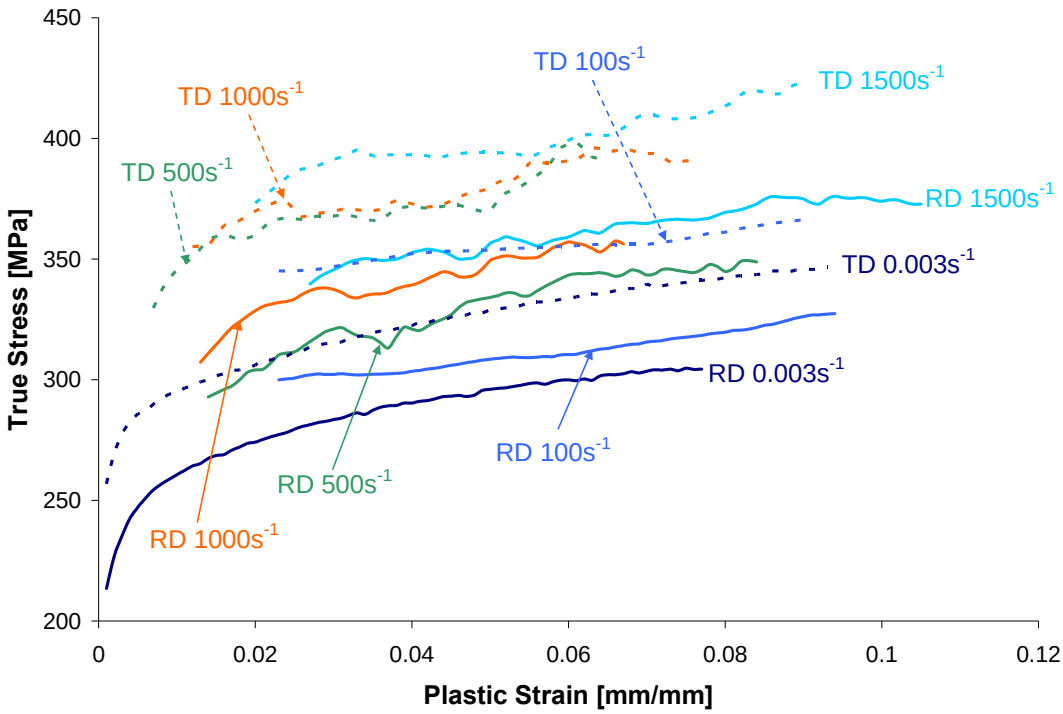

Figure 4.3: Comparison of the flow curves of AZ31B-H24 in the RD and the TD at room temperature

As illustrated by the three figures, there is a clear increase in tensile strength as the strain rate increases. Over the whole range of strain rates considered, the RD shows a stress rise of approximately 60MPa and 70MPa for the TD. This material exhibits a strong anisotropy. Indeed, the TD has a much higher stress level than the RD, with a difference of 30MPa for the $0.003s^{-1}$ tests, increasing to 40MPa for the $1500s^{-1}$ experiments.

Due to the oscillations in the data, it is difficult to detect a change in the work-hardening rate; however, it doesn't seem to be greatly influenced by the change of strain rate. One can also notice that the two directions show a similar work-hardening rate.

Figure 4.4 shows the true stress as a function of the strain rate, plotted using a logarithmic scale for both the RD and the TD at room temperature. The stress levels are plotted for plastic strains from 3% to 7%, since most of the data were acquired at constant strain rate and before the UTS for this range of plastic strain. A comparison of the strain rate sensitivity of the two directions is presented in Figure 4.5, where only the stresses at 5% plastic strain are plotted.

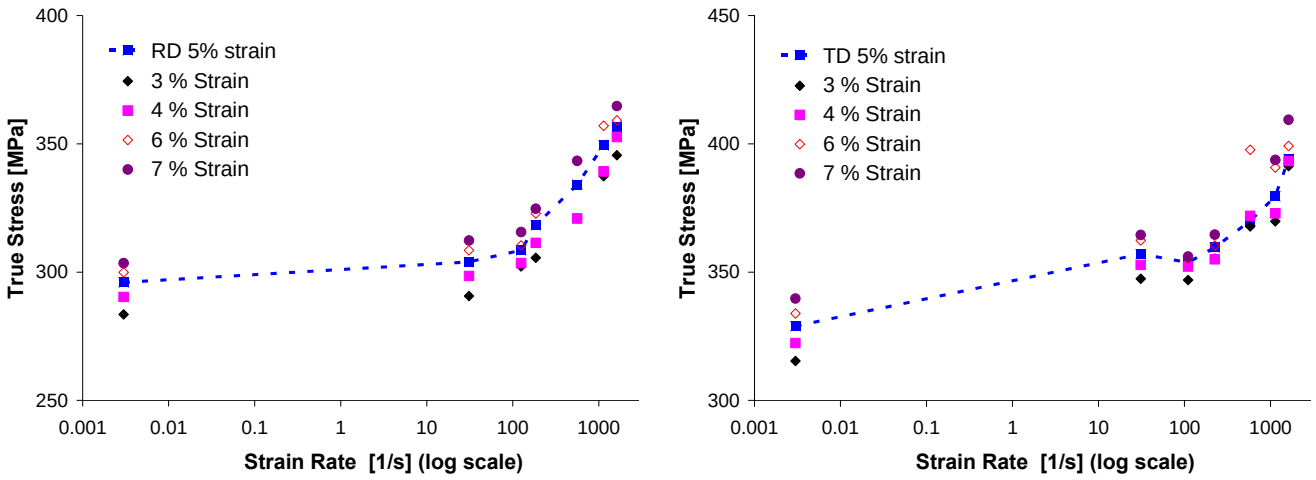

(a) (b)

Figure 4.4: True stress vs. strain rate for AZ31B-H24 in the RD (a) and the TD (b) at room temperature

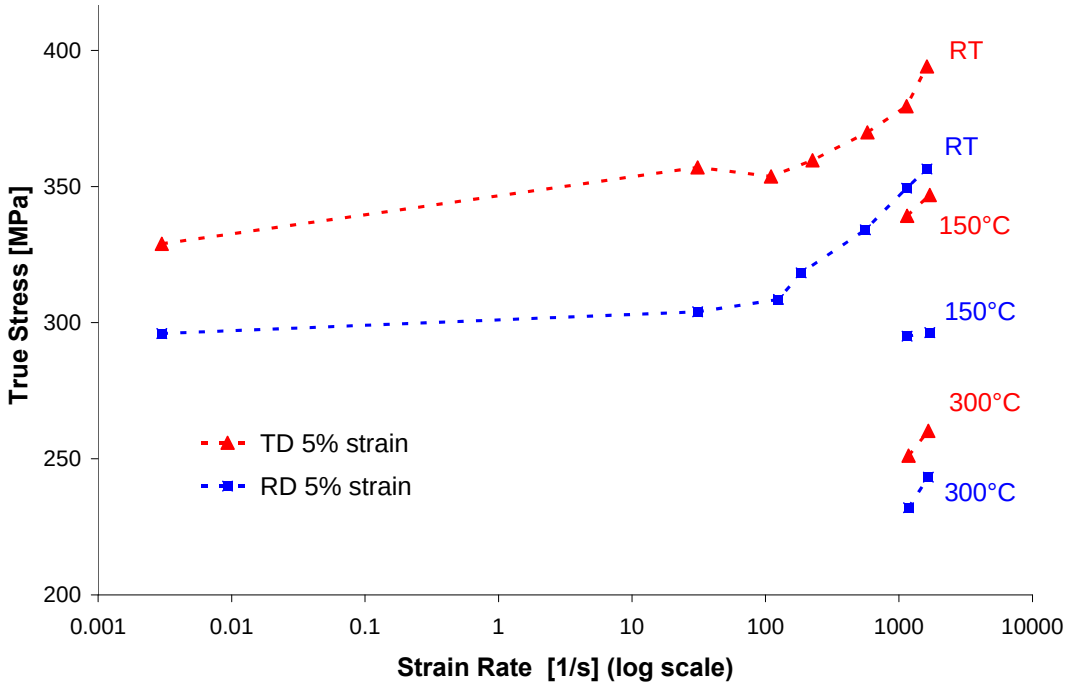

Figure 4.5: True stress vs. strain rate for AZ31B-H24 in the RD and the TD

The two directions show a clear change of strain rate sensitivity as the strain rate increases. This change occurs at a threshold of $100s^{-1}$; furthermore, on either side of this rate, the flow

stress exhibits a log-linear relationship between the stress level and the strain rate. However, the slope of the log-linear relationship is steeper for higher strain rate levels. The strain rate sensitivity is similar for the two directions, especially for strain rates higher than $100s^{-1}$, where the log-linear slopes are almost identical between the two directions.

The temperature sensitivity of AZ31B-H24 is presented in Figure 4.6 and Figure 4.7, where flow curves for high strain rate experiments at elevated temperatures are plotted for the RD and the TD, respectively. The room temperature quasi-static experiments are also included in the figures as references for the stress level of the flow curves.

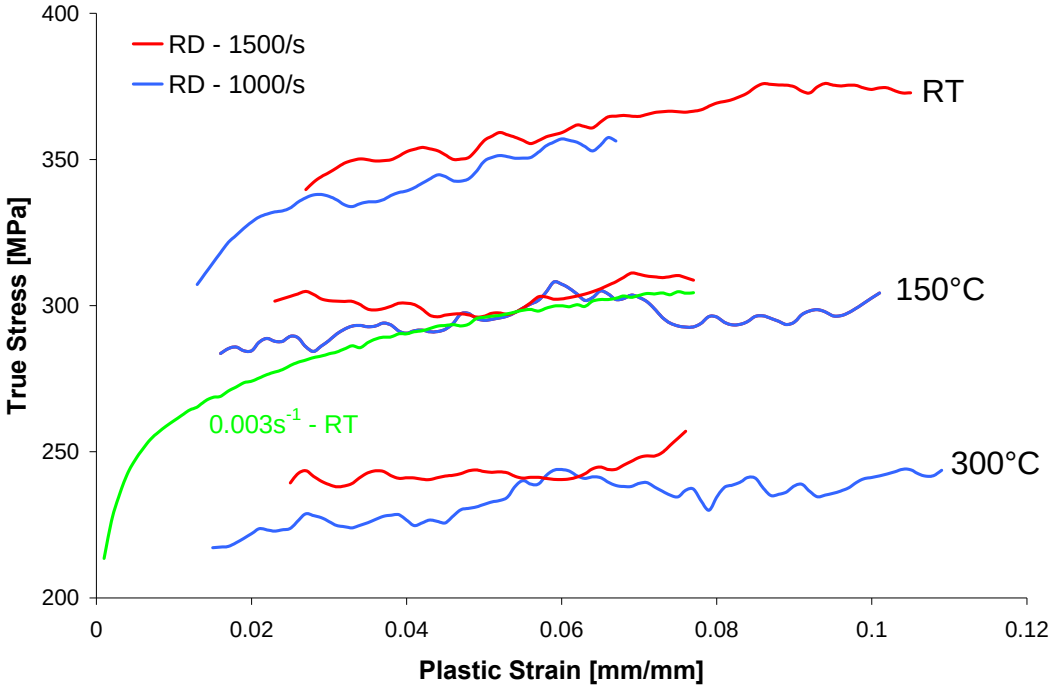

Figure 4.6: Flow curves of AZ31B-H24 in the RD at high strain rates and elevated temperatures

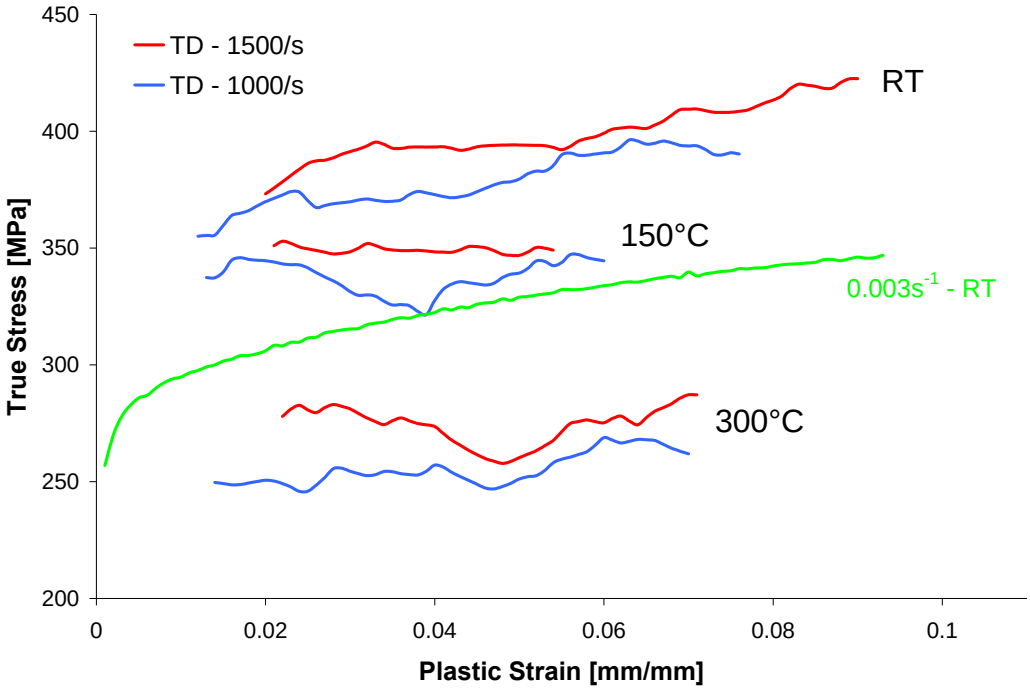

Figure 4.7: Flow curves of AZ31B-H24 in the TD at high strain rates and elevated temperatures

A clear thermal softening can be seen in both directions. The stress level is reduced by approximately 110MPa from room temperature to 300°C in the RD, and 120MPa in the TD. In both directions, the 150°C data has a stress level close to the quasi-static experiments at room temperature. There is also a small reduction of the work-hardening rate as the temperature increases. This change in work-hardening rate is more important between the room temperature and the 150°C data than between the 150°C and 300°C curves.

Figure 4.8 shows the effect of temperature on the stress level. In the figure, the homologous temperature is considered, and is defined by Equation (4.2), where T_0 is absolute zero and T_m is the melting temperature (in Kelvin). The flow stress at 3%, 5% and 7% plastic strain is plotted in the figure, and gives a good estimation of the change of work-hardening rate as the temperature increases.

$$T^* = \frac{T - T_0}{T_m - T_0} \tag{4.2}$$

As seen in Figure 4.8, the thermal softening of AZ31B-H24 is proportional to the homologous temperature for the range of temperature considered in the current research. The small

reduction in work-hardening rate is also confirmed by the figure, as the range of stress is reduced from room temperature to 300°C, especially for the 1500s^{-1} data.

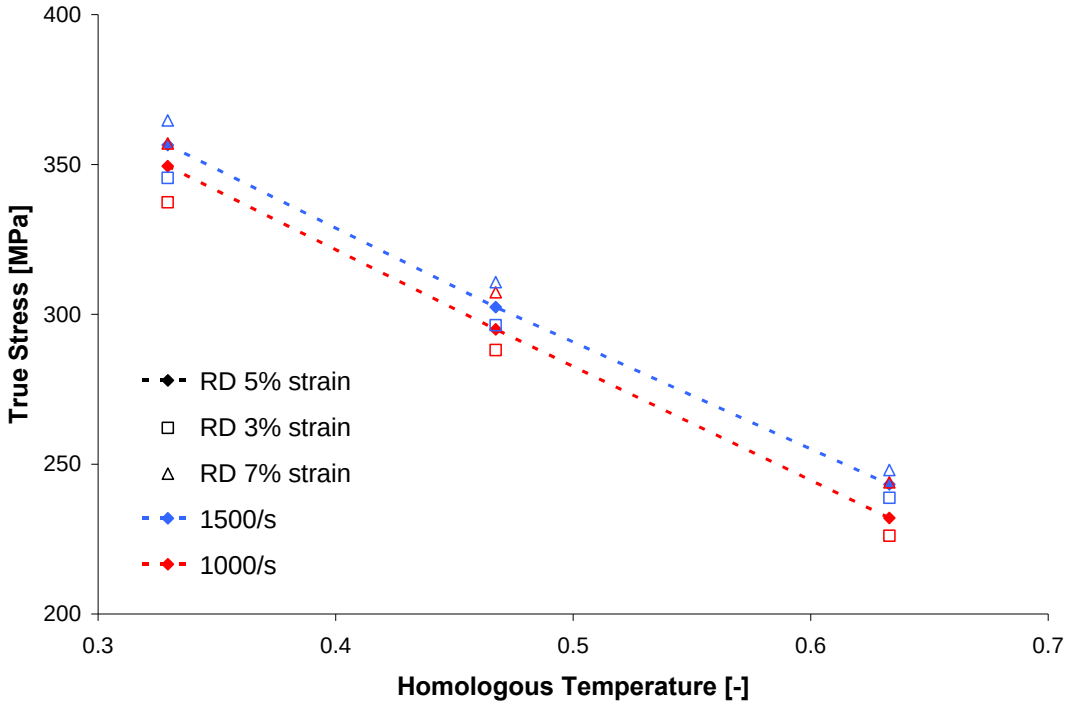

Figure 4.8: True stress vs. homologous temperature for AZ31B-H24 in the RD at high strain rates

Figure 4.5 also shows the effect of the temperature on the strain rate sensitivity. One can notice that the 150°C data for the RD are at the same stress level; this is due to the oscillations of the flow curves that overlapped at 5% plastic strain, as seen in Figure 4.6. The temperature doesn't seem to really affect the strain rate sensitivity at high strain rate. Unfortunately, only few strain rates were considered for the high temperature experiments; lower strain rate experiments would be needed to fully identify the effect of temperature and its possible effect on the 100s^{-1} threshold seen at room temperature.

The effect of strain rate and temperature on the strain-to-failure of the RD and the TD can be seen in Figure 4.9 and Figure 4.10, respectively. The strain-to-failure was measured from the engineering stress-strain curves. Intermediate strain rates were not considered due to their low apparent Young's modulus seen in the engineering stress-strain curves, as explained in

Section 3.2. The error bars in the figures represent the variability of the strain-to-failure among the different samples tested.

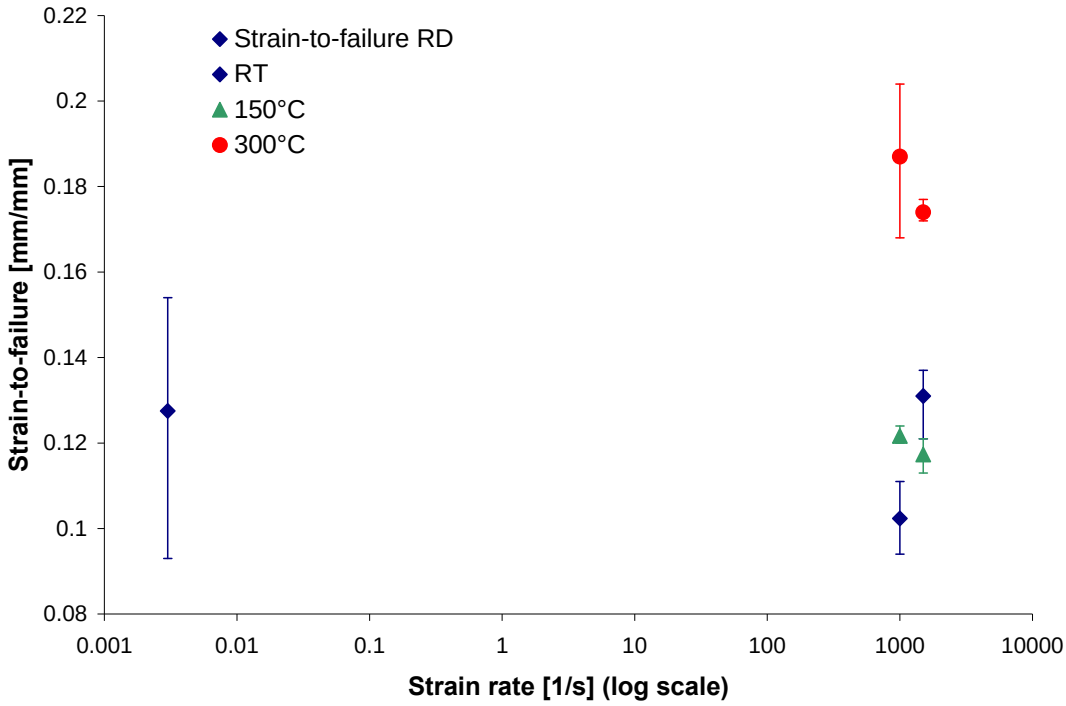

Figure 4.9; Strain-to-failure of AZ31B-H24 in the RD

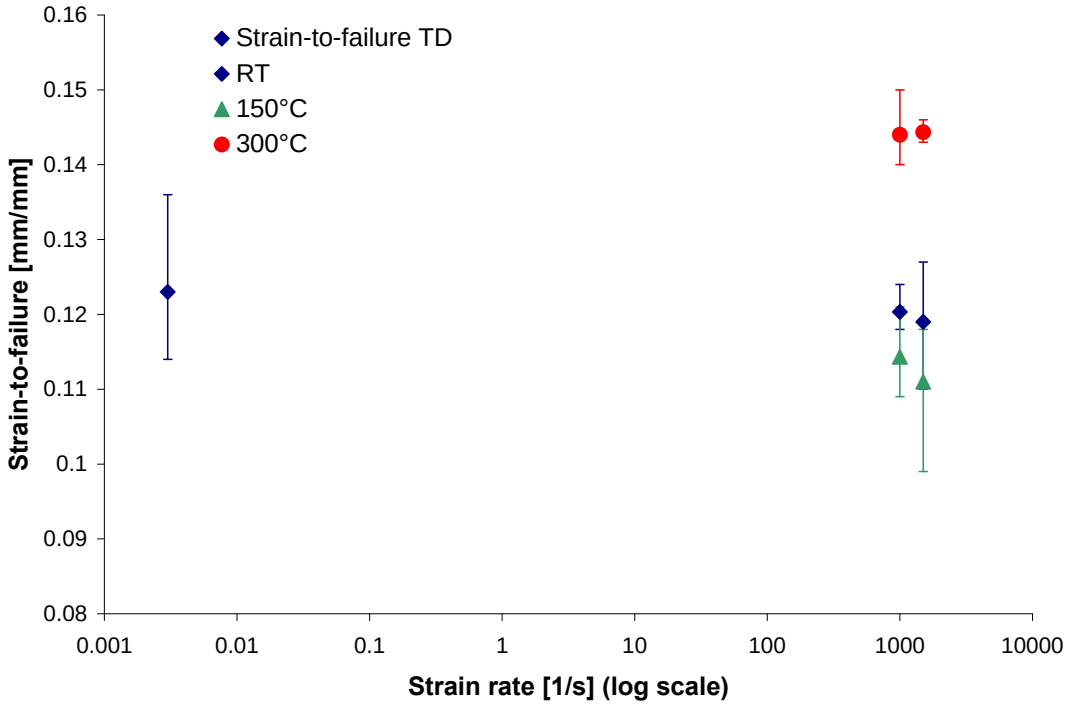

Figure 4.10: Strain-to-failure of AZ31B-H24 in the TD

At room temperature, the strain rate doesn't have a significant effect on the strain-to-failure, with the average elongation corresponding to 12-13% strain. There is a significant level of scatter in the measured data and the room temperature and 150°C high rate data overlaps considerably. There is, however, a clear increase in ductility can be seen at 300°C for the two directions.

Figure 4.11 shows a comparison of the strain-to-failure in the two directions at room temperature. The effect of temperature on the strain-to-failure is presented in Figure 4.12 for the two directions. As seen in the figures, the two directions exhibit a similar strain-to-failure behavior at room temperature and 150°C. However, at 300°C, the rolling direction shows higher ductility, with a strain to failure of approximately 18%, compared to 14% for the TD.

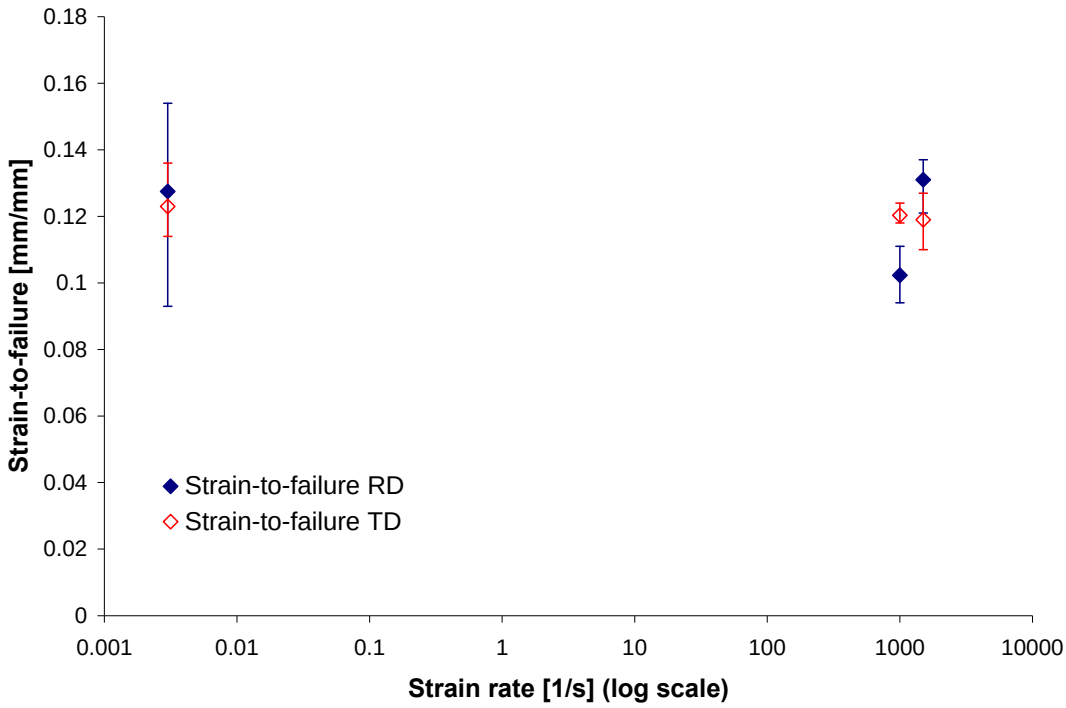

Figure 4.11: Strain rate effect on the strain-to-failure in the RD and the TD at room temperature

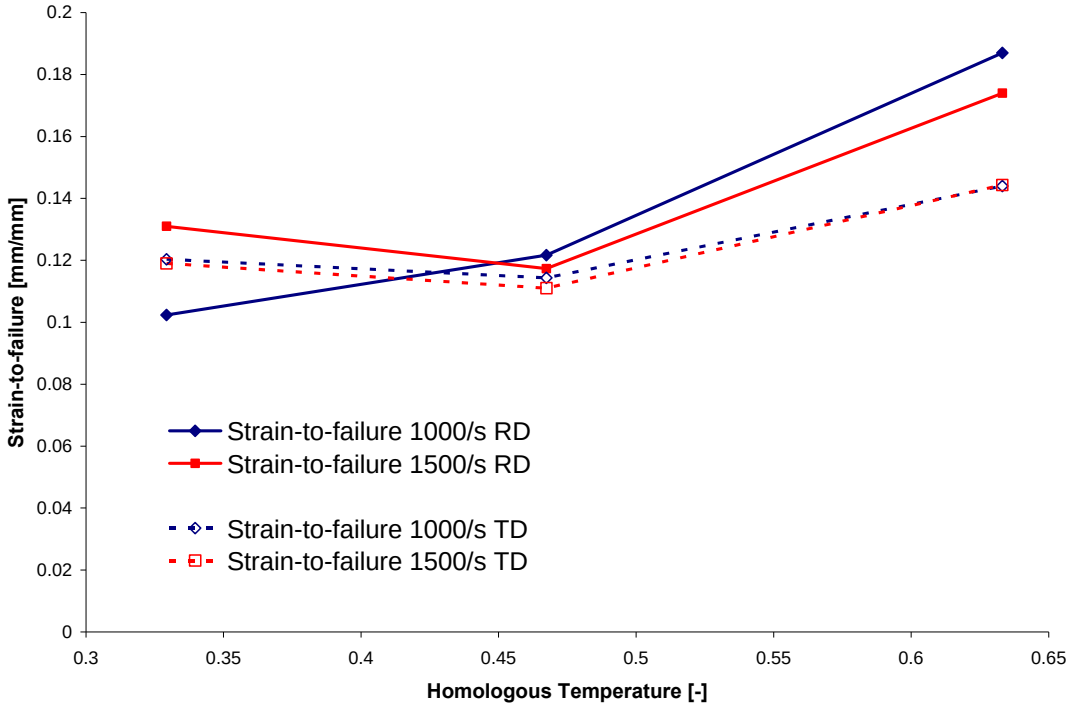

Figure 4.12: Temperature effect on the strain-to-failure in the RD and the TD at high strain rate

The effect of strain rate and temperature on the onset of necking can be estimated by considering the Considère criterion [75]. Considère showed that necking is initiated when the work-hardening rate equals the true stress, which is simply described by Equation (4.3), where σ_T and ε_T are the true stress and true strain respectively.

$$\frac{d\sigma_T}{d\varepsilon_T} = \sigma_T \tag{4.3}$$

To determine the Considère point without the excessive oscillations of the raw data, 5th and 6th order polynomial regressions on the flow curves were used and differentiated to deduce the work-hardening rates. Examples of the fits for quasi-static and high strain rate conditions can be seen in Figure 4.13, where one can observe the large oscillation of the raw work-hardening rate data. The Considère criterion applied to the RD and TD experimental data can be seen in Figure 4.14 and Figure 4.15, respectively. The effects of strain rate and temperature on the onset of necking are also summarized in Figure 4.16 and Figure 4.17, respectively.

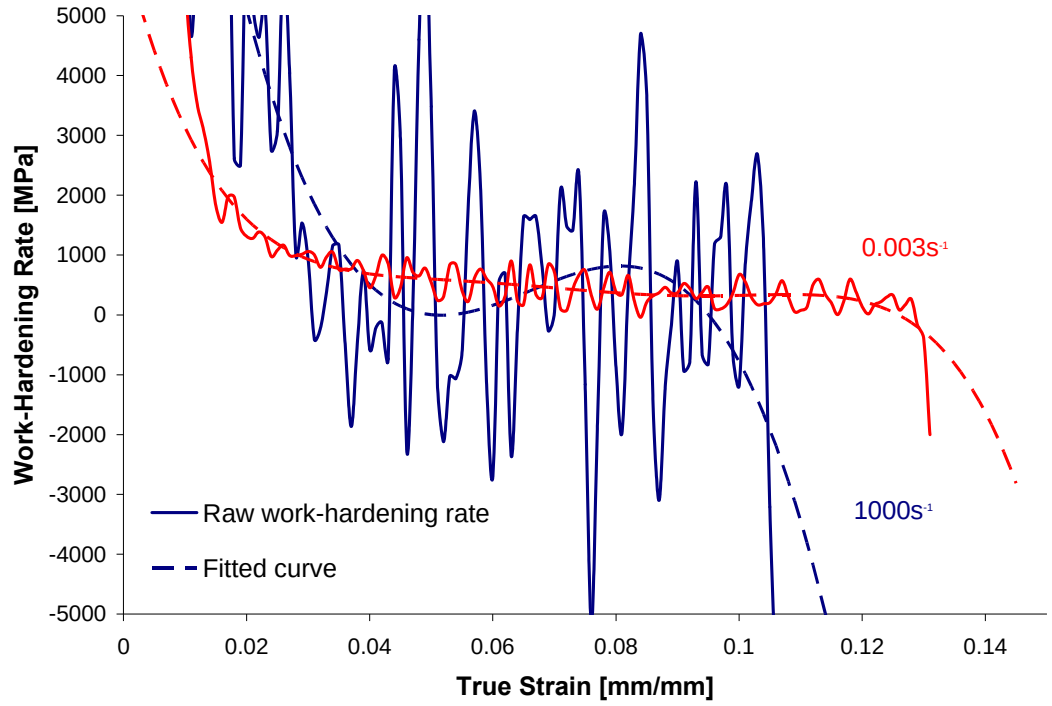

Figure 4.13: Examples of polynomial fits used for the work-hardening rate

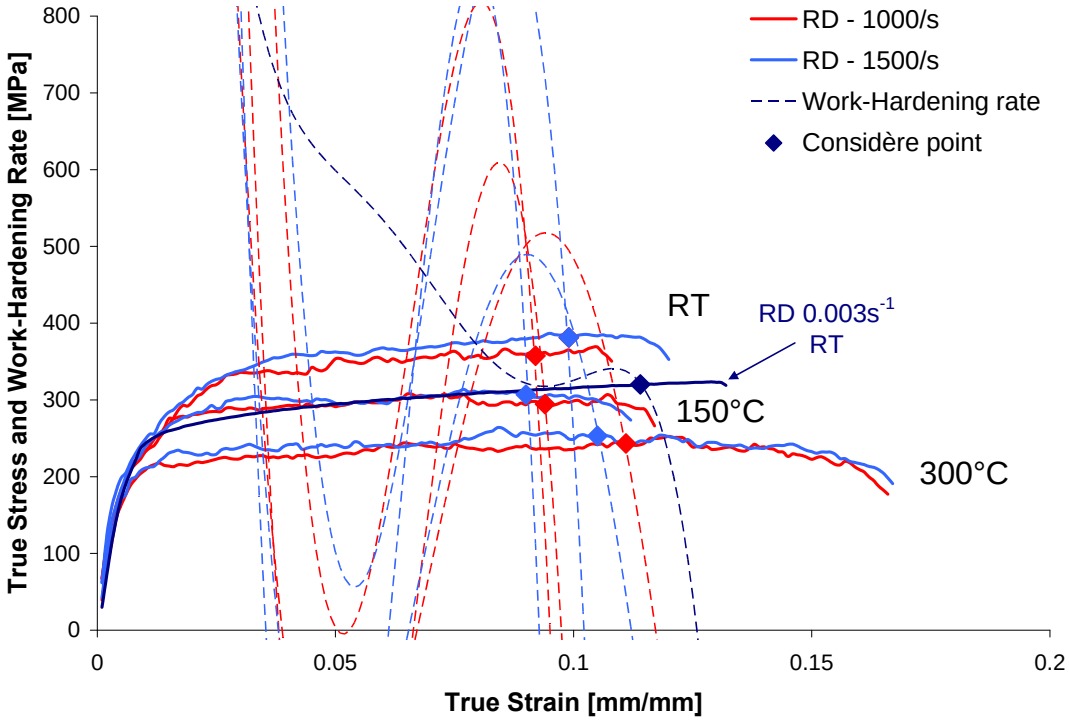

Figure 4.14: Considère criterion for AZ31B-H24 in the RD

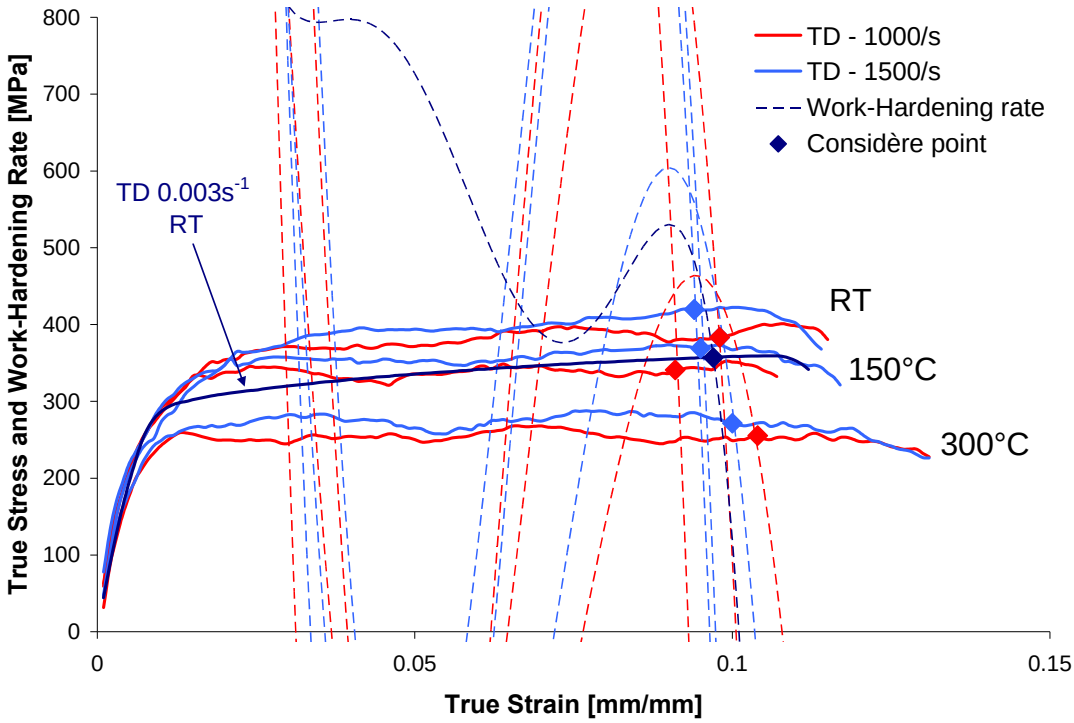

Figure 4.15: Considère criterion for AZ31B-H24 in the TD

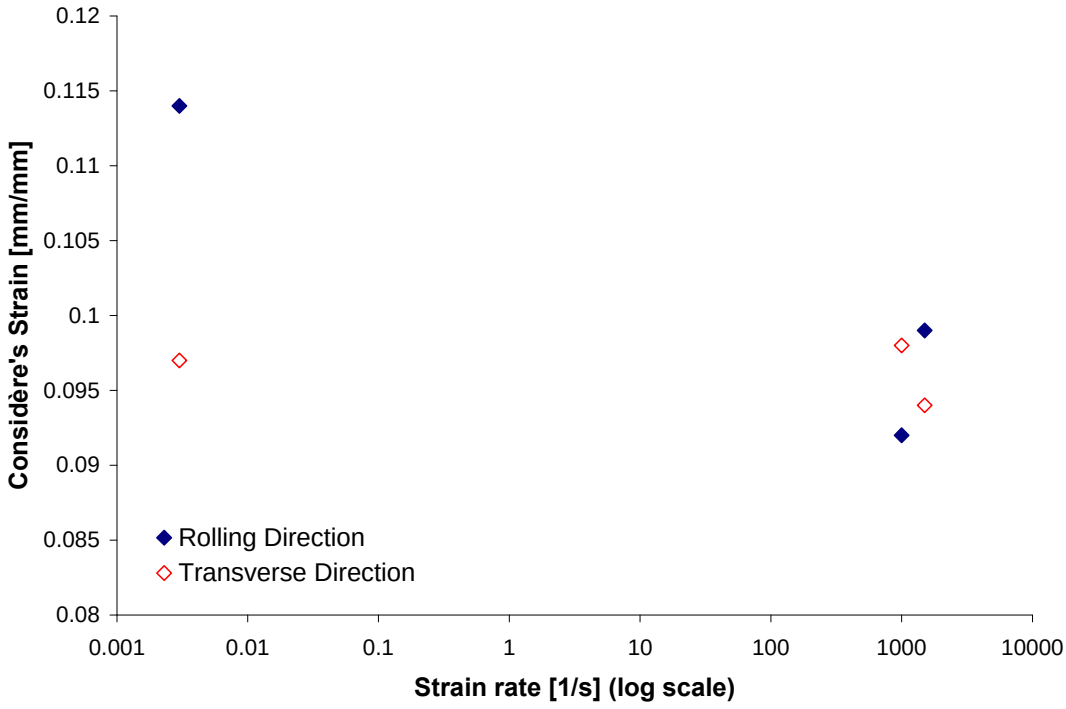

Figure 4.16: Effect of strain rate on the Considère strain for AZ31B-H24 at room temperature

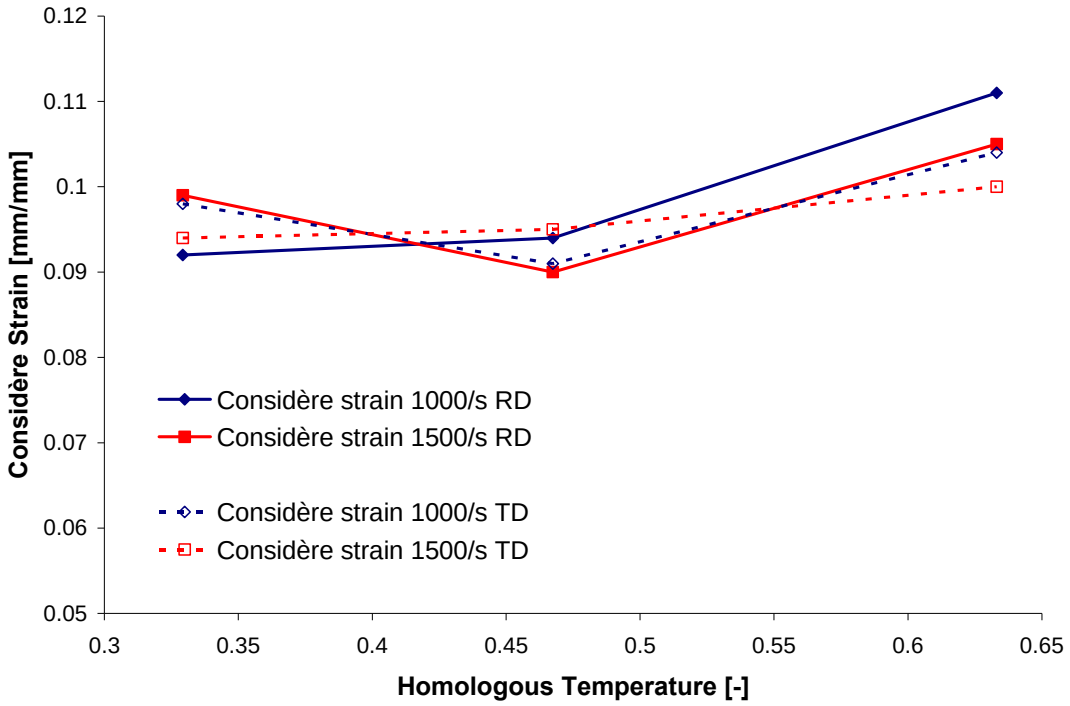

Figure 4.17: Temperature effect on the Considère strain for AZ31B-H24 at high strain rate

As seen in the four figures, the onset of necking for the AZ31B-H24 material doesn't present a significant sensitivity to strain rate and temperature. At room temperature, the Considère strain in the RD at quasi-static strain rates is higher than at high strain rate. However, one can notice that in Figure 4.14 the work-hardening rate of the quasi-static data stays close to the true stress-strain curve from 9% to 11.5% strain, which is a range that encompasses the Considère strain measured for high strain rate data. Both the RD and the TD exhibit an average strain of 10% at which the Considère criterion is satisfied.

A comparison of the Considère strains and the strain-to failure for the two directions is given in Figure 4.18 and Figure 4.19 for the room and elevated temperature conditions, respectively. The room temperature and 150°C data confirm that the ductility of the material is not strongly affected by the strain rate and temperature. However, one can notice that the strain-to-failure is much higher at 300°C, but the onset of necking is only slightly delayed.

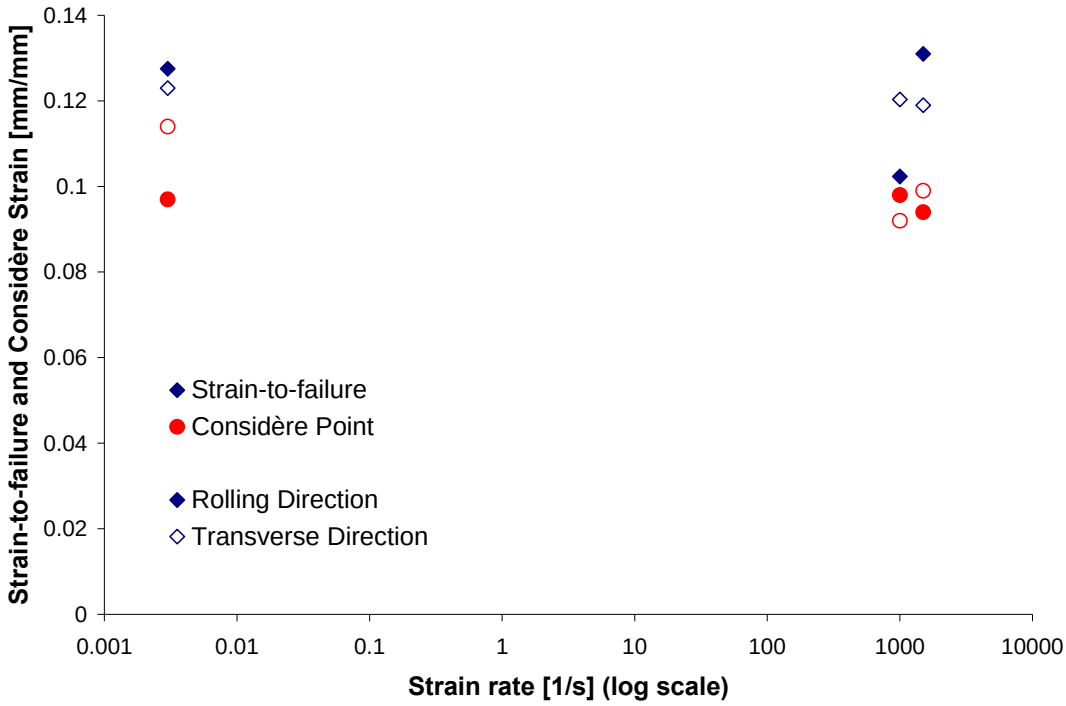

Figure 4.18: Onset of necking and strain-to failure of AZ31B-H24 at room temperature

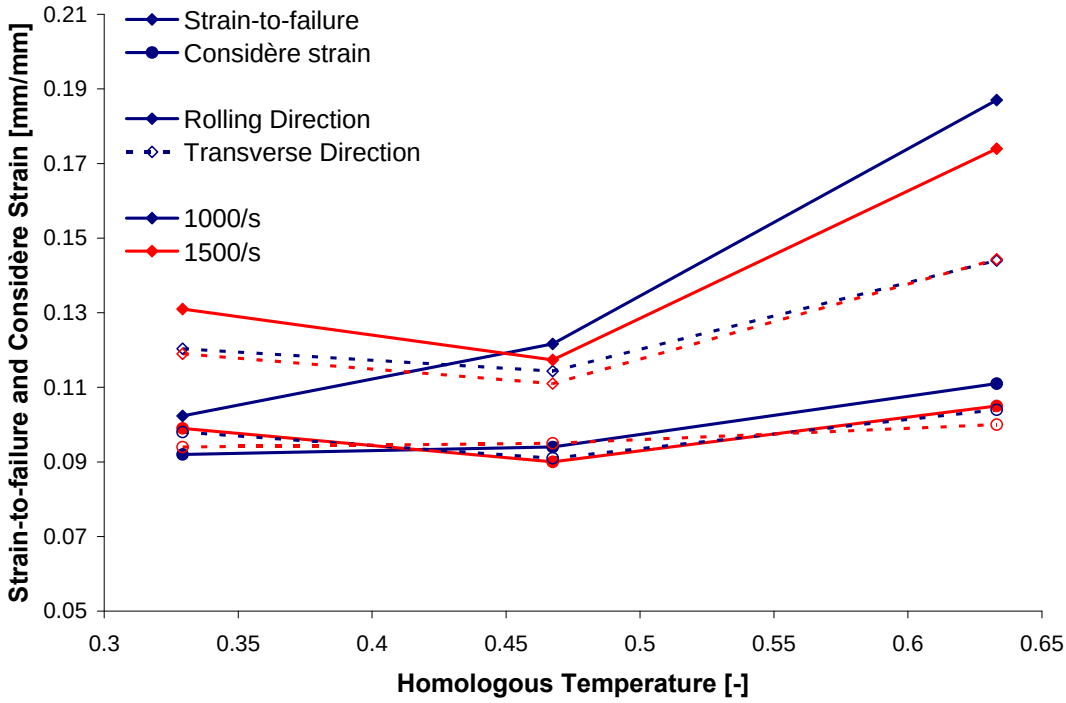

Figure 4.19: Onset of necking and strain-to failure of AZ31B-H24 at different temperatures

4.3 AZ31B-O

In this section, the effects of strain rate, temperature, sheet orientation and sheet thickness are discussed for AZ31B-O. A complete study of the strain rate and temperature sensitivity of the 1.6mm material is given in the first part of this section. The effect of the thickness is discussed in the second part.

4.3.1 Strain Rate and Thermal Sensitivity

The effect of strain rate on the constitutive behaviour of the 1.6mm thick AZ31B-O sheet can be seen respectively in Figure 4.20 and Figure 4.21 for the rolling direction (RD) and the transverse direction (TD). A comparison between the RD and the TD is also given in Figure 4.22, where only five strain rates are shown for clarity.

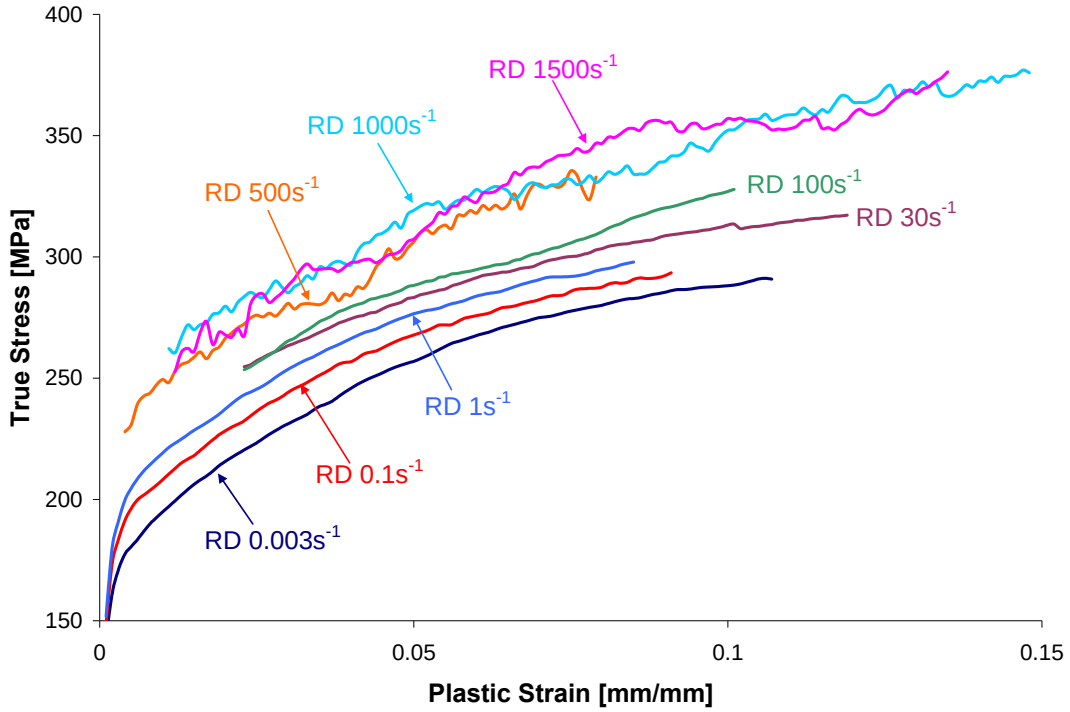

Figure 4.20: Flow curves of AZ31B-O (1.6mm) in the RD at room temperature

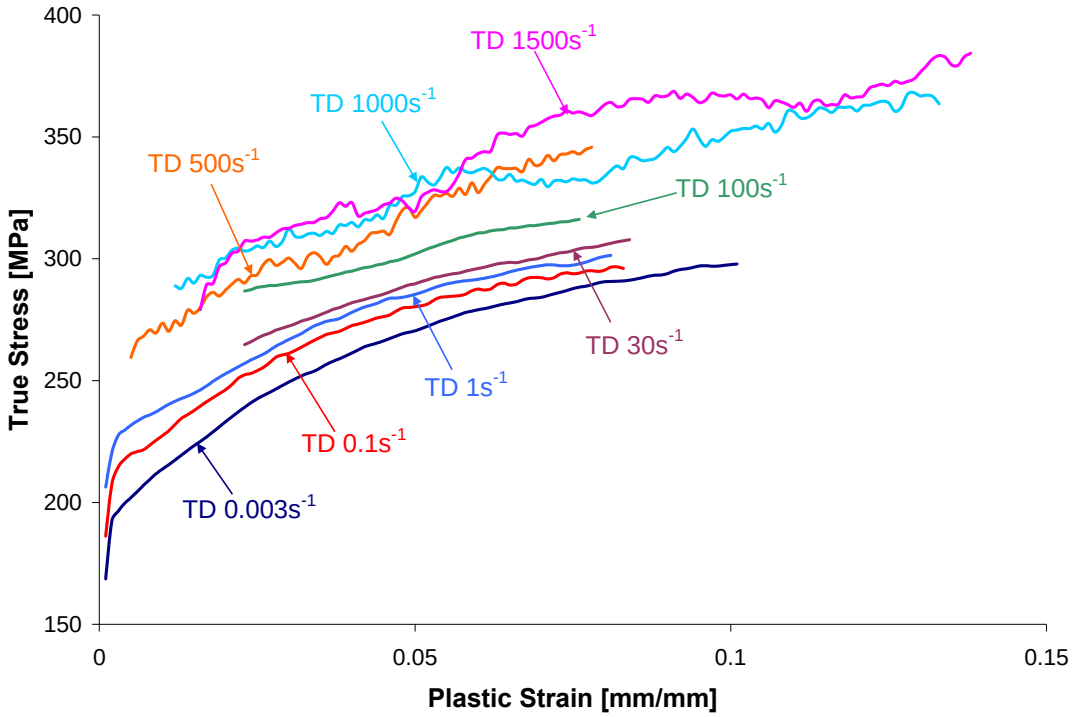

Figure 4.21: Flow curves of AZ31B-O (1.6mm) in the TD at room temperature

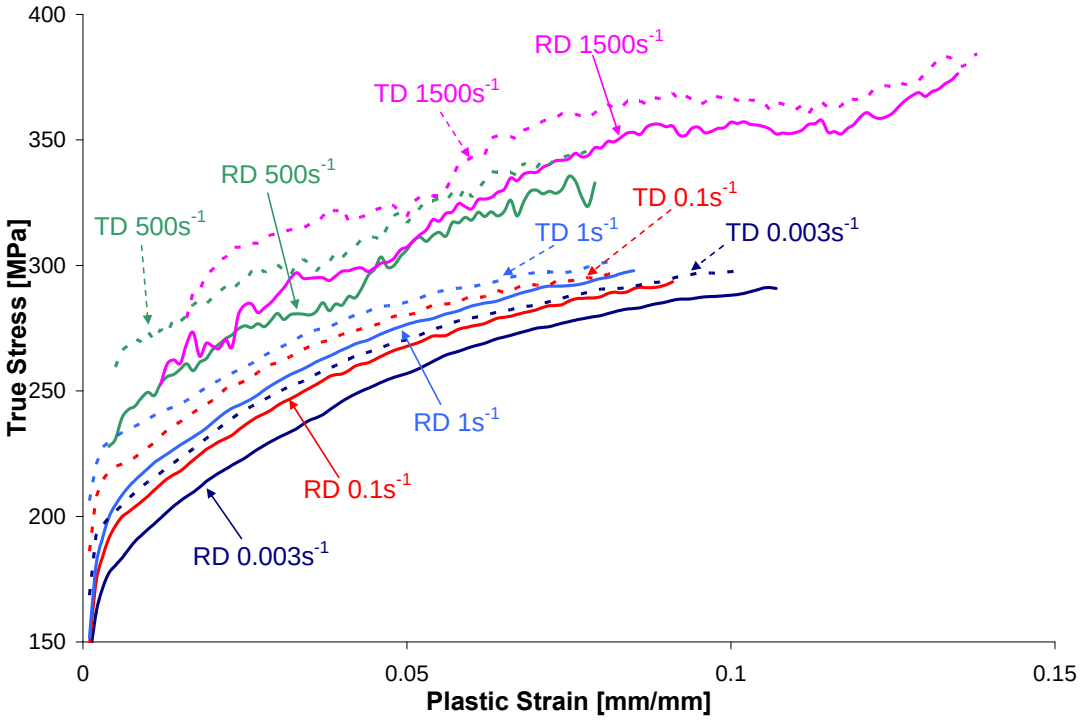

Figure 4.22: Comparison of the flow curves of AZ31B-O (1.6mm) in the RD and the TD at room temperature

In both directions, there is a clear increase of the material strength as the strain rate increases. Over the whole range of strain rates considered (from $0.003s^{-1}$ to $1500s^{-1}$), the stress level increases approximately 60 MPa for the RD, and 65 MPa for the TD, which represents an average increase of 23% for both directions. A clear anisotropy can also be seen in the flow curves. Indeed, the flow curves show an average of 15 MPa difference between the two directions, the TD being at a higher stress level than the RD for all of the strain rates considered.

In Figure 4.22, the work-hardening rate varies very little as the strain rate increases. This can be seen for both the rolling and the transverse directions and is confirmed by Figure 4.23 where the work-hardening rate versus plastic strain is plotted. The work-hardening data shows significant oscillations but it is still clear that strain rate has little effect on the work-hardening rate.

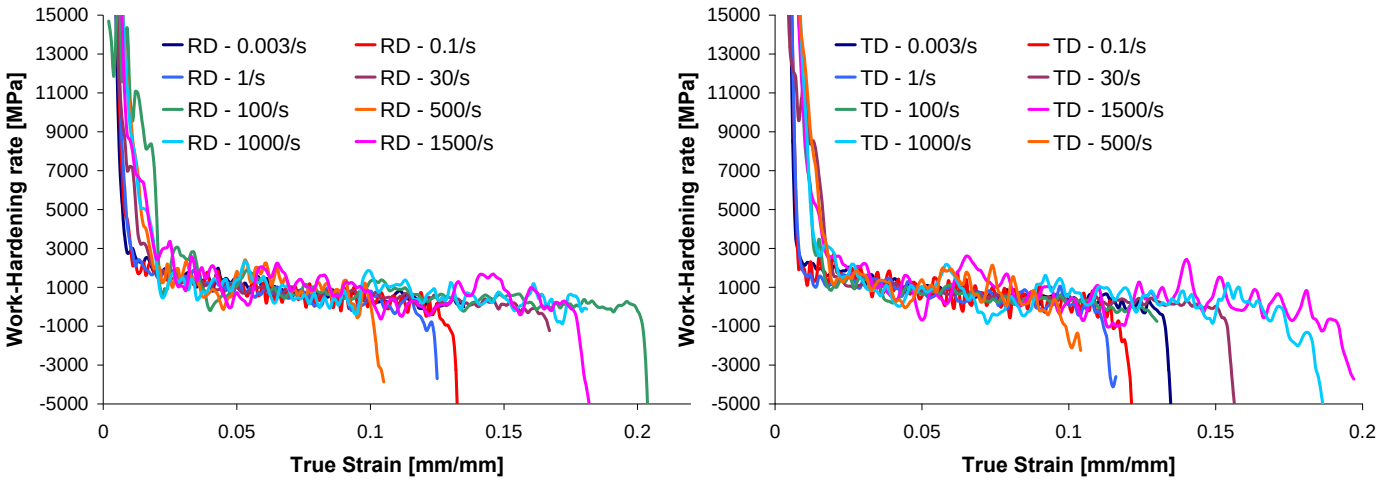

(a) (b)

Figure 4.23: Work-hardening rate vs. true strain for AZ31B-O (1.6mm) in the RD (a) and the TD (b) at room temperature

The effect of strain rate on the strain-to-failure for the RD and the TD is seen in Figure 4.24 and Figure 4.25, respectively. The strain-to-failure was determined from the engineering stress-strain curves. Intermediate strain rates were not considered due to their low apparent Young's modulus that artificially increases the strain-to-failure; also, the $500s^{-1}$ experiments

did not exhibit failure during the first pulse of loading in the TSHB experiments. A comparison of the strain-to-failure of the two directions is also given in Figure 4.26.

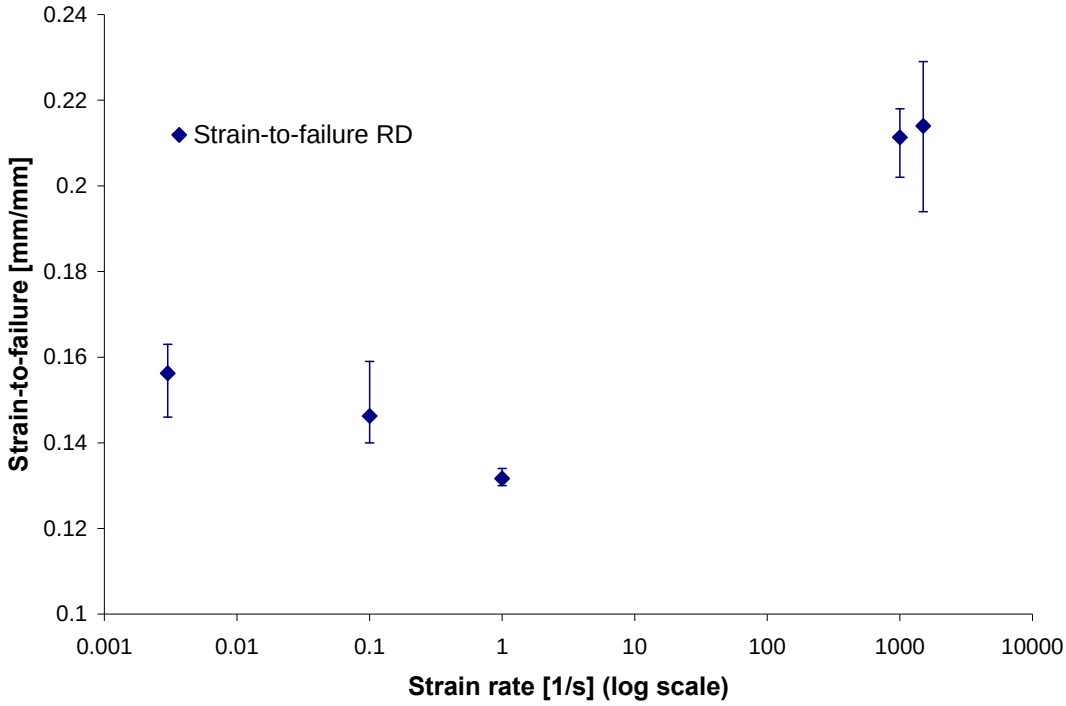

Figure 4.24; Strain-to-failure of AZ31B-O in the RD at room temperature

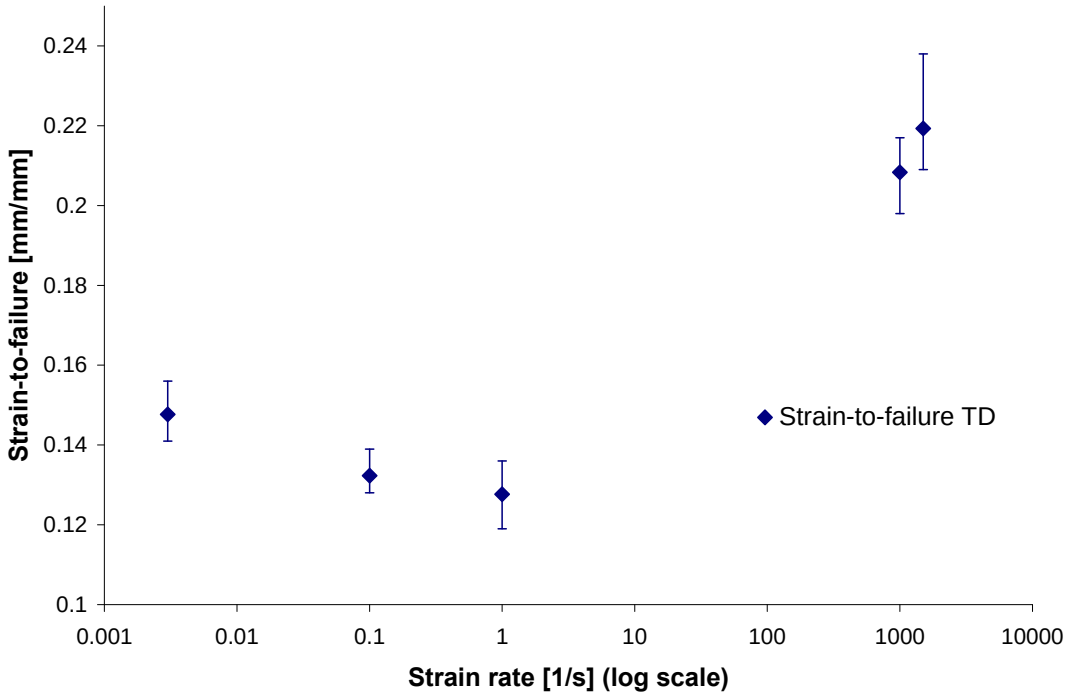

Figure 4.25; Strain-to-failure of AZ31B-O in the RD at room temperature

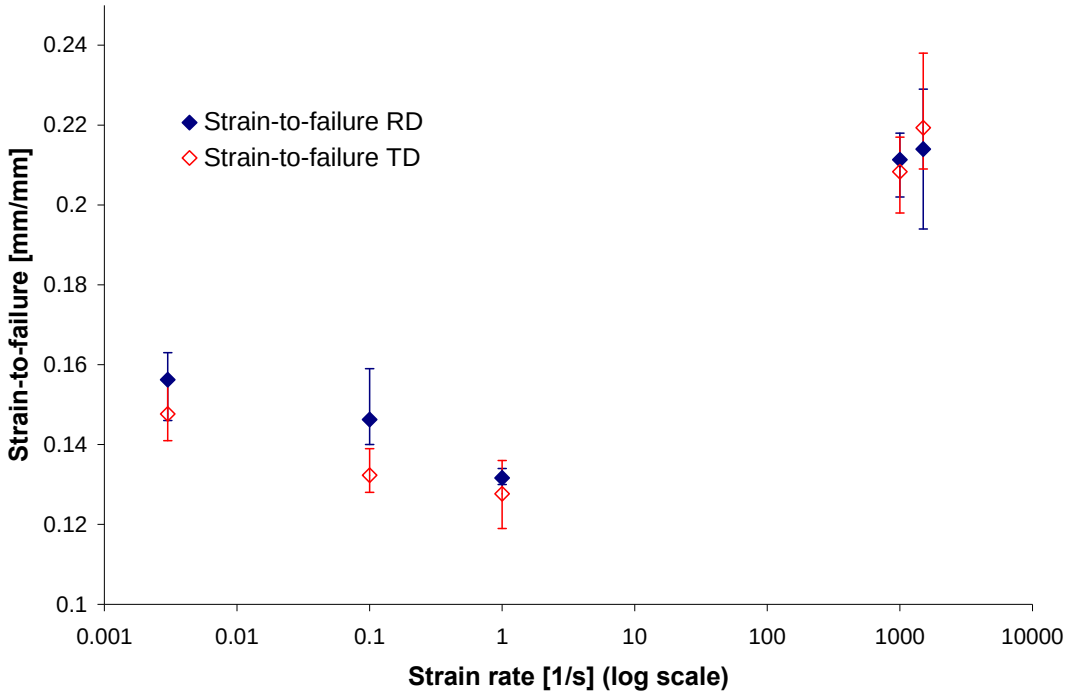

Figure 4.26; Comparison of strain-to-failure of AZ31B-O in the RD and the TD at room temperature

As seen in the figures, the two directions exhibit a similar strain-to-failure behavior at different strain rates. The average strain-to-failure is slightly higher for the RD than the TD, but this difference is smaller than the uncertainties on the measurements. Therefore no strong conclusions can be drawn on the difference between the RD and the TD. At low strain rates (below $1s^{-1}$) the strain-to-failure decreases with increasing strain rate. The ductility drops from 15% strain at $0.003s^{-1}$ to 13% strain at $1s^{-1}$. However, at strain rates above $1000s^{-1}$, the ductility of the material is clearly improved, with an average strain-to-failure of 21% strain.

According to the Considère criterion, necking is initiated when the work-hardening rate equals the true stress, as presented earlier in Equation (4.3). As was done for the H24 data, 5^{th} and 6^{th} order polynomial regressions on the flow curves were used and differentiated to deduce the work-hardening rates. Experimental data at $500s^{-1}$ was not considered since these samples didn't reach the UTS during the first pulse of loading in the TSHB experiments.

The work-hardening rate from the room temperature data is shown in Figure 4.27 and Figure 4.28 for the RD and the TD respectively. At increasing strain rate, the strain at which the Considère criterion is satisfied varies with strain rate in a non-monotonic fashion. Indeed, for strain rates lower than $1s^{-1}$, the Considère strain value decreases; whereas strain rates above $1s^{-1}$ clearly delay the onset of necking in the specimen. The strain rate dependency of the Considère strain at room temperature can be seen in Figure 4.29.

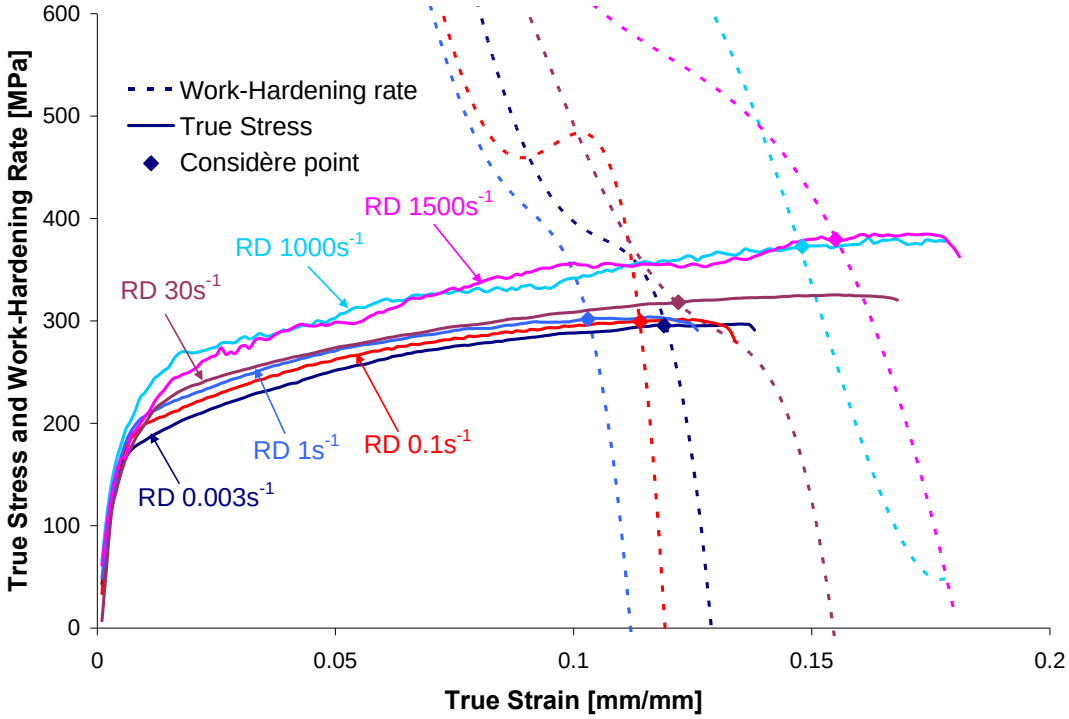

Figure 4.27: Considère criterion for AZ31B-O (1.6mm) in the RD at room temperature

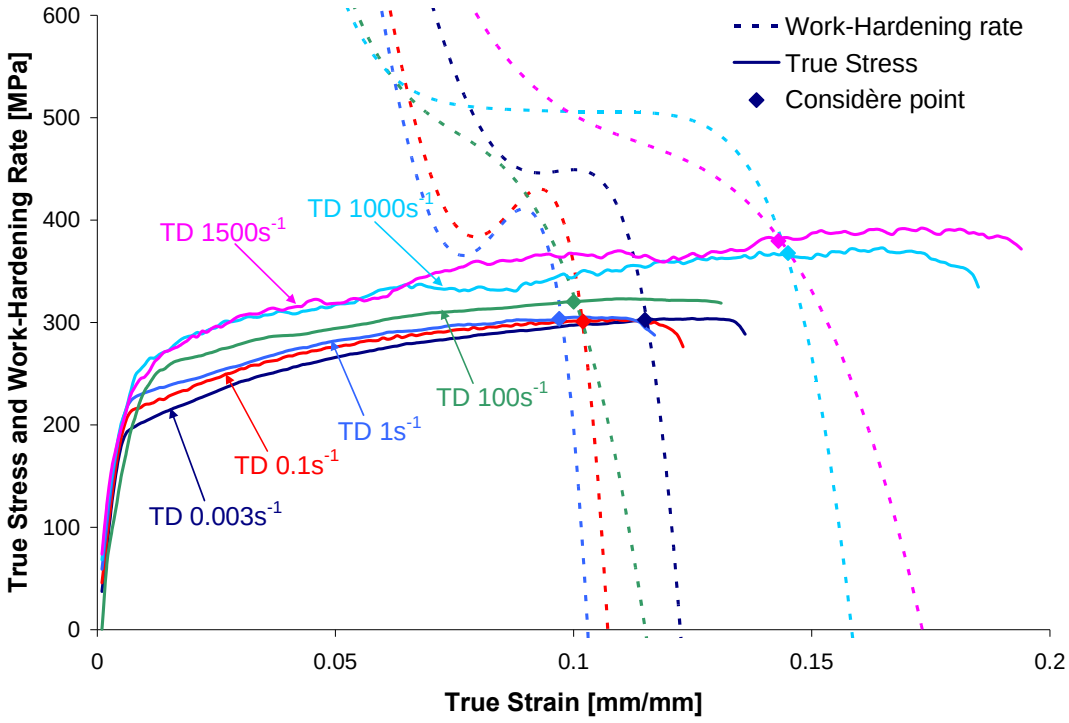

Figure 4.28: Considère criterion for AZ31B-O (1.6mm) in the TD at room temperature

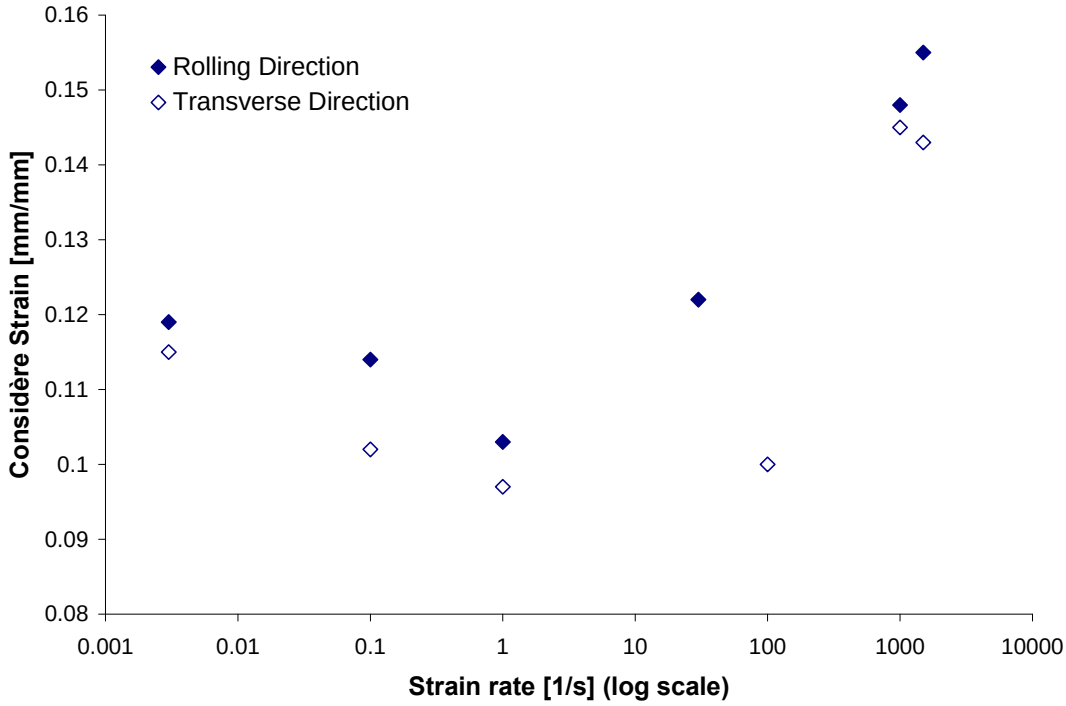

Figure 4.29: Effect of strain rate on the Considère strain for AZ31B-O (1.6mm) at room temperature

Figure 4.30 shows the true stress as a function of the strain rate for both the RD and the TD. The stress levels are plotted for plastic strains from 3% to 7. A comparison of the strain rate sensitivities for two directions is also given in Figure 4.31, in which the stress at 5% plastic strain range is plotted.

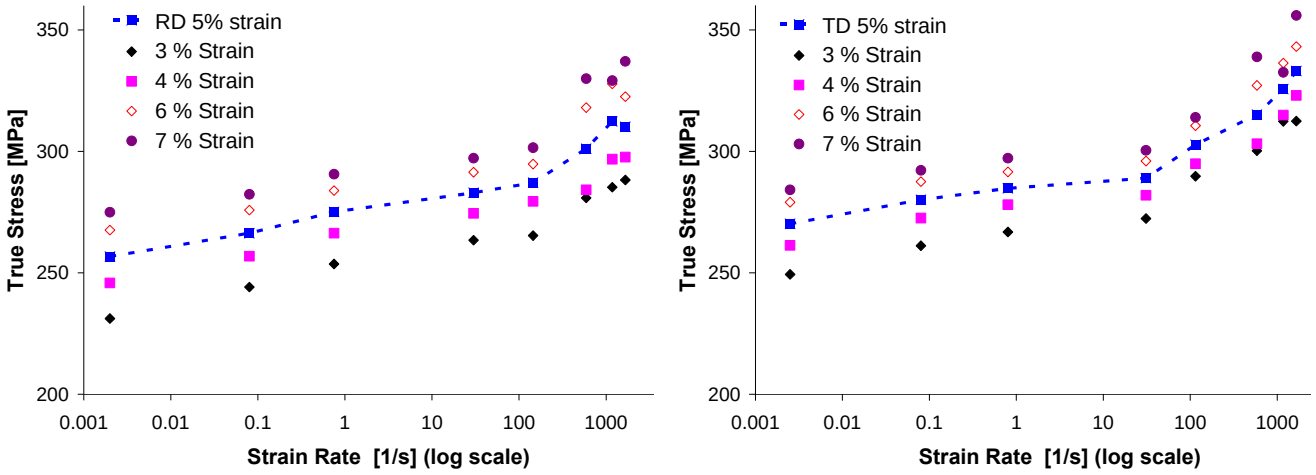

(a) (b)

Figure 4.30: True stress vs. strain rate for AZ31B-O (1.6mm) in the RD (a) and the TD (b)

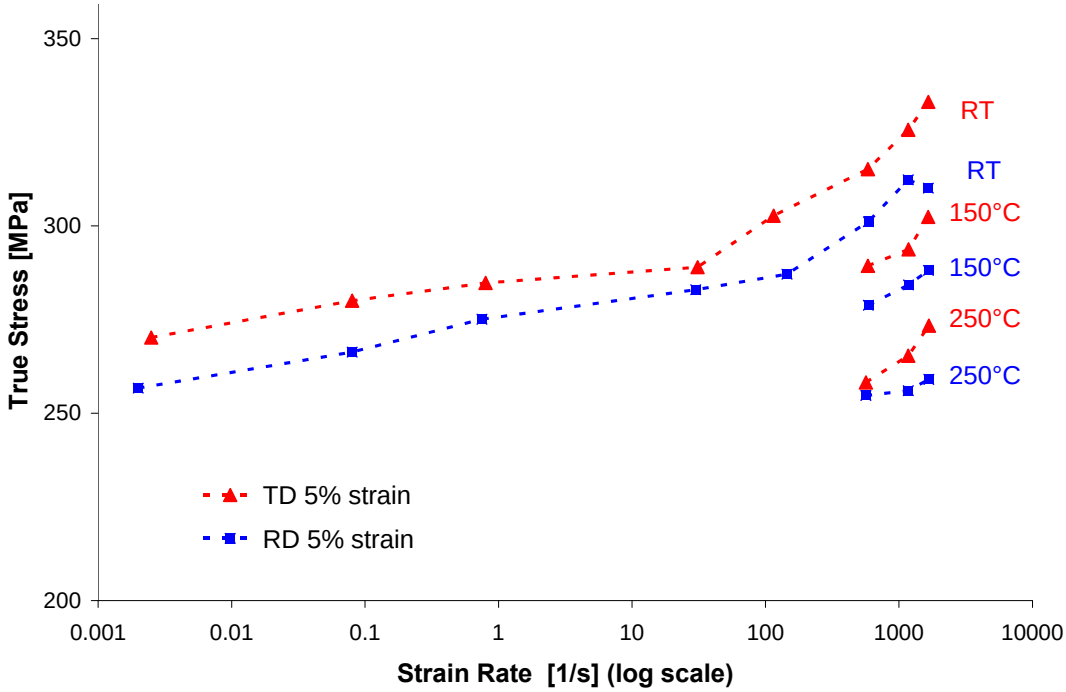

Figure 4.31: Comparison of the true stress vs. strain rate for AZ31B-O (1.6mm) in the RD and the TD

As seen in the figures, there is a clear change in the slope of the curves as the strain rate increases. Prior to strain rate values of $30s^{-1}$ – $100s^{-1}$, the flow stress and the strain rate have a log-linear relationship. However, when the strain rate exceeds $100s^{-1}$, a higher strain rate sensitivity can be seen. The strain rate dependence in this region also seems to be log-linear with a higher slope. The strain rate sensitivities are close for the two directions.

Figure 4.31 also shows the effect of temperature on the strain rate sensitivity. Overall, an increase in temperature leads to a slight reduction in the strain rate sensitivity. However, one should be cautious with this interpretation since only three temperatures were considered in the current research, and only over a limited range of strain rate.

The temperature sensitivity is further examined in Figure 4.32 and Figure 4.33, where the flow curves for the RD and the TD are plotted for high strain rate experiments performed at room temperature (RT), 150°C and 250°C.

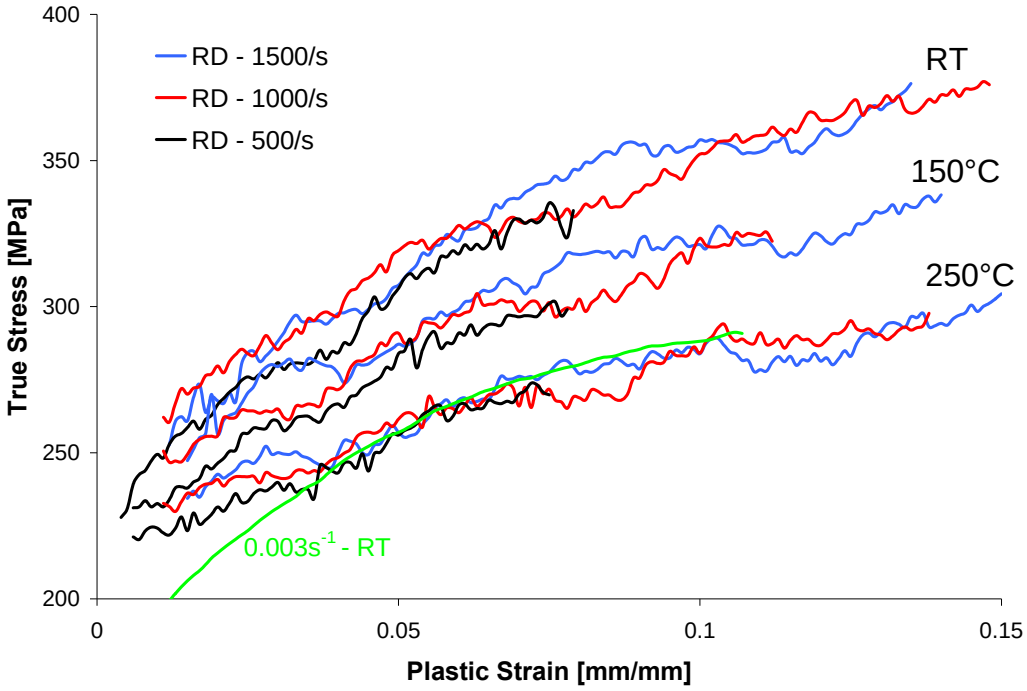

Figure 4.32: Flow curves of AZ31B-O (1.6mm) in the RD at high strain rates and elevated temperatures

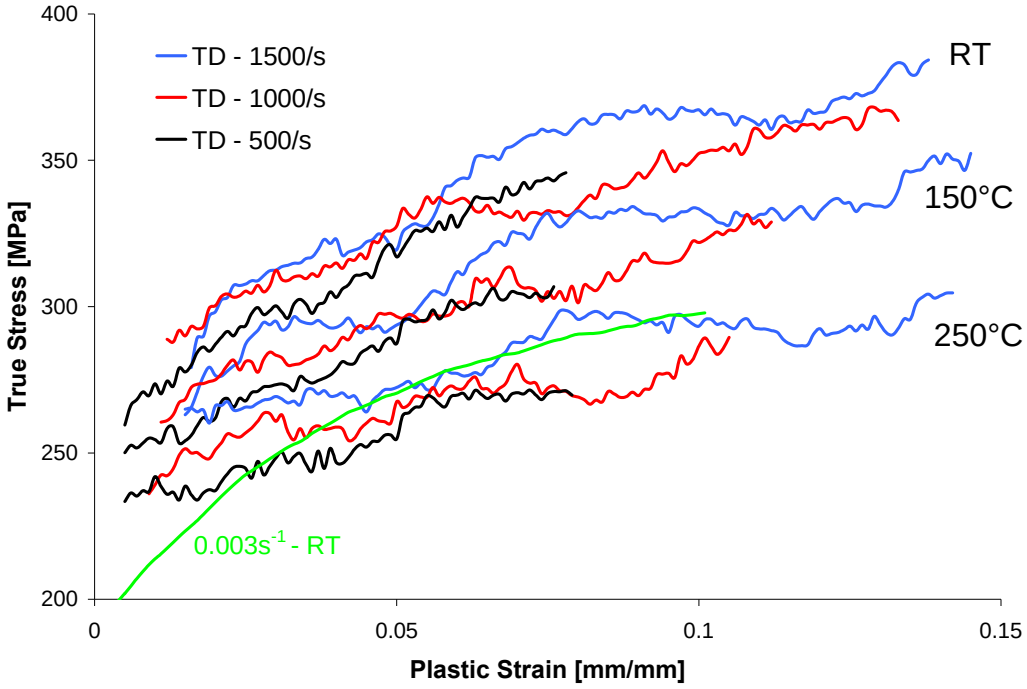

Figure 4.33: Flow curves of AZ31B-O (1.6mm) in the TD at high strain rates and elevated temperatures

Both sheet orientations exhibit thermal softening. From room temperature to 250°C, the flow stress is reduced by approximately 55 MPa in both directions. Due to the high strain rate nature of the deformation, the stress stays at a high level, even at elevated temperatures. Indeed, as seen in the figures, the 250°C experiments in both directions demonstrate a stress level close to the quasi-static experiments at room temperature.

Figure 4.34 shows the evolution of the stress level at the different temperatures; the three testing temperatures being represented by the homologous temperature T*, defined in Equation (4.2). The stress value for 3%, 5% and 7% plastic strain are given in the figure, and the range of stress represented by these values gives a good estimation of the decrease of work-hardening rate as the temperature increases.

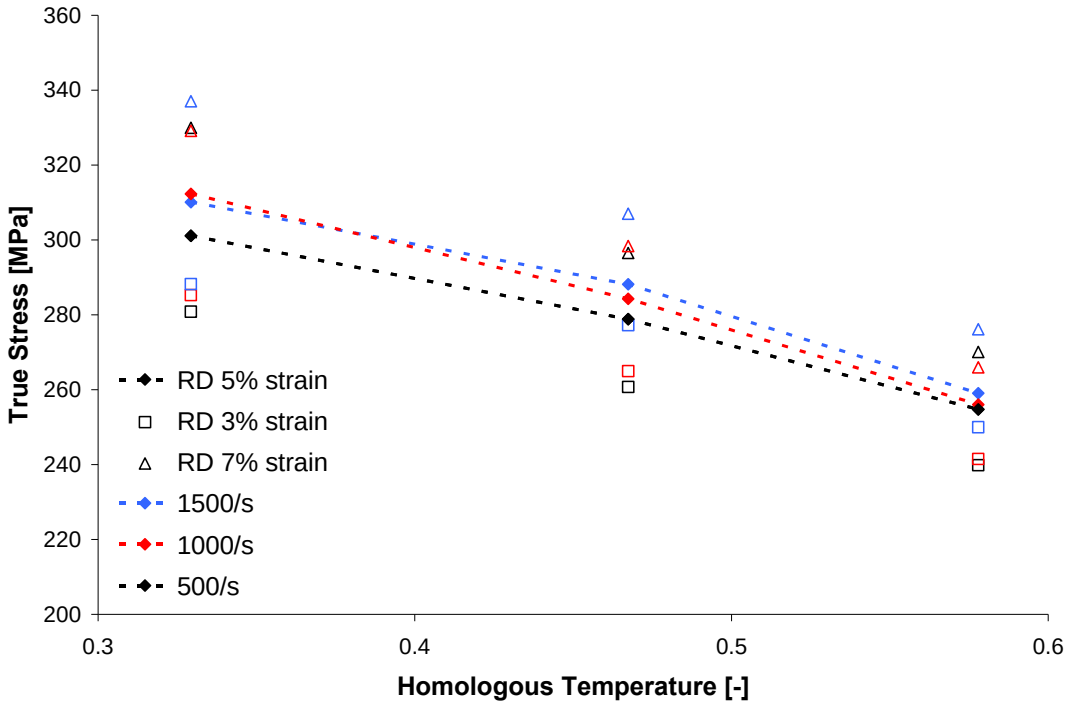

Figure 4.34: True stress vs. homologous temperature for AZ31B-O (1.6mm) in the RD at high strain rate

The effect of temperature on the strain-to-failure for the RD and the TD are shown in Figure 4.35 and Figure 4.36, respectively. As seen in the figures, the temperature rise at high strain rate doesn't significantly affect the failure of the material, especially for the RD which shows overlapping of the error bars representing the variability in the measurement. In the TD, the strain-to-failure is slightly reduced at elevated temperature. For the two directions and three temperatures considered, the strain-to-failure is still clearly higher than the quasi-static level at room temperature. The effect of temperature on the strain-to-failure of the two directions at high strain rate can be seen in Figure 4.37. Similar to the room temperature data, the orientation of the sheet doesn't have a significant effect on the strain-to-failure of the material.

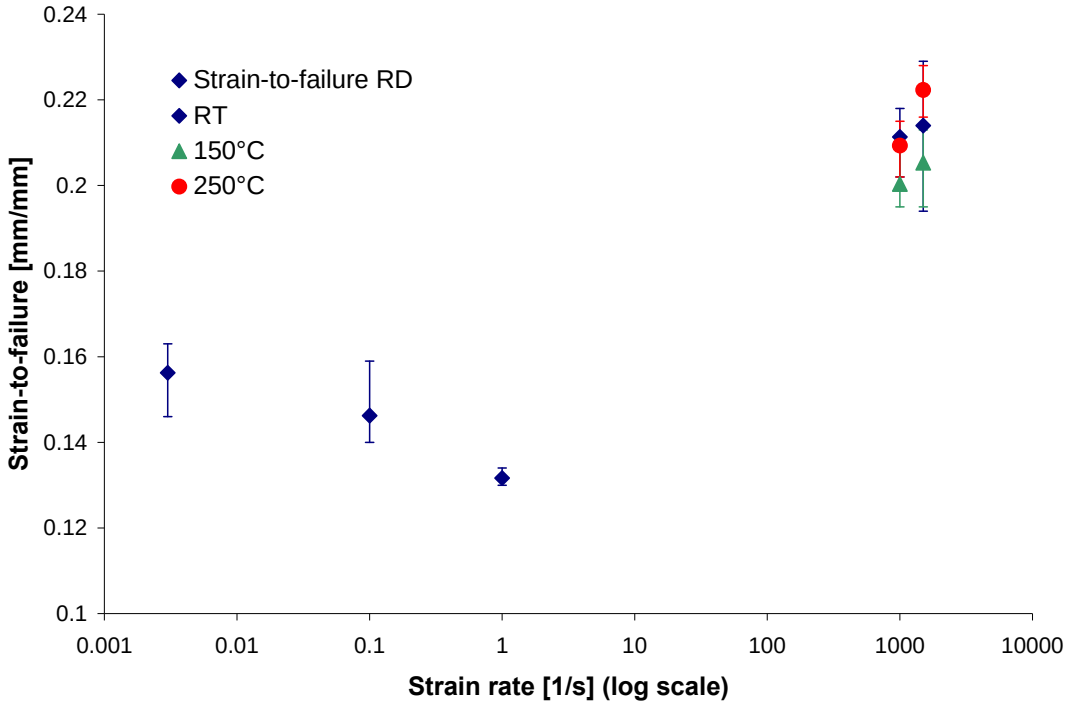

Figure 4.35: Strain-to-failure for the RD at different temperatures

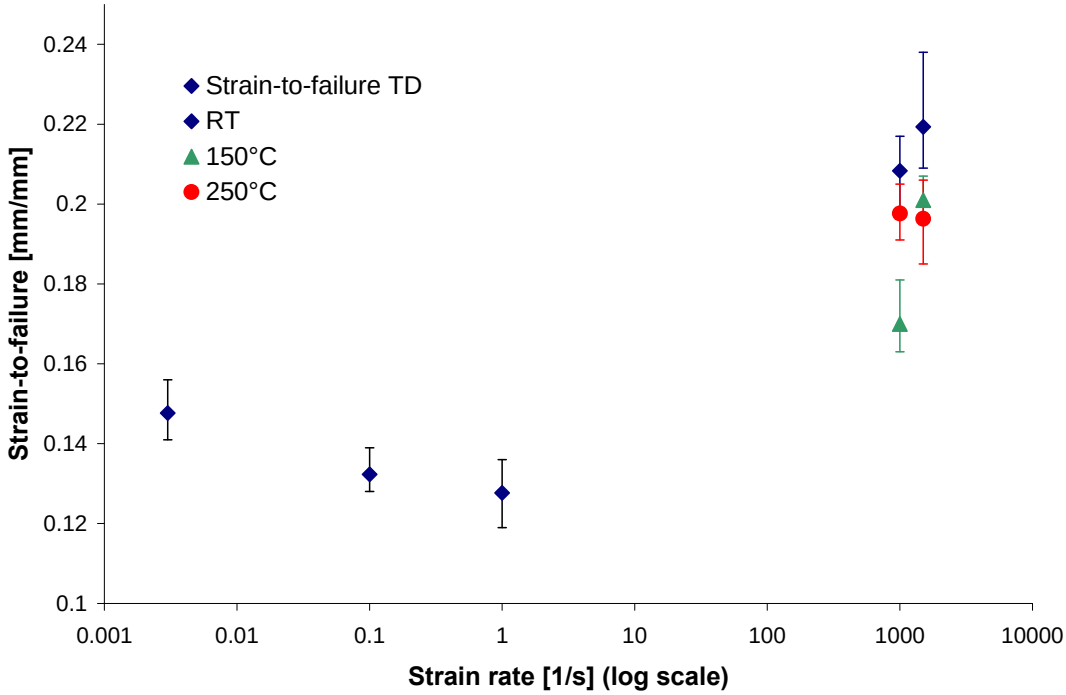

Figure 4.36: Strain-to-failure for the TD at different temperatures

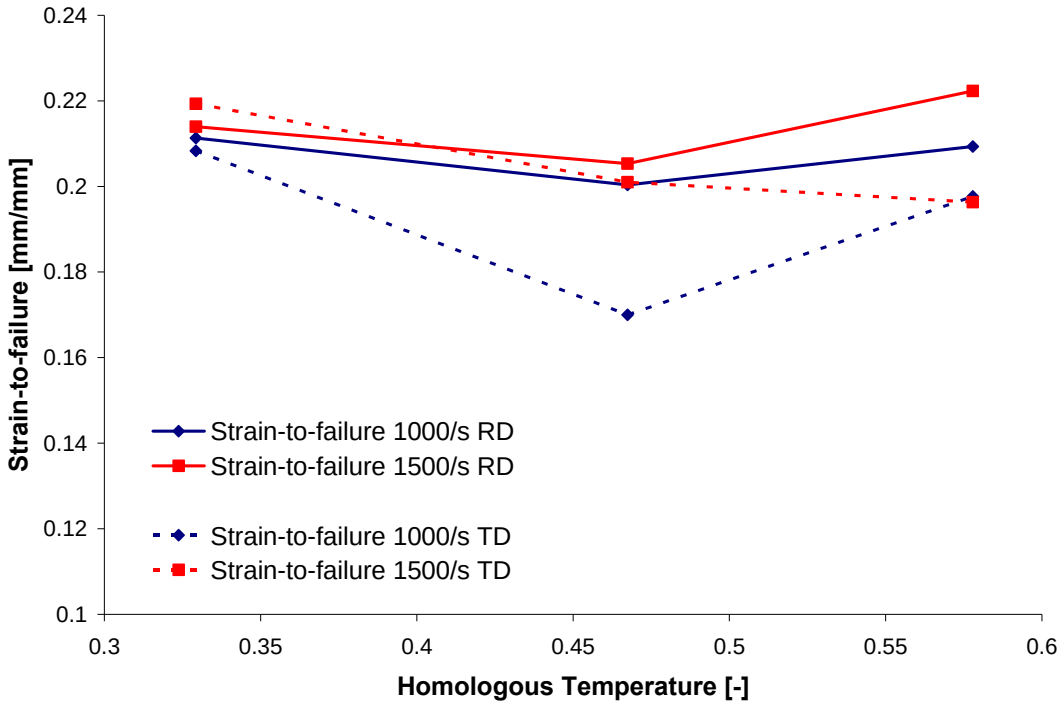

Figure 4.37: Strain-to-failure in the RD and the TD at different temperatures and high strain rate

The work-hardening rate is also slightly affected by the temperature. Figure 4.38 shows a lower work-hardening rate as the temperature increases. The difference of work-hardening rate is small but can still be detected in the flow curves, as in Figure 4.32 for example.

Similarly to the room temperature data, the Considère criterion was applied to determine the onset of necking for elevated temperature experiments, as illustrated in Figure 4.39 and Figure 4.40 for the two directions. A comparison of the two directions at different temperatures can also be seen in Figure 4.41. As seen in those three figures, temperature has little effect on the onset of necking. As the temperature increases, the necking appears earlier in the test, with a maximum difference of 2% strain for the TD and 1.5% for the RD.

A comparison of the strains-to-failure and Considère strains are shown in Figure 4.42 and Figure 4.43 for room and elevated temperatures, respectively. Both show similar trends with temperature for the O-temper material.

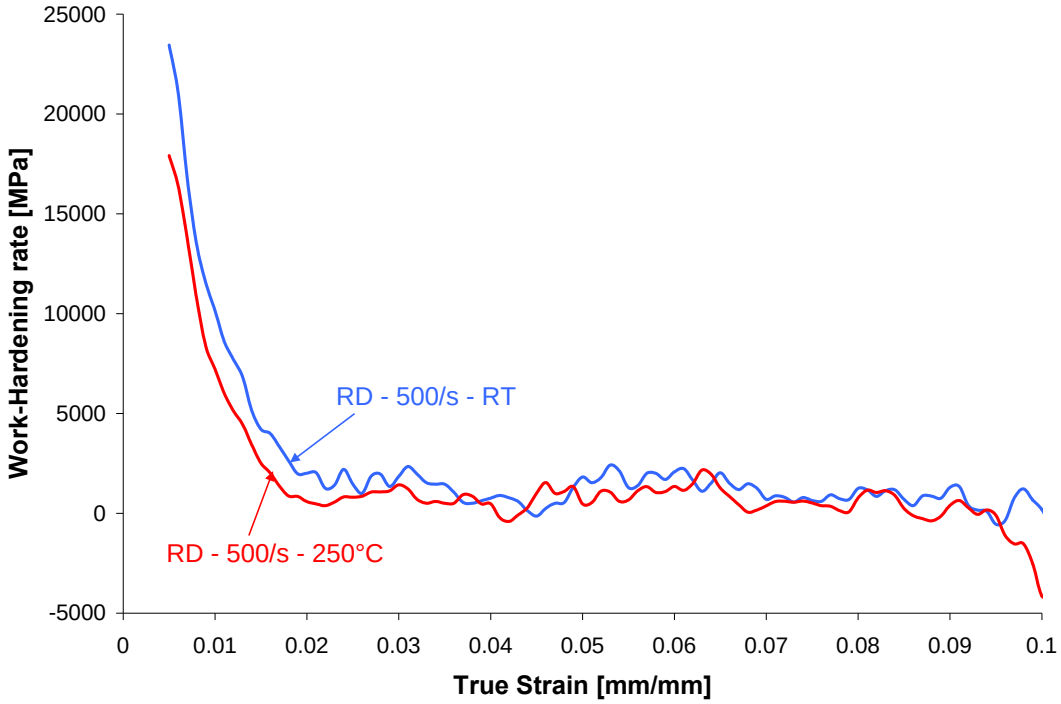

Figure 4.38: Effect of temperature on the work-hardening rate for AZ31B-O (1.6mm)

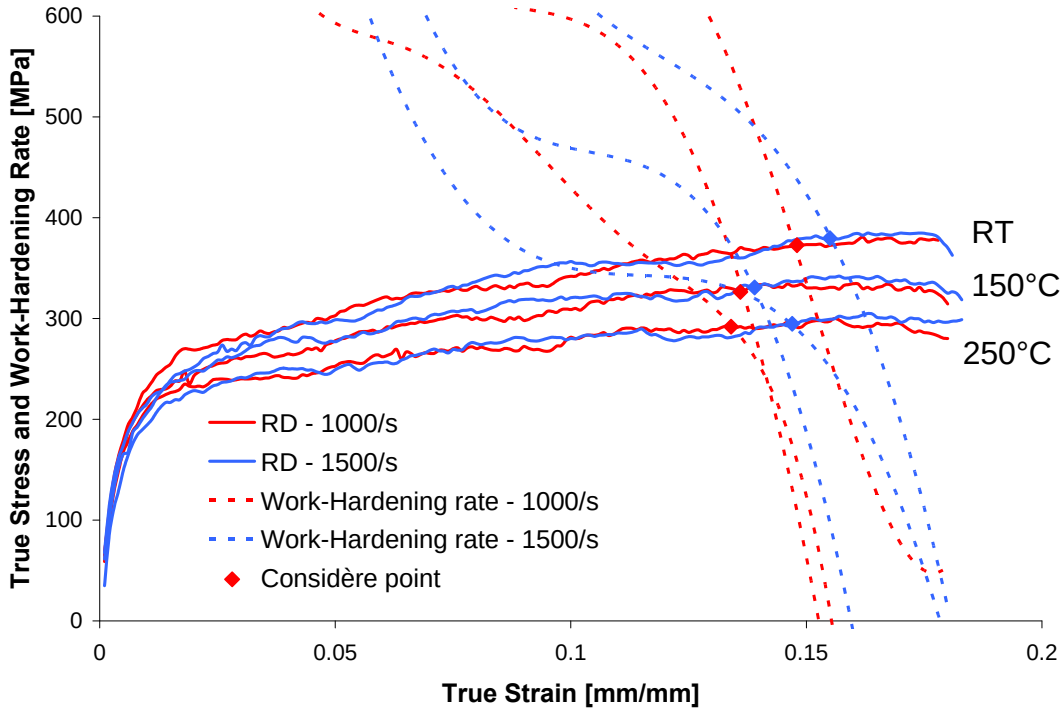

Figure 4.39: Considère criterion for AZ31B-O (1.6mm) in the RD at high strain rates and elevated temperatures

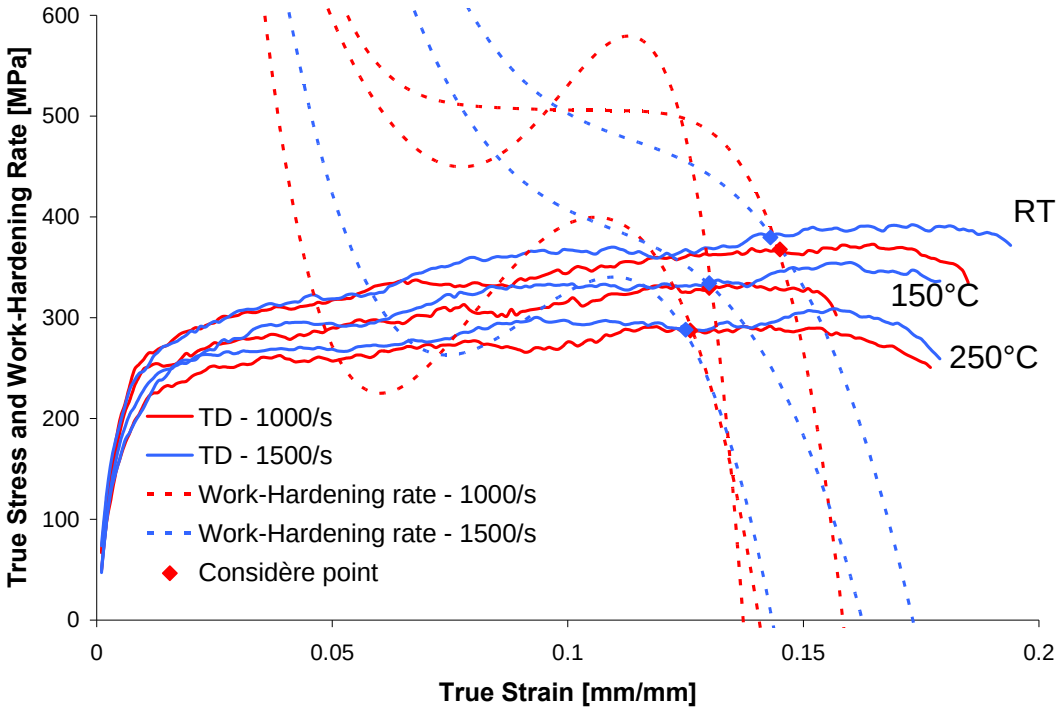

Figure 4.40: Considère criterion for AZ31B-O (1.6mm) in the TD at high strain rates and elevated temperatures

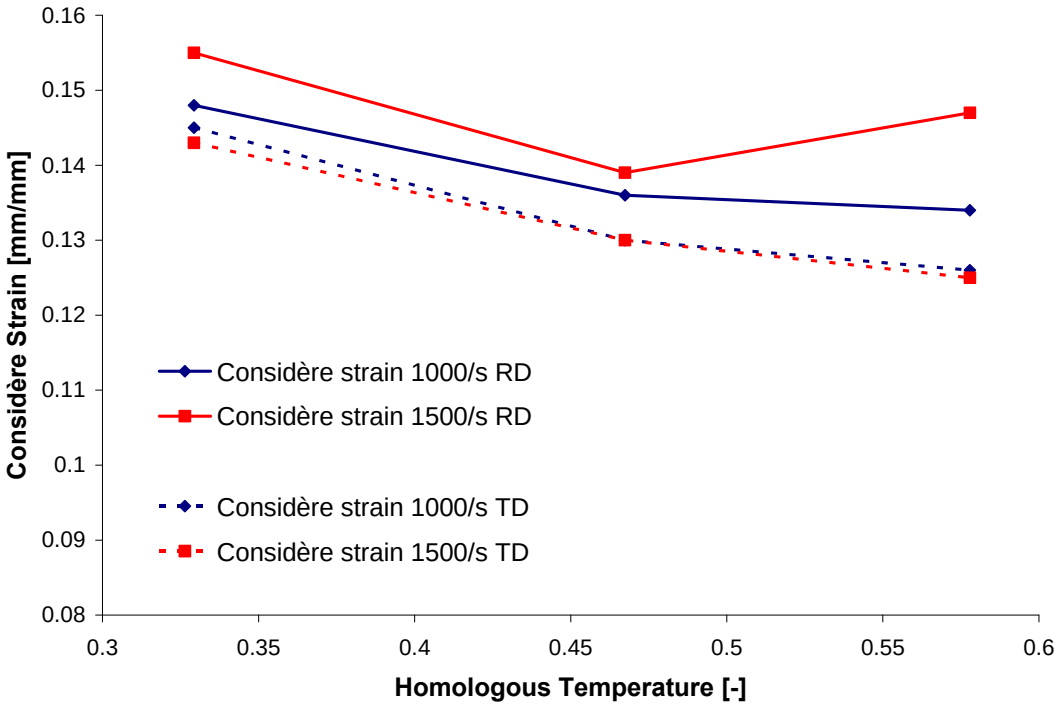

Figure 4.41: Effect of temperature and sheet orientation on the Considère strains for AZ31B-O

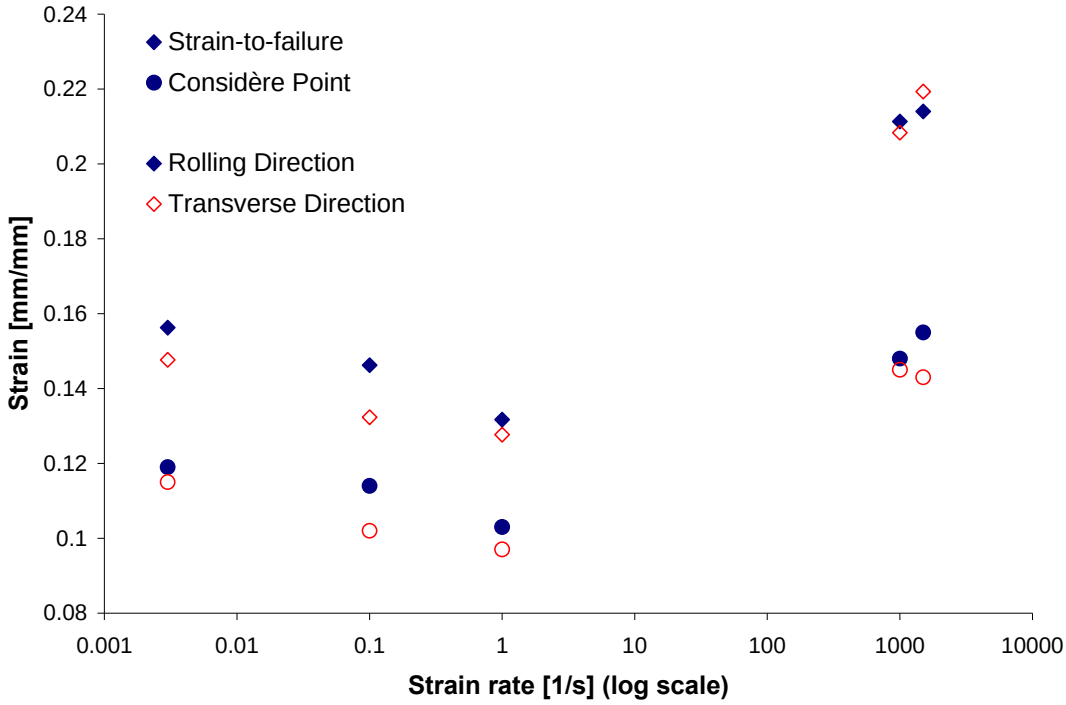

Figure 4.42: Strain to failure and Considère strain of AZ31B-O (1.6mm) at room temperature

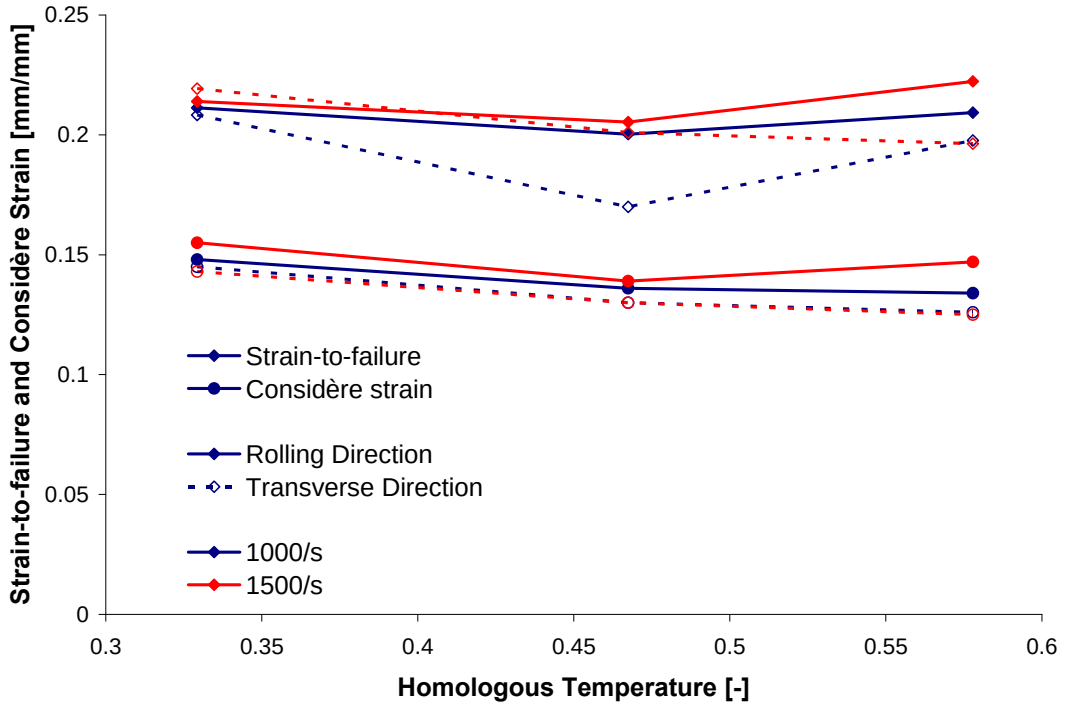

Figure 4.43: Strain to failure and Considère strain of AZ31B-O (1.6mm) at different temperatures

4.3.2 Effect of Thickness

The effect of thickness on the constitutive behaviour of AZ31B-O is presented in this section. Here, room temperature experiments only were performed on 1mm and 2.5mm thick sheets over the range of strain rates. Since the three sheets were rolled during their forming process, different strain paths will result from the production of each sheet. Any residual stresses due to the rolling process were removed by annealing the metal sheets. However, the grain sizes and textures of the materials in the different sheet thicknesses can be different [18], which can affect the constitutive response of the materials.

A comparison of the different flow curves is presented in Figure 4.44 and Figure 4.45 for strain rates from $0.003s^{-1}$ to $30s^{-1}$, respectively, in the RD and the TD. High strain rate flow curves are given in Figure 4.46 for the RD and in Figure 4.47 for the TD.

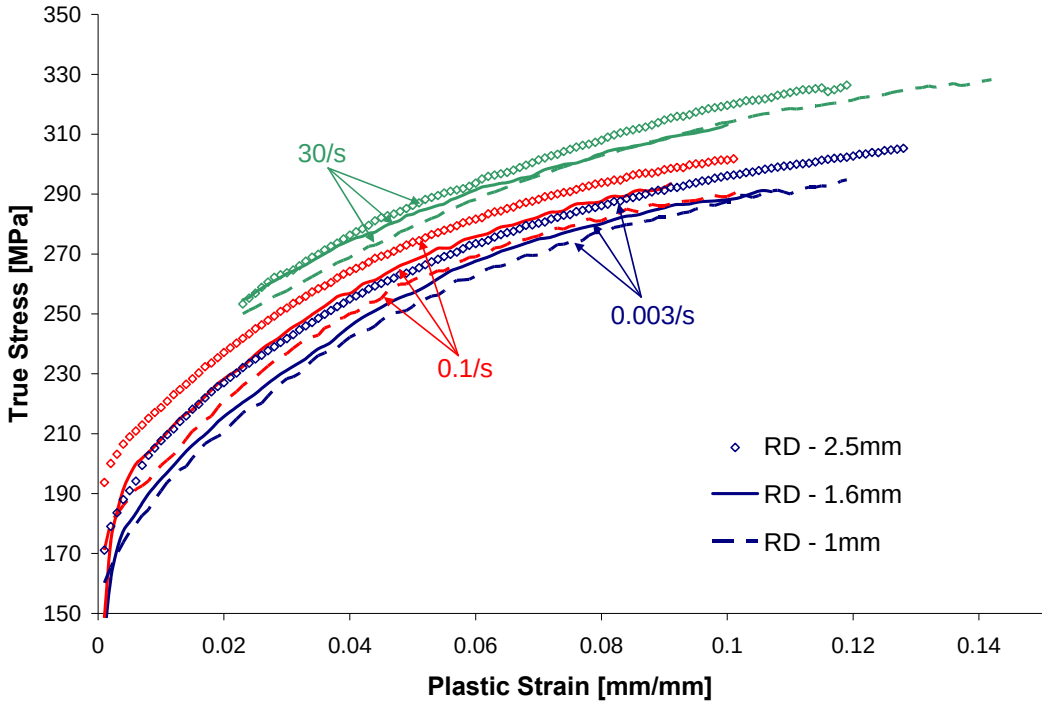

Figure 4.44: Effect of thickness on flow curves for strain rates from $0.003s^{-1}$ to $30s^{-1}$ in the RD

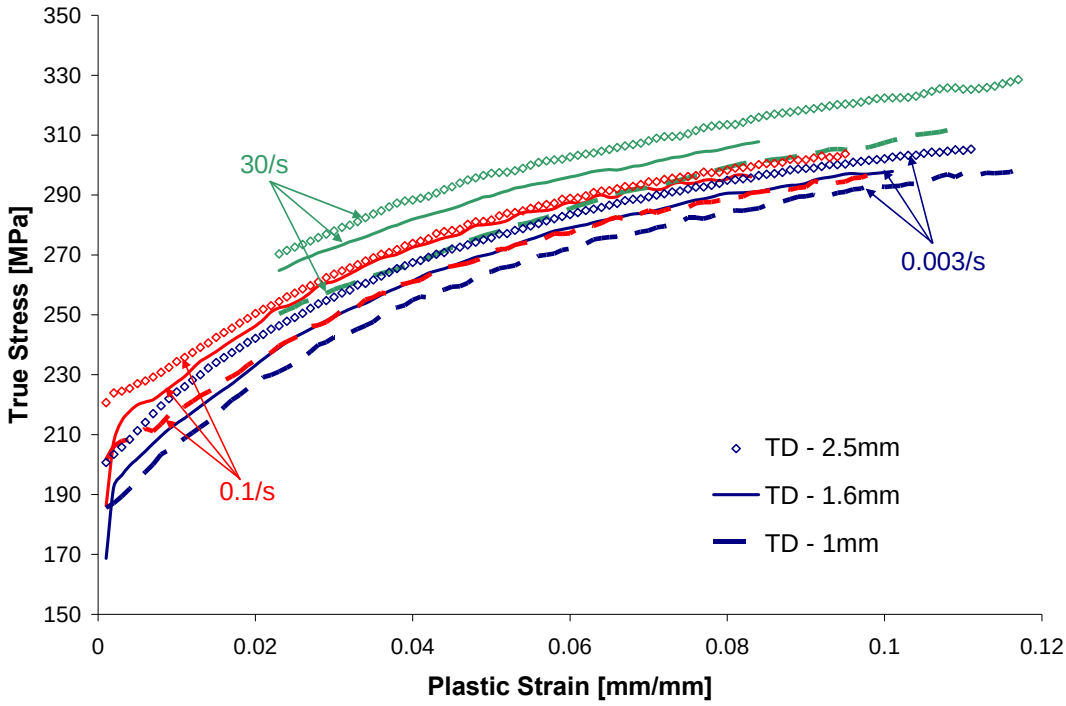

Figure 4.45: Effect of thickness on flow curves for strain rates from $0.003s^{-1}$ to $30s^{-1}$ in the TD

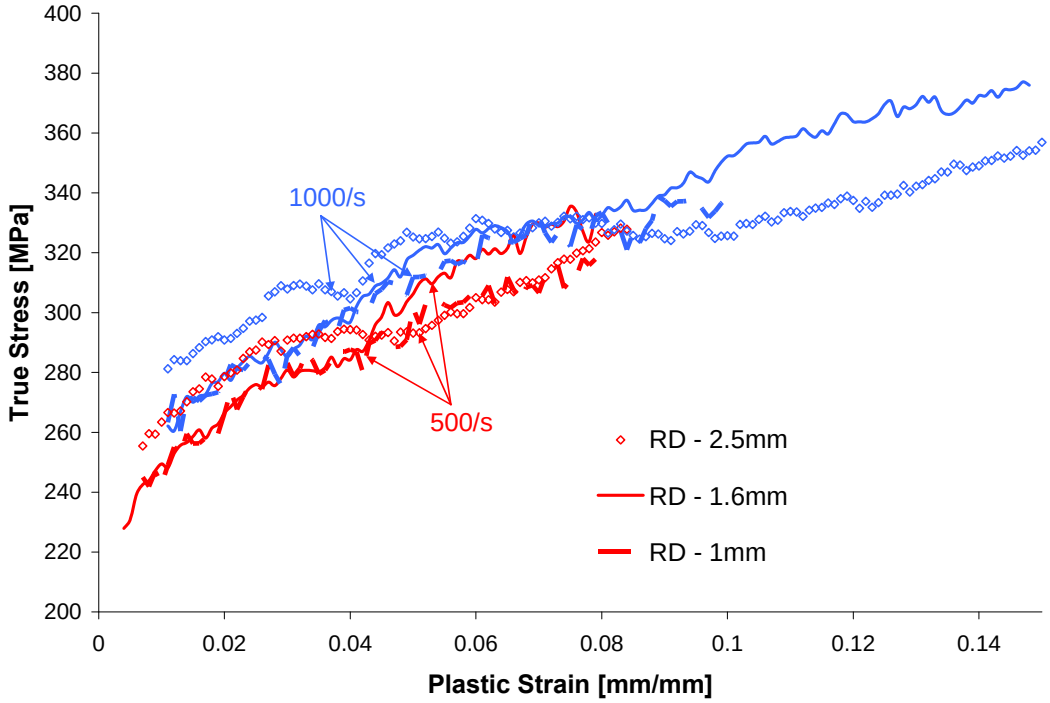

Figure 4.46: Effect of thickness on flow curves at high strain rates in the RD

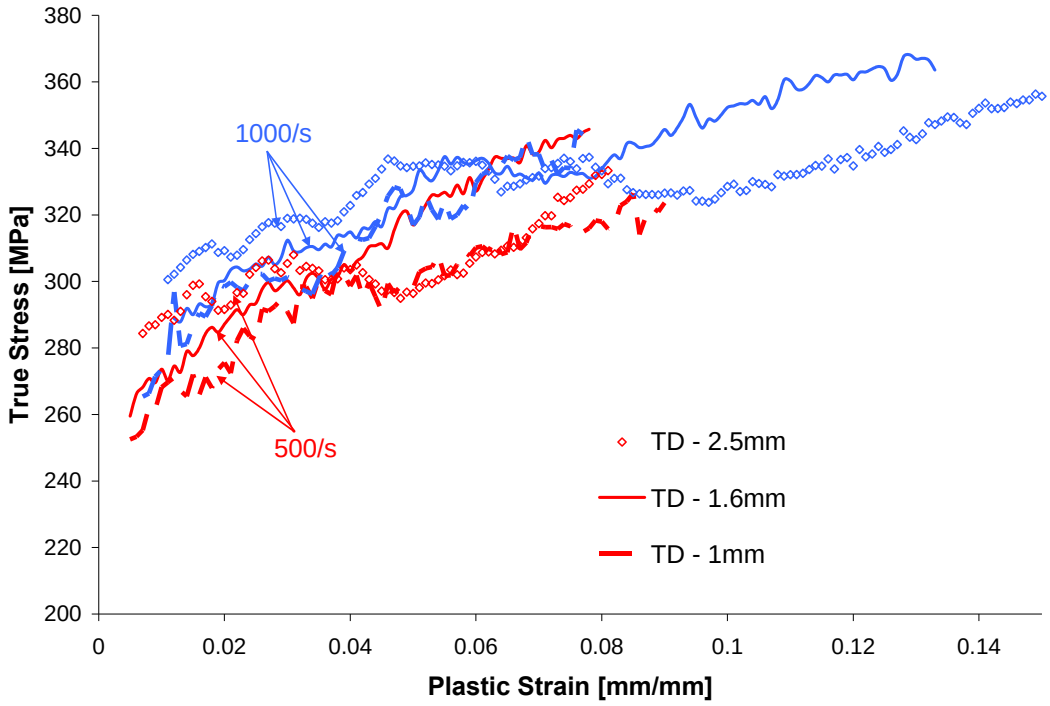

Figure 4.47: Effect of thickness on flow curves at high strain rates in the TD

Figure 4.44 and Figure 4.45 show that both directions present a mild difference in stress level at low and intermediate strain rates. The flow stress increases with increasing thickness of the material. There is an average difference of 10 MPa between the 1mm and 2.5mm sheets. A similar work-hardening rate can be seen from one thickness to another.

As seen in Figure 4.46 and Figure 4.47, the high strain rate flow curves show significant oscillations that make comparison of the different thicknesses difficult. The 2.5mm experimental data is particularly affected by oscillations that were difficult to remove from experimental results; the source of these oscillations remains unclear. Nonetheless, comparison of the data from 1.0mm and 1.6mm specimens reveals a slight difference in stress, with the stresses for the thinner sheet being lower.

The effect of thickness on the strain rate sensitivity of AZ31B-O is illustrated in Figure 4.48 and Figure 4.49 for the RD and the TD respectively. Again, the oscillations present in the data for the 2.5mm specimen confounded the comparison at the higher rates. However, it is still

evident that thickness does play a mild role in determining the flow stress of these alloys. The dashed line represents the curve without considering the $500s^{-1}$ data for the 2.5mm sheet that presents excessive oscillations and reduces the stress at 5% plastic strain.

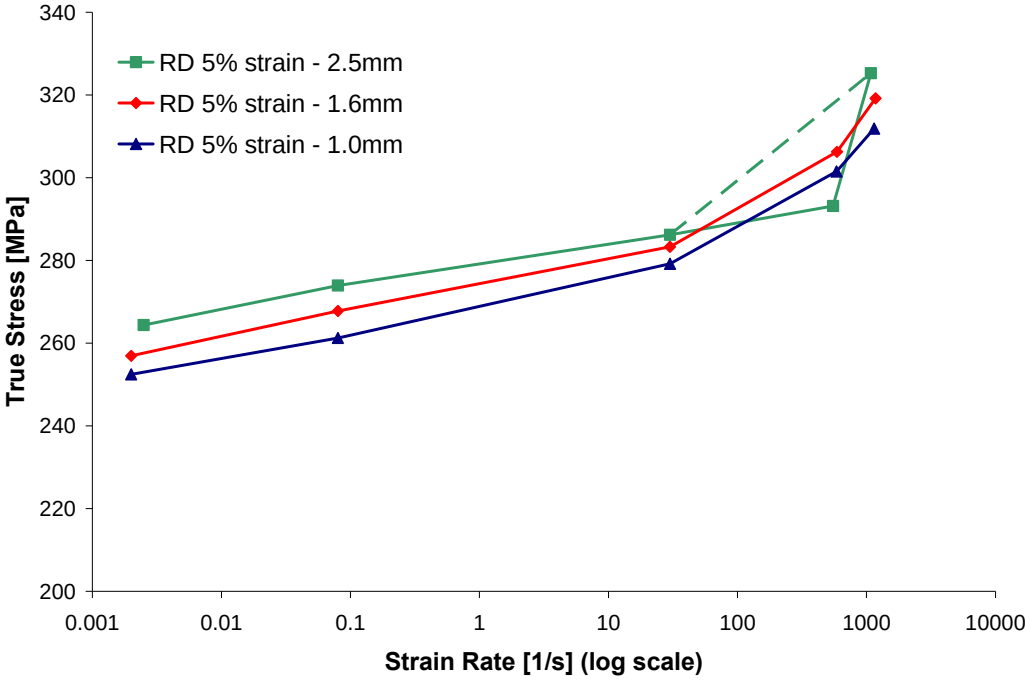

Figure 4.48: Effect of thickness on the strain rate sensitivity in the RD

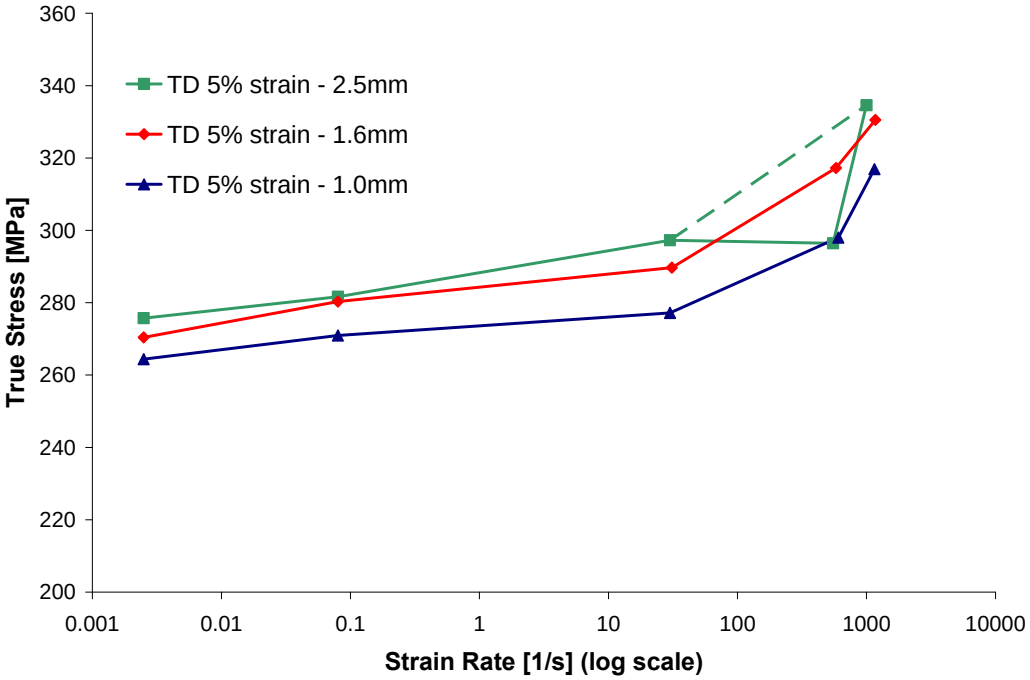

Figure 4.49: Effect of thickness on the strain rate sensitivity in the TD

For both the RD and the TD, the different thicknesses have a similar behavior in terms of the strain rate sensitivity. Indeed, the three thicknesses all exhibit the two regions of strain rate sensitivity, above and below $100s^{-1}$.

5 CONSTITUTIVE FITS

Experimental data was used to fit: the Johnson-Cook constitutive model; and a modified version of the Johnson-Cook model with a Cowper-Symonds formulation for the strain rate sensitivity; and, the Zerilli-Armstrong constitutive model for BCC materials. Both the H24 and O conditions were fit with these models. Constitutive parameters are given for each material tested in both the RD and the TD.

To simplify the presentation of the models, the modified Johnson-Cook model with a Cowper-Symonds formulation will be referred as the "Cowper-Symonds model" for the balance of this thesis.

5.1 Fitting Procedure

The constitutive model fit was performed by non-linear regression analysis using the statistical software MYSTAT [76]. For each testing condition, a median flow curve was calculated from at least three experimental curves and was used to fit the constitutive models. The flow curve was reduced to the plastic strain range for which: (i) the strain rate was approximately constant; and, (ii) the stress was prior to the UTS. Thus, the strain rate was assumed to be constant and the stress state was uniaxial.

Quasi-static experiments are isothermal, so the temperature was considered constant for strain rates from $0.003s^{-1}$ to $1s^{-1}$. For higher strain rates, the temperature rise was calculated using the method presented in Section 2.4.2.

Due to the large range of strain rate considered, the number of data points recorded during a test varies considerably between each condition. Approximately two times more stress-strain data points were measured at quasi-static rates than at at a strain rate of $1500s^{-1}$. In order to prevent the quasi-static data from biasing the regression analysis, each flow curve was interpolated at a plastic strain increment of 0.001. Figure 5.1 shows that the strain increment is small enough, so that the interpolation doesn't disturb the shape of the curves.

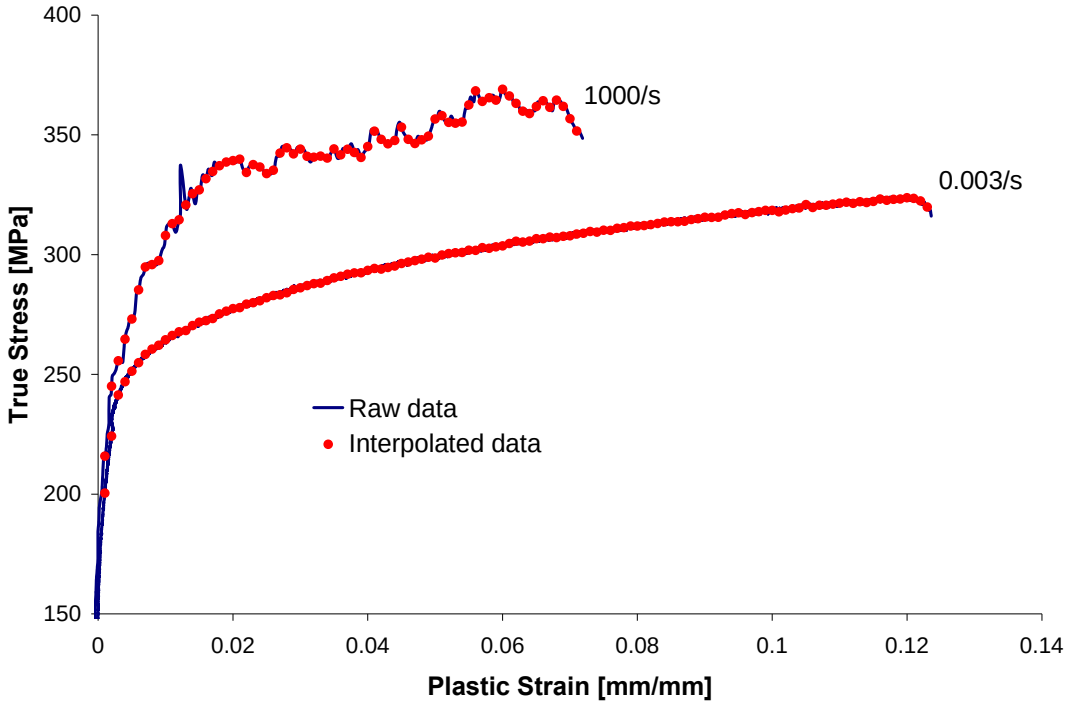

Figure 5.1: Comparison of raw data and interpolated data at $0.003s^{-1}$ and $1000s^{-1}$

The Johnson-Cook and the Cowper-Symonds models are both implemented in LS-DYNA as material model 15 [9]. The Johnson-Cook model has the following expression:

$$\sigma_y = \left(A + B\,\varepsilon_p^n\right)\left(1 + c\ln\left[\frac{\dot{\varepsilon}}{\dot{\varepsilon}_0}\right]\right)\left(1 - \left[\frac{T - T_{room}}{T_{melt} - T_{room}}\right]^m\right) \tag{5.1}$$

The Cowper-Symonds (Modified Johnson-Cook) expression is given by:

$$\sigma_y = \left(A + B\,\varepsilon_p^n\right)\left(1 + \left[\frac{\dot{\varepsilon}}{C}\right]^{\frac{1}{p}}\right)\left(1 - \left[\frac{T - T_{room}}{T_{melt} - T_{room}}\right]^m\right) \tag{5.2}$$

In the Cowper-Symonds model, the parameter C is a scale factor for the strain rate sensitivity. For all of the data fit, the non-linear regression gives a very large range for the 95% confidence interval of the C parameter. This important uncertainty has also an effect on the accuracy of the other parameters. Therefore, an "initial fit" was done including the C parameter; then an "adjusted fit" was done, assuming the C parameter to be constant and equal to the rounded value of the parameter obtained in the initial fit. This procedure reduces the uncertainty of the other parameters and doesn't reduce the R-squared value of the regression.

The Zerilli-Armstrong model is implemented in LS-DYNA as material model 65 [9]. Unfortunately, LS-DYNA only includes the FCC and BCC formulations. Since the experimental flow curves show an increasing yield stress and no clear change in the strain hardening rate as the strain rate increases, the BCC formulation was used to fit the data. Its expression in LS-DYNA is given by Equation (1.31).

$$\sigma_y = C_1 + C_2 \exp\left[\left(-C_3 + C_4 \ln \dot{\varepsilon}^*\right)T\right] + \left(C_5\, \varepsilon^n + C_6\right)\left(B_1 + B_2 T + B_3 T^2\right) \tag{5.3}$$

Constitutive parameters are given in the next sections of this chapter. For each fit, the lower and upper bound of the 95% confidence intervals are also given, as well as the "uncertainty" that the 95% confidence interval represents on the parameter. This "uncertainty" gives a good assessment of the accuracy of each parameter. The overall accuracy of the regression is assessed by its R-squared value. Unfortunately the R-squared value only indicates how close the fit points are from the raw data, but it doesn't give any information on how well the model captures the experimental data. A discussion of the general trend of the fitted flow curves is given for each model.

5.2 AZ31B-H24

5.2.1 Johnson-Cook Fits

The Johnson-Cook parameters for the rolling and the transverse direction are given respectively in Table 5.1 and Table 5.2. The two fits have a fair R-squared value of 0.896 and 0.93, but the model doesn't represent the experimental data very well, as seen in Figure 5.2 through Figure 5.5 that show the fits for different strain rates at room temperature.

Elevated temperature fits at high strain rate can be seen in Figure 5.3 and Figure 5.5 respectively for the rolling and the transverse directions. The thermal softening is well captured by the model.

Table 5.1: Johnson-Cook constitutive parameters for AZ31B-H24 in the RD

Parameter	Estimate	Lower 95%	Upper 95%	Uncertainty
A [MPa]	225.171	200.372	249.970	+/- 11.01 %
B [MPa]	168.346	150.682	186.010	+/- 10.49 %
n	0.242	0.160	0.324	+/- 33.88 %
C	0.013	0.012	0.014	+/- 7.69 %
m	1.550	1.523	1.577	+/- 1.74 %
	R^2	0.896		

Table 5.2: Johnson-Cook constitutive parameters for AZ31B-H24 in the TD

Parameter	Estimate	Lower 95%	Upper 95%	Uncertainty
A [MPa]	279.827	258.412	301.242	+/- 7.65 %
B [MPa]	159.000	144.702	173.298	+/- 8.99 %
n	0.279	0.177	0.381	+/- 36.56 %
C	0.013	0.012	0.014	+/- 7.69 %
m	1.573	1.547	1.599	+/- 1.65 %
	R^2	0.930		

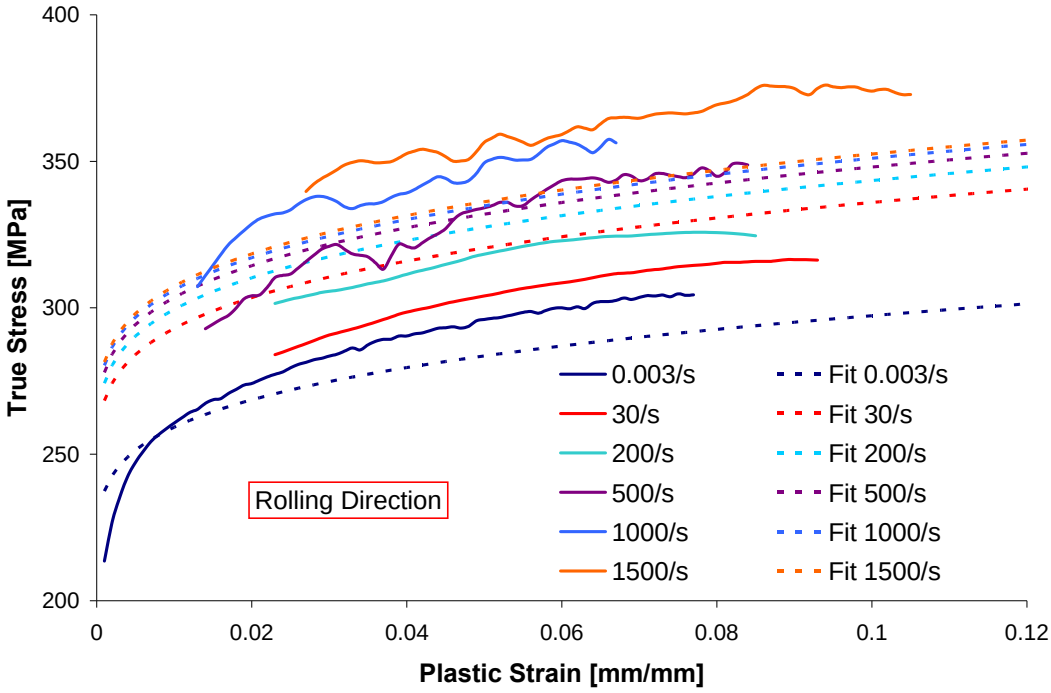

Figure 5.2: Johnson-Cook fits for AZ31B-H24 in the Rolling Direction at room temperature

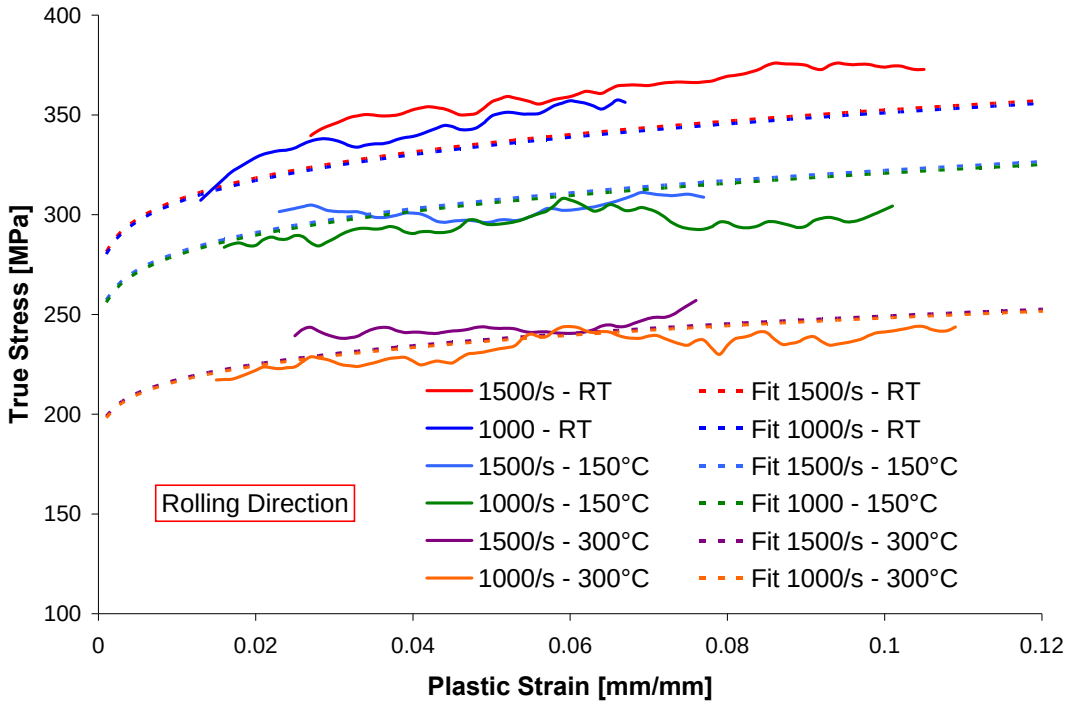

Figure 5.3: Johnson-Cook fits for AZ31B-H24 in the Rolling Direction at elevated temperatures

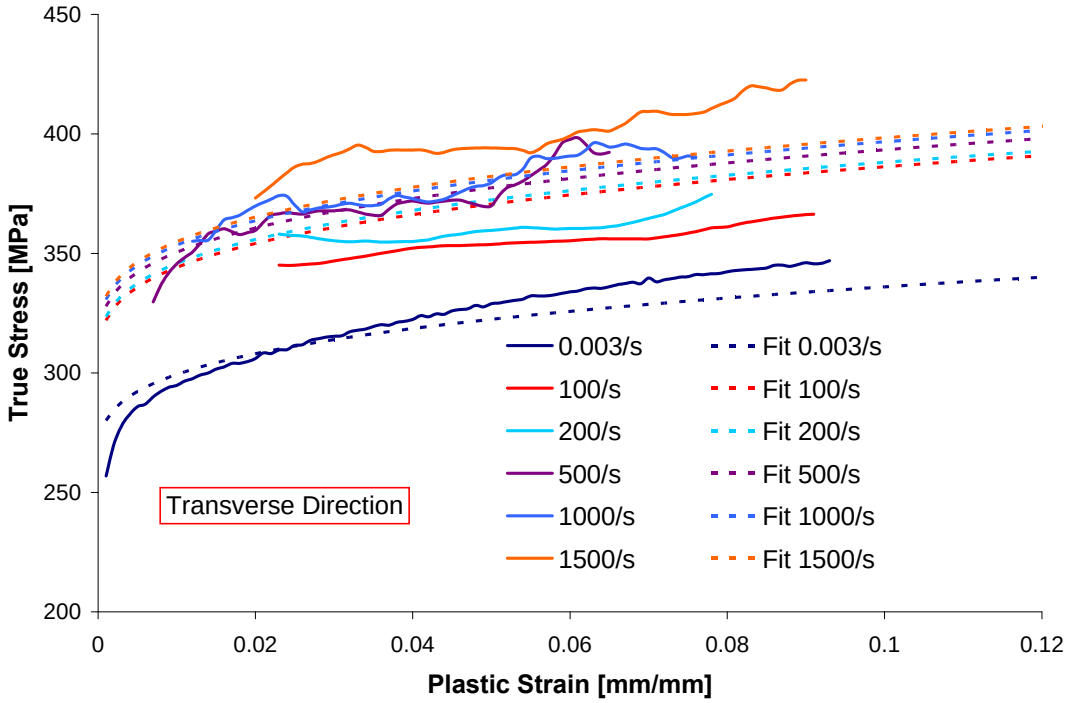

Figure 5.4: Johnson-Cook fits for AZ31B-H24 in the Transverse Direction at room temperature

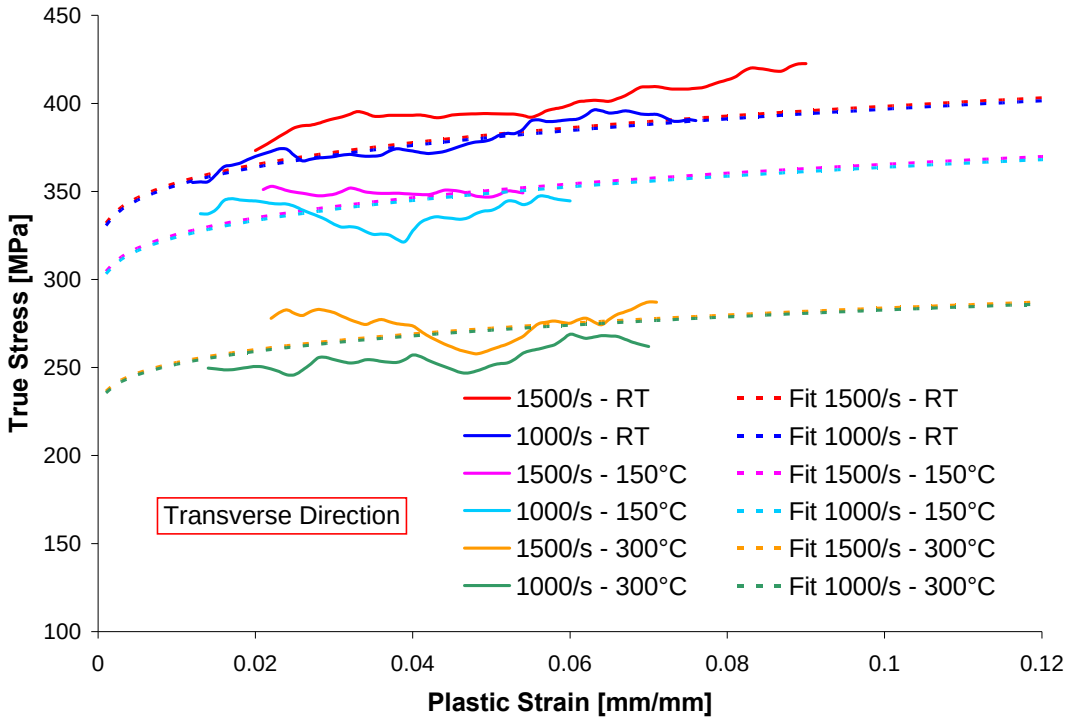

Figure 5.5: Johnson-Cook fits for AZ31B-H24 in the Transverse Direction at elevated temperatures

The lack of fit is due to the important change of strain rate sensitivity that occurs for this material after $100s^{-1}$, as seen in Figure 5.6 where the predicted strain rate sensitivity at 2, 4 and 6% plastic strains are compared with the experimental data. The Johnson-Cook model assumes a constant log-linear strain rate sensitivity (Equation (1.22)); it thus could represent the behavior of this material for strain rate greater than $100s^{-1}$, but a new fit would be needed for the low strain rate conditions.

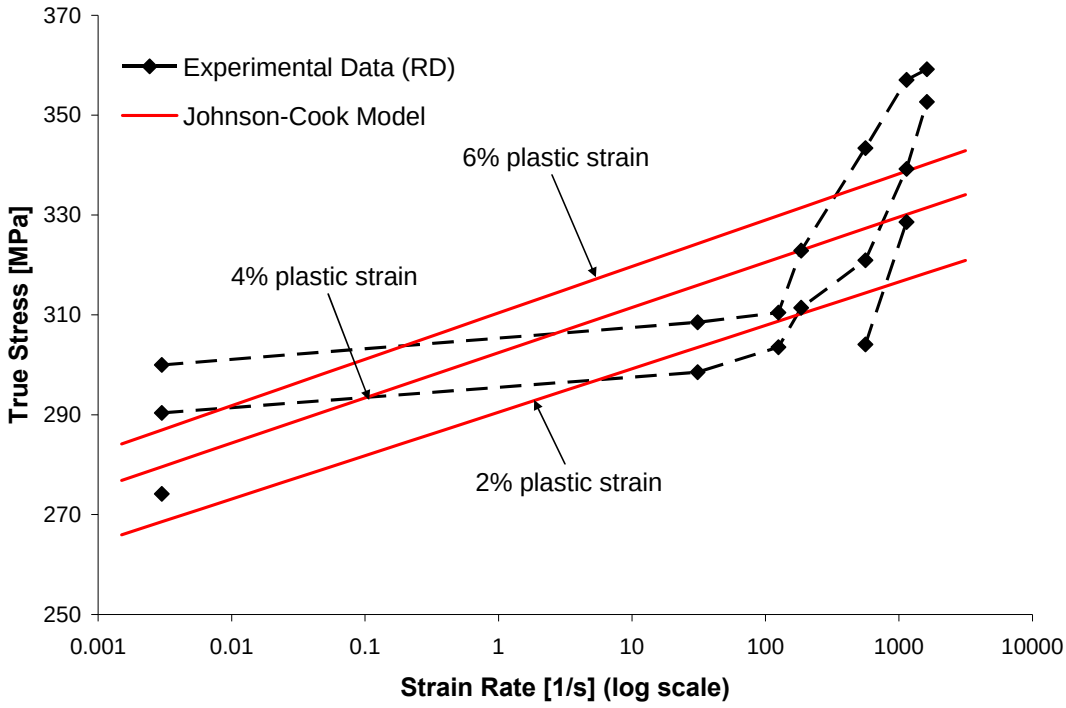

Figure 5.6: Strain rate sensitivity of the Johnson-Cook fits for the AZ31B-H24

5.2.2 Cowper-Symonds (Modified Johnson-Cook) Fits

To capture the strain rate sensitivity, a Cowper-Symonds model was fit to the measured data. The constitutive parameters for the rolling and the transverse directions are given in Table 5.3 and Table 5.4, respectively. The two fits have a good R-squared value of 0.97. The model captures the effects of strain rate well, as seen in Figure 5.7 and Figure 5.9 for different strain rates at room temperature.

As the model uses the same temperature sensitivity expression as the Johnson-Cook model, the thermal softening is also captured well by this model, as seen in Figure 5.8 and Figure 5.10 for the high strain rate tests at elevated temperature. There is a change in the work-hardening rate with the temperature increase that the model doesn't capture. Other work-hardening rate issues can be seen in the quasi-static curves where the model overestimates the flow stress for low strain values.

Table 5.3: Cowper-Symonds constitutive parameters for AZ31B-H24 in the RD

Parameter	Estimate	Lower 95%	Upper 95%	Uncertainty
		Initial Fit		
A [MPa]	202.708	190.058	215.358	+/- 6.24 %
B [MPa]	181.234	171.619	190.849	+/- 5.31 %
n	0.229	0.193	0.265	+/- 15.72 %
C [1/s]	47978.426	37620.752	58336.100	+/- 21.59 %
p	2.130	1.981	2.279	+/- 7 %
m	1.392	1.378	1.406	+/- 1.01 %
	R^2	0.971		
		Adjusted Fit		
A [MPa]	202.768	190.136	215.400	+/- 6.23 %
B [MPa]	180.932	171.468	190.396	+/- 5.23 %
n	0.229	0.193	0.265	+/- 15.72 %
C [1/s]	5.0E+04	-	-	
p	2.157	2.109	2.205	+/- 2.23 %
m	1.393	1.380	1.406	+/- 0.93 %
	R^2	0.971		

Table 5.4: Cowper-Symonds constitutive parameters for AZ31B-H24 in the TD

Parameter	Estimate	Lower 95%	Upper 95%	Uncertainty
		Initial Fit		
A [MPa]	253.312	240.308	266.316	+/- 5.13 %
B [MPa]	167.304	158.416	176.192	+/- 5.31 %
n	0.265	0.211	0.319	+/- 20.38 %
C [1/s]	251919.349	167909.699	335928.999	+/- 33.35 %
p	3.183	2.958	3.408	+/- 7.07 %
m	1.464	1.448	1.48	+/- 1.09 %
	R^2	0.97		
		Adjusted Fit		
A [MPa]	253.129	240.083	266.175	+/- 5.15 %
B [MPa]	168.244	159.406	177.082	+/- 5.25 %
n	0.264	0.210	0.318	+/- 20.45 %
C [1/s]	2.0E+05	-	-	
p	3.032	2.968	3.096	+/- 2.11 %
m	1.460	1.445	1.475	+/- 1.03 %
	R^2	0.97		

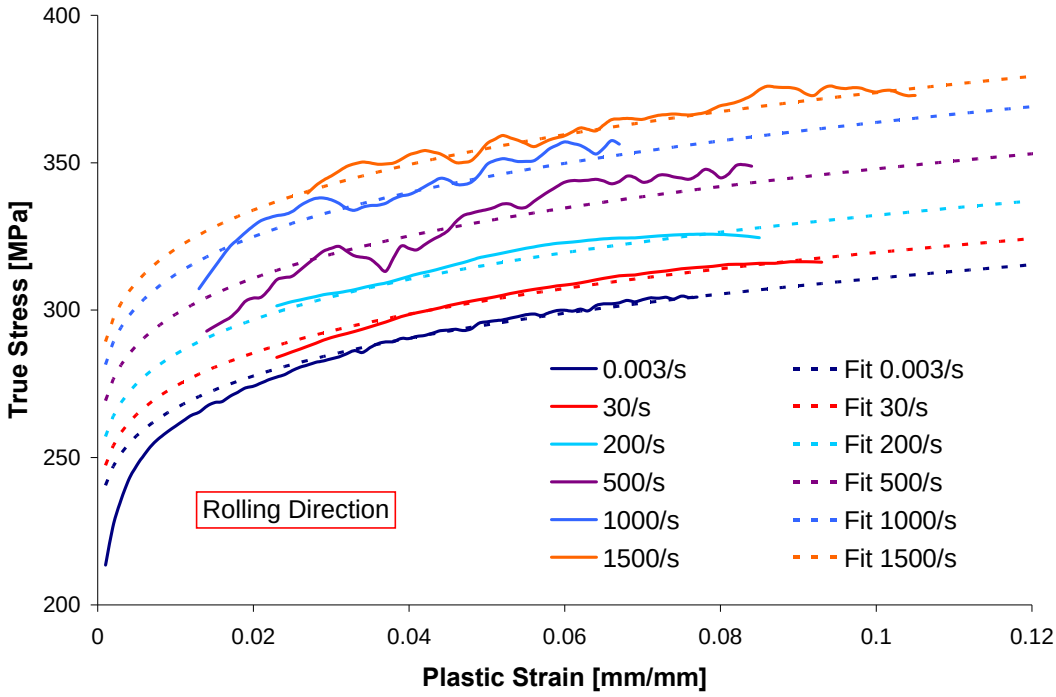

Figure 5.7: Cowper-Symonds fits for AZ31B-H24 in the Rolling Direction at room temperature

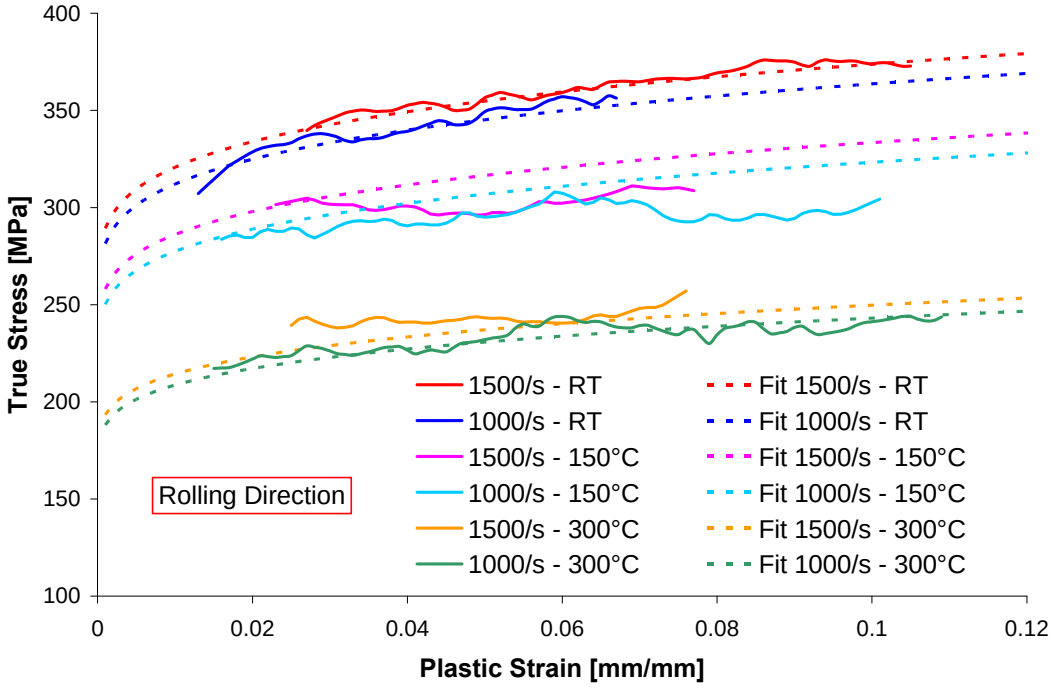

Figure 5.8: Cowper-Symonds fits for AZ31B-H24 in the Rolling Direction at elevated temperatures

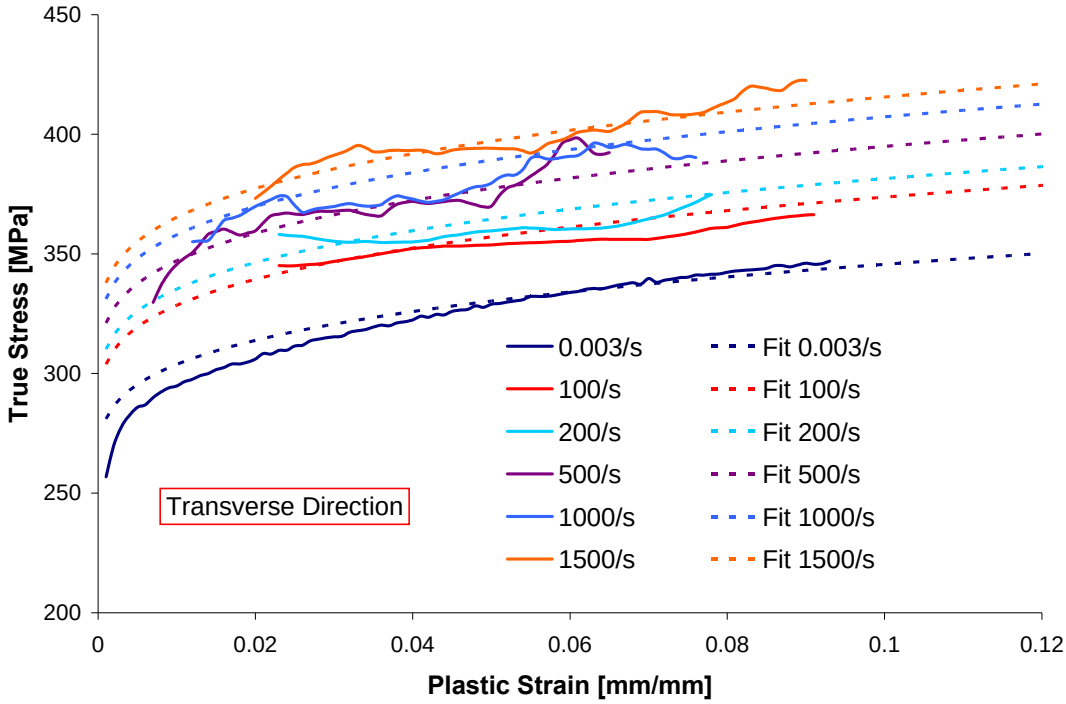

Figure 5.9: Cowper-Symonds fits for AZ31B-H24 in the Transverse Direction at room temperature

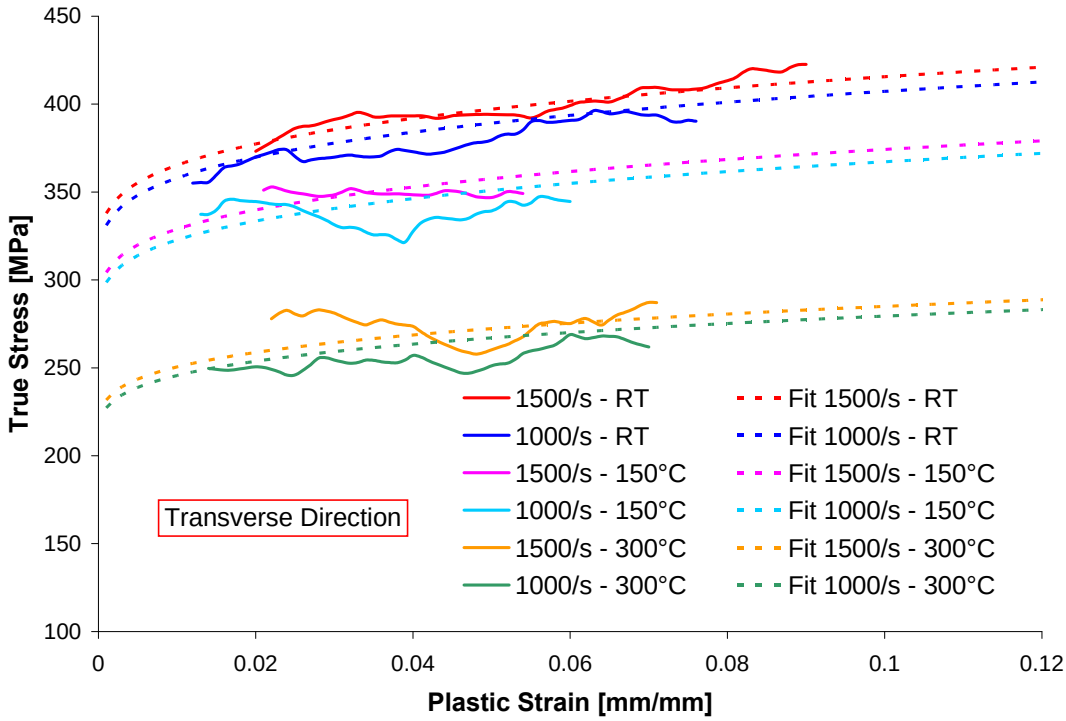

Figure 5.10: Cowper-Symonds fits for AZ31B-H24 in the Transverse Direction at elevated temperatures

The improvement of the predicted strain rate sensitivity can be seen in Figure 5.11, where the strain rate sensitivity at 2, 4 and 6% plastic strains are plotted. As seen in the figure, the model captures the important increase in strain rate sensitivity.

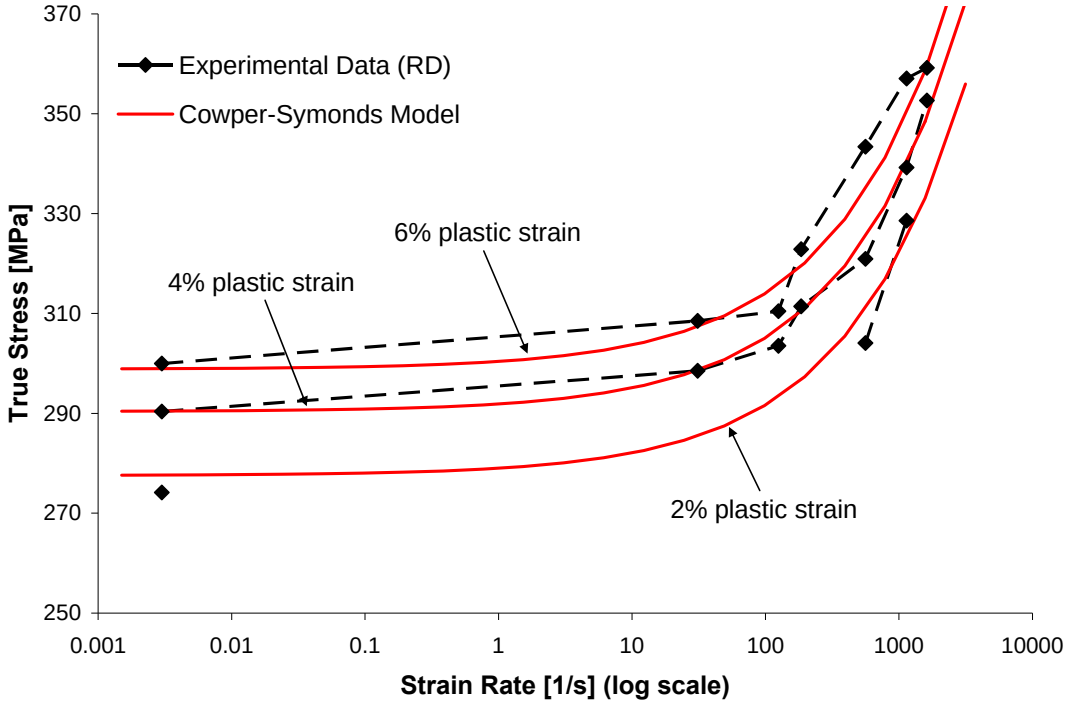

Figure 5.11: Strain rate sensitivity of the Cowper-Symonds fits for the AZ31B-H24

5.2.3 Zerilli-Armstrong Fits

In order to better capture the effect of strain rate and the temperature dependence of the work-hardening rate, a Zerilli-Armstrong model was fit to the measured data. The constitutive parameters for the rolling and the transverse directions are given in Table 5.5 and Table 5.6, respectively.

The RD fit has a high R-squared value of 0.984 and the TD fit has a lower R-squared value of 0.912. As seen in Figure 5.12 and Figure 5.14 for the room temperature data, the model captures the different flow curves very well. Unfortunately, the model becomes less accurate as the temperature increases, as seen in Figure 5.13 and Figure 5.15, especially for the TD. The

model also captures the decrease of the work-hardening rate that was seen at elevated temperature.

Table 5.5: Zerilli-Armstrong constitutive parameters for AZ31B-H24 in the RD

Parameter	Estimate	Lower 95%	Upper 95%	Uncertainty
C_1 [MPa]	148.341	139.676	157.006	+/- 5.84 %
C_2 {MPa]	160.095	131.808	188.382	+/- 17.67 %
C_3 [1/K]	1.6210E-02	0.01427	1.815E-02	+/- 11.97 %
C_4 [1/K]	1.7800E-03	0.0015625	1.997E-03	+/- 12.22 %
C_5 [MPa]	573.813	525.931	621.695	+/- 8.34 %
n	0.17	0.155	0.185	+/- 8.82 %
C_6 [MPa]	0	-	-	-
B_1	0.82	0.779902	8.601E-01	+/- 4.89 %
B_2 [1/K]	-1.58E-03	-6.09E-04	-2.551E-03	+/- 61.48 %
B_3 [1/K²]	8.450E-07	7.565E-07	9.335E-07	+/- 10.47 %
	R^2	0.984		

Table 5.6: Zerilli-Armstrong constitutive parameters for AZ31B-H24 in the TD

Parameter	Estimate	Lower 95%	Upper 95%	Uncertainty
C_1 [MPa]	177.452	157.147	197.757	+/- 11.44 %
C_2 {MPa]	160.095	98.923	221.267	+/- 38.21 %
C_3 [1/K]	1.3100E-02	9.7100E-03	1.649E-02	+/- 25.88 %
C_4 [1/K]	1.3900E-03	1.0410E-03	1.739E-03	+/- 25.11 %
C_5 [MPa]	573.813	513.237	6.344E+02	+/- 10.56 %
n	0.17	0.1455	0.1945	+/- 14.41 %
C_6 [MPa]	0	-	-	-
B_1	1.17	0.9104	1.430E+00	+/- 22.19 %
B_2 [1/K]	-3.24E-03	-0.002827	-3.653E-03	+/- 12.75 %
B_3 [1/K²]	2.660E-06	2.034E-06	3.286E-06	+/- 23.53 %
	R^2	0.912		

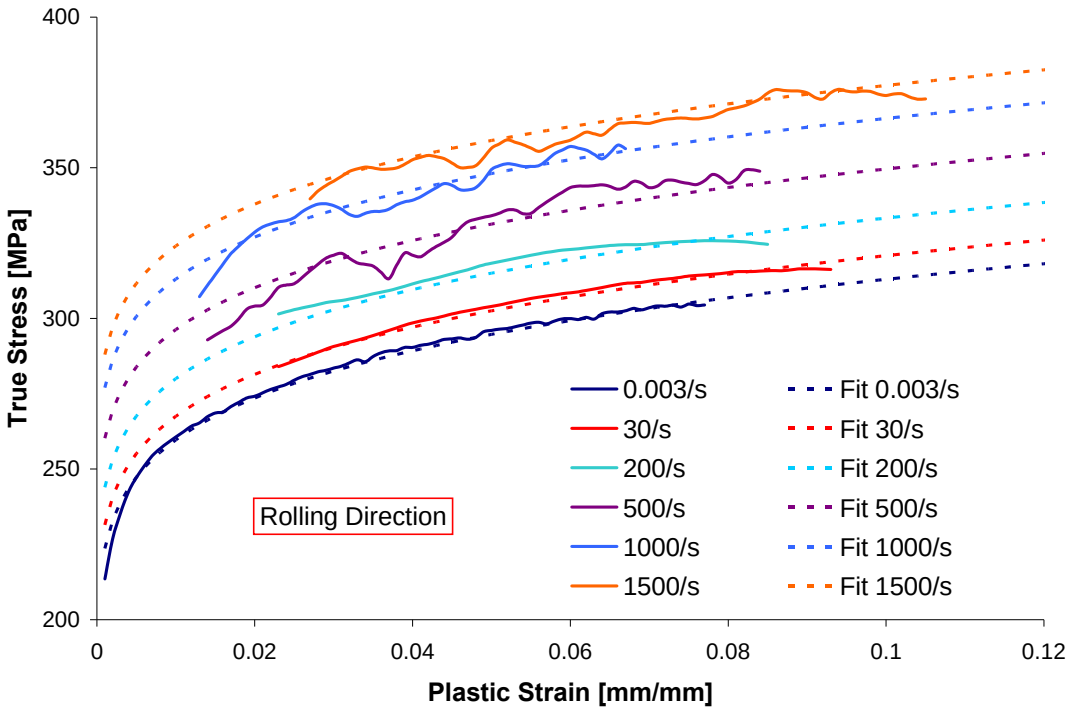

Figure 5.12: Zerilli-Armstrong fits for AZ31B-H24 in the Rolling Direction at room temperature

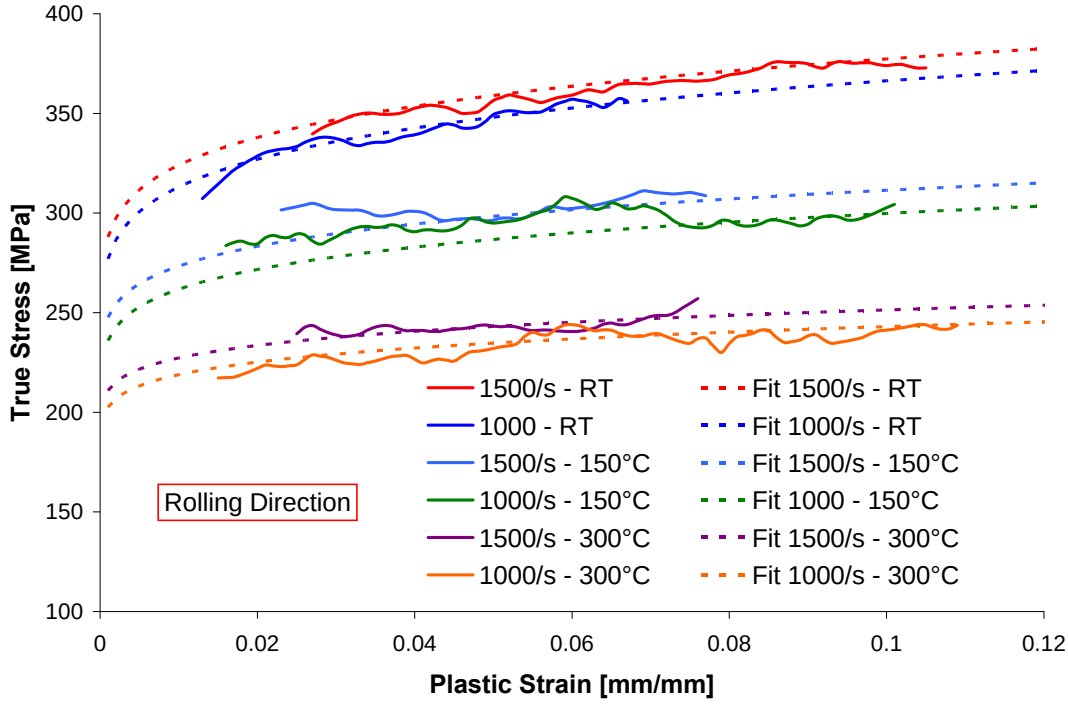

Figure 5.13: Zerilli-Armstrong fits for AZ31B-H24 in the Rolling Direction at elevated temperatures

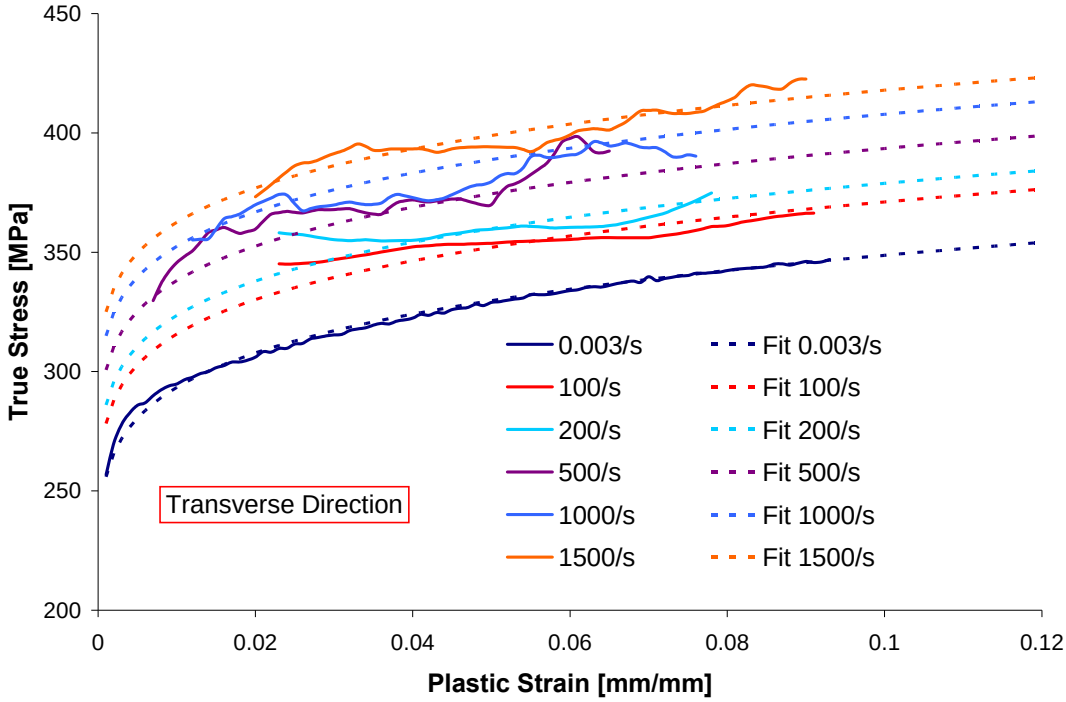

Figure 5.14: Zerilli-Armstrong fits for AZ31B-H24 in the Transverse Direction at room temperature

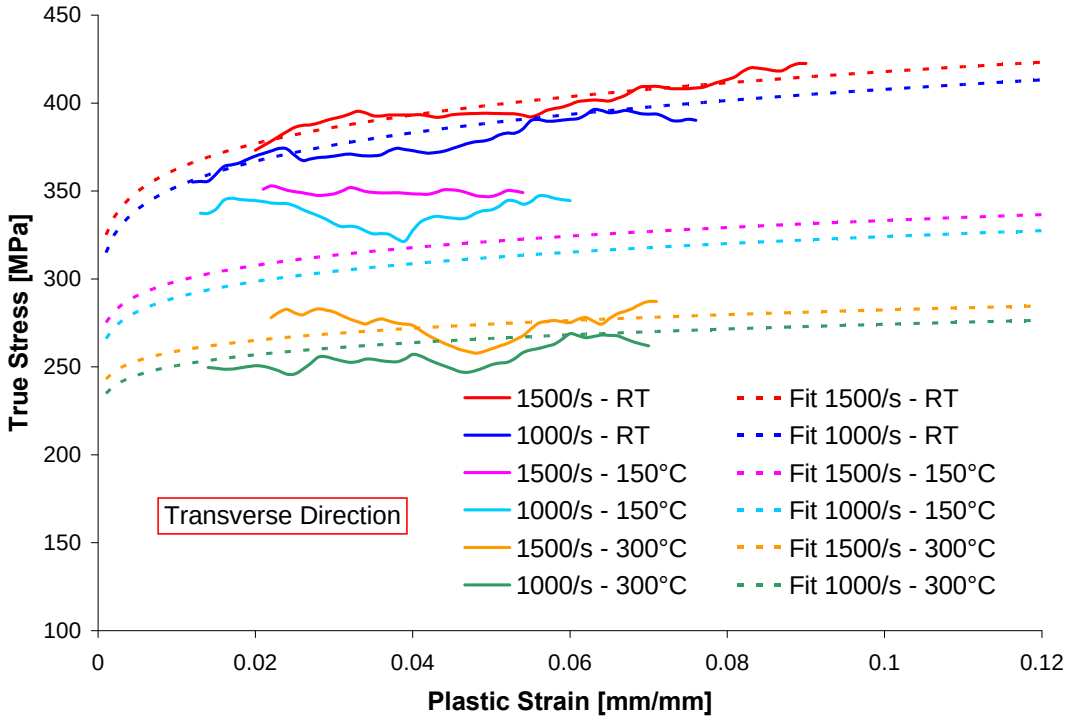

Figure 5.15: Zerilli-Armstrong fits for AZ31B-H24 in the Transverse Direction at elevated temperatures

The Zerilli-Armstrong model also captures the change of strain rate sensitivity, as seen in Figure 5.16.

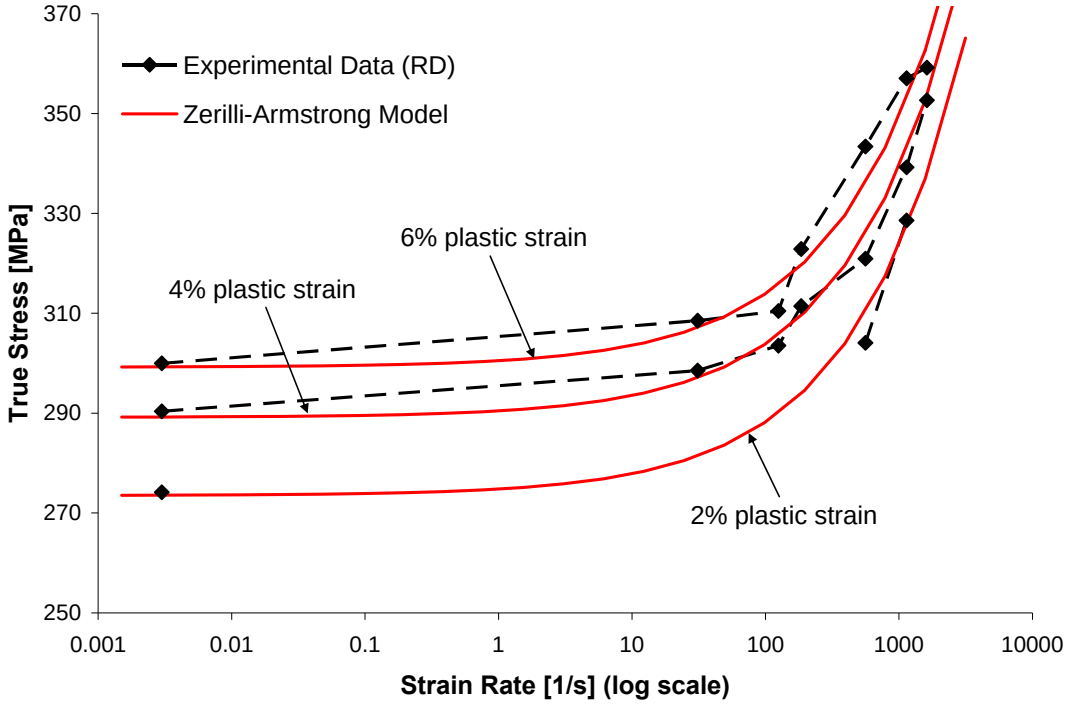

Figure 5.16: Strain rate sensitivity of the Zerilli-Armstrong fits for the AZ31B-H24

5.3 AZ31B-O

AZ31B-O experimental data were also fit using the Johnson-Cook, Cowper-Symonds and Zerilli-Armstrong constitutive models. This section presents a detailed description of the results of the constitutive fits for the 1.6mm thick sheet. In addition, a summary of the constitutive parameters for the data from the 1mm and 2.5mm sheets are given in at the end of this section

5.3.1 Constitutive Fits for the 1.6mm Experimental Data

5.3.1.1 Johnson-Cook Fits

The Johnson-Cook fits are shown in Figure 5.17 and Figure 5.19 for room temperature data; and in Figure 5.18 and Figure 5.20 for elevated temperature data. The corresponding

constitutive parameters are given in Table 5.7 and Table 5.8 for the RD and the TD, respectively.

Table 5.7: Johnson-Cook constitutive parameters for AZ31B-O (1.6mm) in the RD

Parameter	Estimate	Lower 95%	Upper 95%	Uncertainty
A [MPa]	133.082	120.292	145.872	+/- 9.61 %
B [MPa]	345.821	340.346	351.296	+/- 1.58 %
n	0.293	0.265	0.321	+/- 9.56 %
C	0.016	0.015	0.017	+/- 6.25 %
m	1.849	1.830	1.868	+/- 1.03 %
	R^2	0.961		

Table 5.8: Johnson-Cook constitutive parameters for AZ31B-O (1.6mm) in the TD

Parameter	Estimate	Lower 95%	Upper 95%	Uncertainty
A [MPa]	193.762	184.046	203.478	+/- 5.01 %
B [MPa]	296.834	288.216	305.452	+/- 2.9 %
n	0.380	0.338	0.422	+/- 11.05 %
C	0.016	0.015	0.017	+/- 6.25 %
m	1.808	1.787	1.829	+/- 1.16 %
	R^2	0.942		

The Johnson-Cook model captures the quasi-static curves relatively well, but clearly underestimates the high rate data. This lack of fit is due to the simple log-linear strain rate expression in the Johnson-Cook model. Thus, the change in strain rate sensitivity for strain rate above $100s^{-1}$ cannot be capture by the Johnson-Cook model, as seen in Figure 5.21.

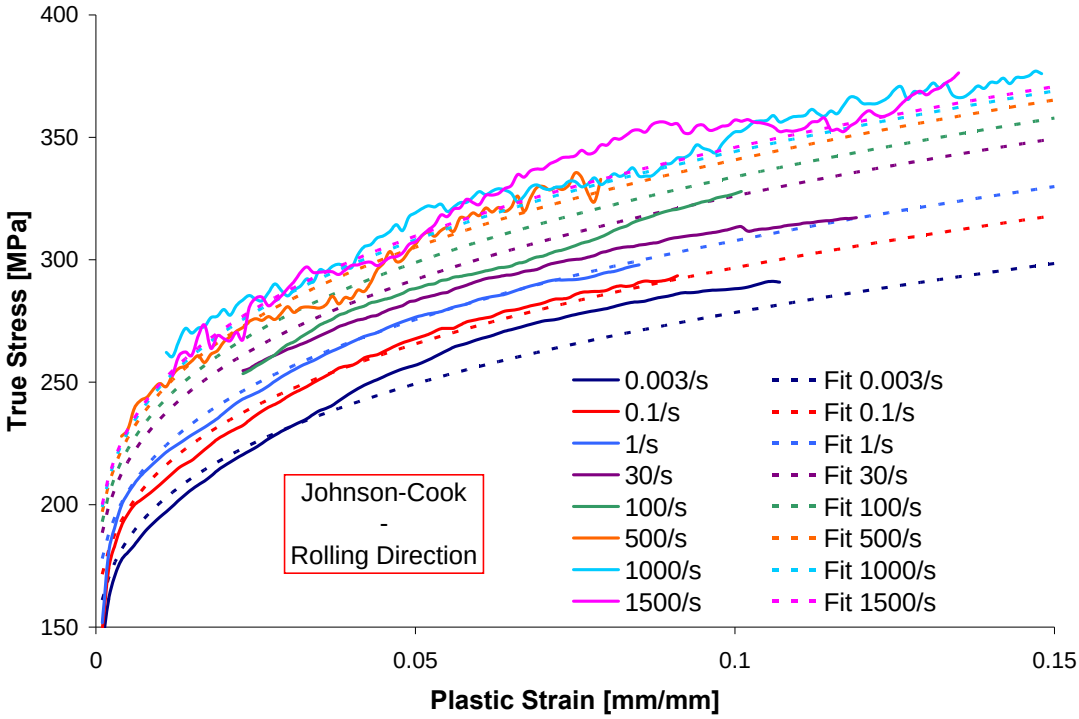

Figure 5.17: Johnson-Cook fits for AZ31B-O (1.6mm) in the Rolling Direction at room temperature

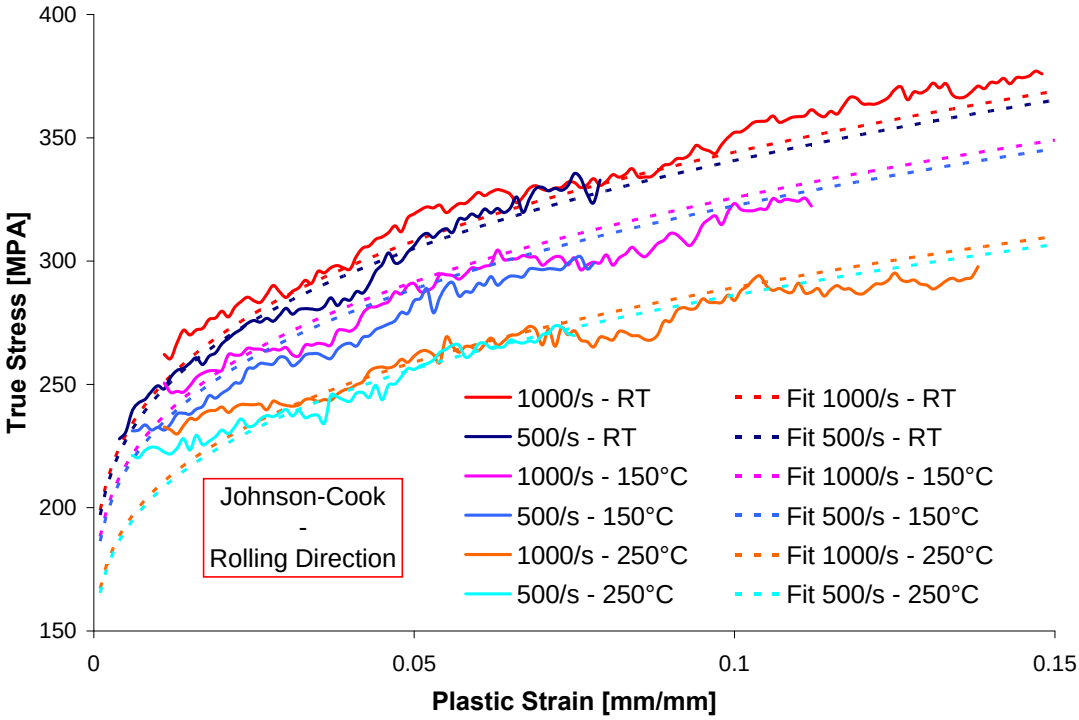

Figure 5.18: Johnson-Cook fits for AZ31B-O (1.6mm) in the Rolling Direction at elevated temperatures

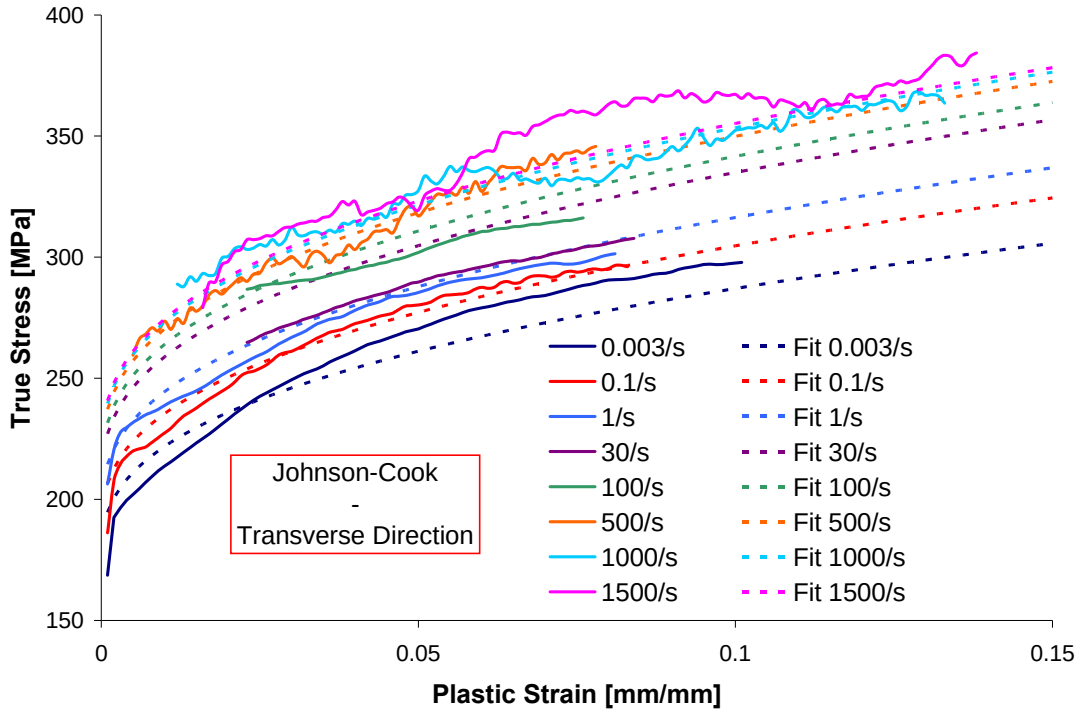

Figure 5.19: Johnson-Cook fits for AZ31B-O (1.6mm) in the Transverse Direction at room temperature

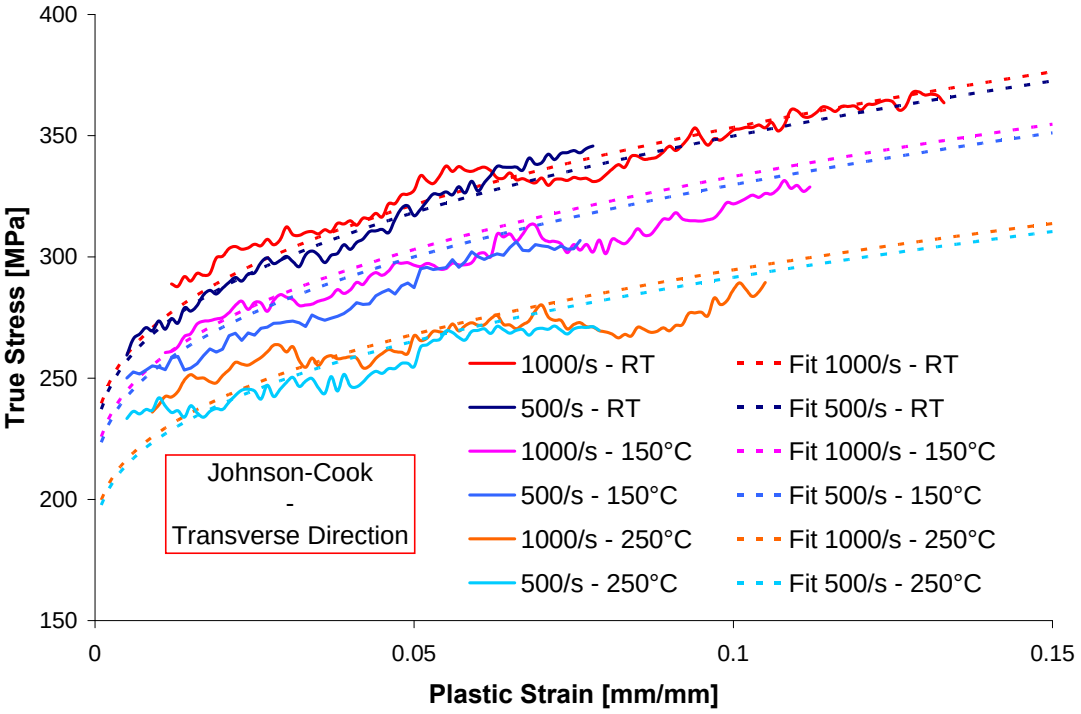

Figure 5.20: Johnson-Cook fits for AZ31B-O (1.6mm) in the Transverse Direction at elevated temperatures

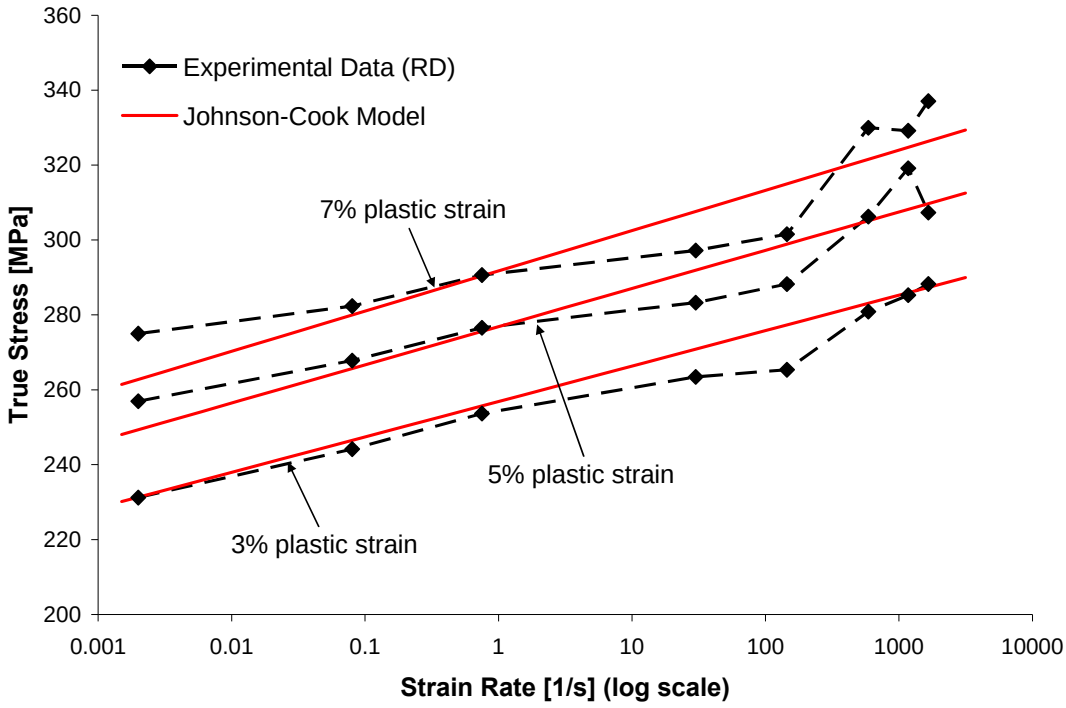

Figure 5.21: Strain rate sensitivity of the Johnson-Cook fits for AZ31B-O (1.6mm) at room temperature

5.3.1.2 Cowper-Symonds (Modified Johnson-Cook) Fits

The Cowper-Symonds curve fits are shown in Figure 5.22 and Figure 5.24 for room temperature data and in Figure 5.23 and Figure 5.25 for elevated temperature data. The corresponding constitutive parameters are given in Table 5.9 and Table 5.10 for the RD and the TD, respectively.

Table 5.9: Cowper-Symonds constitutive parameters for AZ31B-O (1.6mm) in the RD

Parameter	Estimate	Lower 95%	Upper 95%	Uncertainty
		Initial Fit		
A [MPa]	105.724	93.428	118.020	+/- 11.63 %
B [MPa]	313.856	306.664	321.048	+/- 2.29 %
n	0.256	0.233	0.279	+/- 8.98 %
C [1/s]	7126468.447	3569573.82	10683363.074	+/- 49.91 %
p	6.045	5.54	6.550	+/- 8.35 %
m	1.787	1.771	1.803	+/- 0.9 %
	R^2	0.973		
		Adjusted Fit		
A [MPa]	105.698	93.409	117.987	+/- 11.63 %
B [MPa]	313.947	307.171	320.723	+/- 2.16 %
n	0.256	0.233	0.279	+/- 8.98 %
C [1/s]	7.0E+06	-	-	
p	6.028	5.888	6.168	+/- 2.32 %
m	1.787	1.772	1.802	+/- 0.84 %
	R^2	0.973		

Table 5.10: Cowper-Symonds constitutive parameters for AZ31B-O (1.6mm) in the TD

Parameter	Estimate	Lower 95%	Upper 95%	Uncertainty
		Initial Fit		
A [MPa]	156.631	143.990	169.272	+/- 8.07 %
B [MPa]	256.789	250.835	262.743	+/- 2.32 %
n	0.276	0.242	0.31	+/- 12.32 %
C [1/s]	898574.533	515763.547	1281385.519	+/- 42.6 %
p	4.266	3.924	4.608	+/- 8.02 %
m	1.747	1.731	1.763	+/- 0.92 %
	R^2	0.963		
		Adjusted Fit		
A [MPa]	156.637	144.112	169.162	+/- 8 %
B [MPa]	256.786	250.884	262.688	+/- 2.3 %
n	0.276	0.243	0.309	+/- 11.96 %
C [1/s]	9.0E+05	-	-	
p	4.268	4.184	4.352	+/- 1.97 %
m	1.747	1.731	1.763	+/- 0.92 %
	R^2	0.963		

The Cowper-Symonds model captures the change of strain rate sensitivity at high strain rate, as seen in Figure 5.26. Therefore the stress level is modeled well over the large range of strain rate considered. The overall thermal softening is also captured well. Unfortunately, in the Cowper-Symonds model the strain rate and temperature only act as scale factors applied to the hardening. Thus, this model cannot represent the small changes in the work-hardening rate and the important increase in yield stress over the range of strain rate considered. This leads to a lack of fit to the actual shape of each flow curve, especially for small strain values, as seen in the quasi-static curves and in the high temperature data.

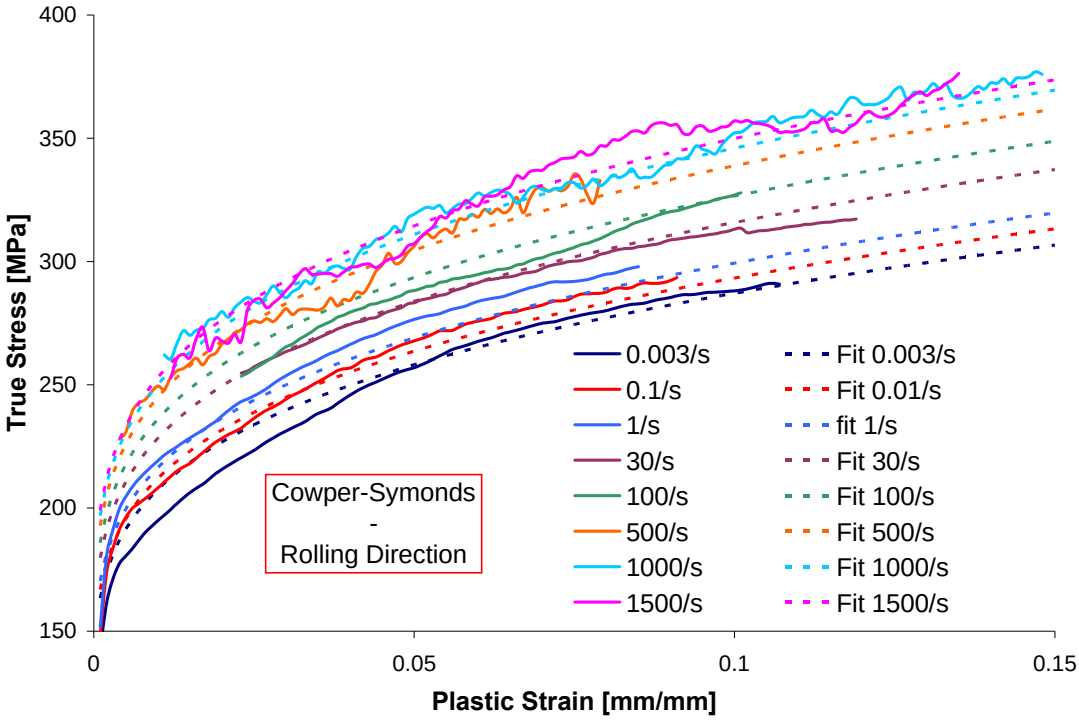

Figure 5.22: Cowper-Symonds fits for AZ31B-O (1.6mm) in the Rolling Direction at room temperature

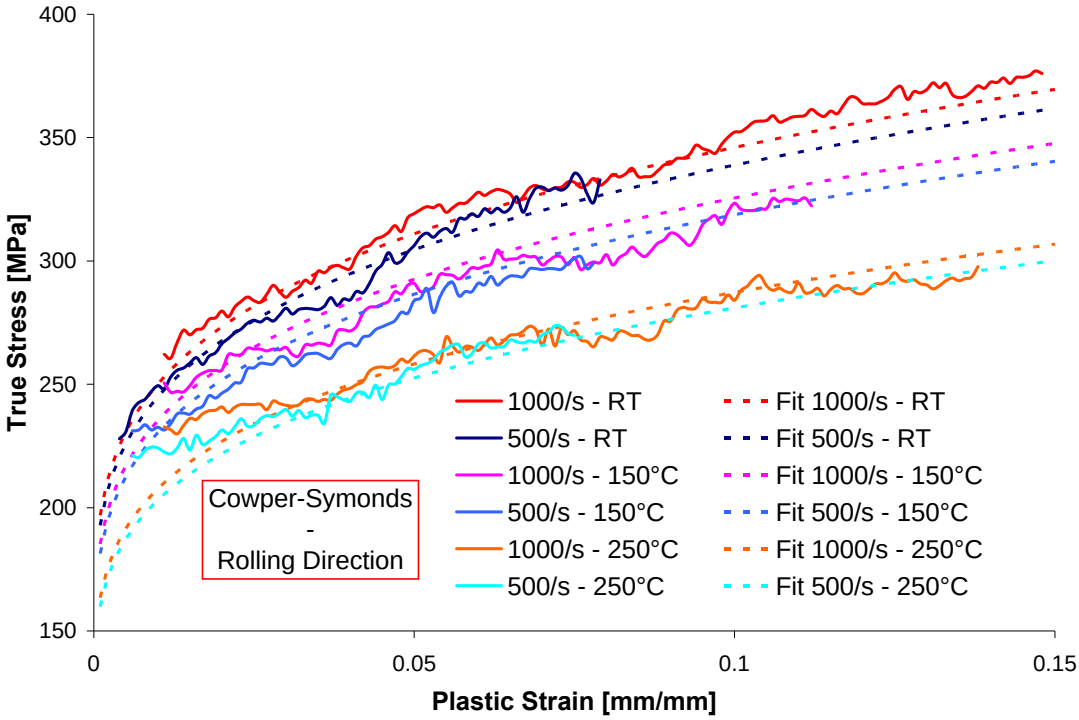

Figure 5.23: Cowper-Symonds fits for AZ31B-O (1.6mm) in the Rolling Direction at elevated temperatures

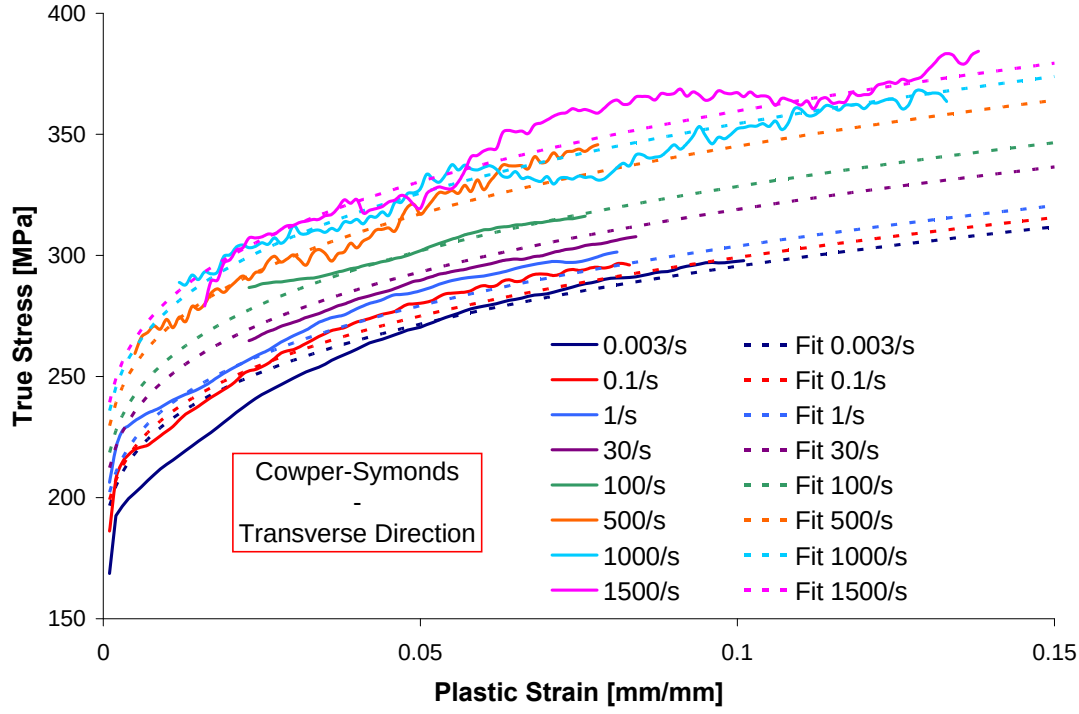

Figure 5.24: Cowper-Symonds fits for AZ31B-O (1.6mm) in the Transverse Direction at room temperature

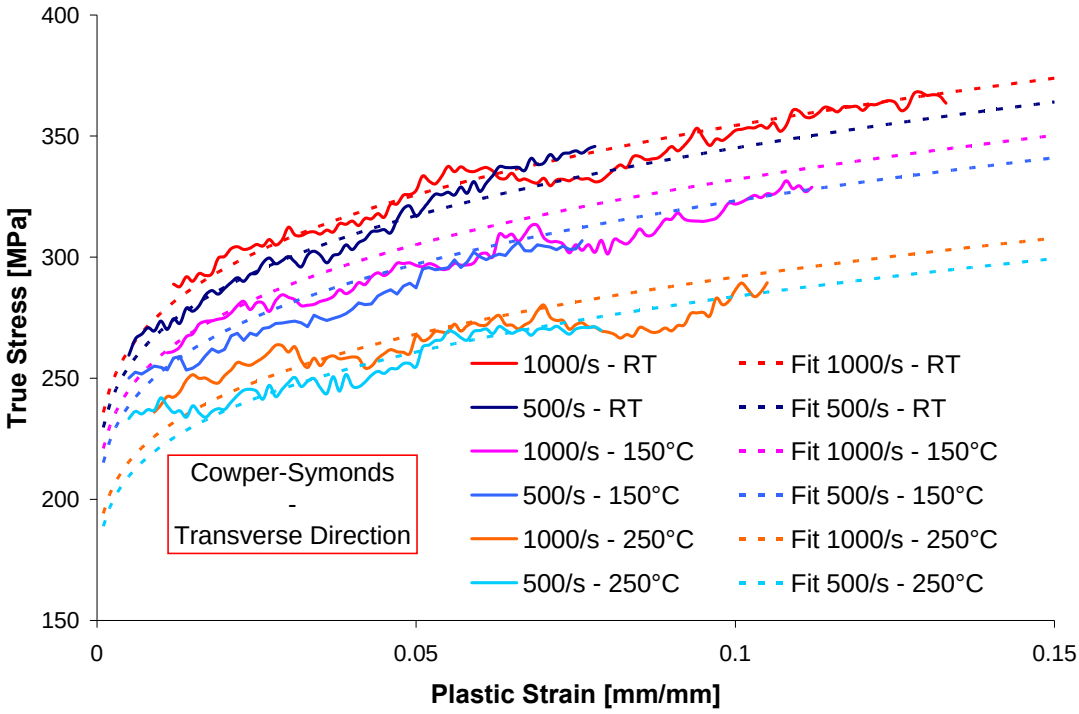

Figure 5.25: Cowper-Symonds fits for AZ31B-O (1.6mm) in the Transverse Direction at elevated temperatures

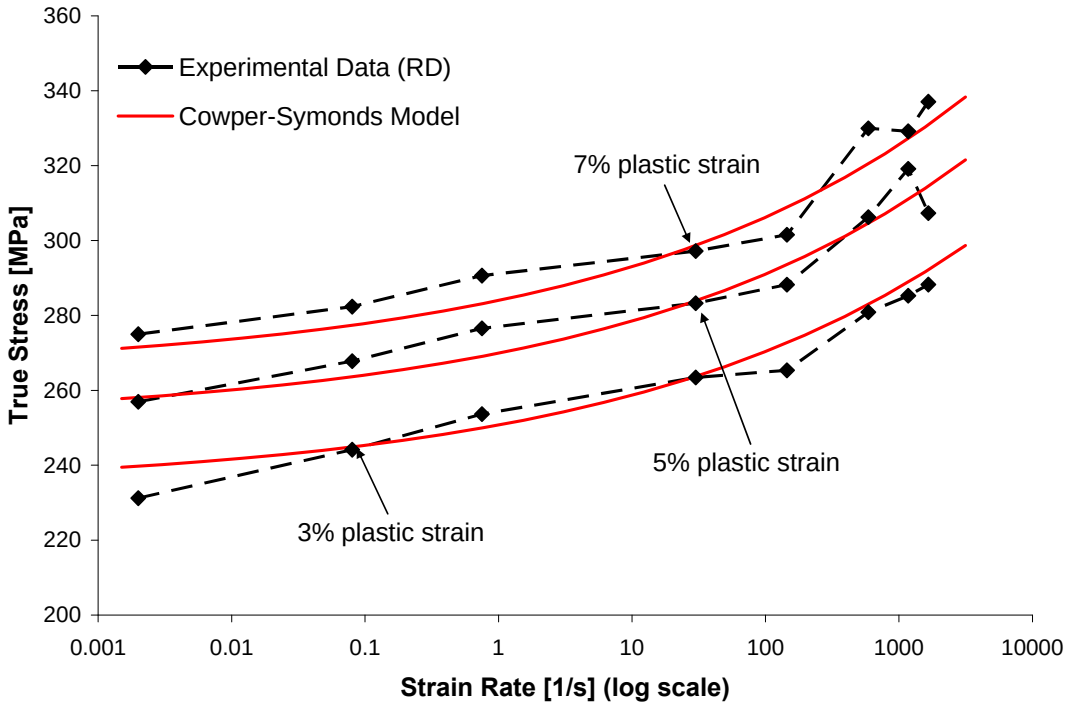

Figure 5.26: Strain rate sensitivity of the Cowper-Symonds fits for AZ31B-O (1.6mm) at room temperature

5.3.1.3 Zerilli-Armstrong Fits

The Zerilli-Armstrong fits are presented in Figure 5.27 and Figure 5.29 for room temperature data and in Figure 5.28 and Figure 5.30 for the elevated temperature data. The corresponding constitutive parameters are given in Table 5.11 and Table 5.12 for the RD and the TD, respectively.

Table 5.11: Zerilli-Armstrong constitutive parameters for AZ31B-O (1.6mm) in the RD

Parameter	Estimate	Lower 95%	Upper 95%	Uncertainty
C_1 [MPa]	0	-12.55	12.55	-
C_2 {MPa]	57.42	50.217	64.623	+/- 12.54 %
C_3 [1/K]	0	-	-	-
C_4 [1/K]	2.304E-04	2.061E-04	2.547E-04	+/- 10.55 %
C_5 [MPa]	413.083	-	-	-
n	0.4	0.377	0.423	+/- 5.75 %
C_6 [MPa]	95.247	81.994	108.5	+/- 13.91 %
B_1	1.105	1.050E+00	1.160E+00	+/- 4.98 %
B_2 [1/K]	3.840E-04	1.510E-04	6.170E-04	+/- 60.68 %
B_3 [1/K²]	-2.660E-06	-2.963E-06	-2.357E-06	+/- 11.39 %
	R^2	0.976		

Table 5.12: Zerilli-Armstrong constitutive parameters for AZ31B-O (1.6mm) in the TD

Parameter	Estimate	Lower 95%	Upper 95%	Uncertainty
C_1 [MPa]	14.533	0.894	28.172	+/- 93.85 %
C_2 {MPa]	42.167	38.213	46.121	+/- 9.38 %
C_3 [1/K]	0	-	-	-
C_4 [1/K]	3.150E-04	2.929E-04	3.371E-04	+/- 7.02 %
C_5 [MPa]	444.326	417.074	471.578	+/- 6.13 %
n	0.461	0.429	0.493	+/- 6.94 %
C_6 [MPa]	168.312	150.941	185.683	+/- 10.32 %
B_1	0.929	-	-	-
B_2 [1/K]	3.640E-04	1.500E-04	5.780E-04	+/- 58.79 %
B_3 [1/K²]	-2.512E-06	-2.873E-06	-2.151E-06	+/- 14.37 %
	R^2	0.971		

The Zerilli-Armstrong model offers independent treatment of the strain rate and temperature dependence of the yield stress. It also has a strain rate sensitivity formulation equivalent to a

power law, as shown by Equation (5.4). As a result, the model accurately captures the stress level at most of the strain rates considered (Figure 5.31), as well as the shape of the flow curves over the large range of strain rate considered in the experiments. The thermal softening is also captured well, in particular the decrease of the work-hardening rate as the temperature increases.

$$\sigma_{Z-A}(\dot{\varepsilon}) = C_2 \exp\left[\left(-C_3 + C_4 \ln \dot{\varepsilon}\right)T\right] = C_2 \exp\left(-C_3 T\right)\dot{\varepsilon}^{C_4 T} \tag{5.4}$$

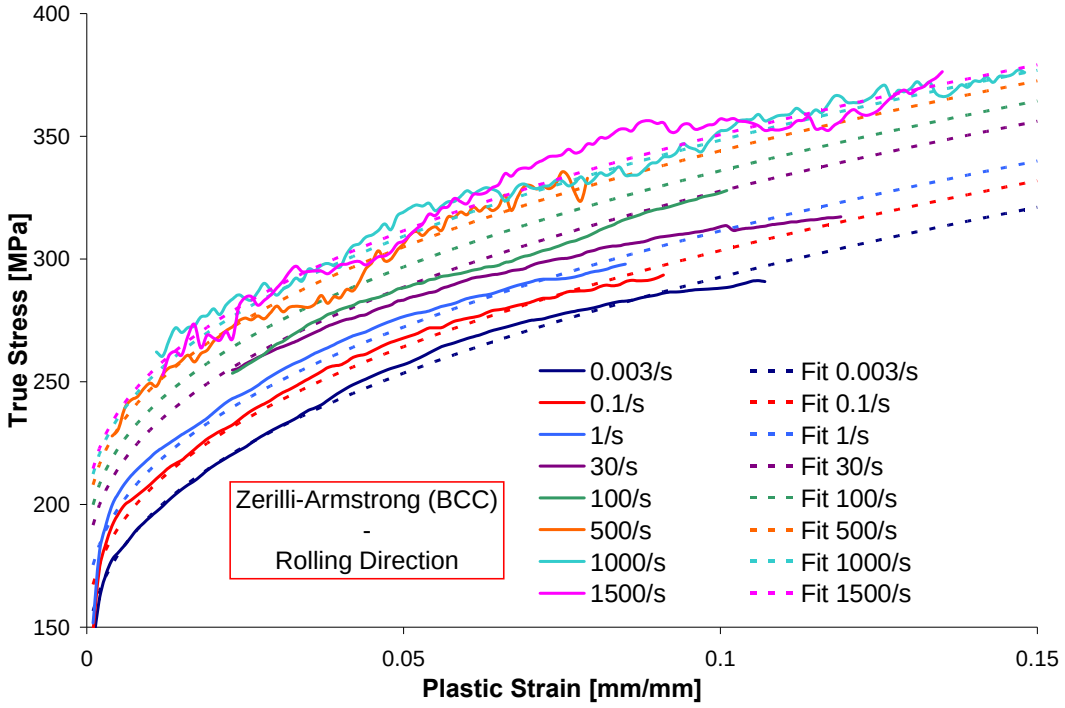

Figure 5.27: Zerilli-Armstrong fits for AZ31B-O (1.6mm) in the Rolling Direction at room temperature

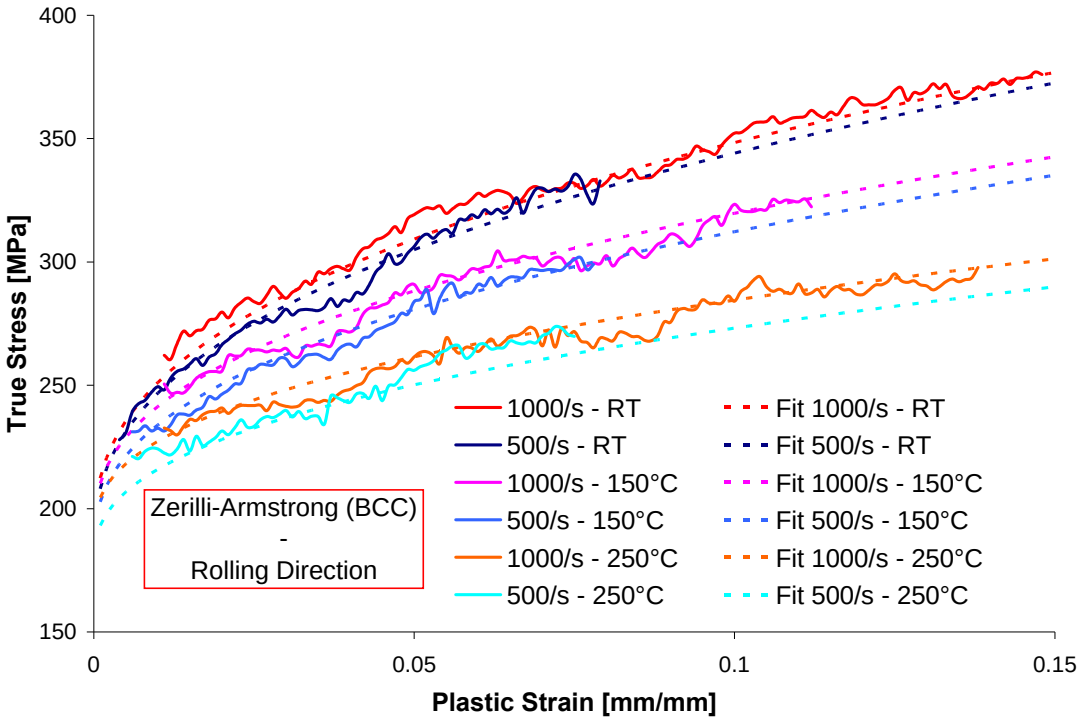

Figure 5.28: Zerilli-Armstrong fits for AZ31B-O (1.6mm) in the Rolling Direction at elevated temperatures

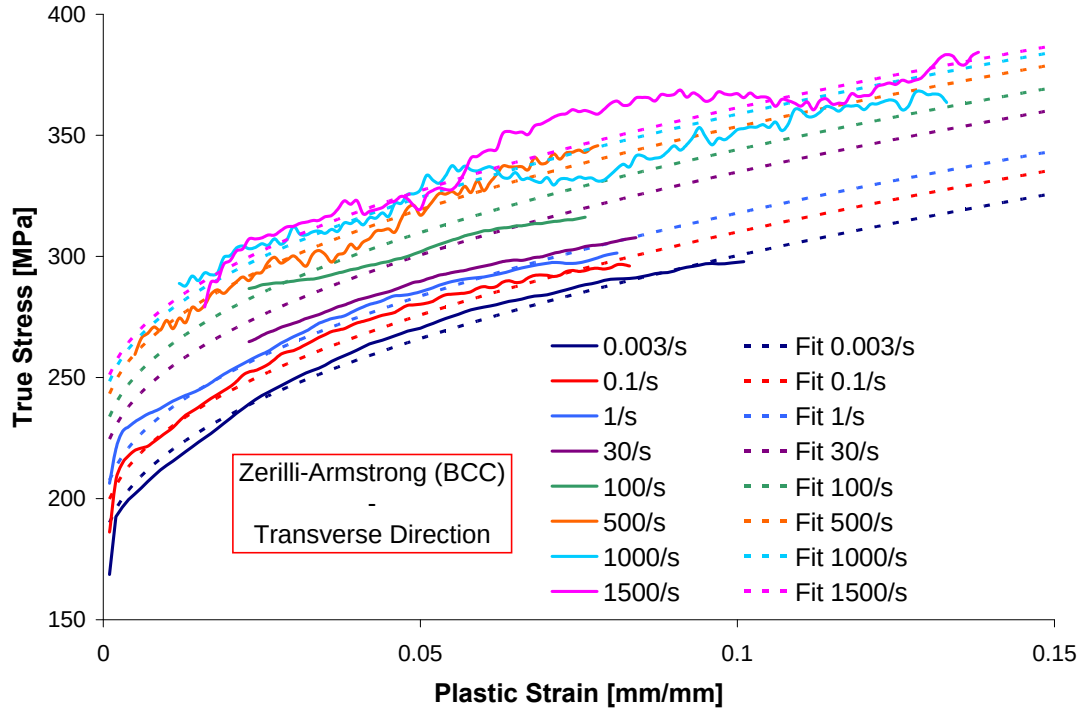

Figure 5.29: Zerilli-Armstrong fits for AZ31B-O (1.6mm) in the Transverse Direction at room temperature

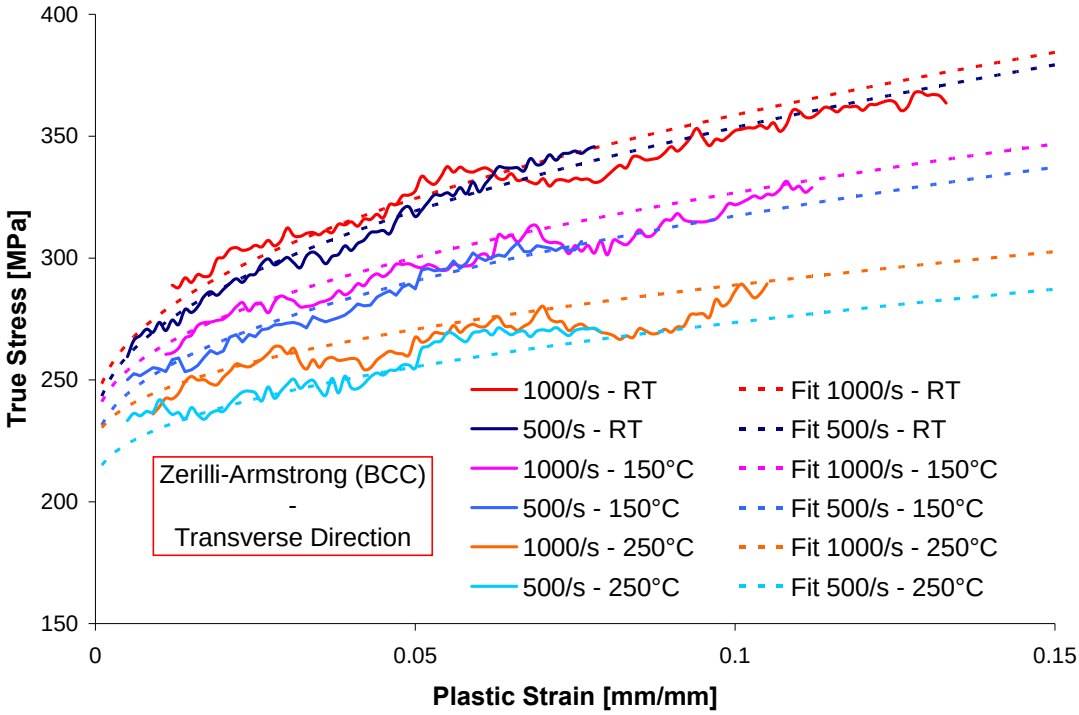

Figure 5.30: Zerilli-Armstrong fits for AZ31B-O (1.6mm) in the Transverse Direction at elevated temperatures

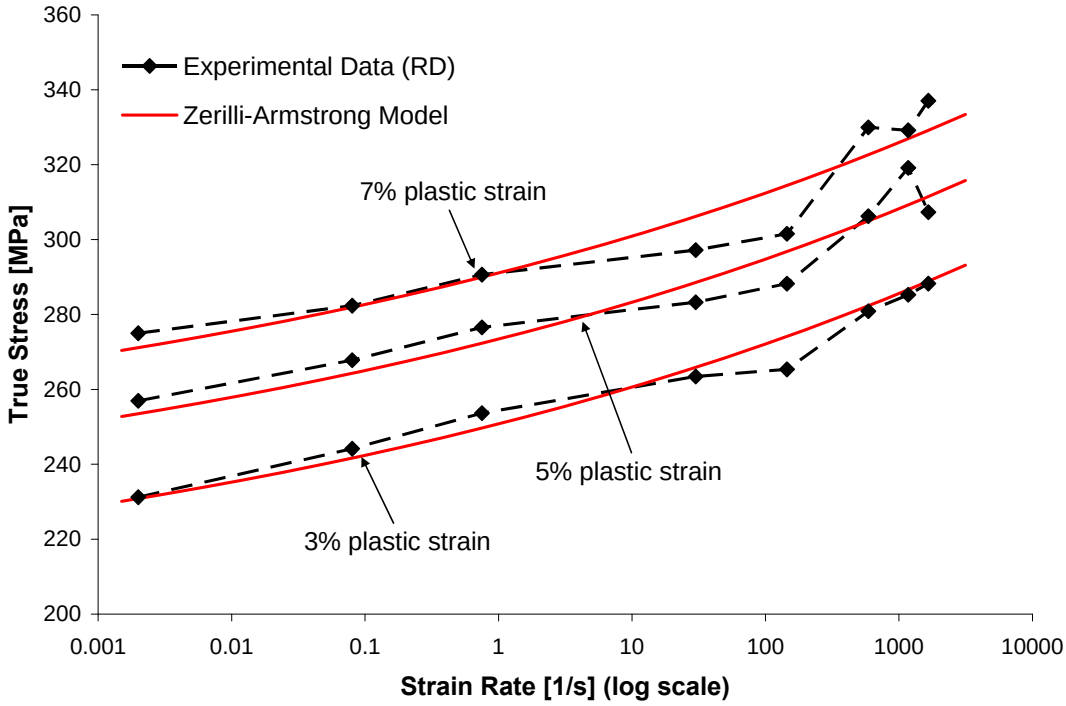

Figure 5.31: Strain rate sensitivity of the Zerilli-Armstrong fits for AZ31B-O (1.6mm) at room temperature

5.3.2 Comparison of the Constitutive Fits

Within the three constitutive models considered, the Zerilli-Armstrong model is the most accurate to represent the experimental data. The Zerilli-Armstrong model has the advantage of being physically based, whereas the others are purely empirical [23]. A comparison of the three models can be seen in Figure 5.32 and Figure 5.33 for the RD data, as well as in Figure 5.34 and Figure 5.35 for the TD. In the figures, results from selected testing conditions at room and elevated temperatures are plotted. As seen in the figures, the Zerilli-Armstrong fits capture best the experimental data at quasi-static and high strain rates at both room and elevated temperatures. However, at the intermediate rates, the three models overestimate the flow curves, especially for the TD data. The Cowper-Symonds model is the most accurate at intermediate strain rates.

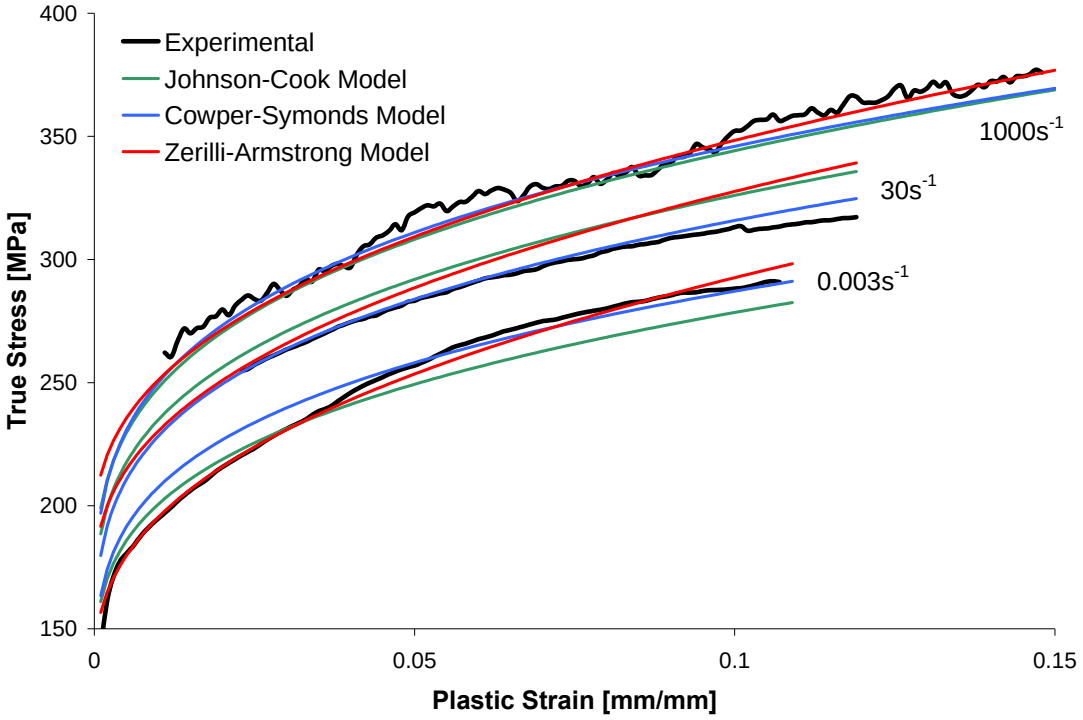

Figure 5.32: Comparison of constitutive models for AZ31B-O (1.6mm) in the RD at room temperature

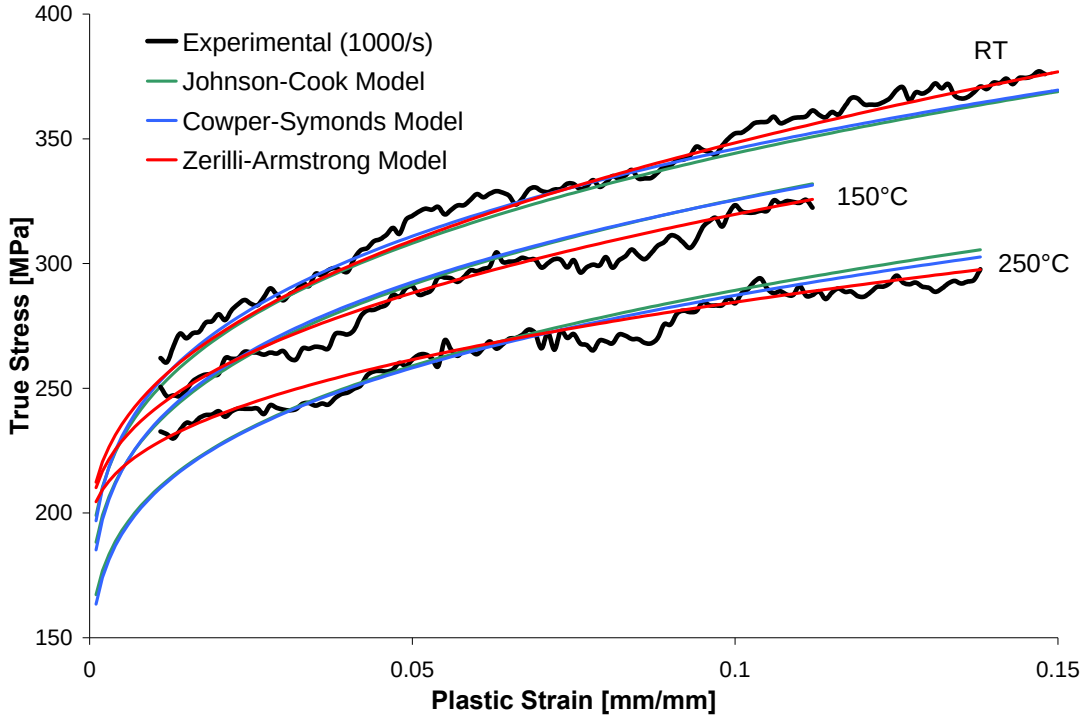

Figure 5.33: Comparison of constitutive models for AZ31B-O (1.6mm) in the RD at elevated temperatures and at $1000s^{-1}$

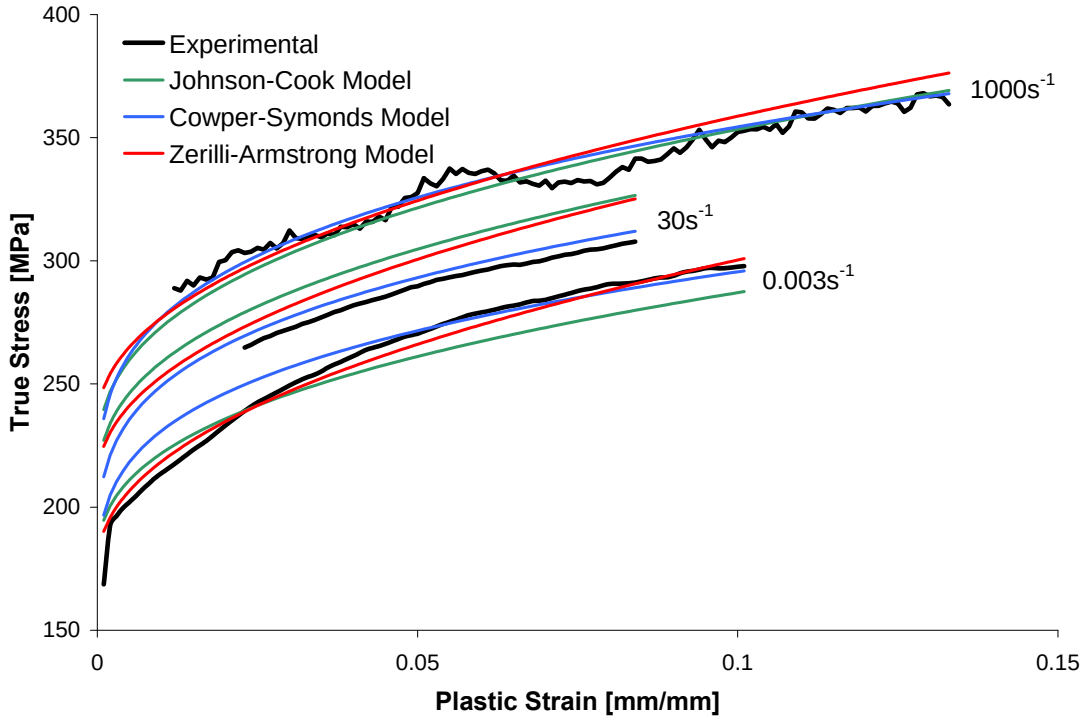

Figure 5.34: Comparison of constitutive models for AZ31B-O (1.6mm) in the TD at room temperature

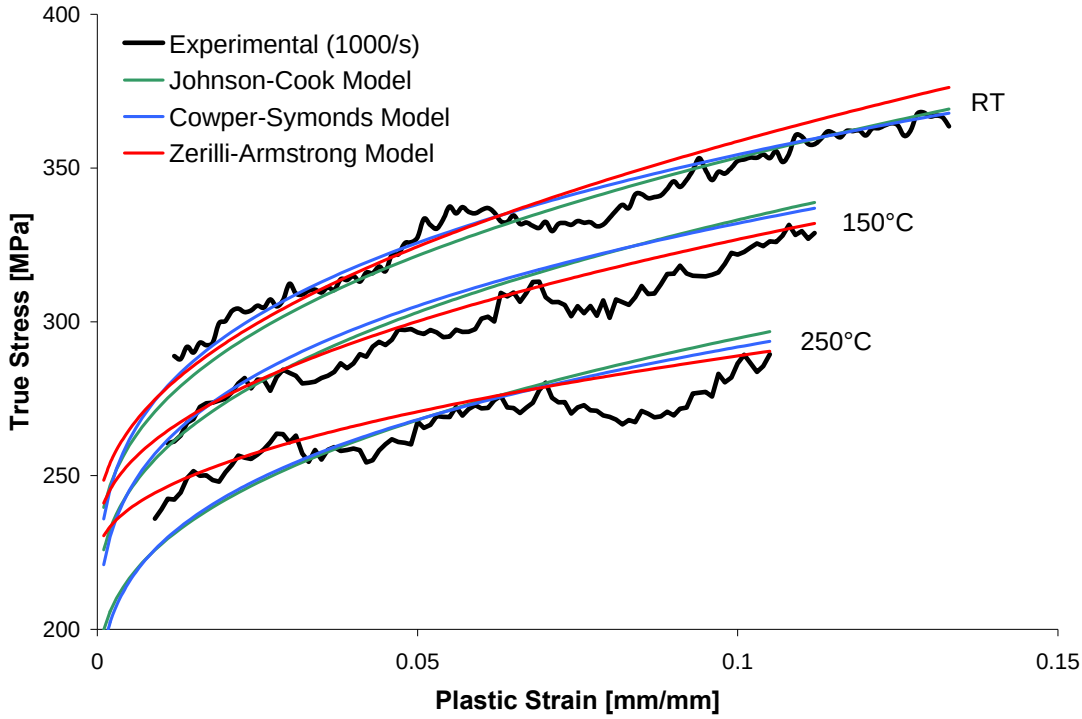

Figure 5.35: Comparison of constitutive models for AZ31B-O (1.6mm) in the TD at elevated temperatures and at $1000s^{-1}$

The strain rate sensitivity of each model is assessed in Figure 5.36 and Figure 5.37 for the RD and the TD, respectively. In the figures, the true stress vs. strain rate curves are plotted for a constant plastic strain of 5%. Due to its power-law formulation, the Cowper-Symonds model captures the best the strain rate sensitivity at 5% plastic strain, even if it underestimates low strain rates (0.1 and $1s^{-1}$). The Zerilli-Armstrong model captures accurately the low and high strain rates, but clearly overestimates the intermediate rates. It is also the only model to capture the thermal softening for the two elevated temperatures, in particular the 150°C conditions for which the two other models overestimate the stress levels.

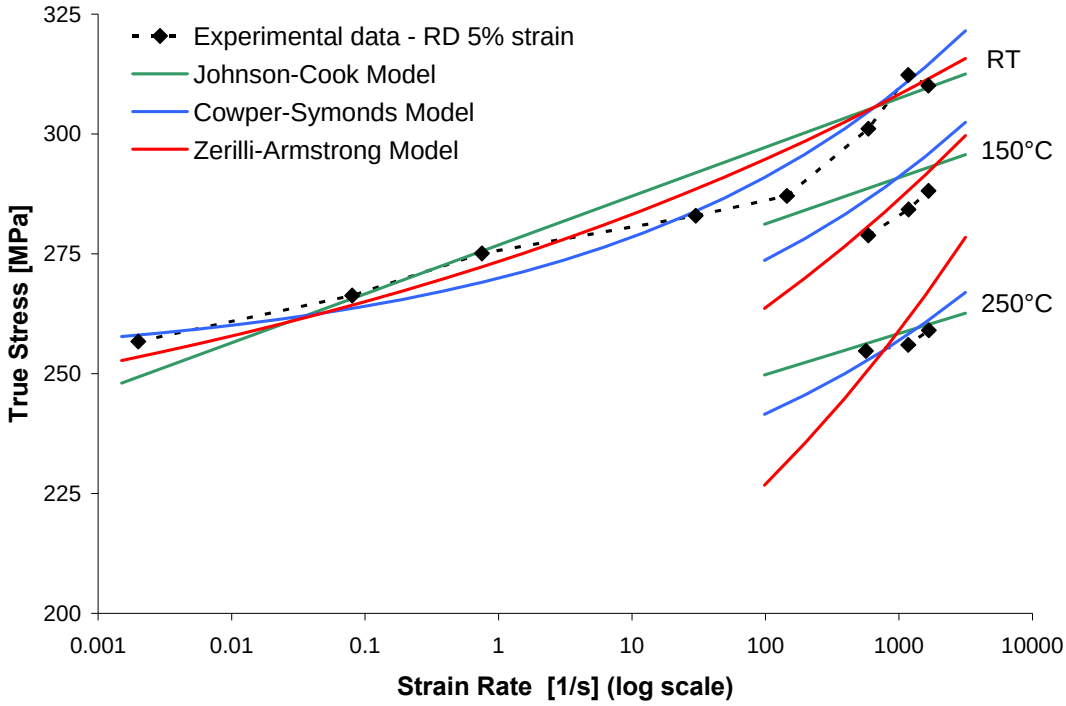

Figure 5.36: Comparison of the strain rate sensitivity of the constitutive fits at 5% plastic strain for AZ31B-O in the RD

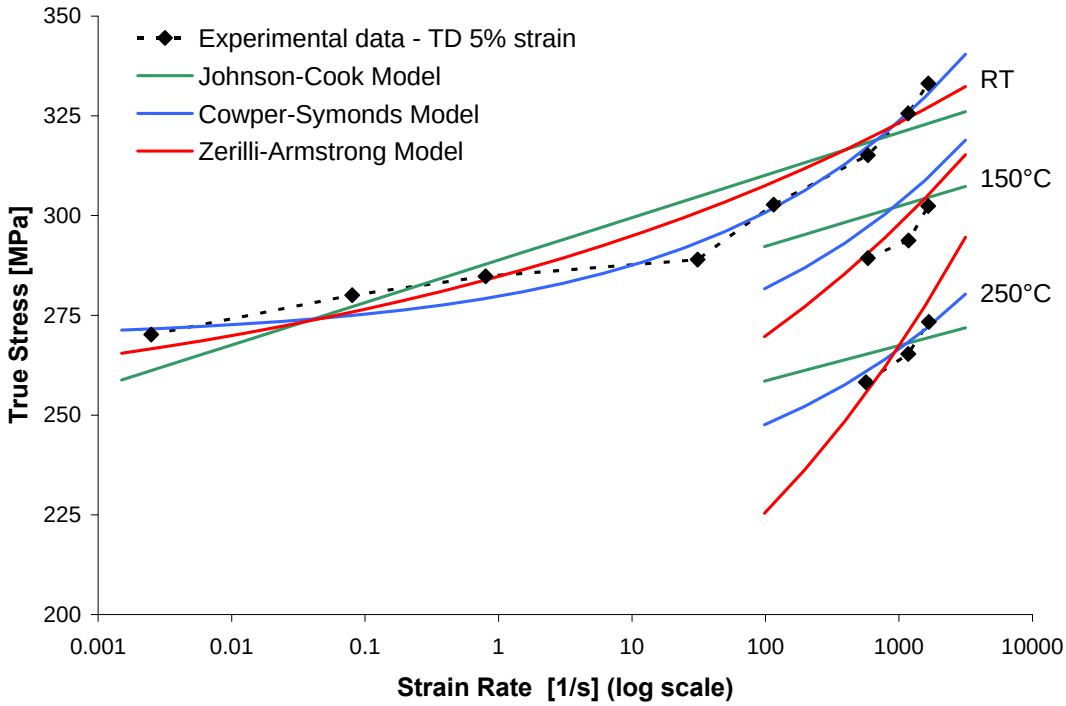

Figure 5.37: Comparison of the strain rate sensitivity of the constitutive fits at 5% plastic strain for AZ31B-O in the TD

5.3.3 Constitutive Fits to the 1.0mm and 2.5mm Experimental Data

Experimental data from AZ31B-O sheet with a thickness of 1mm and 2.5mm were also fit to the three different models. Since those two materials have similar strain rate sensitivities to the 1.6mm thick material, the different constitutive models show the same accuracy in capturing the flow curves. Therefore a complete description of each fit is not provided; and only the constitutive parameters for each material are given.

The constitutive parameters of the three models are summarized in Table 5.13 and Table 5.14 for the 1mm and 2.5 mm thick materials, respectively. One should also note that no elevated temperature experiments were performed for the 1.0 and 2.5mm sheets. Therefore constitutive parameters associated with temperature effects were taken from the 1.6mm sheet fits and considered as constants during the fit.

Table 5.13: Constitutive parameters for AZ31B-O, 1mm thick sheet

Parameter	Estimate	Lower 95%	Upper 95%	Uncertainty
		Johnson-Cook		
Rolling Direction:			R^2 =	0.866
A [MPa]	**151.561**	133.916	169.206	+/- 11.64 %
B [MPa]	**294.735**	281.664	307.806	+/- 4.43 %
n	**0.296**	0.247	0.345	+/- 16.55 %
C	**0.016**	0.015	0.017	+/- 6.25 %
m	**1.849**	-	-	-
Transverse Direction:			R^2 =	0.849
A [MPa]	**161.375**	120.178	202.572	+/- 25.53 %
B [MPa]	**286.760**	271.318	302.202	+/- 5.38 %
n	**0.284**	0.175	0.393	+/- 38.38 %
C	**0.016**	0.015	0.017	+/- 6.25 %
m	**1.808**	-	-	-
		Cowper-Symonds		
Rolling Direction:			R^2 =	0.979
A [MPa]	**151.686**	145.933	157.439	+/- 3.79 %
B [MPa]	**318.303**	311.180	325.426	+/- 2.24 %
n	**0.375**	0.351	0.399	+/- 6.4 %
C [1/s]	**3.150E+04**	-	-	-
p	**2.206**	2.175	2.237	+/- 1.41 %
m	**1.787**	-	-	-

Parameter	Estimate	Lower 95%	Upper 95%	Uncertainty
Cowper-Symonds				
Transverse Direction:			R^2 =	0.969
A [MPa]	**158.647**	144.846	172.448	+/- 8.7 %
B [MPa]	**285.089**	277.388	292.79	+/- 2.7 %
n	**0.326**	0.278	0.374	+/- 14.72 %
C [1/s]	**2.150E+04**	-	-	-
p	**1.926**	1.895	1.957	+/- 1.61 %
m	**1.747**	-	-	-
Zerilli-Armstrong				
Rolling Direction:			R^2 =	0.988
C_1 [MPa]	**0**	-122.254	122.254	-
C_2 {MPa]	**2.202**	2.302	2.102	+/- -4.54 %
C_3 [1/K]	**0**	-	-	-
C_4 [1/K]	**1.566E-03**	1.504E-03	0.0016286	+/- 3.99 %
C_5 [MPa]	**359.71**	354.854	364.566	+/- 1.35 %
n	**0.317**	0.293	0.341	+/- 7.57 %
C_6 [MPa]	**119.287**	-5.331	243.905	+/- 104.47 %
B_1	**1.105**	-	-	-
B_2 [1/K]	**3.84E-04**	-	-	-
B_3 [1/K²]	**-2.66E-06**	-	-	-
Transverse Direction:			R^2 =	0.976
C_1 [MPa]	**0**	-160.724	160.724	-
C_2 {MPa]	**1.9**	1.529	2.271	+/- 19.53 %
C_3 [1/K]	**0**	-	-	-
C_4 [1/K]	**1.616E-03**	1.529E-03	0.0017018	+/- 5.34 %
C_5 [MPa]	**377.789**	365.435	390.143	+/- 3.27 %
n	**0.349**	0.305	0.393	+/- 12.61 %
C_6 [MPa]	**192.636**	-5.926	391.198	+/- 103.08 %
B_1	**0.929**	-	-	-
B_2 [1/K]	**3.64E-04**	-	-	-
B_3 [1/K²]	**-2.51E-06**	-	-	-

Table 5.14: Constitutive parameters for AZ31B-O, 2.5mm thick sheet

Parameter	Estimate	Lower 95%	Upper 95%	Uncertainty
Johnson-Cook				
Rolling Direction:			R^2 =	0.949
A [MPa]	**114.978**	80.741	149.215	+/- 29.78 %
B [MPa]	**306.102**	282.450	329.754	+/- 7.73 %
n	**0.205**	0.160	0.25	+/- 21.95 %
C	**0.014**	0.014	0.014	+/- 0 %
m	**1.849**	-	-	-
Transverse Direction:			R^2 =	0.909
A [MPa]	**168.200**	130.403	205.997	+/- 22.47 %
B [MPa]	**237.273**	212.729	261.817	+/- 10.34 %
n	**0.216**	0.146	0.286	+/- 32.41 %
C	**0.012**	0.011	0.013	+/- 8.33 %
m	**1.808**	-	-	-
Cowper-Symonds				
Rolling Direction:			R^2 =	0.95
A [MPa]	**116.800**	110.423	123.177	+/- 5.46 %
B [MPa]	**182.317**	177.367	187.267	+/- 2.72 %
n	**0.316**	0.285	0.347	+/- 9.81 %
C [1/s]	**3.890E+07**	-	-	-
p	**24.345**	22.842	25.848	+/- 6.17 %
m	**1.787**	-	-	-
Transverse Direction:			R^2 =	0.925
A [MPa]	**118.587**	63.198	173.976	+/- 46.71 %
B [MPa]	**244.134**	198.855	289.413	+/- 18.55 %
n	**0.159**	0.097	0.221	+/- 38.99 %
C [1/s]	**1.9E+07**	-	-	-
p	**5.862**	5.664	6.06	+/- 3.38 %
m	**1.747**	-	-	-
Zerilli-Armstrong				
Rolling Direction:			R^2 =	0.969
C_1 [MPa]	**0**	-158.212	158.212	-
C_2 {MPa]	**17.282**	13.793	20.771	+/- 20.19 %
C_3 [1/K]	**0**	-	-	-
C_4 [1/K]	**5.189E-04**	4.115E-04	0.0006263	+/- 20.7 %
C_5 [MPa]	**312.274**	300.608	323.94	+/- 3.74 %
n	**0.241**	0.2	0.282	+/- 17.01 %
C_6 [MPa]	**108.661**	-64.597	281.919	+/- 159.45 %
B_1	**1.105**	-	-	-
B_2 [1/K]	**3.84E-04**	-	-	-
B_3 [1/K²]	**-2.66E-06**	-	-	-

Parameter	Estimate	Lower 95%	Upper 95%	Uncertainty
		Zerilli-Armstrong		
Transverse Direction:			R^2 =	0.944
C_1 [MPa]	**0**	-172.246	172.246	-
C_2 {MPa]	**12.811**	8.622	17	+/- 32.7 %
C_3 [1/K]	**0**	-	-	-
C_4 [1/K]	**6.607E-04**	5.425E-04	0.0007789	+/- 17.89 %
C_5 [MPa]	**297.183**	281.492	312.874	+/- 5.28 %
n	**0.25**	0.184	0.316	+/- 26.4 %
C_6 [MPa]	**193.453**	-36.351	423.257	+/- 118.79 %
B_1	**0.929**	-	-	-
B_2 [1/K]	**3.64E-04**	-	-	-
B_3 [1/K²]	**-2.51E-06**	-	-	-

The 1.0mm sheet experiment data were fit to the Johnson-Cook model (Figure 5.38 and Figure 5.39), Cowper-Symonds model (Figure 5.40 and Figure 5.41) and Zerilli-Armstrong model (Figure 5.42 and Figure 5.43). Similar to what was seen for the 1.6mm sheet, the Johnson-Cook model fails to capture the constitutive behavior at high strain rate, and the two other models are more accurate. However, the quasi-static and intermediate rates are less accurately captured by the Zerilli-Armstrong than for the 1.6mm data. This is probably due to the temperature dependent parameters imposed during the fit process.

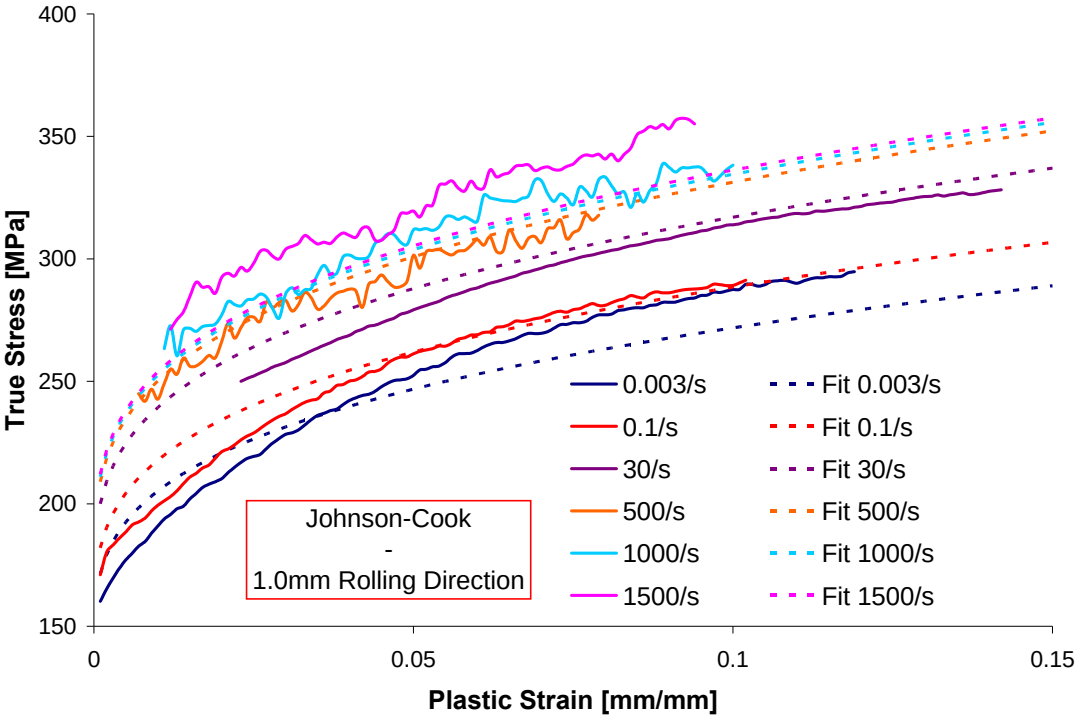

Figure 5.38: Johnson-Cook fits for AZ31B-O (1.0mm) in the RD

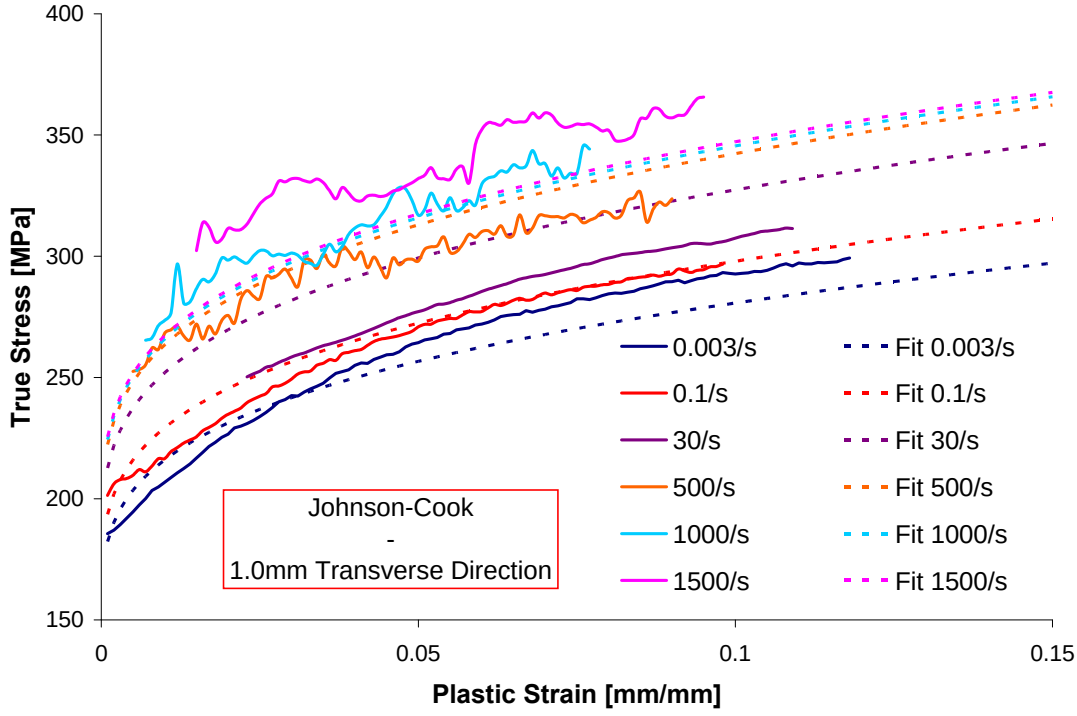

Figure 5.39: Johnson-Cook fits for AZ31B-O (1.0mm) in the TD

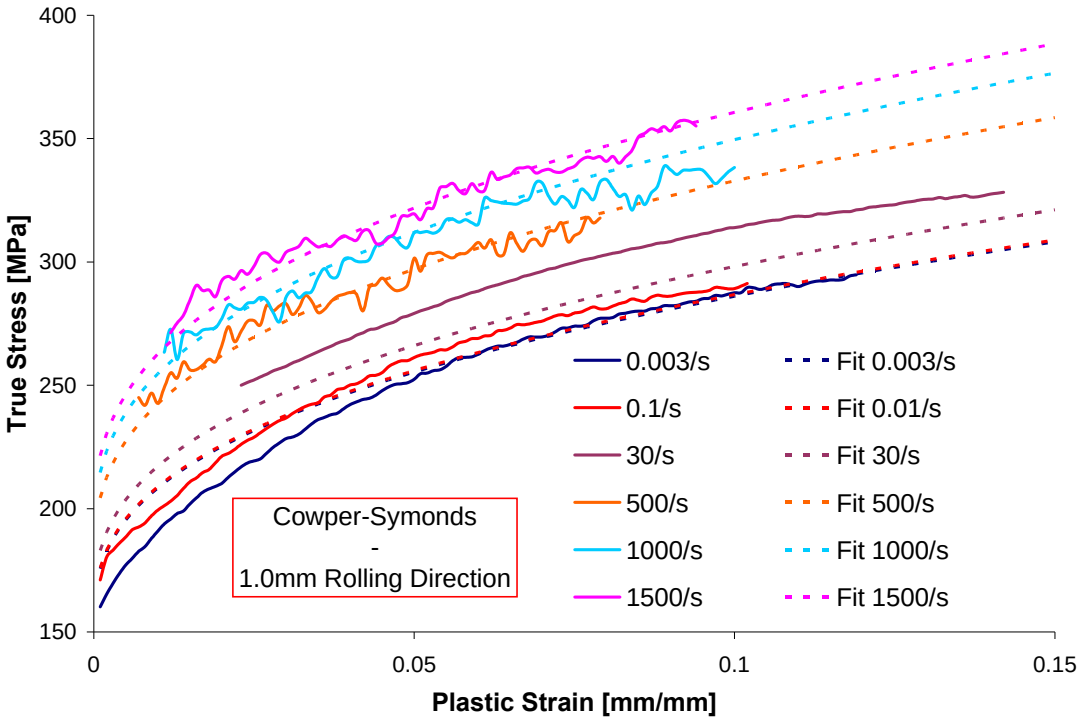

Figure 5.40: Cowper-Symonds fits for AZ31B-O (1.0mm) in the RD

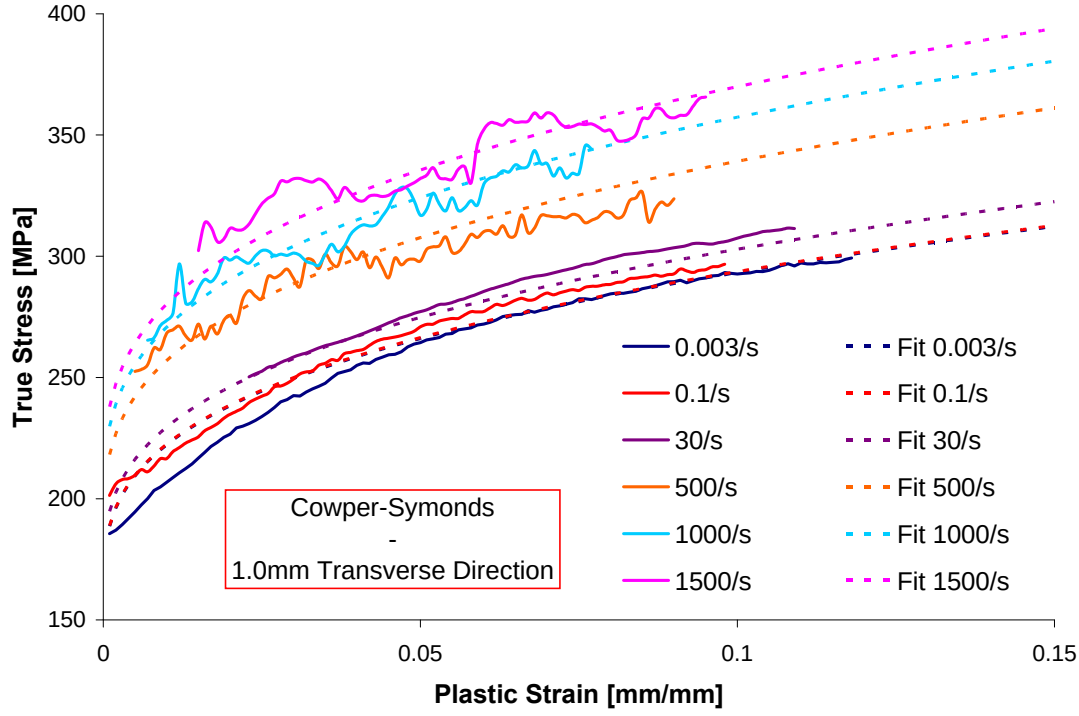

Figure 5.41: Cowper-Symonds fits for AZ31B-O (1.0mm) in the TD

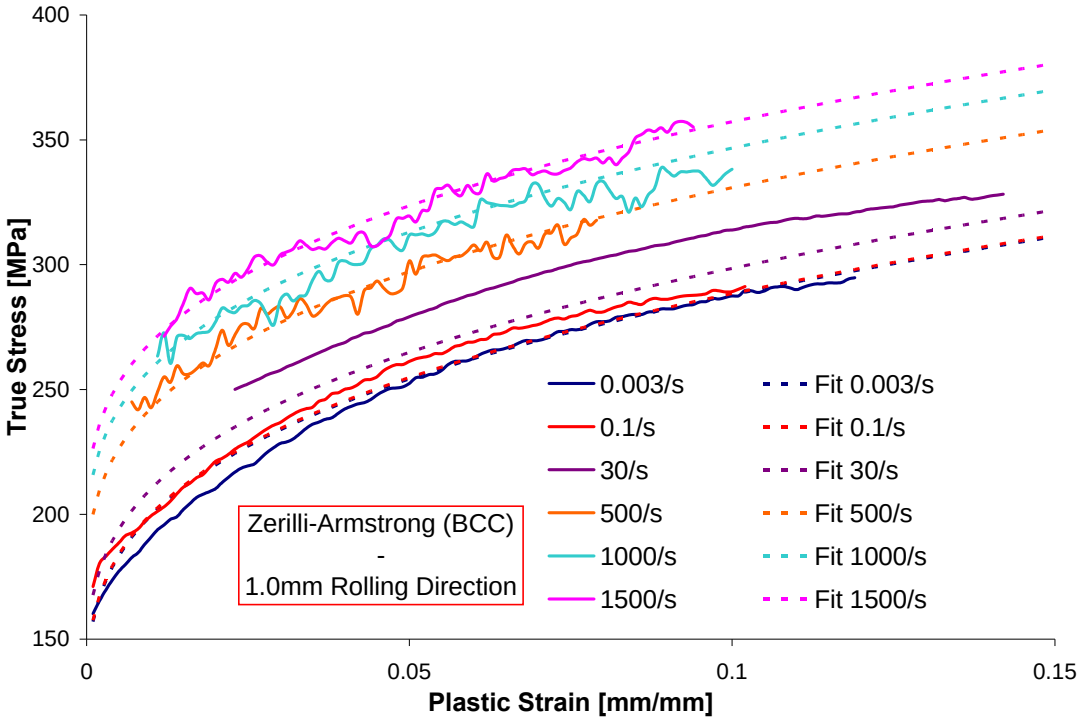

Figure 5.42: Zerilli-Armstrong fits for AZ31B-O (1.0mm) in the RD

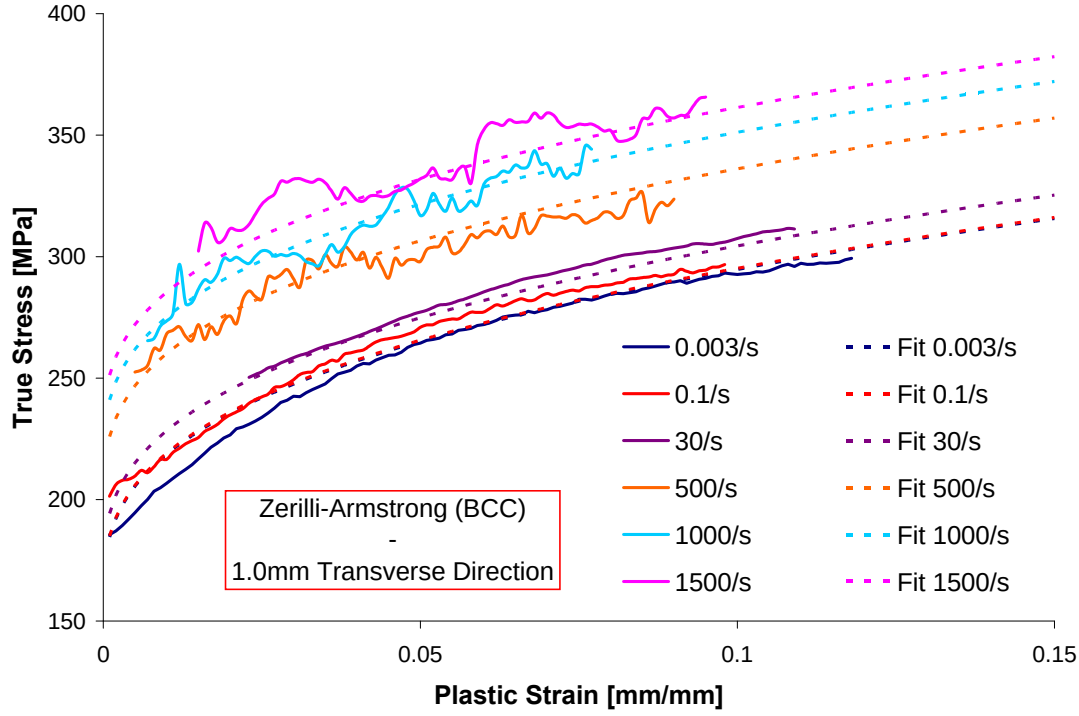

Figure 5.43: Zerilli-Armstrong fits for AZ31B-O (1.0mm) in the TD

Similar to the 1.0mm data, the 2.5mm sheet experimental data was fit to the Johnson-Cook model (Figure 5.44 and Figure 5.45), Cowper-Symonds model (Figure 5.46 and Figure 5.47), and Zerilli-Armstrong model (Figure 5.48 and Figure 5.49). Once again, the Zerilli-Armstrong model has the highest R-squared values and captures the experimental data better than the two other models. However, the fits are not as good as for the 1.6mm results, especially at low strain values where the three models overestimate the flow curves. This lack of fit could be explained by the imposed parameters related to the temperature, as well as the significant oscillations in the high strain rate data.

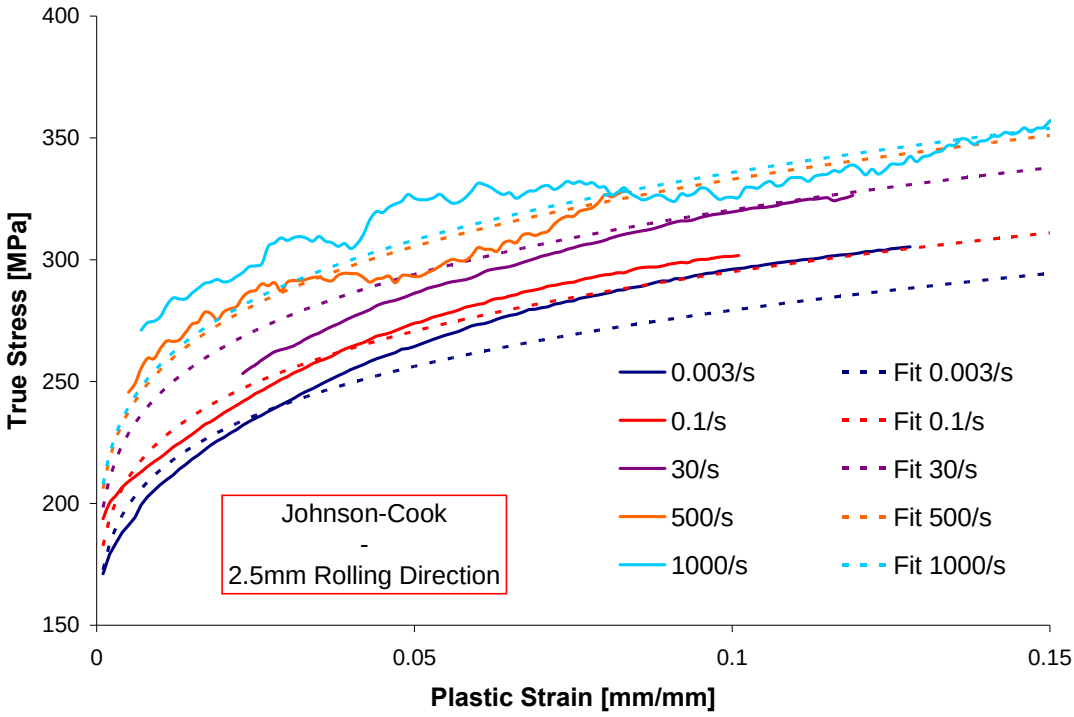

Figure 5.44: Johnson-Cook fits for AZ31B-O (2.5mm) in the RD

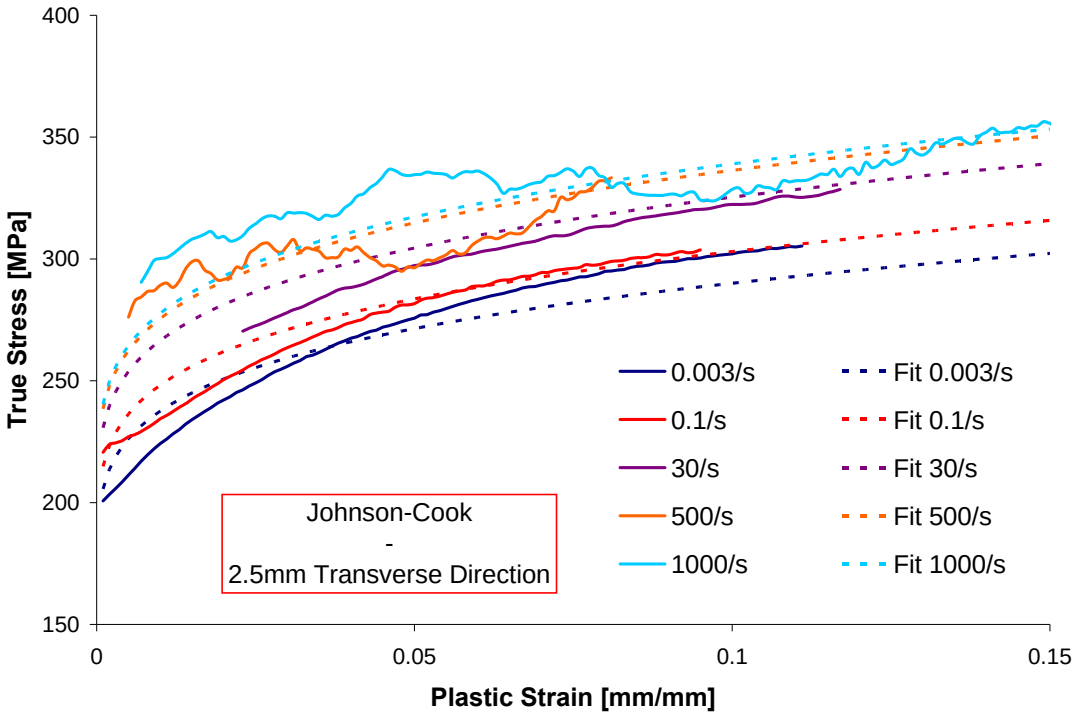

Figure 5.45: Johnson-Cook fits for AZ31B-O (2.5mm) in the TD

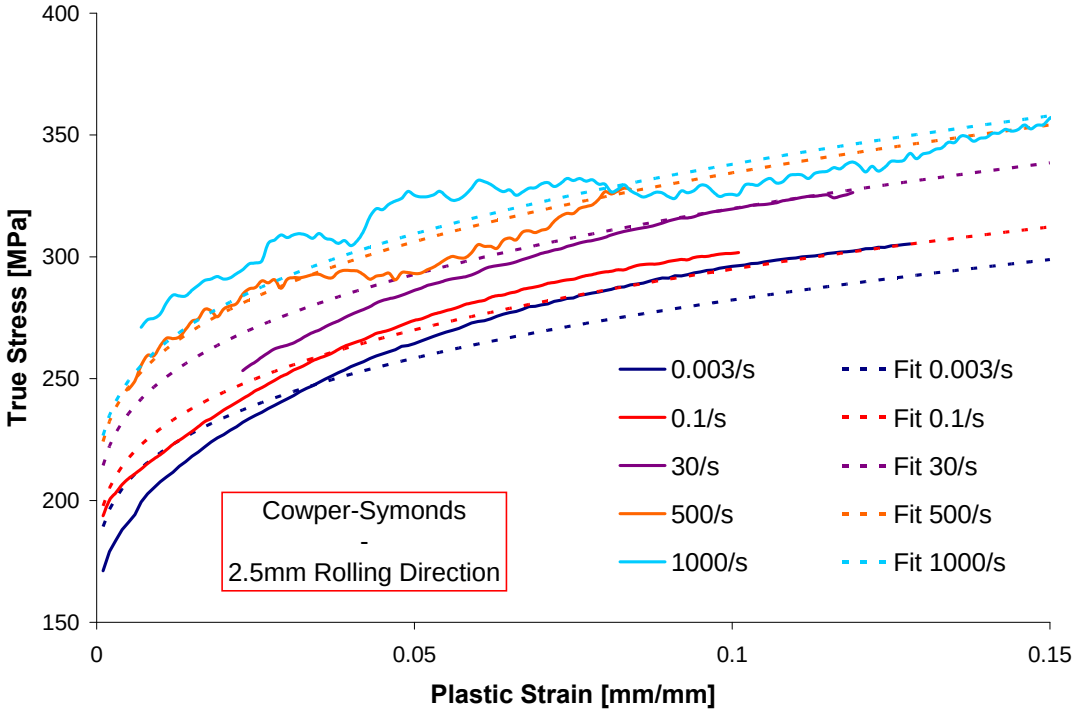

Figure 5.46: Cowper-Symonds fits for AZ31B-O (2.5mm) in the RD

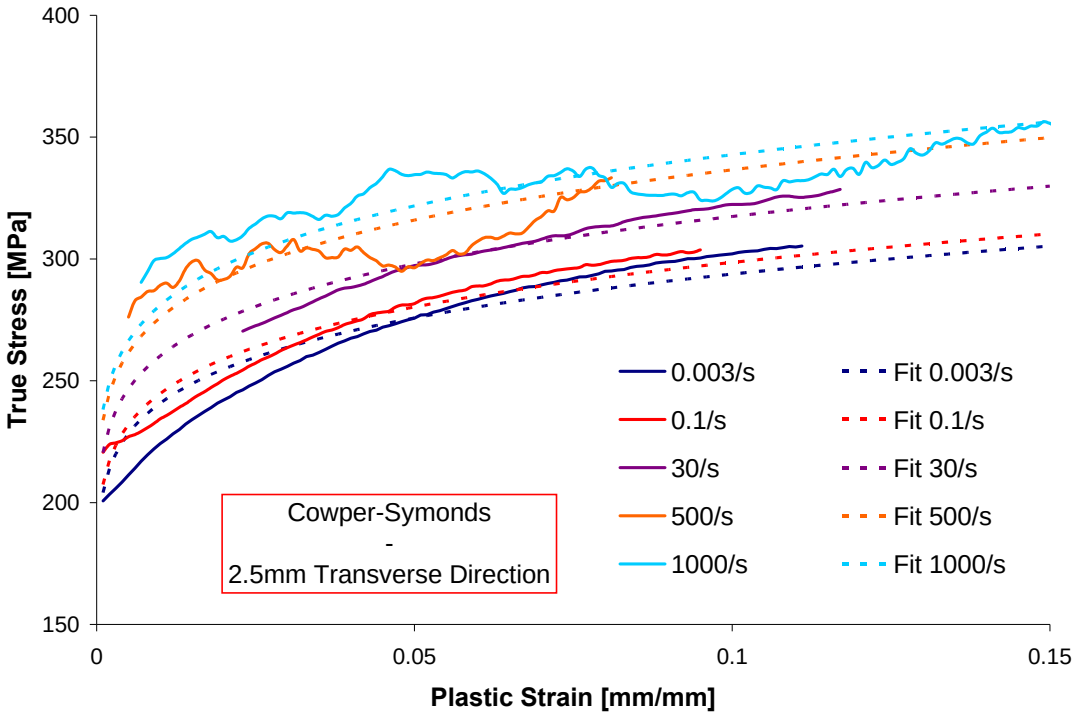

Figure 5.47: Cowper-Symonds fits for AZ31B-O (2.5mm) in the TD

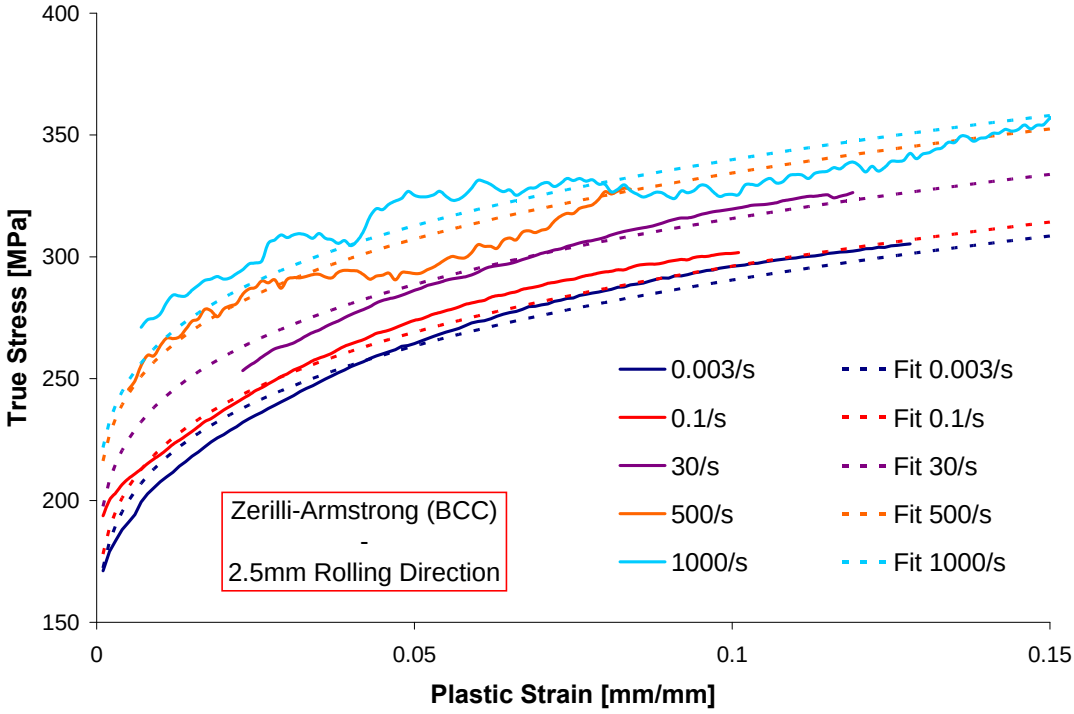

Figure 5.48: Zerilli-Armstrong fits for AZ31B-O (2.5mm) in the RD

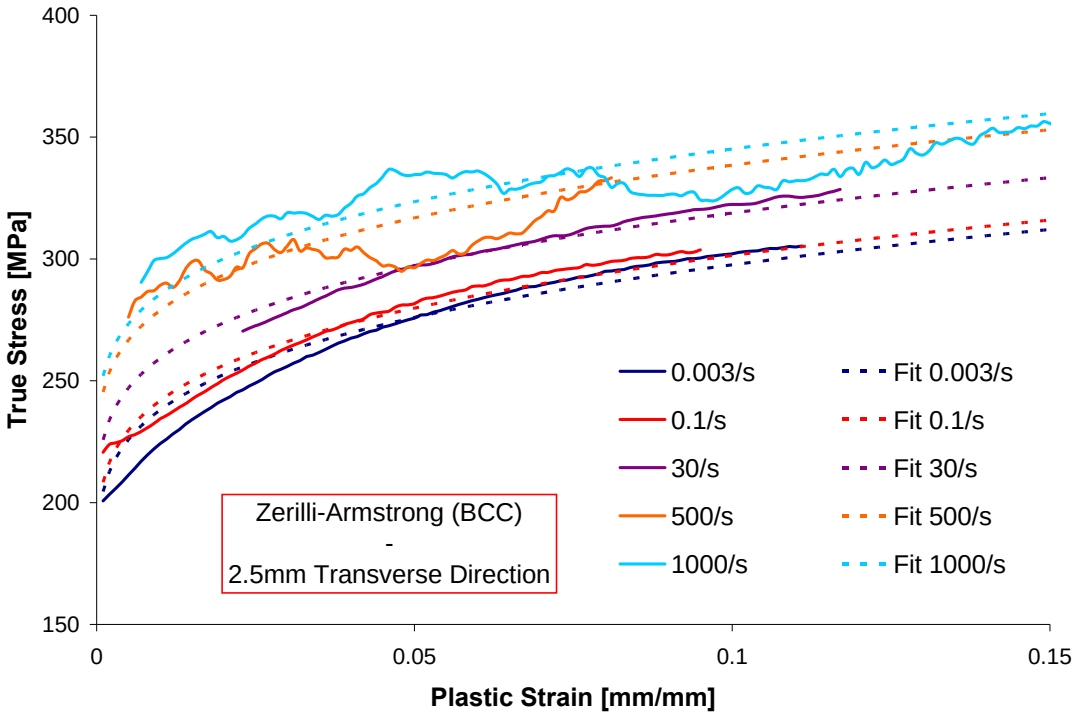

Figure 5.49: Zerilli-Armstrong fits for AZ31B-O (2.5mm) in the TD

6 NUMERICAL RESULTS

Finite element simulations were performed in order to validate the constitutive model parameters determined in Section 5. Since the tensile split Hopkinson bar (TSHB) was mainly used in the current research, this apparatus was modeled and different testing conditions were simulated. During the TSHB experiment, the behaviour of the specimen has an effect on the reflected and transmitted strain waves in the bar. In addition to direct comparison of the stress-strain curves, the different waves in the bars are also compared to validate the models.

The finite element models were created using SolidWorks [77], meshed using Hypermesh [78] and solved using LS-DYNA [9].

6.1 TSHB Finite Element Model

The finite element model of the TSHB can be seen in Figure 6.1; and a magnified view of the specimen region is showed in Figure 6.2. Due to symmetry in the geometry of the bars and the specimen, only a quarter-model is required for the simulations. The striker tube was not modeled to avoid numerical oscillations induced by its impact on the bar end. Therefore a prescribed motion was applied to the nodes at the bar end to simulate the impact of the striker.

The actual TSHB has a length of 2.06m (81") for the incident bar and 1.83m (72") for the transmitted bar, however since the model doesn't include the gas gun and the striker tube, the length of the two bars has been reduced to 1.3m. This still allows the elastic waves to be fully recorded at the strain gauge position without superposition due to bar end reflections. The strain gauges are positioned at 65cm from the end of the bar for the incident bar, and 25cm for the transmitter bar; element sets were then defined in this region of the model to record the strain history of the bars.

The duration of the simulation was fixed to 0.75ms, which permits complete propagation and reflection of the elastic wave in the incident bar.

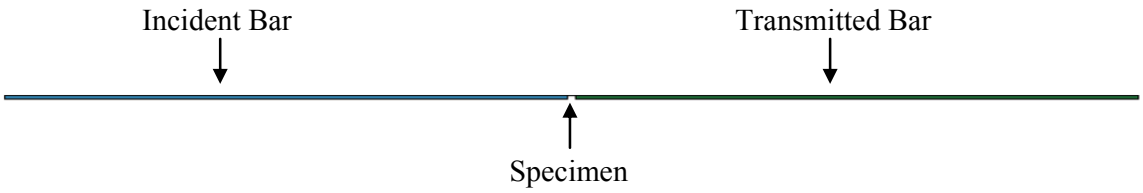

Figure 6.1: TSHB finite element model

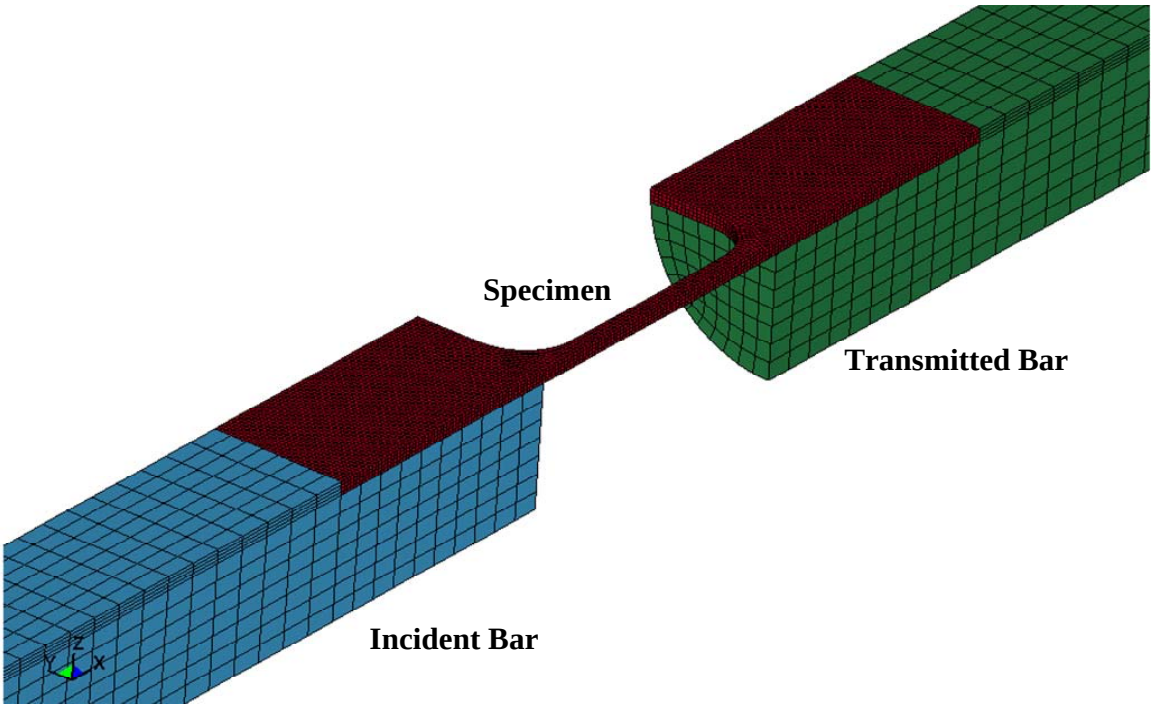

Figure 6.2: Magnified view of the specimen region of the TSHB finite element model

The specimen is meshed using 18,204 solid elements, mostly hexahedral elements, with an average size of 0.5mm. A detailed view of the specimen mesh can be seen in Figure 6.3. The two bars have a similar mesh, each comprising 55,838 elements, mostly hexahedral, with an average size of 2mm. The cross-section of the mesh for the bars can be seen in Figure 6.4, the grip regions of the bars have a finer mesh to reduce contact issues between the two meshes.

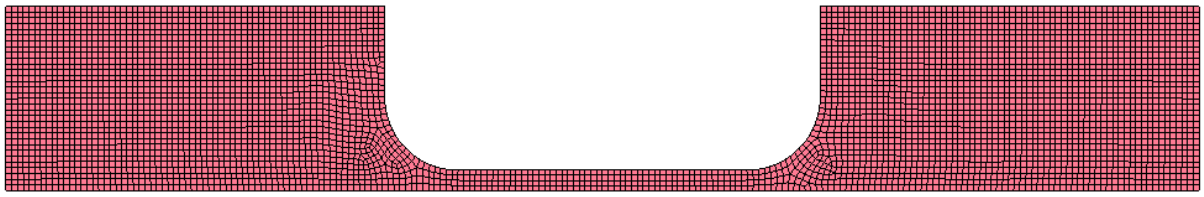

Figure 6.3: Specimen mesh

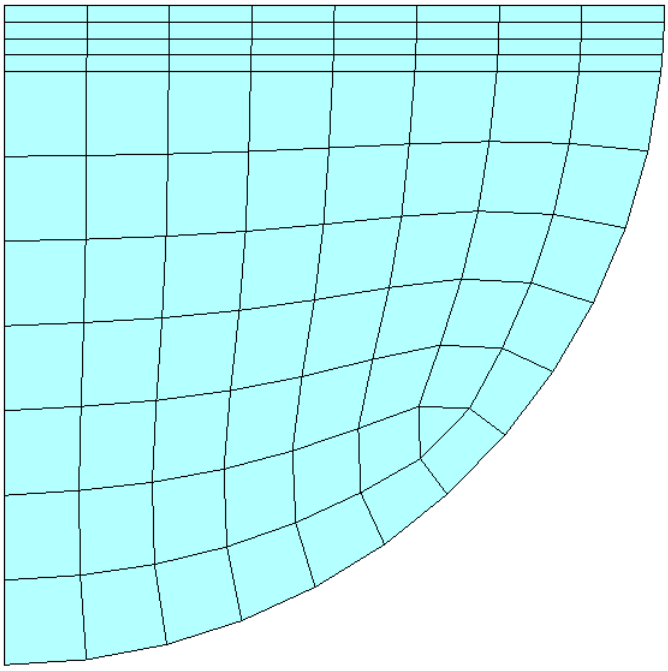

Figure 6.4: Cross-section mesh of the bars

The gas gun and the striker were not modeled to reduce the length of the incident bar and to avoid dealing with additional oscillation that the impact would cause in the numerical solution. Therefore, a velocity boundary condition was applied at the end of the incident bar. As seen in Section 1.3.2, Equation (1.13) can be used to calculate the particle velocity V_p knowing the strain ε_0 of the bar, and the wave velocity C_0. The measured strain history of the incident wave was used to calculate the prescribed velocity of the nodes at the end of the bar. The input velocity curve can be seen in Figure 6.5.

$$V_p = C_0 \varepsilon_x \tag{6.1}$$

Since only a quarter-model was considered, symmetry boundary conditions were applied at the appropriate nodes. Tied contacts were defined between the specimen and the bars in order to model the pressure applied by the screw to prevent the specimen from slipping in the slot.

An elastic material model was used to characterize the incident and transmitted bars. Their density (2.7 g/cm^3) and Young's modulus (68.9 GPa) are the same as Al 6061, so that the elastic waves have the same velocity as the actual bars.

Several material models were used for the specimen. Material model 15 [9] was used for the Johnson-Cook and its modified formulation with a Cowper-Symonds strain rate sensitivity (Equation (5.1) and (5.2)). The Zerilli-Armstrong for BCC materials (Equation (5.3)) is implemented as material model 65 [9]. The input files for each material are given in Appendix C.

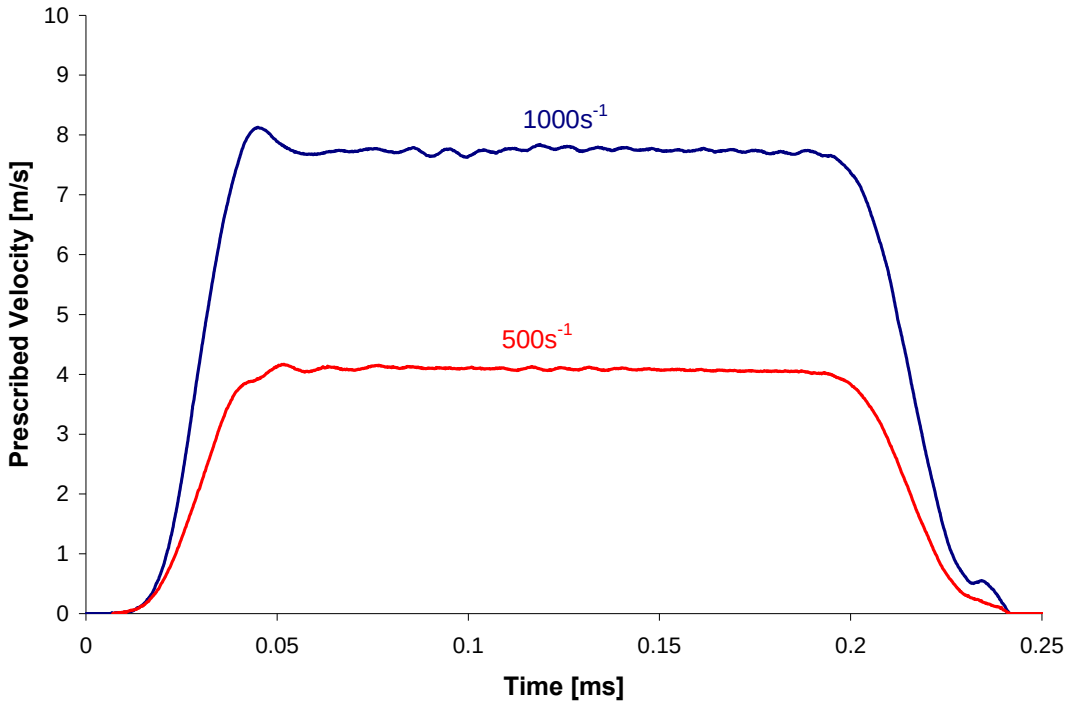

Figure 6.5: Velocity vs. Time applied at the end of the incident bar for the 500s^{-1} and 1000s^{-1} simulations

6.2 TSHB Finite Element Results

The TSHB finite element model was analysed for several testing conditions. Simulations at $500s^{-1}$ and $1000s^{-1}$ were performed to compare the different strain rate sensitivity of the models. The thermal sensitivity of the models was assessed by simulations at $1000s^{-1}$ performed at room temperature, 150°C and 250°C.

Figure 6.6 shows the predicted true stress contour plots for the $1000s^{-1}$ simulation at room temperature using the Zerilli-Armstrong model. As seen in the figure, the deformation is uniform during the entire simulation, even during the unloading of the specimen. Similar results were obtained for all the other simulations (with different conditions and models). Therefore, none of the finite element models were able to predict the onset of necking in the specimen. This can be a mesh effect; a refined mesh in the gauge length would be needed to see if necking can be predicted by the models, or if a damage criterion should be used.

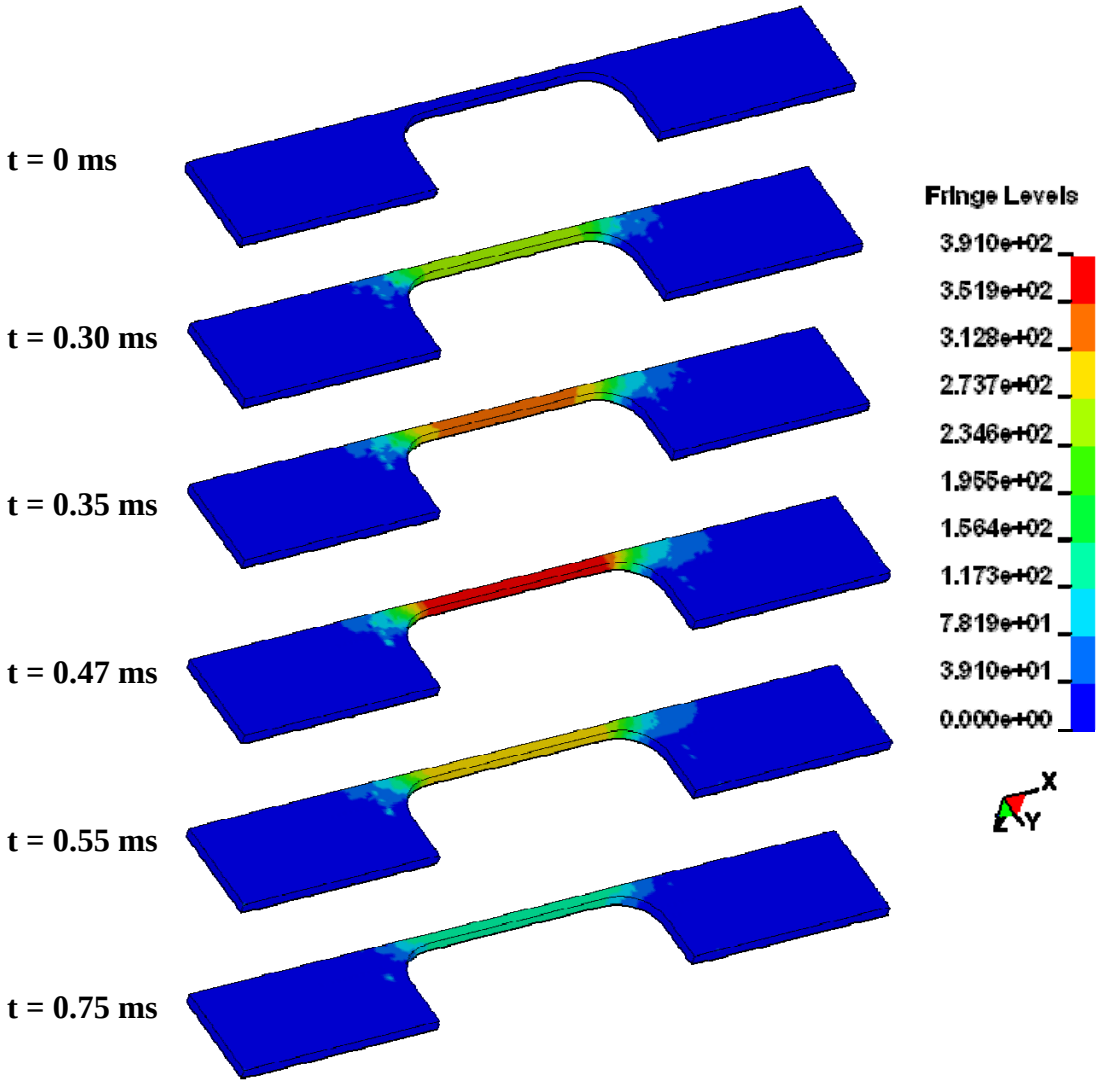

Figure 6.6: Predicted true stress levels in the TSHB at $1000s^{-1}$ and room temperature (Zerilli-Armstrong model)

6.3 Predicted Waves and Specimen Necking

In order to validate the finite element models and the different constitutive models, the incident, reflected and transmitted elastic waves from the numerical model are compared with the measured wave forms from the experiments. The incident wave is directly imposed by the prescribed velocity. Therefore, the close match of predicted and measured curves confirms that the boundary conditions of the model were applied correctly. The reflected wave is proportional to the strain rate in the sample, but is also affected by the interface between the

bar and the specimen. The transmitted wave depends directly on the specimen properties and, thus, on the constitutive model and parameters considered.

A comparison of the strain histories in the incident bar can be seen in Figure 6.7 and Figure 6.8 for the $500s^{-1}$ and $1000s^{-1}$ simulations, respectively. For the two strain rate conditions, the incident pulses are in excellent agreement with the experiments for the three models considered. The boundary velocity is thus correctly applied. The predicted reflected waves are identical for the three models and very close to the measured reflected waves for both the $500s^{-1}$ and $1000s^{-1}$ simulations. The predicted reflected waves have a slightly higher strain level, which implies a higher strain rate in the simulations. This difference is mainly due to the treatment of the interface between the specimen and the bar. Indeed, the model doesn't take into account the effects of the fasteners and the holes in the specimen which can be sources of distortions in the reflection of the wave.

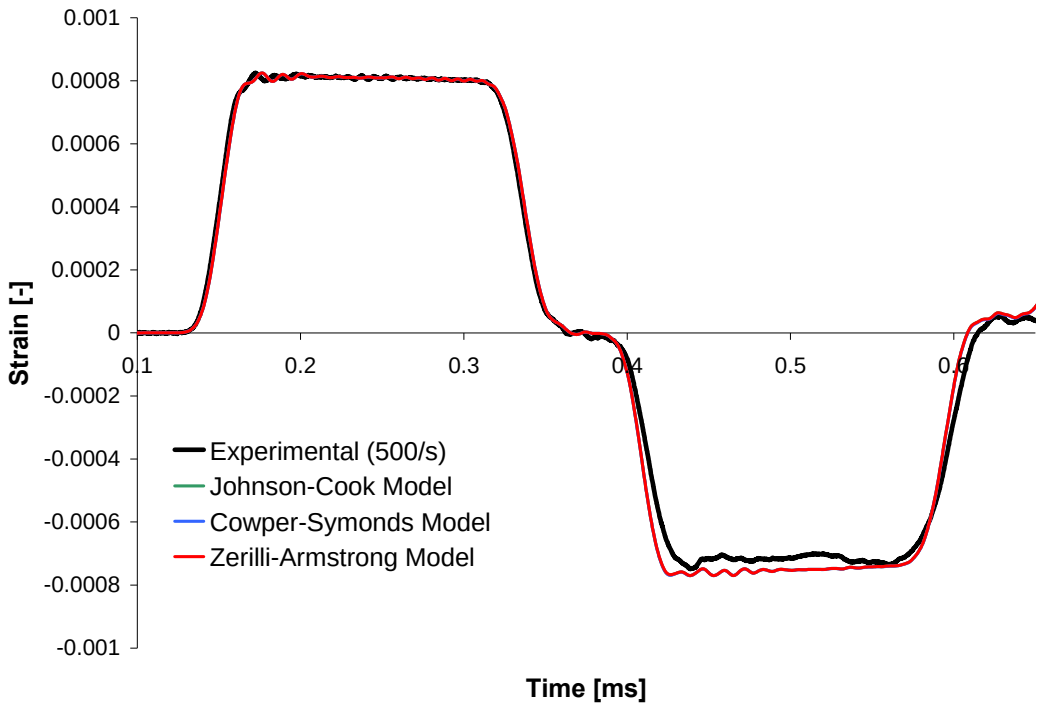

Figure 6.7: Comparison of the strain histories in the incident bar for AZ31B-O at nominal strain rate of $500s^{-1}$

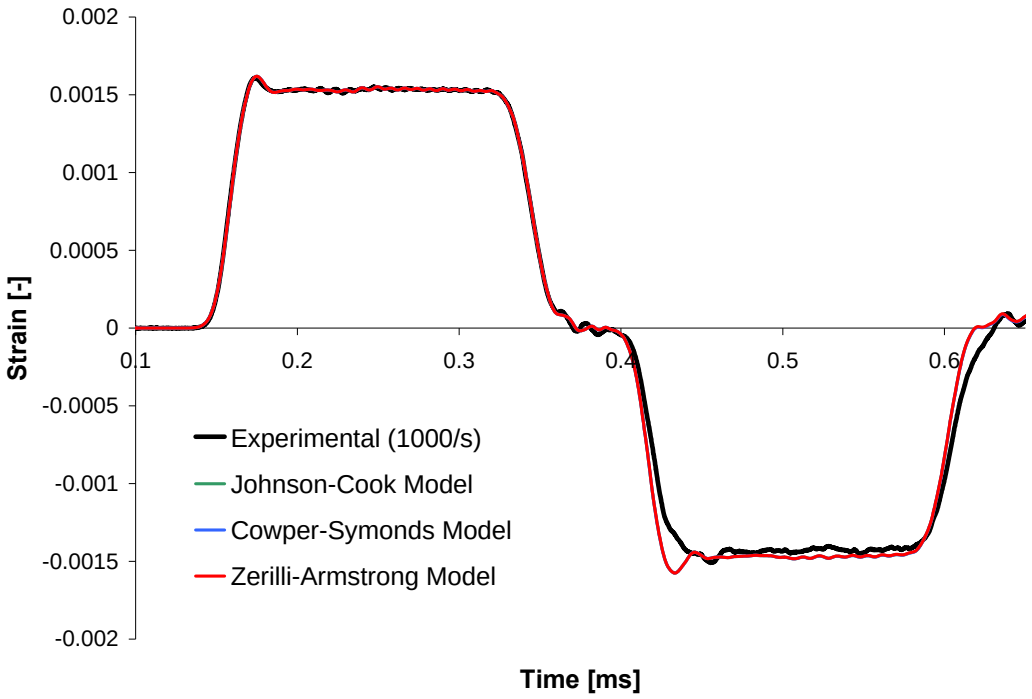

Figure 6.8: Comparison of the strain histories in the incident bar for AZ31B-O at nominal strain rate of $1000s^{-1}$

The comparison of the transmitted waves can be seen in Figure 6.9 and Figure 6.10 for the room temperature simulations at $500s^{-1}$ and $1000s^{-1}$, respectively. As seen in the figures, the Johnson-Cook and Cowper Symonds models have a very similar response, only the unloading of the sample behaves differently between the two models. The Zerilli-Armstrong model shows a higher magnitude in the transmitted wave, and is closer to the experimental wave while the specimen is loaded, especially for the $1000s^{-1}$ simulations. The unloading of the $500s^{-1}$ experimental data is underestimated by the three models. However, during the unloading of the sample at $1000s^{-1}$, all the models overestimate the strain level. This can be explained by the lack of damage consideration in the simulations. Indeed, based on Equation (1.20), the transmitted wave is proportional to the stress in the sample; and Figure 6.14 shows that the experimental unloading occurs after the UTS for the $1000s^{-1}$ data at room temperature. The stress is thus reduced by the necking of the specimen, which is not captured by the simulations.

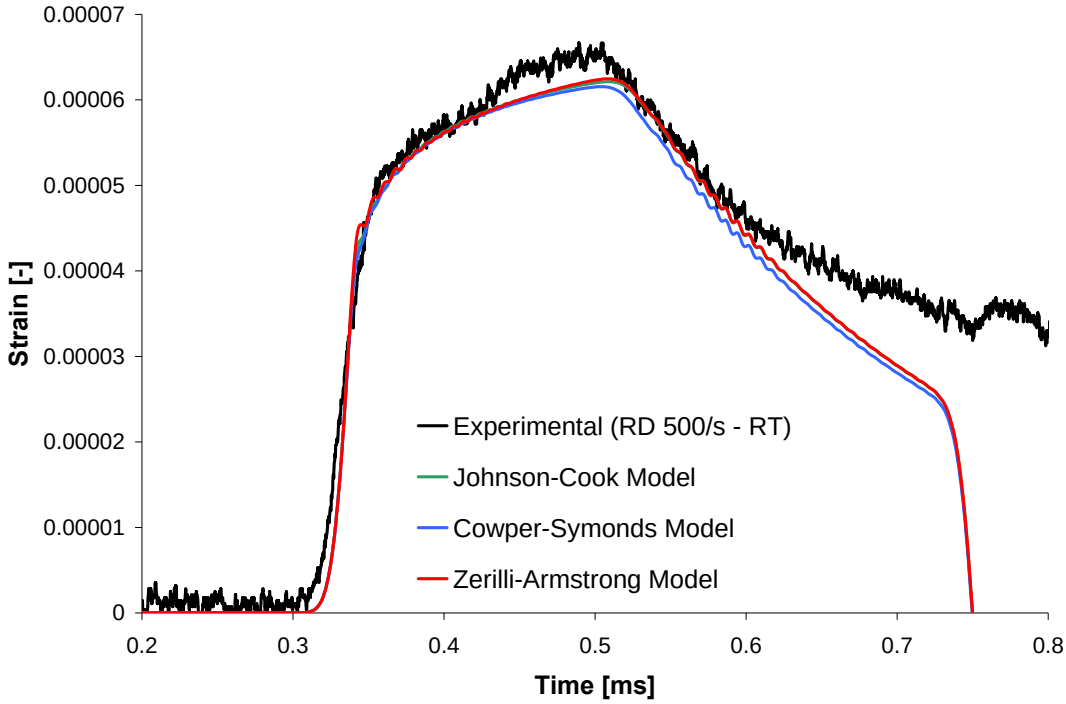

Figure 6.9: Comparison of the strain histories in the transmitted bar for the $500s^{-1}$ simulations at room temperature

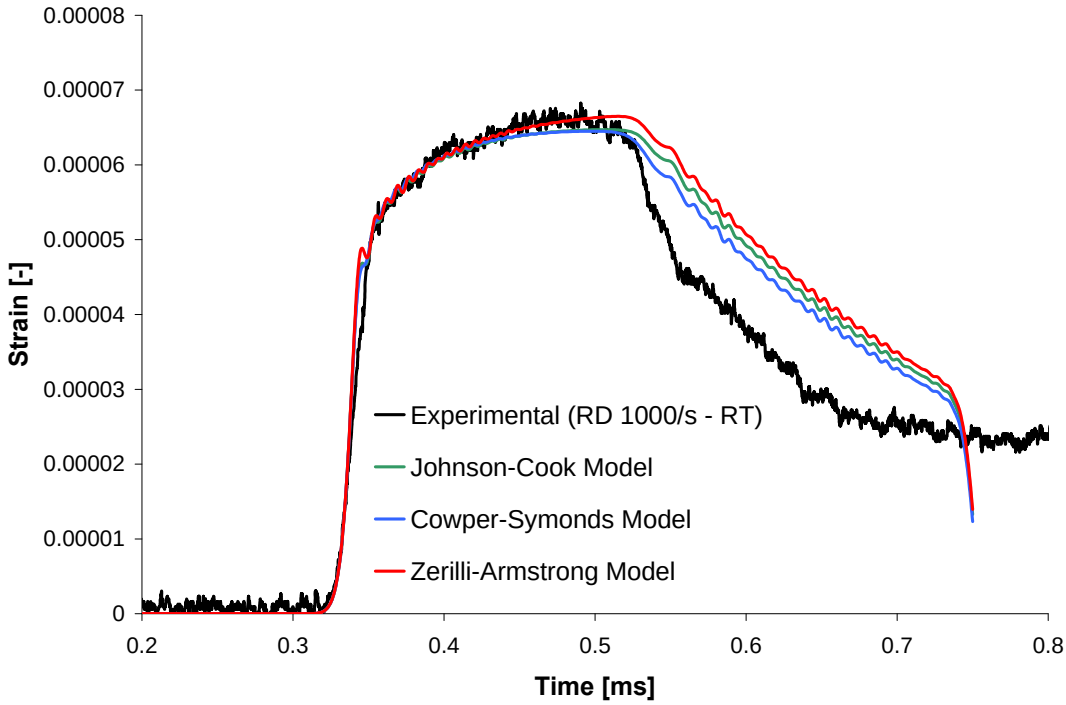

Figure 6.10: Comparison of the strain histories in the transmitted bar for the $1000s^{-1}$ simulations at room temperature

The comparison of the predicted transmitted waves at elevated temperature can be seen in Figure 6.11 and Figure 6.12 for the 150°C and 250°C simulations, respectively. Once again, the Zerilli-Armstrong predictions are better than those of the two other models, especially at 250°C. However, the three models fail to predict the necking of the specimen and its fracture was not captured since no failure criterion was considered in the simulations.

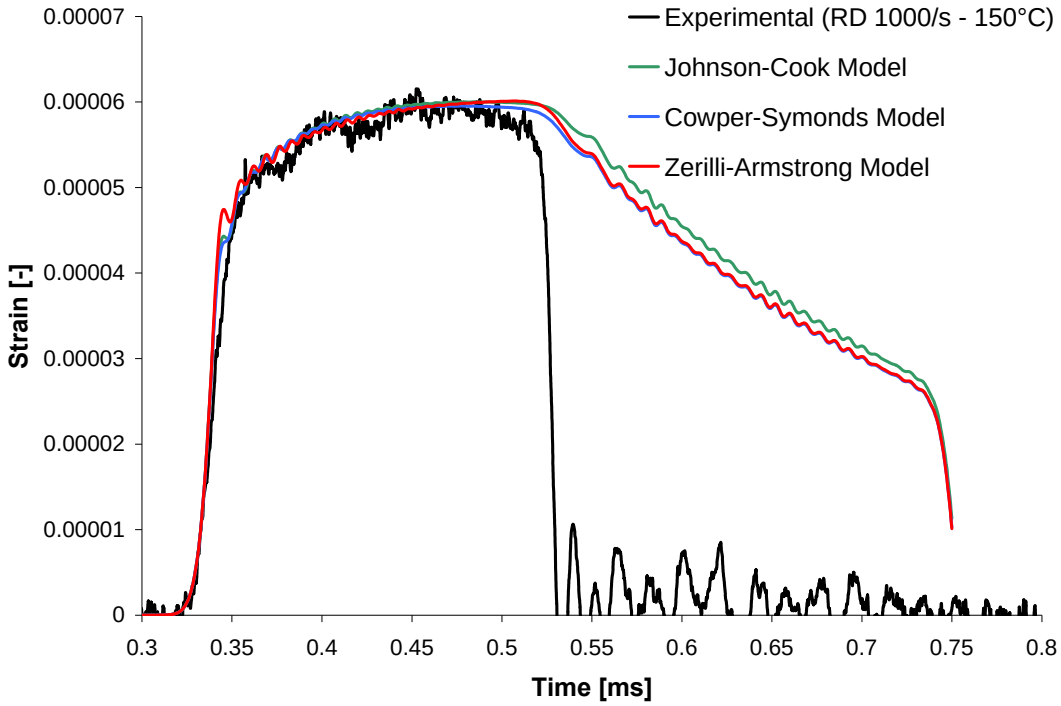

Figure 6.11: Comparison of the strain histories in the transmitted bar for the 1000s^{-1} simulations at 150°C

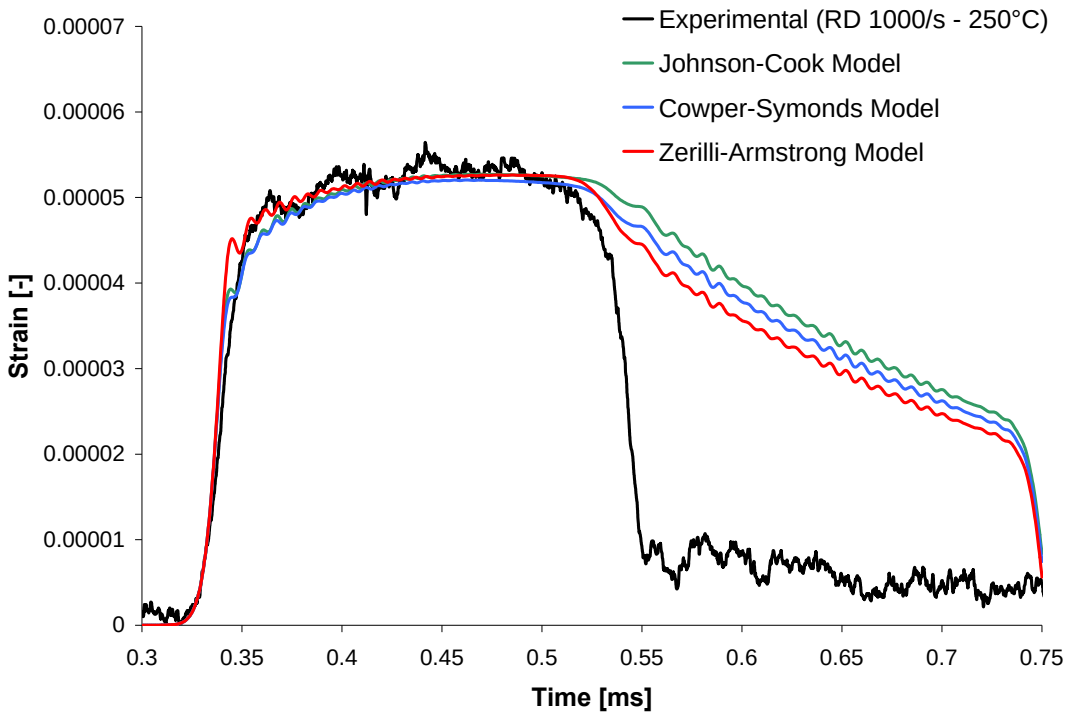

Figure 6.12: Comparison of the strain histories in the transmitted bar for the 1000s^{-1} simulations at 250°C

Each simulation was then processed as an actual experiment using the strain histories in the bars. The engineering stress-strain curves were then compute and compared to the experimental results, as seen in Figure 6.13 and Figure 6.14 for the room temperature simulations. As expected, the Johnson-Cook and Cowper-Symonds models show a similar engineering stress-strain curve, with a slight difference in the unloading behavior. One can also notice that they both underestimate the experimental curves, especially at 1000s^{-1}. For the 500s^{-1} simulations, the three models predict similar results, and all slightly underestimate the experimental engineering stress-strain curve after 6% strain. On the other hand, for the 1000s^{-1} simulations, the Zerilli-Armstrong model shows an engineering stress-strain curves that is very close to the experimental one, with an overestimation of the curve after the UTS as the necking was not captured in the simulation.

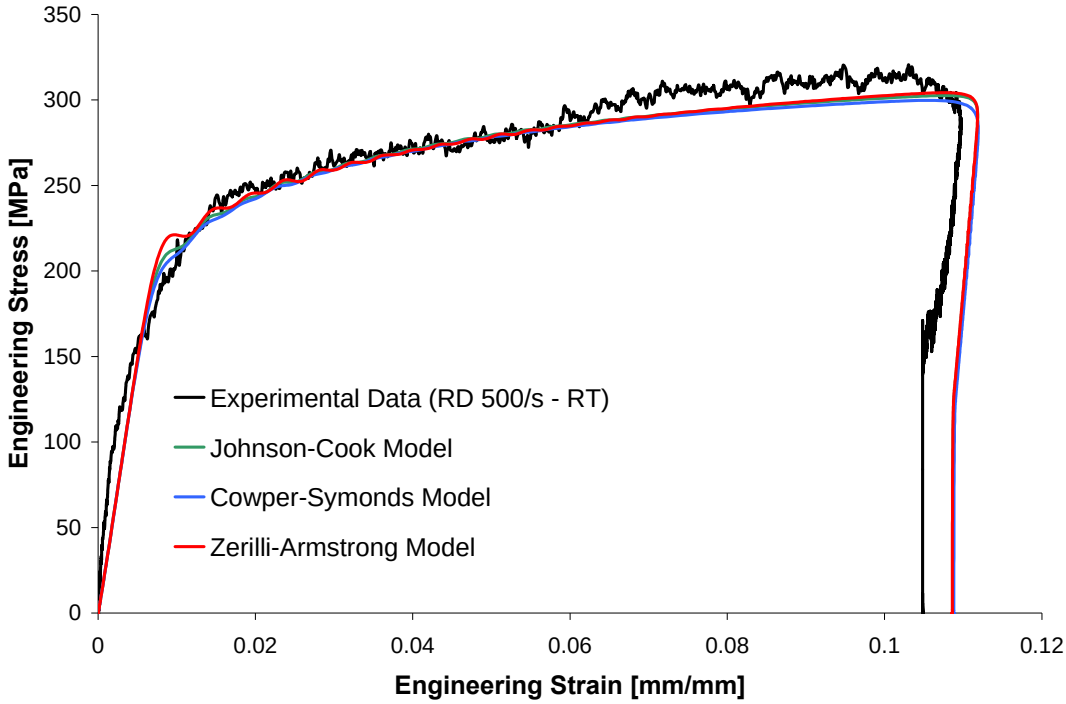

Figure 6.13: Comparison of the experimental and numerical engineering stress-strain curves for AZ31B-O in the RD at room temperature and nominal strain rate of 500/s

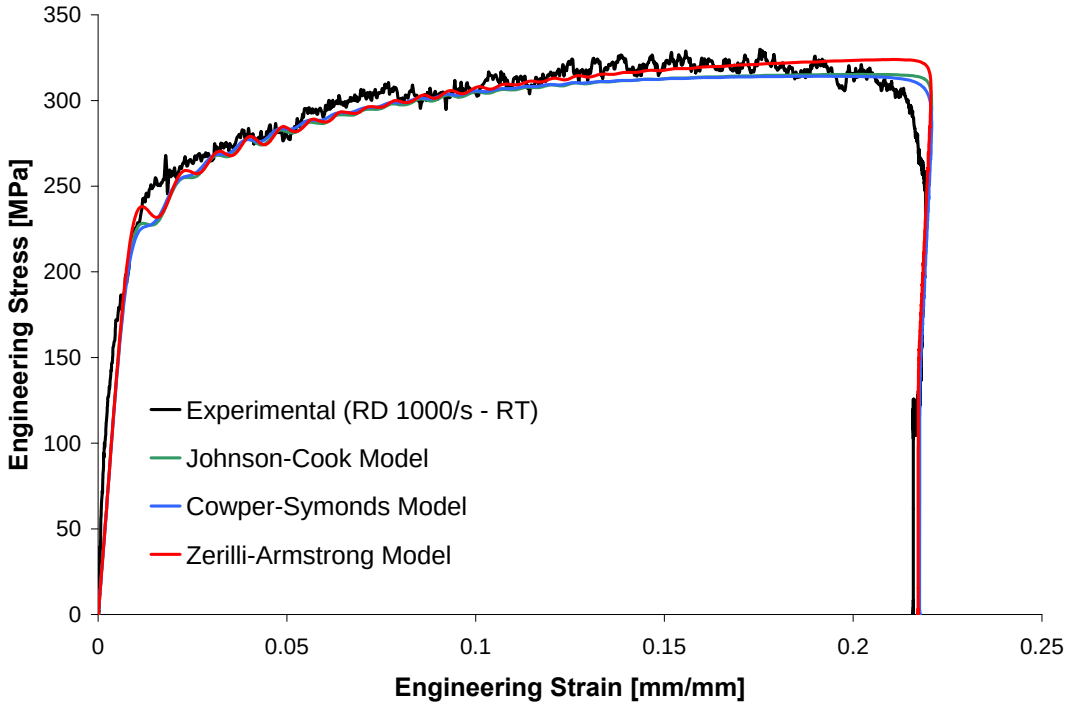

Figure 6.14: Comparison of the experimental and numerical engineering stress-strain curves for AZ31B-O in the RD at room temperature and nominal strain rate of $1000s^{-1}$

The comparison of the engineering stress-strain curves are given in Figure 6.15 for the 150°C and 250°C simulations. No significant difference in the prediction of the three models was seen for the 150°C simulations. They all show very good estimation of the engineering stress-strain curve prior to the UTS, and overestimate the stress level once necking occurs in the experimental data. For the 250°C simulations, the Zerilli-Armstrong model is the only one to capture accurately the stress level at low strain values. However, once again necking was not captured by any of the models.

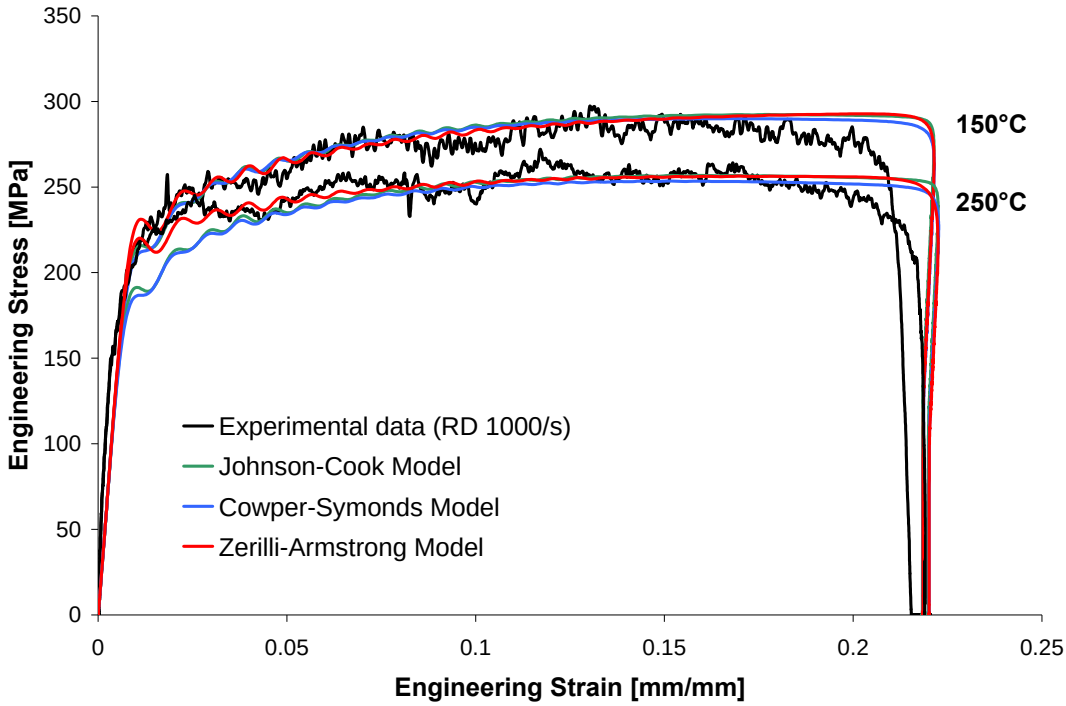

Figure 6.15: Comparison of the experimental and numerical engineering stress-strain curves for AZ31B-O in the RD at 150°C and 250°C at nominal strain rate of $1000s^{-1}$

6.4 Mesh Effect on the Necking Predictions

As seen in previous section, the models failed to capture necking during the TSHB simulations. The maximum strain that can be reached during a TSHB experiment is determined by the duration of the incident pulse, as explained in Section 1.3.1. In order to reach higher strains, a new finite element model was created. In this model, only the gauge region of the specimen

was modeled. Furthermore, due to the symmetry in the geometry of the specimen, only a quarter-model is required for the simulations. Since the Zerilli-Armstrong model is the most accurate to predict the constitutive behavior of AZ31B, this constitutive model was used to capture the necking of the specimen. Deformation at room temperature and a strain rate of $1000s^{-1}$ along the RD was considered for this necking analysis.

In order to assess the effect of the mesh on the necking prediction, two meshes were considered. The "coarse" mesh has an average element size of 0.25 mm. This corresponds to 4 element layers in the thickness and 4 element layers in the width of the specimen, which is similar to the specimen mesh used in the TSHB simulations. The "fine" mesh has an average element size of 0.1 mm, which provides 8 element layers in the thickness and 9 element layers in the width of the specimen. The two meshes can be seen in Figure 6.16.

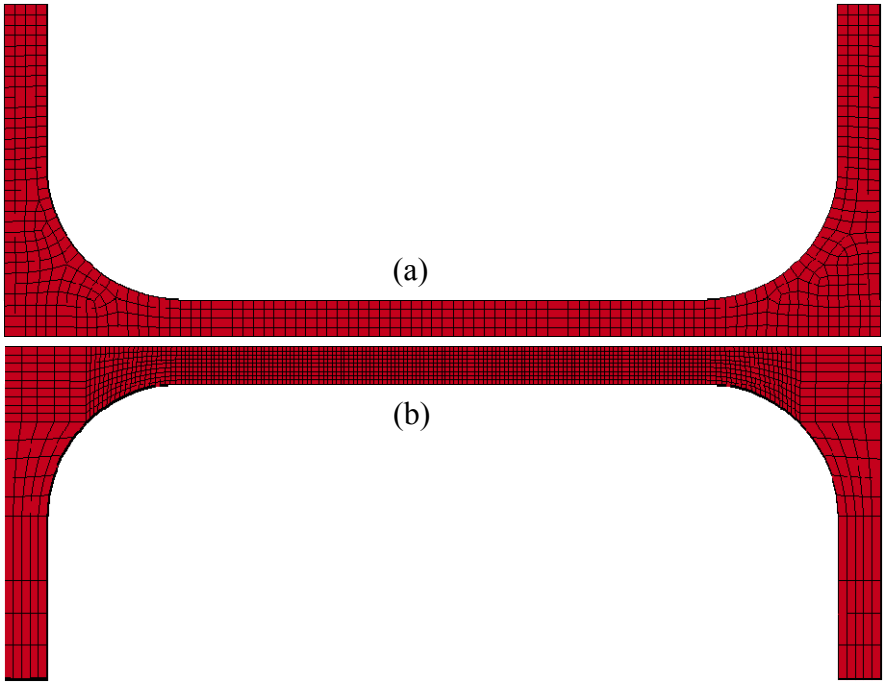

Figure 6.16: Different specimen mesh considered: (a) coarse mesh and (b) fine mesh

At one end of the sample, a constant velocity of 12.5 m/s was applied, which corresponds to a strain rate of $1000s^{-1}$ in the specimen. The other end was fully constrained to create uniaxial tension in the specimen. Since only a quarter-model was considered, symmetry boundary conditions were applied to the appropriate nodes.

Figure 6.17 shows the evolution of the plastic strain contour plots for the two meshes. The two simulations exhibit similar results up to 0.30ms. After 0.50ms, the localization in the specimen becomes clear and the two predictions are slightly different. The fine mesh presents a smaller necking region. However, it is difficult to graphically determine the onset of necking in the two simulations.

In order to estimate the onset of necking, the Considère criterion was applied to the two simulations using the same method as described in Section 4.2 and Section 4.3. The Considère criterion is illustrated in Figure 6.18 and Figure 6.19 for the coarse mesh and the fine mesh simulations, respectively. The two simulations show only 0.3 % strain difference regarding the predicted Considère strains. Therefore, the mesh of the specimen doesn't seem to affect the Considère prediction of the onset of necking in the simulations

.

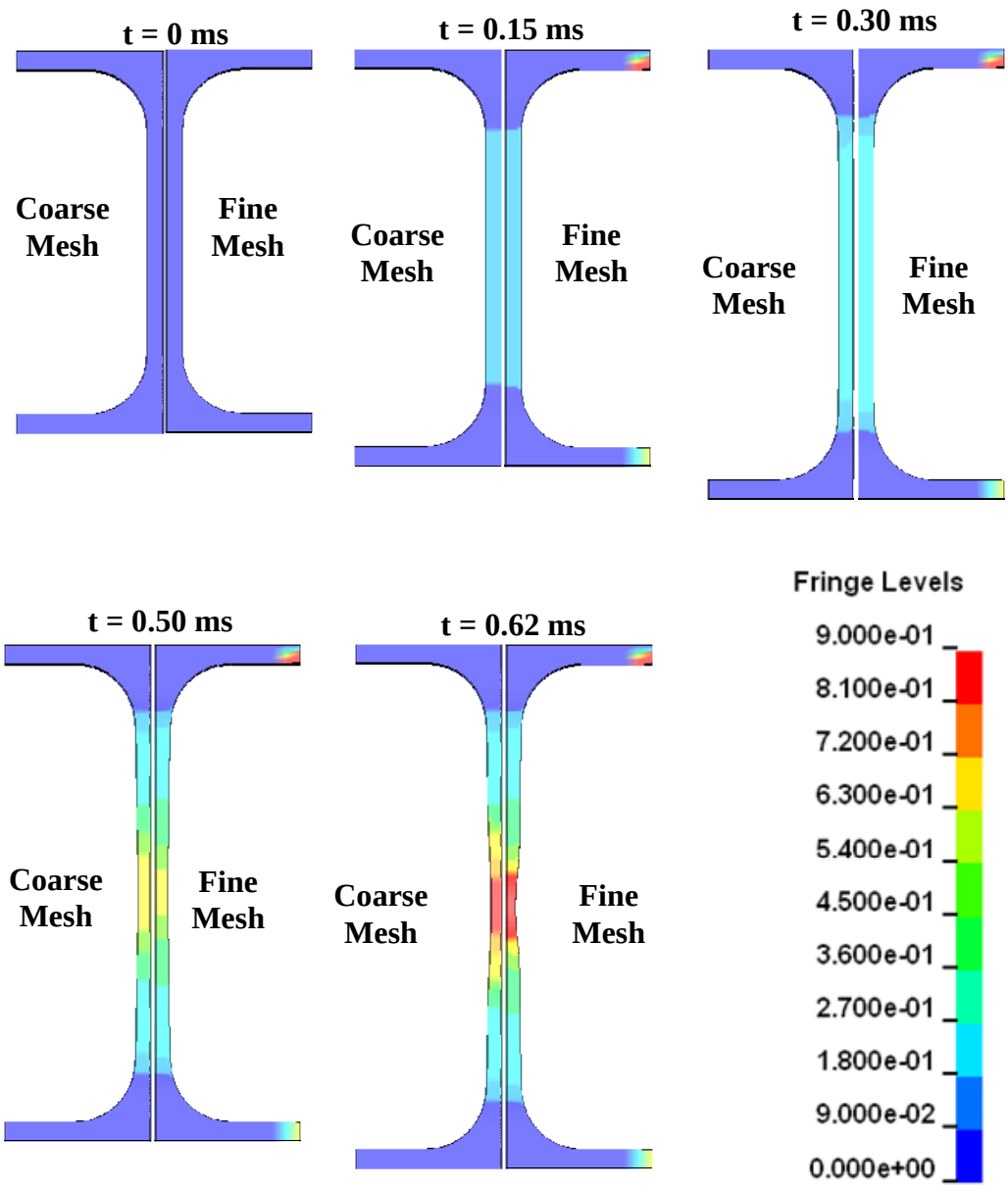

Figure 6.17: Contour plots of the plastic strain for the coarse and fine meshes

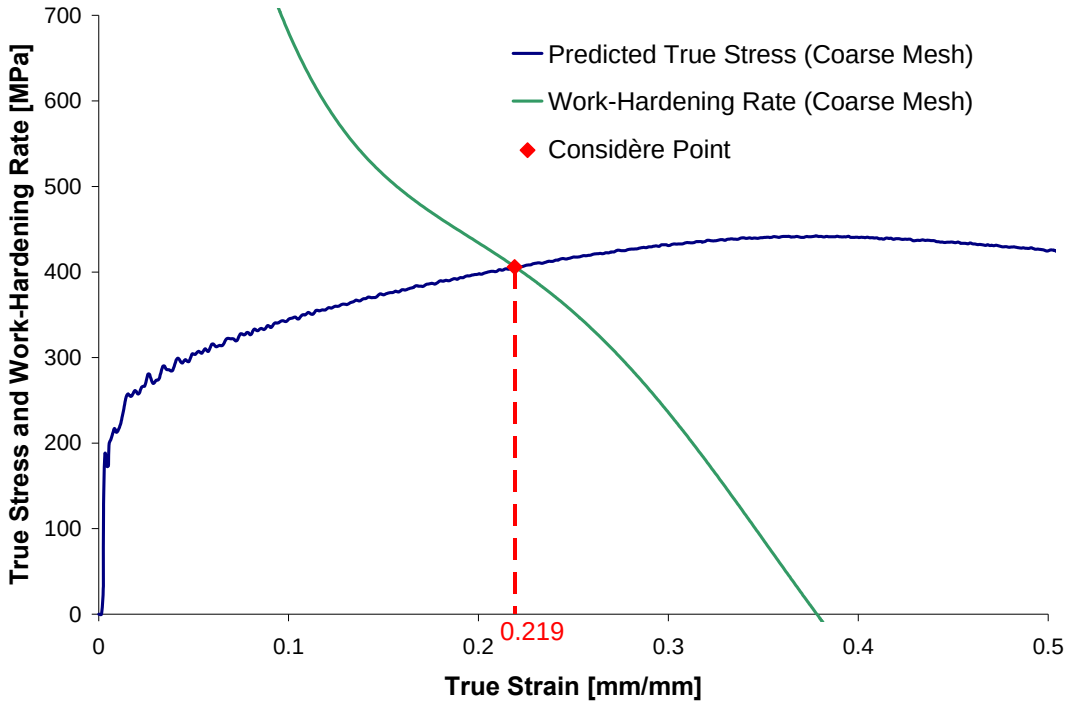

Figure 6.18: Considère criterion applied to the coarse mesh predictions

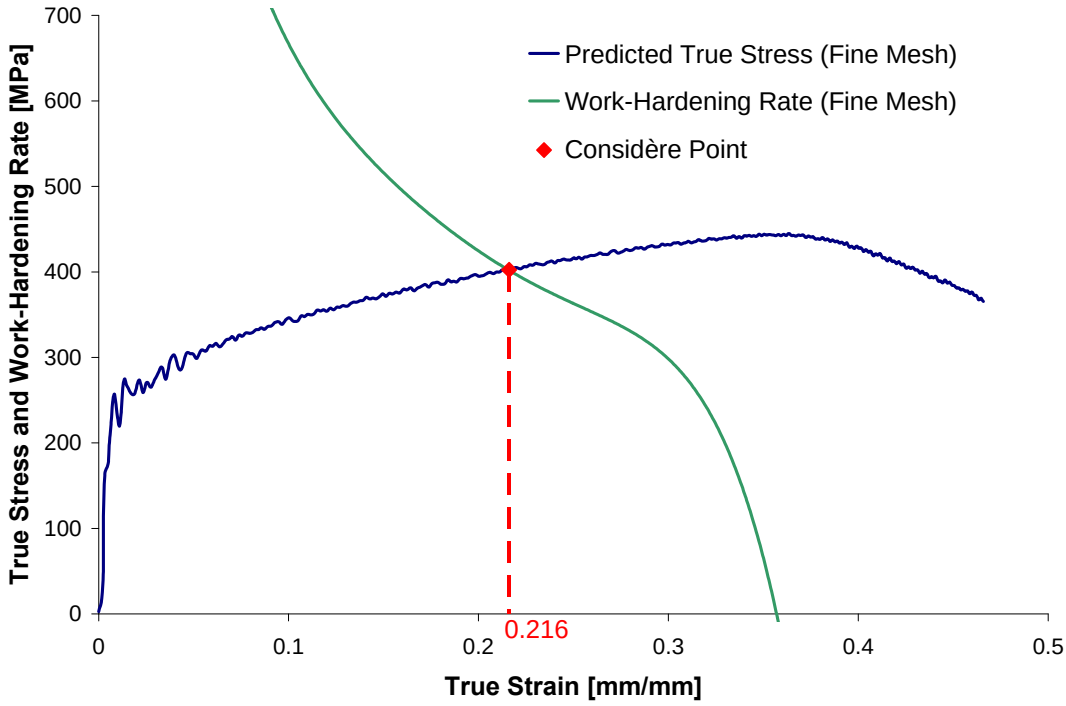

Figure 6.19: Considère criterion applied to the fine mesh predictions

The comparison of the experimental and predicted engineering stress-strain curves is shown in Figure 6.20. As seen in the figure, the two predictions are similar up to 45% engineering strain, which includes the onset of necking in the two simulations. After 45% strain, the fine mesh localize faster than the coarse mesh, resulting in a more important drop in the stress level. The Considère prediction of the onset of necking in the two simulations appears at approximately 24% engineering strain. However, the experimental onset of necking was found to occur at 16% engineering strain, as calculated in Section 4.3 for this testing condition. Therefore, the Zerilli-Armstrong model overestimates the onset of necking by 8% strain. This result was seen for the coarse and the fine meshes, thus the mesh of the sample is not responsible for the lack of necking prediction seen in the TSHB simulations. Therefore, a damage criterion may be needed to accurately predict the necking in the specimen.

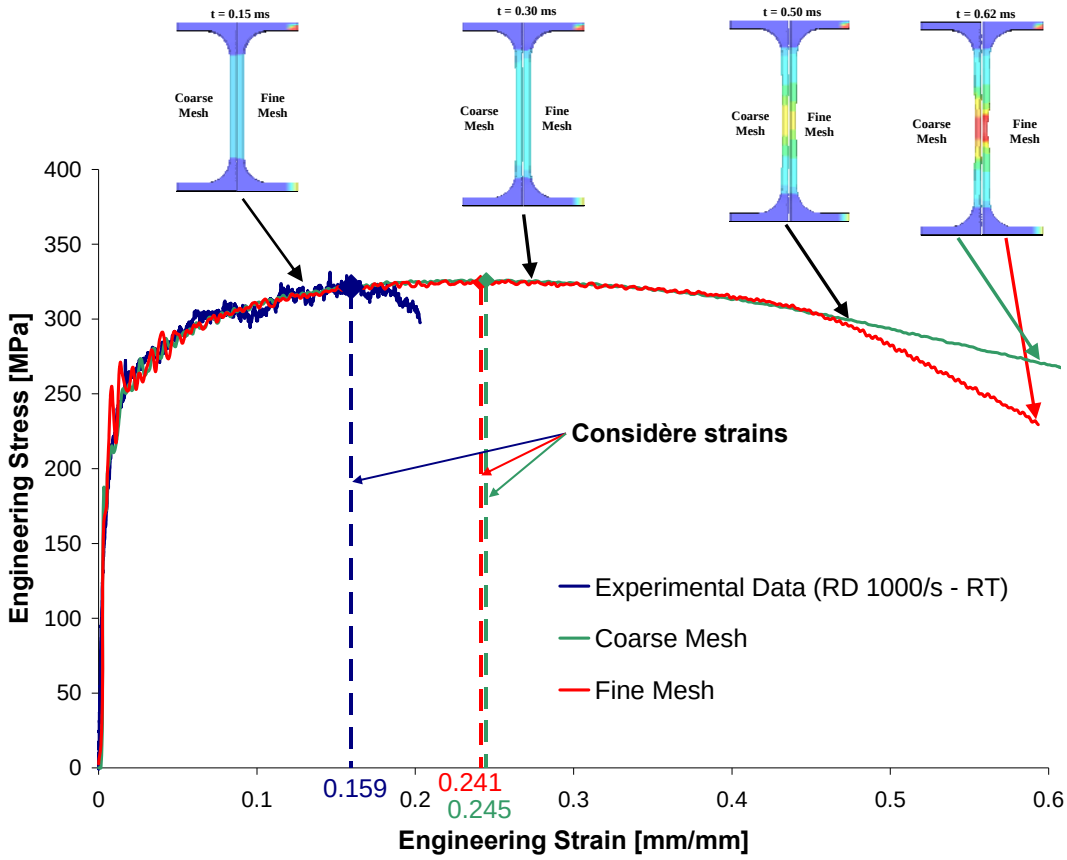

Figure 6.20: Experimental and predicted onset of necking

7 DISCUSSION

Magnesium alloy AZ31B in both the O and H24 tempers presents significant strain rate sensitivity, as seen in Figure 7.1. Over the range of strain rate considered ($0.003s^{-1}$ to $1500s^{-1}$), the two tempers show a similar amount of rate-strengthening, with the stress level at 5% plastic strain increased by approximately 60-65 MPa. However, since the H24 material was work-hardened during its forming process, it has a higher strength than the O-temper material. It was also found that for both temper conditions, the strain rate sensitivity changes with increasing strain rate. There is a threshold strain rate of approximately $100s^{-1}$ at which there is a clear increase in the strain rate sensitivity. For other metals, an increase in strain rate sensitivity is usually seen for strain rates above 10^4s^{-1}, as explained by Meyers [23] and reviewed in Section 1.2 of this thesis. Further investigation of the deformation mechanisms are thus needed to assess if thermally activated dislocation motions are still predominant, or if other mechanisms such as twinning could be responsible for the heightened rate sensitivity above $100s^{-1}$.

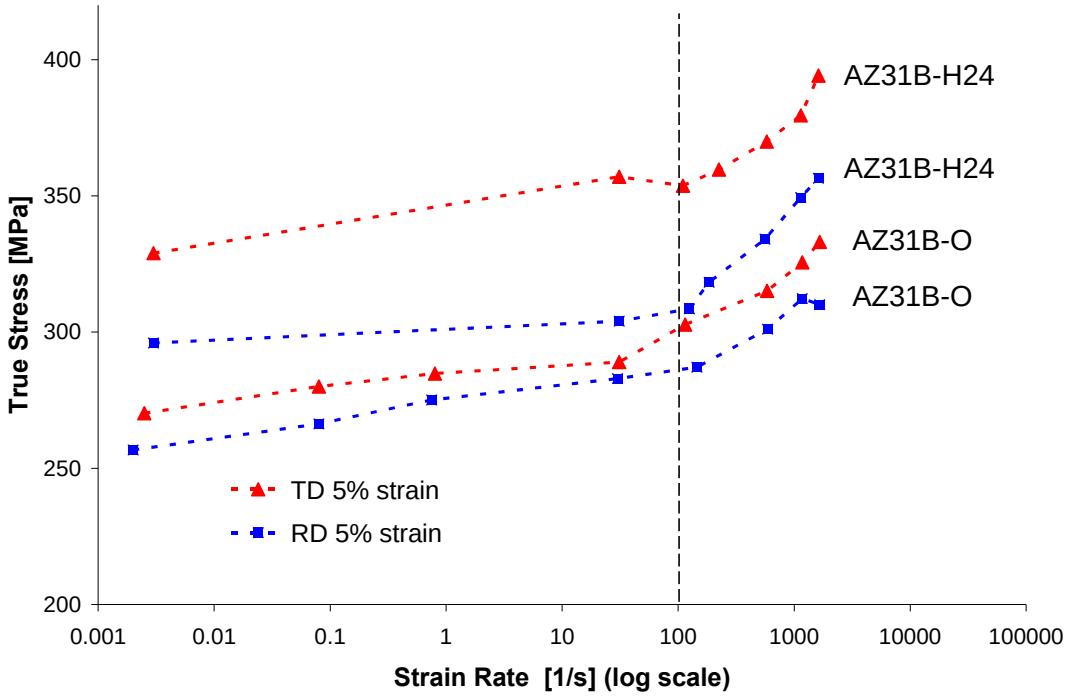

Figure 7.1: Comparison of the strain rate sensitivity of AZ31B-H24 and AZ31B-O at room temperature

AZ31B exhibits a strong in-plane anisotropy for both tempers. In both cases, the TD has a higher stress level than the RD. The strength difference was found to be approximately 15 MPa and 35 MPa for the O temper and H24 temper, respectively. The increase in strain rate doesn't have a significant effect on the anisotropy of the two materials, since the two directions show a fairly constant stress difference as the strain rate varies. For each material, the two directions also show a similar work-hardening rate, which doesn't seem to be strain rate dependent.

In the elevated temperature tests at high strain rates, a clear thermal softening can be seen for the two materials. As seen in Figure 7.2, the H24 temper is more affected by temperature, with an average softening of 50 MPa from room temperature to 150°C, and up to 125 MPa at 300°C, whereas the O temper material is softened by 25 MPa and 55 MPa for the corresponding temperature rise. Since the elevated temperature experiments were performed at high strain rates, the stress levels remain high. The work-hardening rate is slightly affected by the temperature, with a decrease in the work-hardening rate as temperature increases. However, the temperature doesn't have a significant effect on the strain rate sensitivity of the materials. A larger range of strain rates should be considered to fully estimate the effect of temperature on the strain rate sensitivity and also to further study the evolution of the $100s^{-1}$ threshold seen at room temperature.

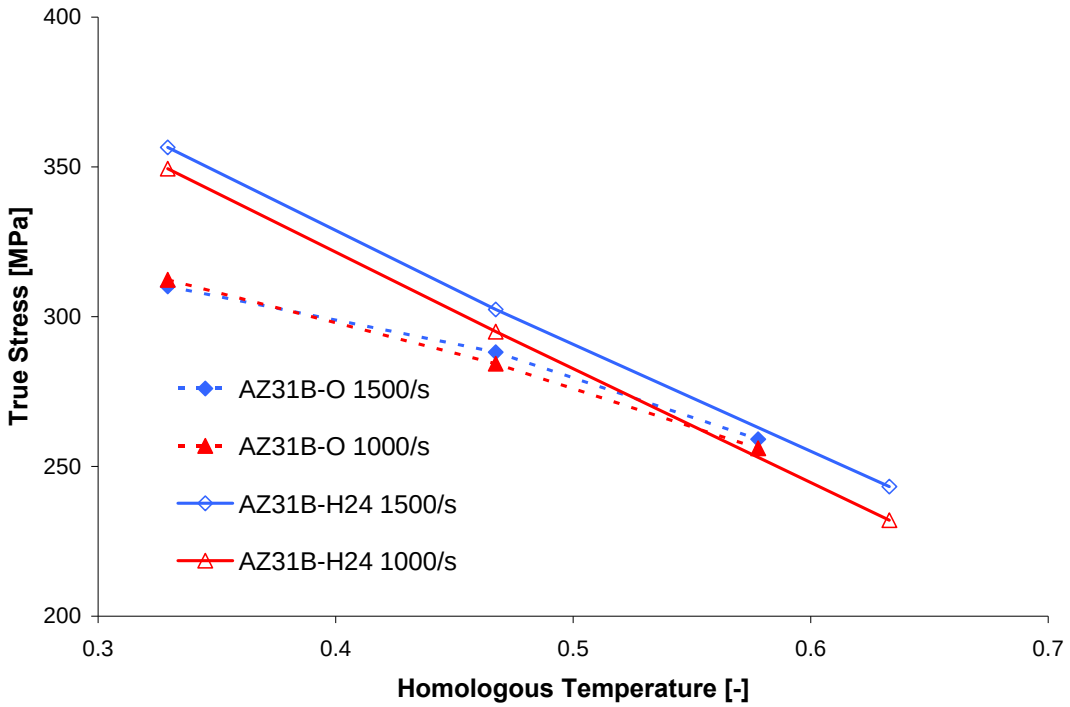

Figure 7.2: Comparison of the thermal softening of AZ31B-H24 and AZ31B-O at 5% plastic strain in the RD

Three thicknesses of AZ31B-O were studied. The thickness of the material had a mild effect on its constitutive behavior. At quasi-static rates, the strength of the material increases as the thickness increases. This effect was also seen at high strain rates, even if oscillations in the data prevented strong conclusions based on the results. Over the range of strain rates considered, the difference of stress level remains fairly constant, with a difference of approximately 10-15 MPa between the 1.0mm and 2.5mm sheets. Once again, the microstructure of the different materials should be investigated to see if the grain sizes or orientations are responsible for this different behavior in the three sheets.

For the two material conditions, the strain to failure and onset of necking were investigated. The failure strain was obtained from the engineering stress-strain curves, while the onset of necking was determined using the Considère criterion. The two tempers exhibit different necking and failure behavior. For strain rates below $1s^{-1}$, the O-temper material shows a decrease in ductility as the strain rate increases, whereas at high strain rates, there is a clear improvement in the ductility of the material. An increase of almost 6% in the strain to failure

was seen between $0.003s^{-1}$ and $1500s^{-1}$ data. This effect was seen for both the strain to failure and the onset of necking. This result is similar to what was found by Tan *et al.* [30] who performed tensile tests at strain rates up to $10s^{-1}$, and by Ulacia [35] for high strain rates. Temperature rise has almost no effect on the elongation of AZ31B-O deformed at high strain rates. The H24 material shows a different response regarding its ductility. Indeed, there is no significant effect of strain rate on its ductility, and an increase in both failure strain and necking strain was only seen for the 300°C experiments. Yokoyama [79] reported a similar behavior of extruded AZ31B-F at room temperature, F-temper material indicating "as fabricated" material, thus without any annealing treatment.

Constitutive parameters for three constitutive models (Johnson-Cook, modified Johnson-Cook with Cowper-Symonds formulation, and Zerilli-Armstrong) were obtained from the experimental data. The BCC Zerilli-Armstrong form was considered since its HCP version is not implemented in the finite element code used in the current research. It was found that the Zerilli-Armstrong model provided a superior fit to the measured data than was obtained using the other models. The reason for this difference is that the Johnson-Cook doesn't capture the change of strain rate sensitivity as the strain rate increases; and its modified form with a Cowper-Symonds strain rate formulation doesn't include a thermal effect on the work-hardening rate. Due to their multiplicative forms, those two models also present a strain rate dependence of the work-hardening rate, which was not seen in the experimental data at room temperature.

Numerical models of the TSHB experiments were created to assess the different constitutive models. The three models predict similar and accurate strain histories in the incident bar. The transmitted wave changes from one model to the other. As expected, the Zerilli-Armstrong model shows the best predictions at both room and elevated temperatures. However, the models failed to capture the necking of the material. Furthermore, the influence of element size on the onset of necking was investigated, and it was found that the adopted mesh doesn't seem to affect the onset of necking. Therefore, the models may be enhanced by a damage criterion to accurately predict the necking and failure of the specimen.

8 CONCLUSIONS AND FUTURE WORK

8.1 Conclusions

Several conclusions can be drawn from this work:

- AZ31B magnesium alloy sheet presents a significant and positive strain rate sensitivity over the complete range of strain rates in both the O and H24 tempers, with an average increase of 60-65 MPa for both material conditions.
- Each temper exhibits an increase in strain rate sensitivity as the strain rate increases. This sensitivity was seen to behave differently for strain rates below and above $100s^{-1}$.
- Each material displayed a thermal softening response at high strain rates. From room temperature to 150°C, the loss in strength at 5% plastic strain was found to be 25 MPa and 55 MPa for the AZ31B-O and AZ31B-H24 materials, respectively. The H24 condition exhibited a higher temperature sensitivity than the O-temper.
- For each material, a difference in strength between the rolling and the transverse directions was seen; the TD being at a higher stress level than the RD. The difference between the two directions was approximately 15 MPa and 35 MPa for the O-temper and H24 materials, respectively. This difference did not change significantly over the range of strain rates considered.
- The ductility of AZ31B-O decreases with increasing strain rates below $1s^{-1}$, and increases under high strain rate deformations. The AZ31B-H24 material demonstrated no effect of strain rate on ductility. For both material conditions, temperature has little effect on ductility at high strain rates, for the range of test temperature considered.
- The AZ31B-O flow curves exhibited a mild dependence on sheet thickness. As the thickness increases from 1.0mm to 2.5mm, the strength of the material increased of approximately 10-15 MPa in both sheet directions. However, similar strain rate sensitivity was seen for the three thicknesses.
- The Zerilli-Armstrong constitutive model was found to be more accurate in predicting the flow stress of AZ31B-O and AZ31B-H24 within the range of strain rates and temperatures considered. The effectiveness of these fits was confirmed by TSHB simulations; however, the model failed to predict necking.

8.2 Future Work

The work presented in this thesis provided some insight into the constitutive behavior of AZ31B magnesium alloy sheets over a large range of strain rates. In order to gain a better understanding of the mechanical behavior of these materials at high strain rates, the following work should be considered in the future:

- Microstructure evolution under different strain rates should be investigated to look at the effect of strain rate on the grain size and orientation. Deformation mechanisms should also be identified at different strain rates.
- In-plane compressive experiments should be carried out over a large range of strain rates to determine the evolution of the tension-compression asymmetry of the materials, as well as their anisotropy in compression.
- Damage criteria should be invesditaged for these materials to accurately predict necking and failure in the specimen.
- Ultimately, a finite element model should be implemented, taking into account the anisotropy and asymmetry of the material, as well as its strain rate and temperature dependence.

REFERENCES

[1] Cole G.S. Magnesium Vision 2020: A North American Automotive Strategic Vision of Magnesium. USAMP report 2007.

[2] Watarai H. Trends of research and development of magnesium alloys—reducing the weight of structural materials in motor vehicles. Sci. Technol. Trends 2006;18:84-97.

[3] Johnson G.R., Cook W.H. A Constitutive Model and Data for Metals Subjected to Large Strains, High Strain Rates, and High Temperatures. 7th international Symposium on Ballistics, Hague, Netherlands 1983:541-547.

[4] Johnson G.R., Cook W.H. Fracture characteristics of three metals subjected to various strains, strain rates, temperatures and pressures. Eng.Fract.Mech. 1985;21(1):31-48.

[5] Cowper G.R., Symonds P.S. Strain hardening and strain rate effects in the impact loading of cantilever beams. Brown University 1957.

[6] Zerilli F.J., Armstrong R.W. The effect of dislocation drag on the stress-strain behavior of F.C.C. metals. Acta Metallurgica et Materialia 1992 8;40(8):1803-1808.

[7] Zerilli F.J., Armstrong R.W. Dislocation-mechanics-based constitutive relations for material dynamics calculations. J.Appl.Phys. 1987 March 1, 1987;61(5):1816-1825.

[8] Zerilli F., J., Armstrong R., W. Dislocation Mechanics Based analysis of Material Dynamics Behavior : Enhanced Ductility, Deformation Twinning, Shock Deformation, Shear Instability, Dynamic Recovery. J.Phys.IV France 1997 /8;07:C3-637; C3-642.

[9] Hallquist J.O. LS-DYNA Theory Manual. Livermore Software Technology Corporation March 2006.

[10] Technology of Magnesium and Magnesium Alloys. Magnesium Technology 2006:219-430.

[11] Mordike B., Lukac P. Physical Metallurgy. Magnesium Technology 2006:63-107.

[12] Lou X.Y., Li M., Boger R.K., Agnew S.R., Wagoner R.H. Hardening evolution of AZ31B Mg sheet. Int.J.Plast. 2007 1;23(1):44-86.

[13] Yoo M. Slip, twinning, and fracture in hexagonal close-packed metals. Metallurgical and Materials Transactions A 1981 03/01;12(3):409-418.

[14] Koike J., Kobayashi T., Mukai T., Watanabe H., Suzuki M., Maruyama K., et al. The activity of non-basal slip systems and dynamic recovery at room temperature in fine-grained AZ31B magnesium alloys. Acta Materialia 2003 4/18;51(7):2055-2065.

[15] Beausir B., Toth L.S., Qods F., Neale K.W. Texture and Mechanical Behavior of Magnesium During Free-End Torsion. 2009;131(1).

[16] Agnew S.R., Yoo M.H., Tomé C.N. Application of texture simulation to understanding mechanical behavior of Mg and solid solution alloys containing Li or Y. Acta Materialia 2001 12/3;49(20):4277-4289.

[17] Styczynski A., Hartig C., Bohlen J., Letzig D. Cold rolling textures in AZ31 wrought magnesium alloy. Scr.Mater. 2004 4;50(7):943-947.

[18] Jeong H.T., Ha T.K. Texture development in a warm rolled AZ31 magnesium alloy. J.Mater.Process.Technol. 2007 6/12;187-188:559-561.

[19] He Z., Ma J., Wang H., Tan G.E.B., Shu D., Zheng J. Dynamic fracture behavior of layered alumina ceramics characterized by a split Hopkinson bar. Mater Lett 2005 4;59(8-9):901-904.

[20] Dong S., Wang Y., Xia Y. A finite element analysis for using Brazilian disk in split Hopkinson pressure bar to investigate dynamic fracture behavior of brittle polymer materials. Polym.Test. 2006 10;25(7):943-952.

[21] Li Q.M., Meng H. About the dynamic strength enhancement of concrete-like materials in a split Hopkinson pressure bar test. Int.J.Solids Structures 2003 1;40(2):343-360.

[22] Van Sligtenhorst C., Cronin D.S., Wayne Brodland G. High strain rate compressive properties of bovine muscle tissue determined using a split Hopkinson bar apparatus. J.Biomech. 2006;39(10):1852-1858.

[23] Meyers M.A. Dynamic behavior of materials. New York: Wiley; 1994.

[24] Campbell J.D., Ferguson W.G. The temperature and strain-rate dependence of the shear strength of mild steel. Philosophical Magazine 1970;21(169):63.

[25] Boyce B.L., Dilmore M.F. The dynamic tensile behavior of tough, ultra-high-strength steels at strain-rates from 0.0002s−1 to 200s−1. Int.J.Impact Eng. 2009 200902;36(2):263-271.

[26] Follansbee P.S., Weertman J. On the question of flow stress at high strain rates controlled by dislocation viscous flow. Mech.Mater. 1982 12;1(4):345-350.

[27] Lindholm U.S., Yeakley L.M., Nagy A. The dynamic strength and fracture properties of dresser basalt. International Journal of Rock Mechanics and Mining Sciences & Geomechanics Abstracts 1974 5;11(5):181-191.

[28] Ishikawa K., Watanabe H., Mukai T. High strain rate deformation behavior of an AZ91 magnesium alloy at elevated temperatures. Mater Lett 2005 5;59(12):1511-1515.

[29] Ishikawa K., Watanabe H., Mukai T. High temperature compressive properties over a wide range of strain rates in an AZ31 magnesium alloy. J.Mater.Sci. 2005 04/30;40(7):1577-1582.

[30] Tan C., Xu S., Wang L., Chen Z., Wang F., Cai H., et al. Deformation behavior of AZ31 magnesium alloy at different strain rates and temperatures. Trans.Nonferrous Met.Soc.China 2007 NOV;17:S347-S352.

[31] Li B., Joshi S., Azevedo K., Ma E., Ramesh K.T., Figueiredo R.B., et al. Dynamic testing at high strain rates of an ultrafine-grained magnesium alloy processed by ECAP. Materials Science and Engineering: A 2009 8/20;517(1-2):24-29.

[32] Mukai T., Mohri T., Mabuchi M., Nakamura M., Ishikawa K., Higashi K. Experimental study of a structural magnesium alloy with high absorption energy under dynamic loading. Scr.Mater. 1998 10/5;39(9):1249-1253.

[33] El-Magd E., Abouridouane M. Characterization, modelling and simulation of deformation and fracture behaviour of the light-weight wrought alloys under high strain rate loading. Int.J.Impact Eng. 2006 5;32(5):741-758.

[34] Tucker M.T., Horstemeyer M.F., Gullett P.M., El Kadiri H., Whittington W.R. Anisotropic effects on the strain rate dependence of a wrought magnesium alloy. Scr.Mater. 2009 2;60(3):182-185.

[35] Ulacia I., Dudamell N.V., Gálvez F., Yi S., Pérez-Prado M.T., Hurtado I. Mechanical behavior and microstructural evolution of a Mg AZ31 sheet at dynamic strain rates. Acta Materialia 2010 5;58(8):2988-2998.

[36] Hopkinson B. A Method of Measuring the Pressure Produced in the Detonation of High Explosives or by the Impact of Bullets. Proceedings of the Royal Society of London.Series A, Containing Papers of a Mathematical and Physical Character 1914 Jan. 1;89(612):411-413.

[37] Kolsky H. An Investigation of the Mechanical Properties of Materials at very High Rates of Loading. Proceedings of the Physical Society.Section B 1949;62(11):676.

[38] Davies E.D.H., Hunter S.C. The dynamic compression testing of solids by the method of the split Hopkinson pressure bar. J.Mech.Phys.Solids 1963;11(3):155-179.

[39] Gama B.A., Lopatnikov S.L., Gillespie J.W., Jr . Hopkinson bar experimental technique: A critical review. Appl.Mech.Rev. 2004 July 2004;57(4):223-250.

[40] Pochhammer L. On the Propagation Velocities of Small Oscillations in an Unlimited Isotropic Circular Cylinder. Journal fur die reine und angewandte Mathematik 1876 01/01;1876(81):324-336.

[41] Chree C. The Equations of an Isotropic Elastic Solid in Polar and Cylindrical Coordinates, Their Solutions and Applications. Cambridge Philosophical Society Transactions 1889;14:250-369.

[42] Davies R.M. A Critical Study of the Hopkinson Pressure Bar. Philosophical Transactions of the Royal Society of London.Series A, Mathematical and Physical Sciences 1948 Jan. 8;240(821):375-457.

[43] Davies R.M. Stress Waves in Solids. British Journal of Applied Physics 1956;7(6):203-209.

[44] Salisbury C. Spectral analysis of wave propagation through a polymeric Hopkinson Bar, MASc. Thesis, Waterloo, Ont.: University of Waterloo, Dept. of Mechanical Engineering; 2001.

[45] Yokoyama T., Kishida K. A novel impact three-point bend test method for determining dynamic fracture-initiation toughness. Exp.Mech. 1989 06/24;29(2):188-194.

[46] Lindholm U., Yeakley L. High strain-rate testing: Tension and compression. Exp.Mech. 1968 01/18;8(1):1-9.

[47] Nicholas T. Tensile testing of materials at high rates of strain. Exp.Mech. 1981 05/18;21(5):177-185.

[48] Nguyen C.H., Schindler H.J. On Spurious Reflection Waves in Hopkinson Bar Tensile Tests Using a Collar. J.Phys.IV France 1997;07(C3):3-85-3-90.

[49] Mouro P. Etude du comportement dynamique des tôles d'acier pour le calcul de crash, PhD Thesis,Ecole Polytechnique; 2002.

[50] Haugou G., Markiewicz E., Fabis J. On the use of the non direct tensile loading on a classical split Hopkinson bar apparatus dedicated to sheet metal specimen characterisation. Int.J.Impact Eng. 2006 5;32(5):778-798.

[51] LeBlanc M.M., Lassila D.H. Dynamic Tensile Testing of Sheet Material Using the Split-Hopkinson Bar Technique. Experimental Techniques 1993;17(1):37-42.

[52] Kang W.J., Cho S.S., Huh H., Chung D.T. Modified Johnson-Cook model for vehicle body crashworthiness simulation. Int.J.Veh.Des. 1999;21(4-5):424-435.

[53] Huh H., Kang W., Han S. A tension split Hopkinson bar for investigating the dynamic behavior of sheet metals. Exp.Mech. 2002 03/22;42(1):8-17.

[54] Smerd R., Winkler S., Salisbury C., Worswick M., Lloyd D., Finn M. High strain rate tensile testing of automotive aluminum alloy sheet. Int.J.Impact Eng. 2005 12;32(1-4):541-560.

[55] Bardelcik A., Salisbury C.P., Winkler S., Wells M.A., Worswick M.J. Effect of cooling rate on the high strain rate properties of boron steel. Int.J.Impact Eng. 2010 6;37(6):694-702.

[56] Thompson A.C., Salisbury C.P., Worswick M.J., Mayer R. Constitutive modelling of dual phase steel sheet and tube. Journal de Physique IV (Proceedings) 2006;134:281; 6-286.

[57] Winkler S., Thompson A., Salisbury C., Worswick M., Van Riemsdijk I., Mayer R. Strain Rate and Temperature Effects on the Formability and Damage of Advanced High-Strength Steels. Metallurgical and Materials Transactions A 2008 06/01/;39(6):1350-1358.

[58] Verleysen P., Degrieck J. Experimental investigation of the deformation of Hopkinson bar specimens. Int.J.Impact Eng. 2004 3;30(3):239-253.

[59] Staab G., Gilat A. A direct-tension split Hopkinson bar for high strain-rate testing. Experimental Mechanics 1991;31(3):232-235.

[60] Gilat A., Goldberg R.K., Roberts G.D. Experimental study of strain-rate-dependent behavior of carbon/epoxy composite. Composites Sci.Technol. 2002 8;62(10-11):1469-1476.

[61] Schwer L. Optional Strain-Rate Forms for the Johnson Cook Constitutive Model and the Role of the Parameter Epsilon_0. 6th German LS-Dyna Forum, Frankenthal, Germany 2007.

[62] Basinski Z.S. Thermally activated glide in face-centred cubic metals and its application to the theory of strain hardening. Philosophical Magazine 1959;4(40):393.

[63] Goldthorpe B.D. Constitutive Equations for Annealed and Explosively Shocked Iron for Application to High Strain Rates and Large Strains. J.Phys.IV 1991 10;01:C3-829; C3-835.

[64] Zerilli F.J., Armstrong R.W. Dislocation Mechanics Based Constitutive Relations for Materials Dynamics Modeling: Slip and Deformation Twinning in Iron. Shock Waves in Condensed Matter, Elsevier Science Publisher 1988:273.

[65] Holt W.H., Mock W., Zerilli F.J., Clark J.B. Experimental and computational study of the impact deformation of titanium Taylor cylinder specimens. Mech.Mater. 1994 199403;17(2-3):195-201.

[66] Zerilli F.J., Armstrong R.W. Constitutive equation for h.c.p. metals and high strength alloy steels. High strain rate effects on polymer, metal and ceramic matrix composites and other advanced materials, ASME 1995;48:121.

[67] Smerd R. Constitutive behavior of aluminum alloy sheet at high strain rates, MASc. Thesis, Waterloo, Ont.: University of Waterloo; 2005.

[68] Thompson A.C. High strain rate characterization of advanced high strength steels, MASc. Thesis, Waterloo, Ont.: University of Waterloo; 2006.

[69] Mason J.J., Rosakis A.J., Ravichandran G. On the strain and strain rate dependence of the fraction of plastic work converted to heat: an experimental study using high speed infrared detectors and the Kolsky bar. Mech.Mater. 1994 3;17(2-3):135-145.

[70] Macdougall D. Determination of the plastic work converted to heat using radiometry. Exp.Mech. 2000 09/18/;40(3):298-306.

[71] Rusinek A., Klepaczko J.R. Experiments on heat generated during plastic deformation and stored energy for TRIP steels. Mater Des 2009 1;30(1):35-48.

[72] Avedesian M.M., Baker H. Magnesium and magnesium alloys. Materials Park, OH: ASM International; 1999.

[73] Kolsky H. An Investigation of the Mechanical Properties of Materials at very High Rates of Loading. Proceedings of the Physical Society.Section B 1949;62(11):676.

[74] Dally J.W., Riley W.F. Experimental stress analysis. 3rd ed. New York ; Montréal: McGraw-Hill; 1991.

[75] Havner K.S. On the onset of necking in the tensile test. Int.J.Plast. 2004 5;20(4-5):965-978.

[76] Wilkinson L. MYSTAT: A personal version of SYSTAT. The American Statistician 1987(41):334.

[77] Dassault Systemes. SolidWorks 2007 SP3.1.

[78] Altair Engineering Inc. HyperMesh v. 10.0.

[79] Yokoyama T. Impact Tensile Stress–strain Characteristics of Wrought Magnesium Alloys. Strain 2003;39(4):167-175.

APPENDIX A: SPECIMEN CHARACTERISTICS

Material	Sample label	Initial Gauge Dimensions [mm]			Strain Rate [1/s]		Temperature [°C]
		Length	Width	Thickness	Nominal	Achieved	
AZ31B-H24 - 1.6mm - RD	RD1	12.5	1.74	1.575	0.003	0.0025	RT
	RD2	12.5	1.745	1.608	0.003	0.0025	RT
	RD4	12.5	1.729	1.573	0.003	0.0025	RT
	RD5	12.5	1.762	1.585	0.003	0.0025	RT
	RD15	12.5	1.75	1.57	30	30	RT
	RD16	12.5	1.74	1.59	30	31	RT
	RD19	12.5	1.75	1.58	30	32	RT
	RD12	12.5	1.763	1.657	100	125	RT
	RD13	12.5	1.758	1.584	100	121	RT
	RD14	12.5	1.747	1.588	100	127	RT
	RD2	12.5	1.752	1.611	200	220	RT
	RD5	12.5	1.743	1.585	200	221	RT
	RD7	12.5	1.736	1.652	200	218	RT
	RD11	12.5	1.737	1.577	500	570	RT
	RD12	12.5	1.756	1.57	500	560	RT
	RD13	12.5	1.748	1.567	500	550	RT
	RD3	12.5	1.735	1.574	1000	1130	RT
	RD9	12.5	1.761	1.584	1000	1140	RT
	RD10	12.5	1.743	1.58	1000	1140	RT
	RD8	12.5	1.748	1.572	1000	1150	150
	RD9	12.5	1.743	1.569	1000	1150	150
	RD10	12.5	1.738	1.572	1000	1150	150
	RD1	12.5	1.742	1.576	1000	1190	300
	RD2	12.5	1.755	1.57	1000	1180	300
	RD3	12.5	1.749	1.574	1000	1180	300
	RD14	12.5	1.732	1.572	1500	1620	RT
	RD15	12.5	1.731	1.585	1500	1620	RT
	RD16	12.5	1.756	1.588	1500	1620	RT
	RD3	12.5	1.751	1.572	1500	1700	150
	RD4	12.5	1.767	1.568	1500	1700	150
	RD5	12.5	1.765	1.572	1500	1700	150
	RD1	12.5	1.732	1.582	1500	1650	300
	RD4	12.5	1.748	1.578	1500	1670	300
	RD5	12.5	1.765	1.569	1500	1670	300

Material	Sample label	Initial Gauge Dimensions [mm]			Strain Rate [1/s]		Temperature [°C]
		Length	Width	Thickness	Nominal	Achieved	
AZ31B-H24 - 1.6mm - TD	TD2	12.5	1.746	1.614	0.003	0.0025	RT
	TD3	12.5	1.81	1.604	0.003	0.0025	RT
	TD4	12.5	1.748	1.61	0.003	0.0025	RT
	TD5	12.5	1.808	1.586	0.003	0.0025	RT
	TD9	12.5	1.76	1.57	30	31	RT
	TD10	12.5	1.76	1.59	30	31	RT
	TD11	12.5	1.76	1.58	30	30	RT
	TD2	12.5	1.805	1.595	100	119	RT
	TD3	12.5	1.747	1.607	100	124	RT
	TD4	12.5	1.745	1.593	100	110	RT
	TD6	12.5	1.749	1.623	200	245	RT
	TD7	12.5	1.739	1.596	200	245	RT
	TD8	12.5	1.754	1.605	200	249	RT
	TD10	12.5	1.742	1.564	500	580	RT
	TD11	12.5	1.748	1.568	500	580	RT
	TD14	12.5	1.744	1.573	500	580	RT
	TD6	12.5	1.779	1.565	1000	1120	RT
	TD7	12.5	1.809	1.583	1000	1130	RT
	TD8	12.5	1.804	1.577	1000	1130	RT
	TD2	12.5	1.75	1.566	1000	1160	150
	TD10	12.5	1.755	1.575	1000	1160	150
	TD11	12.5	1.755	1.575	1000	1160	150
	TD2	12.5	1.749	1.556	1000	1160	300
	TD5	12.5	1.759	1.57	1000	1160	300
	TD6	12.5	1.813	1.583	1000	1160	300
	TD15	12.5	1.802	1.58	1500	1620	RT
	TD16	12.5	1.743	1.56	1500	1650	RT
	TD17	12.5	1.743	1.561	1500	1660	RT
	TD1	12.5	1.757	1.564	1500	1650	150
	TD2	12.5	1.751	1.575	1500	1650	150
	TD3	12.5	1.746	1.564	1500	1650	150
	TD4	12.5	1.753	1.575	1500	1660	300
	TD5	12.5	1.745	1.57	1500	1680	300
	TD6	12.5	1.772	1.572	1500	1680	300

Material	Sample Label	Initial Gauge Dimensions [mm]			Strain Rate [1/s]		Temperature [°C]
		Length	Width	Thickness	Nominal	Achieved	
AZ31B-O - 1.6mm - RD	RD1	12.5	1.774	1.584	0.003	0.0025	RT
	RD2	12.5	1.775	1.583	0.003	0.0025	RT
	RD3	12.5	1.794	1.59	0.003	0.0025	RT
	RD4	12.5	1.771	1.578	0.003	0.0025	RT
	RD3	12.5	1.769	1.592	0.1	0.08	RT
	RD4	12.5	1.774	1.577	0.1	0.08	RT
	RD5	12.5	1.774	1.577	0.1	0.08	RT
	RD6	12.5	1.774	1.577	0.1	0.08	RT
	RD1	12.5	1.769	1.588	1	0.8	RT
	RD2	12.5	1.767	1.589	1	0.8	RT
	RD3	12.5	1.786	1.588	1	0.8	RT
	RD1	12.5	1.789	1.597	30	30	RT
	RD2	12.5	1.795	1.584	30	30	RT
	RD3	12.5	1.777	1.571	30	31	RT
	RD3	12.5	1.78	1.583	100	123	RT
	RD8	12.5	1.794	1.58	100	117	RT
	RD9	12.5	1.774	1.573	100	121	RT
	RD1	12.5	1.771	1.604	500	594	RT
	RD2	12.5	1.776	1.586	500	587	RT
	RD3	12.5	1.773	1.582	500	588	RT
	RD1	12.5	1.773	1.604	500	592	150
	RD2	12.5	1.771	1.604	500	588	150
	RD3	12.5	1.775	1.593	500	585	150
	RD1	12.5	1.787	1.588	500	568	250
	RD2	12.5	1.791	1.566	500	559	250
	RD3	12.5	1.789	1.585	500	563	250
	RD1	12.5	1.789	1.587	1000	1171	RT
	RD2	12.5	1.77	1.585	1000	1175	RT
	RD4	12.5	1.767	1.591	1000	1175	RT
	RD2	12.5	1.793	1.585	1000	1184	150
	RD4	12.5	1.77	1.595	1000	1179	150
	RD5	12.5	1.793	1.579	1000	1188	150
	RD1	12.5	1.794	1.577	1000	1174	250
	RD2	12.5	1.79	1.578	1000	1176	250
	RD3	12.5	1.777	1.576	1000	1180	250
	RD1	12.5	1.793	1.59	1500	1662	RT
	RD2	12.5	1.793	1.583	1500	1667	RT
	RD3	12.5	1.796	1.583	1500	1661	RT
	RD1	12.5	1.787	1.592	1500	1670	150
	RD2	12.5	1.771	1.595	1500	1668	150
	RD3	12.5	1.792	1.576	1500	1663	150
	RD1	12.5	1.767	1.604	1500	1684	250
	RD2	12.5	1.775	1.59	1500	1671	250
	RD3	12.5	1.769	1.584	1500	1677	250

Material	Sample Label	Initial Gauge Dimensions [mm]			Strain Rate [1/s]		Temperature [°C]
		Length	Width	Thickness	Nominal	Achieved	
AZ31B-O - 1.6mm - TD	TD2	12.5	1.769	1.568	0.003	0.0025	RT
	TD3	12.5	1.776	1.582	0.003	0.0025	RT
	TD5	12.5	1.774	1.567	0.003	0.0025	RT
	TD2	12.5	1.759	1.567	0.1	0.08	RT
	TD3	12.5	1.77	1.583	0.1	0.08	RT
	TD5	12.5	1.769	1.559	0.1	0.08	RT
	TD1	12.5	1.771	1.565	1	0.8	RT
	TD2	12.5	1.768	1.57	1	0.8	RT
	TD3	12.5	1.763	1.576	1	0.8	RT
	TD2	12.5	1.759	1.588	30	31	RT
	TD3	12.5	1.762	1.574	30	30	RT
	TD4	12.5	1.767	1.567	30	31	RT
	TD1	12.5	1.764	1.569	100	110	RT
	TD2	12.5	1.767	1.553	100	114	RT
	TD3	12.5	1.764	1.571	100	118	RT
	TD4	12.5	1.761	1.571	100	120	RT
	TD1	12.5	1.765	1.584	500	955	RT
	TD2	12.5	1.77	1.57	500	579	RT
	TD3	12.5	1.773	1.578	500	581	RT
	TD1	12.5	1.768	1.582	500	584	150
	TD3	12.5	1.771	1.582	500	588	150
	TD4	12.5	1.768	1.582	500	585	150
	TD1	12.5	1.777	1.586	500	567	250
	TD2	12.5	1.777	1.569	500	568	250
	TD3	12.5	1.775	1.57	500	567	250
	TD1	12.5	1.763	1.571	1000	1177	RT
	TD2	12.5	1.769	1.579	1000	1178	RT
	TD3	12.5	1.774	1.563	1000	1176	RT
	TD1	12.5	1.767	1.602	1000	1185	150
	TD2	12.5	1.772	1.58	1000	1189	150
	TD4	12.5	1.769	1.581	1000	1178	150
	TD1	12.5	1.763	1.587	1000	1177	250
	TD2	12.5	1.767	1.58	1000	1176	250
	TD3	12.5	1.772	1.568	1000	1175	250
	TD1	12.5	1.775	1.596	1500	1664	RT
	TD2	12.5	1.766	1.573	1500	1659	RT
	TD3	12.5	1.784	1.58	1500	1650	RT
	TD1	12.5	1.768	1.574	1500	1654	150
	TD2	12.5	1.78	1.585	1500	1653	150
	TD3	12.5	1.769	1.582	1500	1662	150
	TD1	12.5	1.767	1.566	1500	1680	250
	TD2	12.5	1.765	1.561	1500	1680	250
	TD3	12.5	1.772	1.582	1500	1668	250

Material	Sample Label	Initial Gauge Dimensions [mm]			Strain Rate [1/s]		Temperature [°C]
		Length	Width	Thickness	Nominal	Achieved	
AZ31B-O - 1.0mm - RD	RD1	12.5	1.779	1.017	0.003	0.0025	RT
	RD2	12.5	1.772	1.019	0.003	0.0025	RT
	RD3	12.5	1.775	1.019	0.003	0.0025	RT
	RD1	12.5	1.779	1.04	0.1	0.08	RT
	RD2	12.5	1.772	1.027	0.1	0.08	RT
	RD3	12.5	1.777	1.017	0.1	0.08	RT
	RD1	12.5	1.775	1.026	30	33	RT
	RD2	12.5	1.772	1.025	30	34	RT
	RD3	12.5	1.783	1.021	30	33	RT
	RD1	12.5	1.756	1.014	500	588	RT
	RD2	12.5	1.759	1.001	500	586	RT
	RD3	12.5	1.755	1.012	500	583	RT
	RD1	12.5	1.763	1.005	1000	1147	RT
	RD2	12.5	1.762	1.012	1000	1147	RT
	RD3	12.5	1.742	1.005	1000	1185	RT
	RD1	12.5	1.759	1.018	1500	1638	RT
	RD2	12.5	1.752	1.016	1500	1630	RT
	RD3	12.5	1.77	1.012	1500	1631	RT

Material	Sample Label	Initial Gauge Dimensions [mm]			Strain Rate [1/s]		Temperature [°C]
		Length	Width	Thickness	Nominal	Achieved	
AZ31B-O - 1.0mm - TD	TD1	12.5	1.756	1.006	0.003	0.0025	RT
	TD2	12.5	1.757	0.998	0.003	0.0025	RT
	TD3	12.5	1.763	1.018	0.003	0.0025	RT
	TD1	12.5	1.754	1.007	0.1	0.08	RT
	TD2	12.5	1.759	1.011	0.1	0.08	RT
	TD3	12.5	1.76	1.012	0.1	0.08	RT
	TD2	12.5	1.762	1.017	30	33	RT
	TD3	12.5	1.756	1.008	30	33	RT
	TD4	12.5	1.758	1.009	30	32	RT
	TD1	12.5	1.742	1.015	500	608	RT
	TD2	12.5	1.758	1.012	500	605	RT
	TD3	12.5	1.754	1.005	500	605	RT
	TD1	12.5	1.762	1.013	1000	1144	RT
	TD2	12.5	1.76	1.015	1000	1148	RT
	TD3	12.5	1.752	1.009	1000	1152	RT
	TD1	12.5	1.752	1.012	1500	1625	RT
	TD2	12.5	1.757	1.009	1500	1628	RT
	TD3	12.5	1.755	1.016	1500	1624	RT

Material	Sample Label	Initial Gauge Dimensions [mm]			Strain Rate [1/s]		Temperature [°C]
		Length	Width	Thickness	Nominal	Achieved	
AZ31B-O - 2.5mm - RD	RD1	12.5	1.78	2.493	0.003	0.0025	RT
	RD2	12.5	1.784	2.488	0.003	0.0025	RT
	RD3	12.5	1.795	2.499	0.003	0.0025	RT
	RD1	12.5	1.776	2.484	0.1	0.08	RT
	RD2	12.5	1.782	2.487	0.1	0.08	RT
	RD4	12.5	1.775	2.491	0.1	0.08	RT
	RD1	12.5	1.779	2.501	30	30	RT
	RD2	12.5	1.779	2.487	30	30	RT
	RD3	12.5	1.779	2.502	30	29	RT
	RD1	12.5	1.78	2.508	500	557	RT
	RD2	12.5	1.775	2.495	500	554	RT
	RD3	12.5	1.777	2.495	500	545	RT
	RD1	12.5	1.775	2.481	1000	1089	RT
	RD3	12.5	1.772	2.462	1000	1096	RT
	RD4	12.5	1.791	2.519	1000	1093	RT

Material	Sample Label	Initial Gauge Dimensions [mm]			Strain Rate [1/s]		Temperature [°C]
		Length	Width	Thickness	Nominal	Achieved	
AZ31B-O - 2.5mm - TD	TD1	12.5	1.787	2.474	0.003	0.0025	RT
	TD2	12.5	1.792	2.47	0.003	0.0025	RT
	TD3	12.5	1.791	2.474	0.003	0.0025	RT
	TD1	12.5	1.791	2.482	0.1	0.08	RT
	TD2	12.5	1.789	2.462	0.1	0.08	RT
	TD3	12.5	1.775	2.491	0.1	0.08	RT
	TD2	12.5	1.789	2.466	30	31	RT
	TD3	12.5	1.788	2.469	30	28	RT
	TD4	12.5	1.787	2.457	30	30	RT
	TD1	12.5	1.783	2.47	500	546	RT
	TD2	12.5	1.785	2.46	500	547	RT
	TD3	12.5	1.782	2.467	500	552	RT
	TD1	12.5	1.785	2.459	1000	1073	RT
	TD3	12.5	1.791	2.459	1000	1083	RT
	TD4	12.5	1.783	2.476	1000	1083	RT

APPENDIX B: ENGINEERING STRESS-STRAIN CURVES

Appendix B1:

AZ31B-H24, Rolling Direction, room temperature

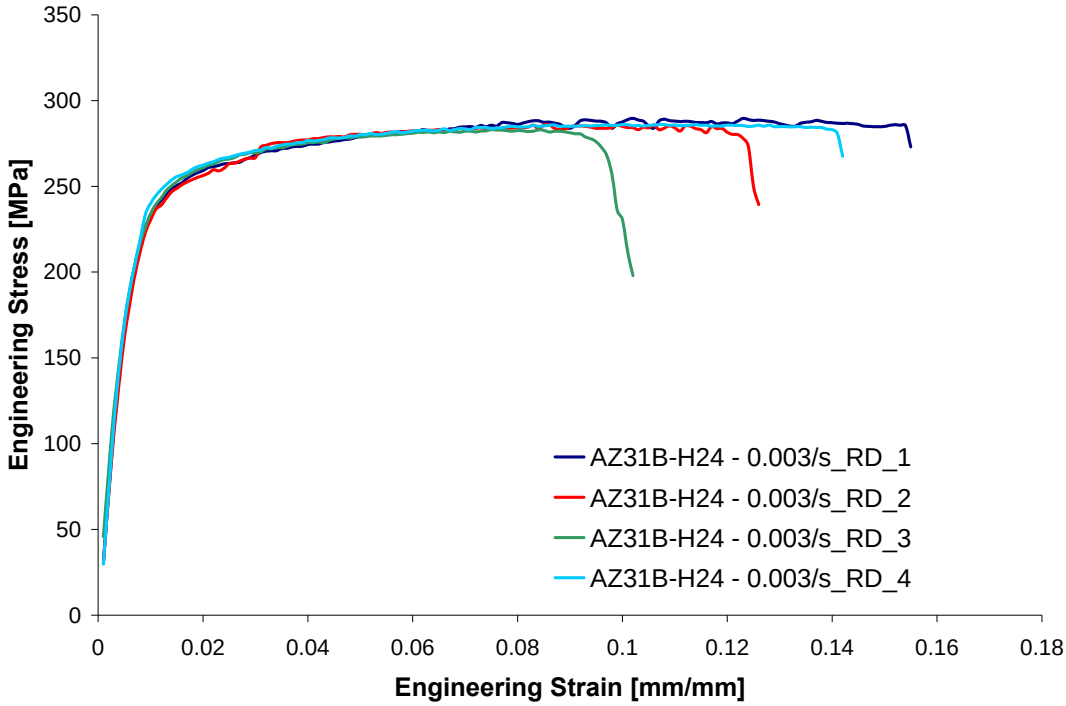

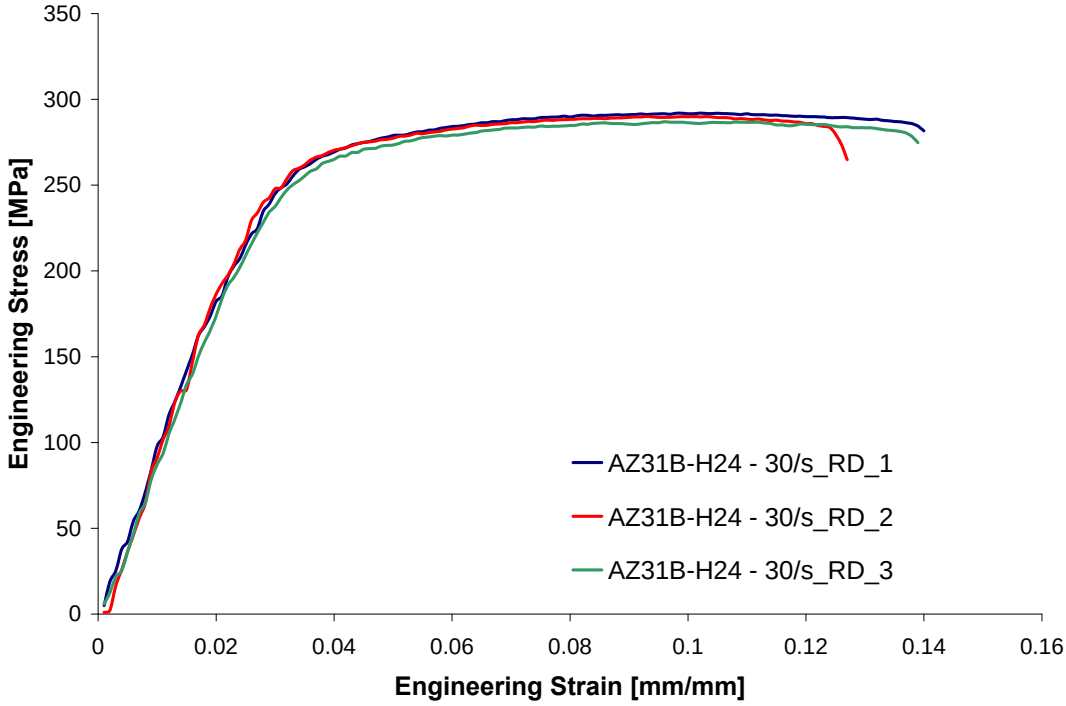

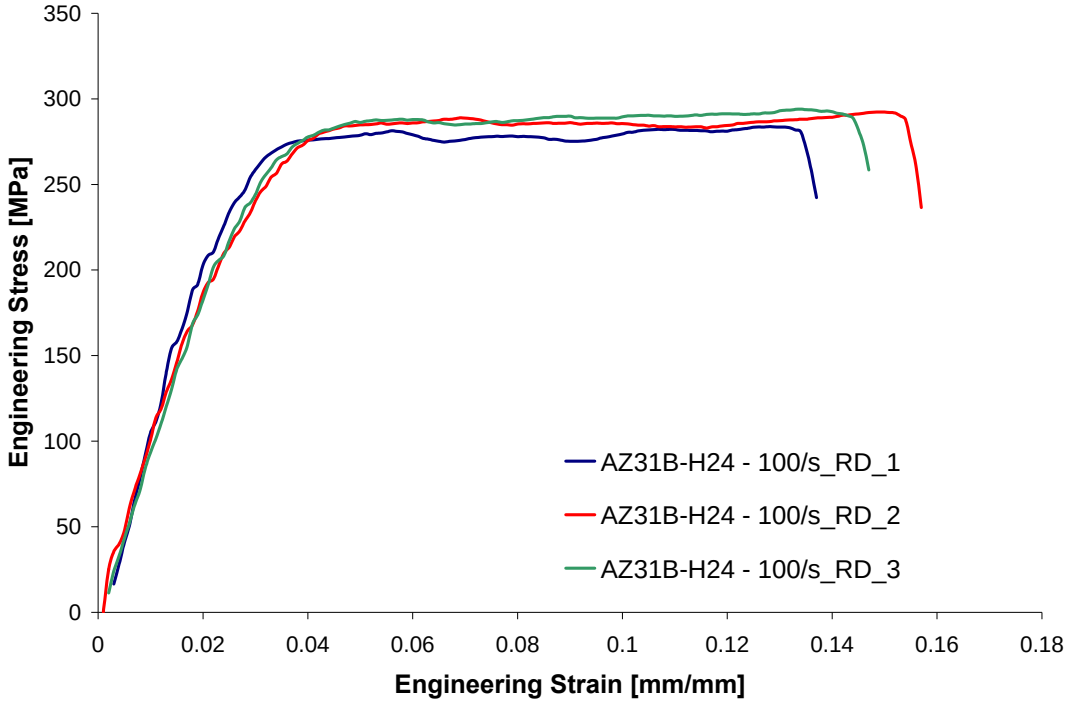
Engineering Stress [MPa]
350
300
250
200
150
100
50
0
0
0.02
0.04
0.06
0.08
0.1
0.12
0.14
0.16
0.18
Engineering Strain [mm/mm]
AZ31B-H24 - 100/s_RD_1
AZ31B-H24 - 100/s_RD_2
AZ31B-H24 - 100/s_RD_3

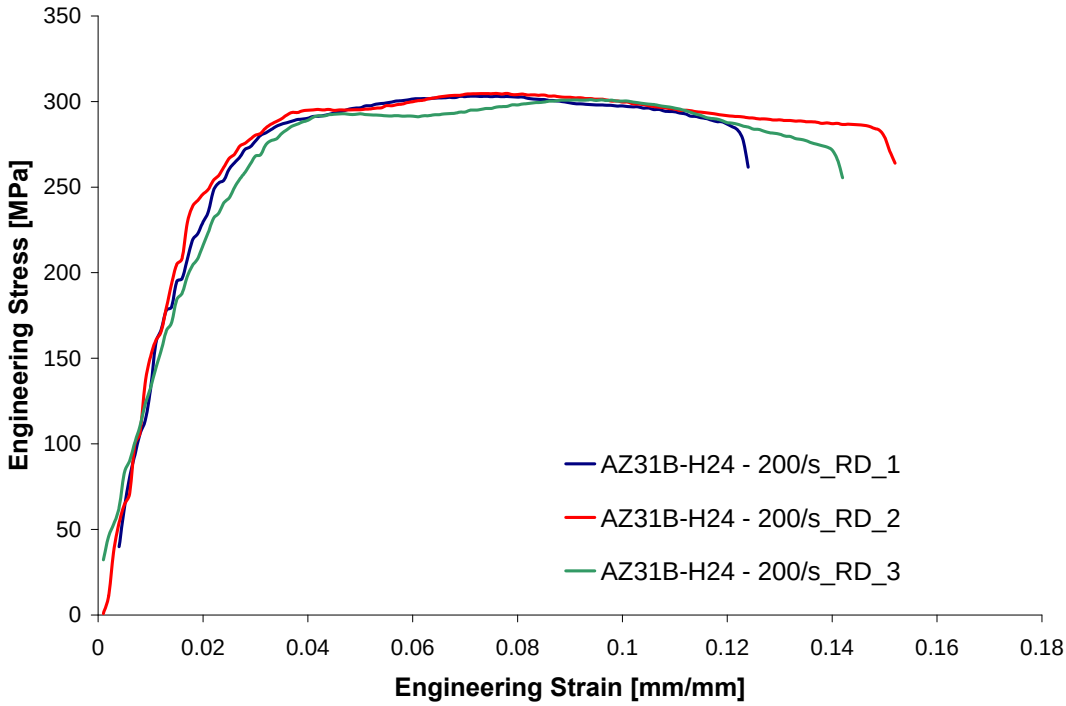
Engineering Stress [MPa]
350
300
250
200
150
100
50
0
0
0.02
0.04
0.06
0.08
0.1
0.12
0.14
0.16
0.18
Engineering Strain [mm/mm]
AZ31B-H24 - 200/s_RD_1
AZ31B-H24 - 200/s_RD_2
AZ31B-H24 - 200/s_RD_3

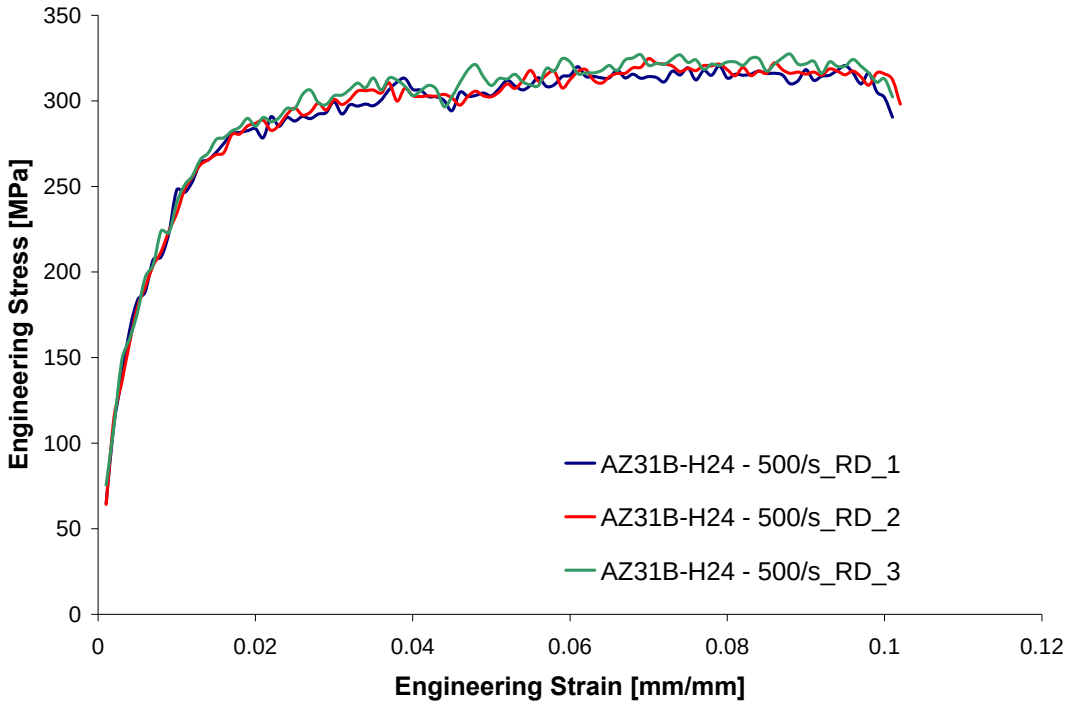
Engineering Stress [MPa]
350
300
250
200
150
100
50
0
0
0.02
0.04
0.06
0.08
0.1
0.12
Engineering Strain [mm/mm]
AZ31B-H24 - 500/s_RD_1
AZ31B-H24 - 500/s_RD_2
AZ31B-H24 - 500/s_RD_3

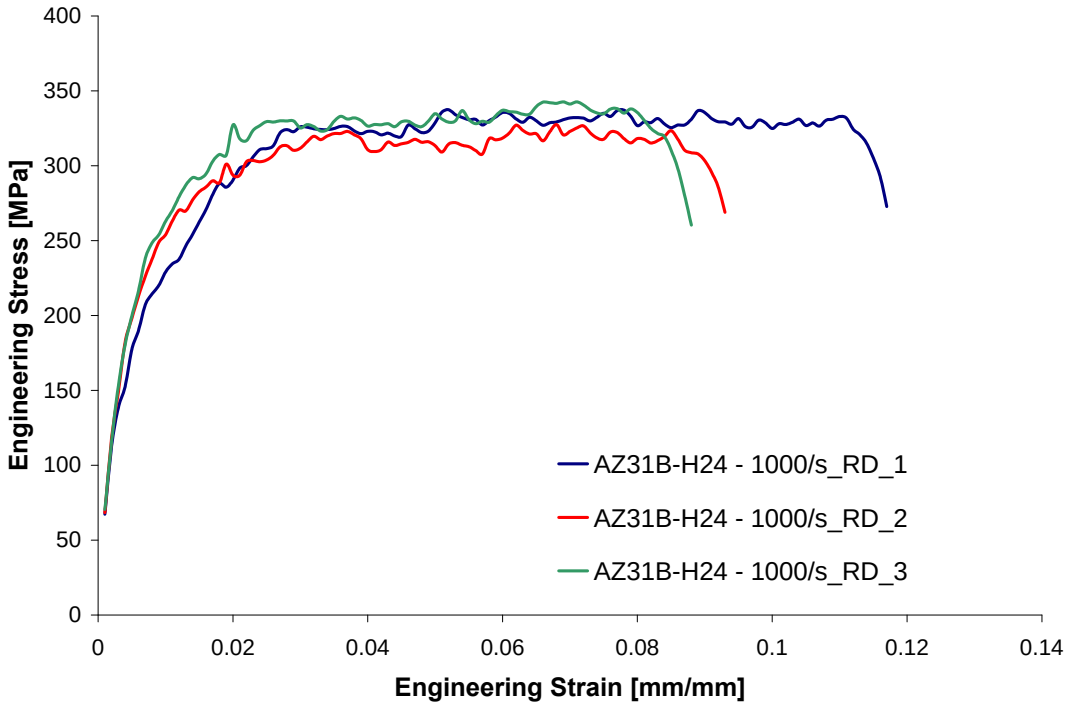
Engineering Stress [MPa]
400
350
300
250
200
150
100
50
0
0
0.02
0.04
0.06
0.08
0.1
0.12
0.14
Engineering Strain [mm/mm]
AZ31B-H24 - 1000/s_RD_1
AZ31B-H24 - 1000/s_RD_2
AZ31B-H24 - 1000/s_RD_3

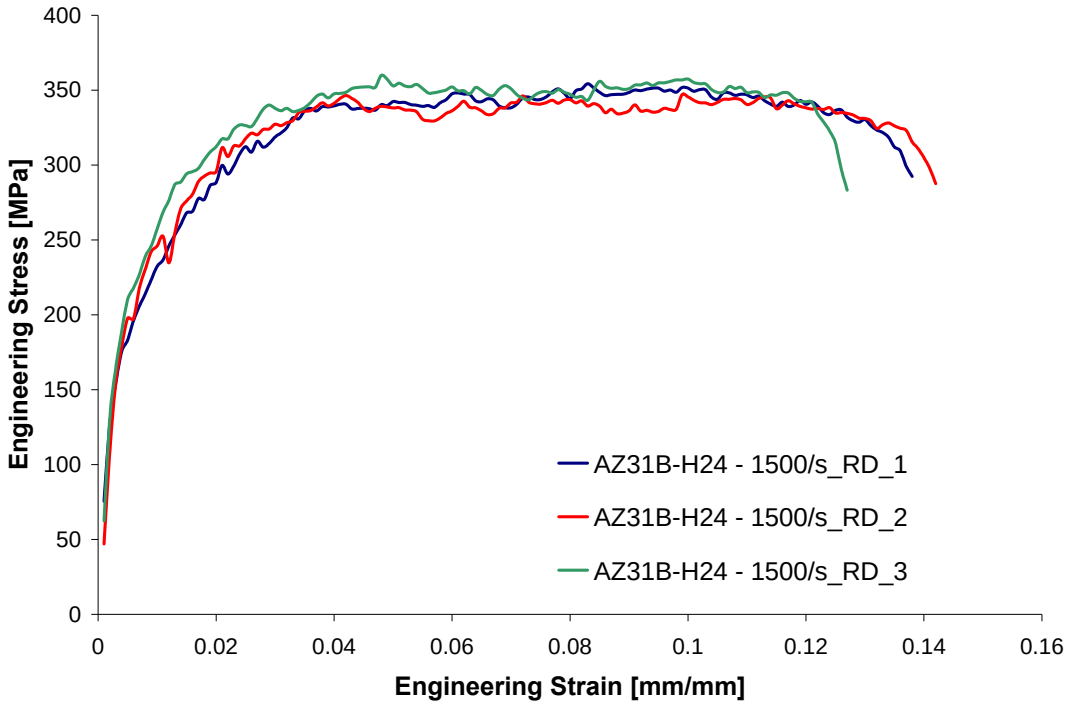

AZ31B-H24, Rolling Direction, elevated temperatures

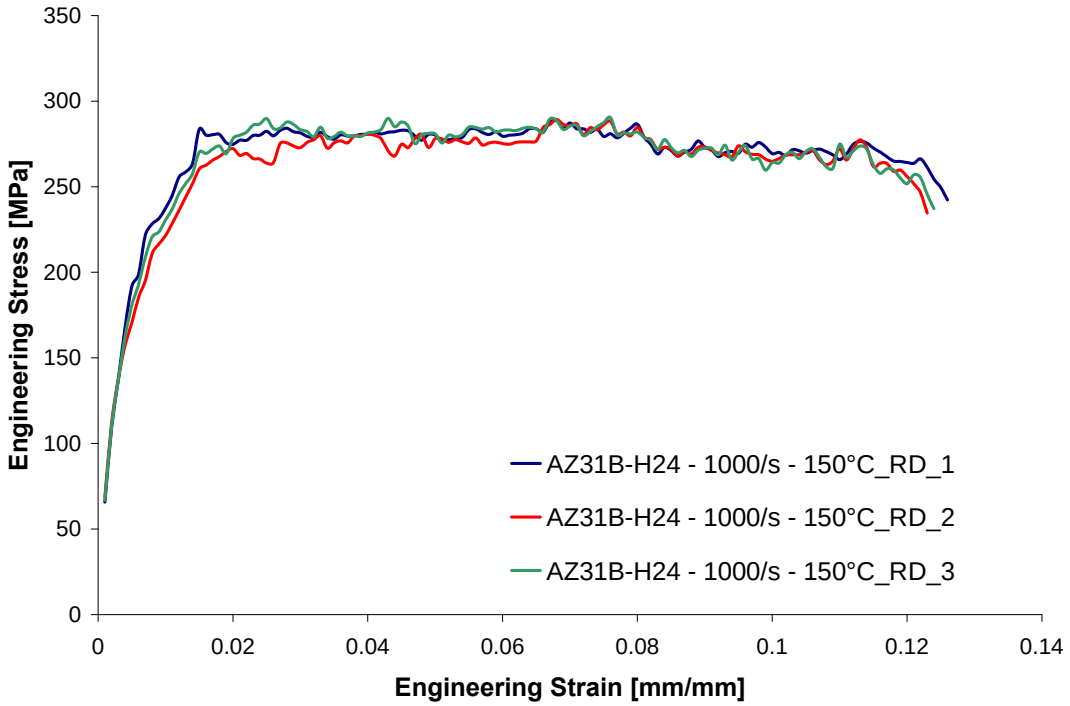

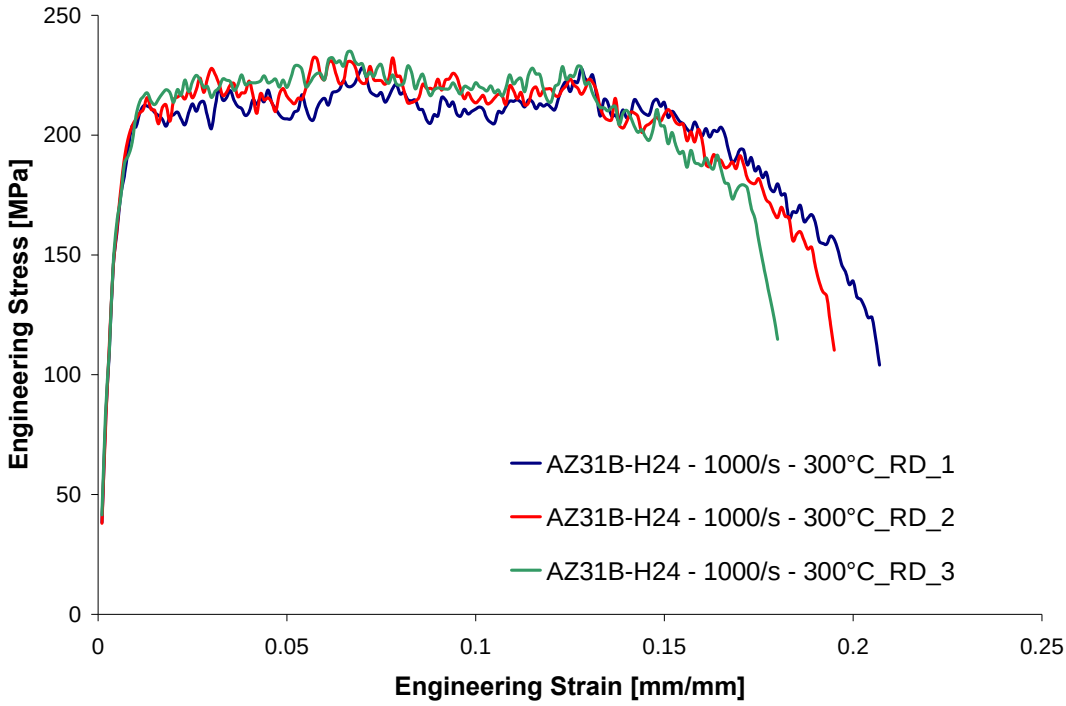
250
200
150
100
50
0
Engineering Stress [MPa]
0
0.05
0.1
0.15
0.2
0.25
Engineering Strain [mm/mm]
AZ31B-H24 - 1000/s - 300°C_RD_1
AZ31B-H24 - 1000/s - 300°C_RD_2
AZ31B-H24 - 1000/s - 300°C_RD_3

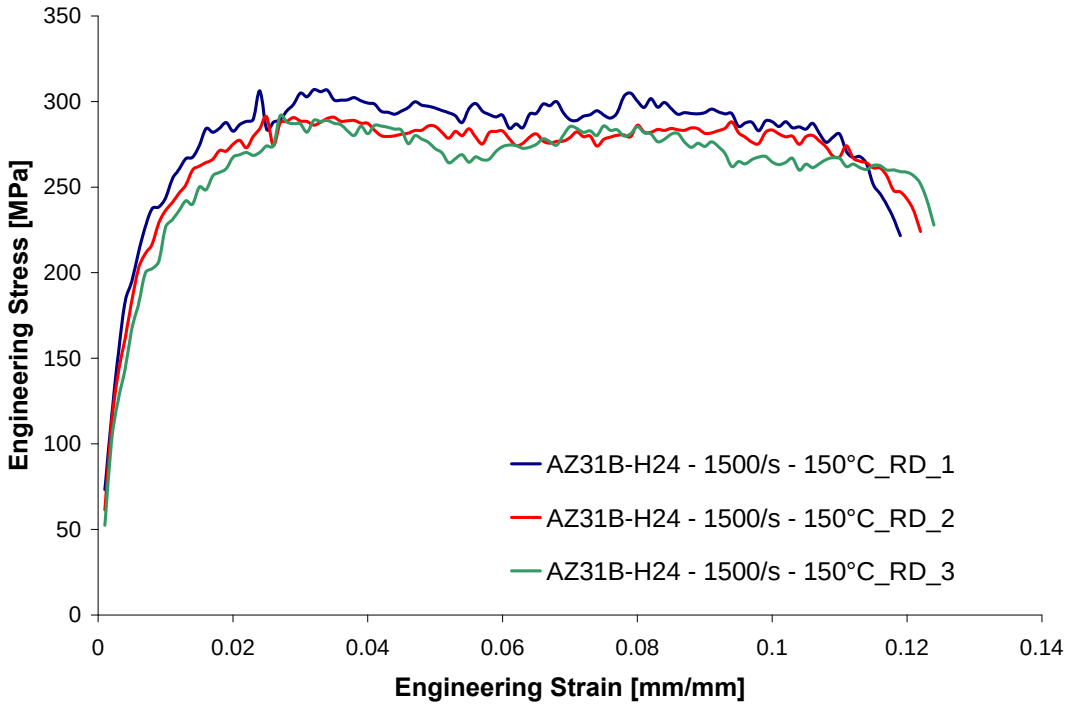
350
300
250
200
150
100
50
0
Engineering Stress [MPa]
0
0.02
0.04
0.06
0.08
0.1
0.12
0.14
Engineering Strain [mm/mm]
AZ31B-H24 - 1500/s - 150°C_RD_1
AZ31B-H24 - 1500/s - 150°C_RD_2
AZ31B-H24 - 1500/s - 150°C_RD_3

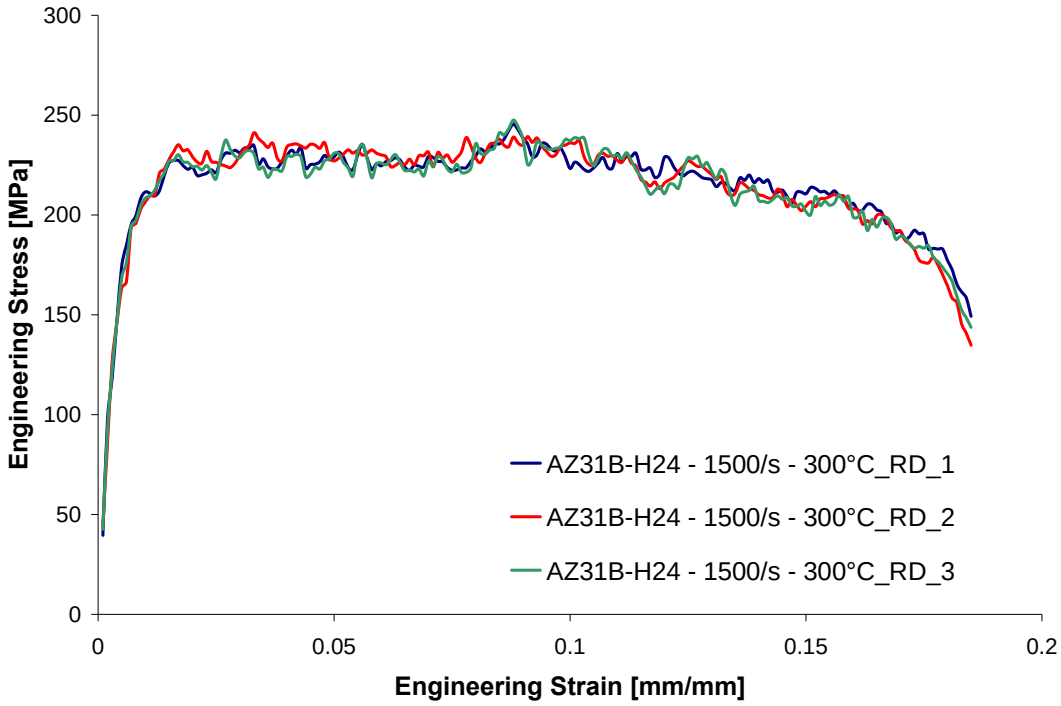

AZ31B-H24, Transverse Direction, room temperature

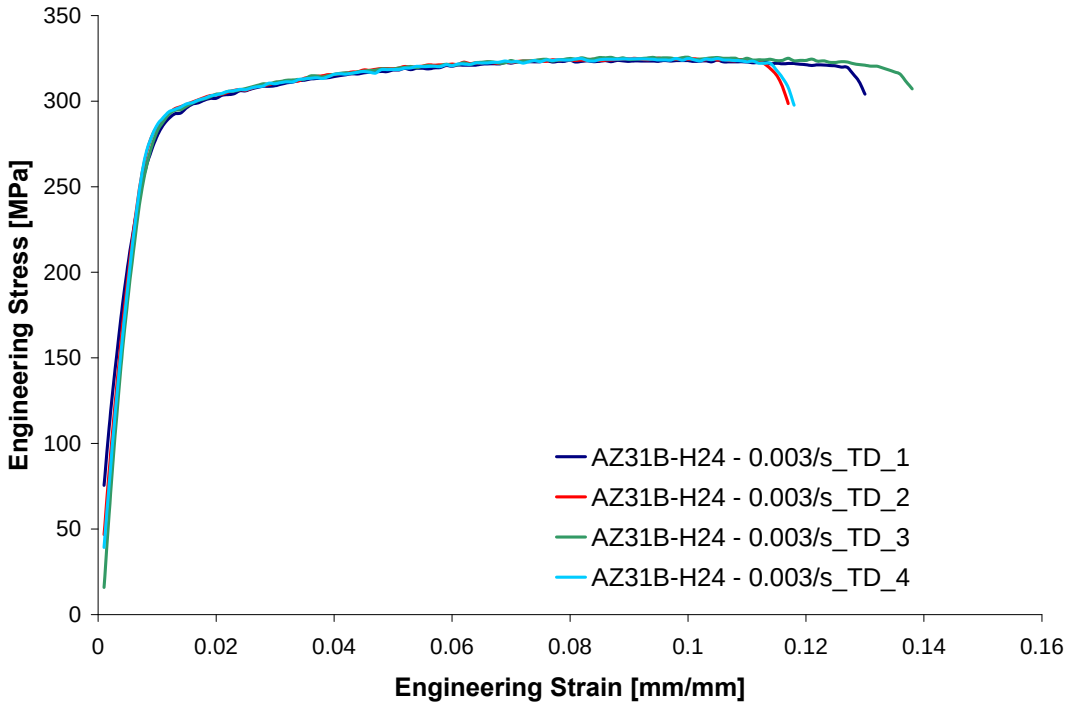

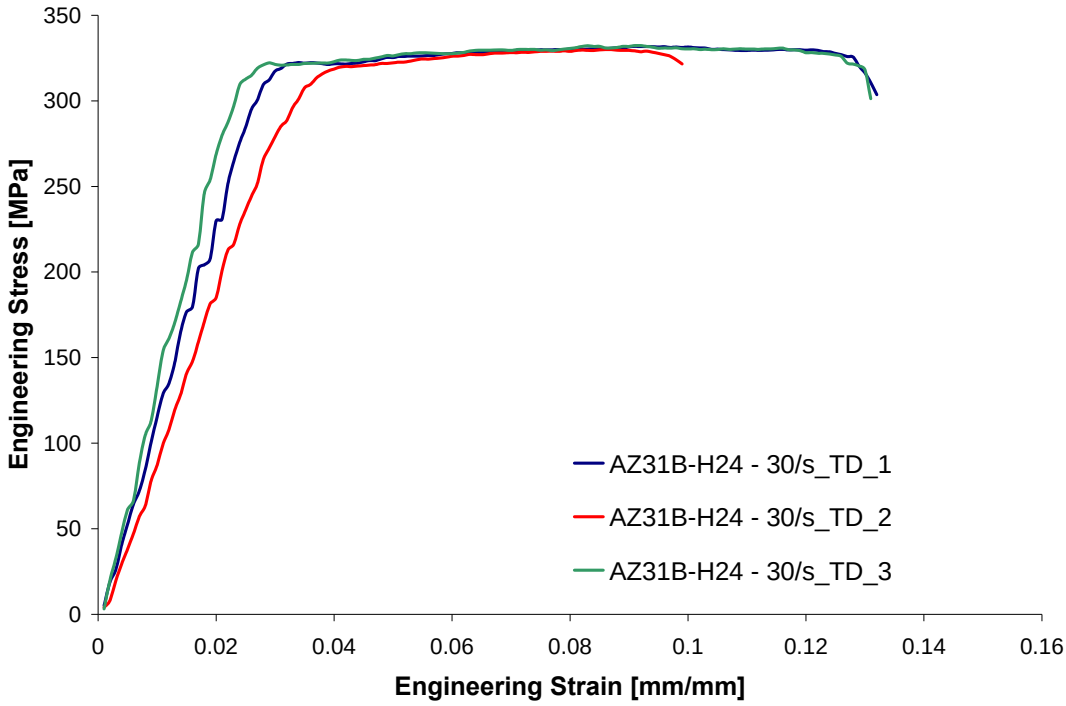
Engineering Stress [MPa]
350
300
250
200
150
100
50
0
0
0.02
0.04
0.06
0.08
0.1
0.12
0.14
0.16
Engineering Strain [mm/mm]
AZ31B-H24 - 30/s_TD_1
AZ31B-H24 - 30/s_TD_2
AZ31B-H24 - 30/s_TD_3

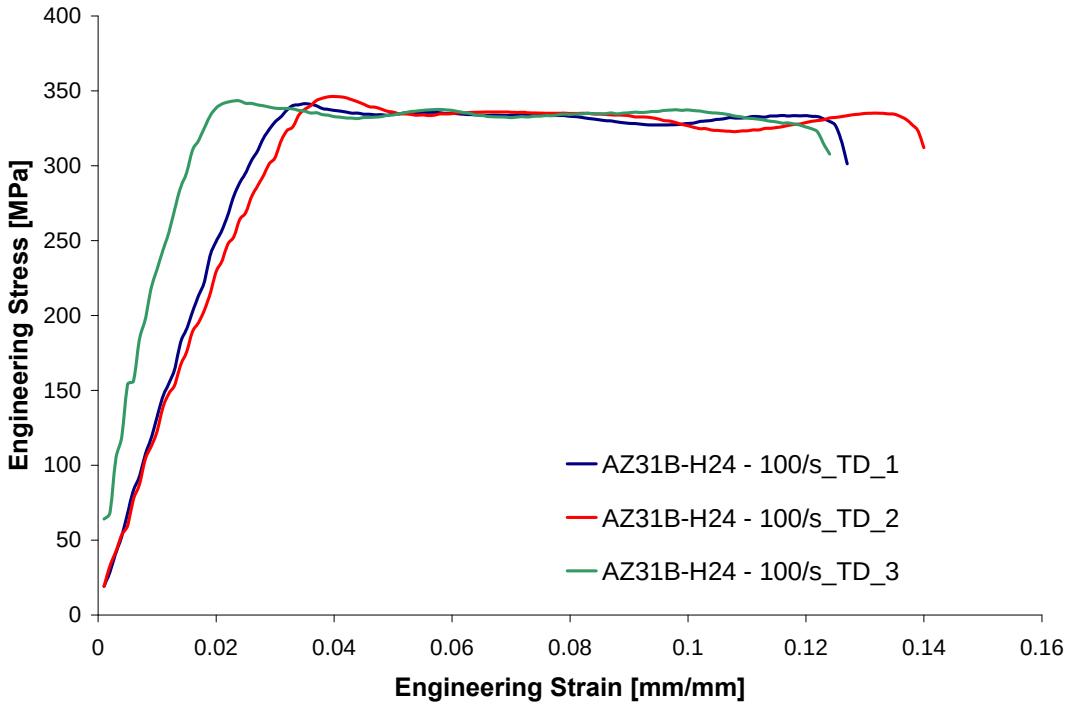
Engineering Stress [MPa]
400
350
300
250
200
150
100
50
0
0
0.02
0.04
0.06
0.08
0.1
0.12
0.14
0.16
Engineering Strain [mm/mm]
AZ31B-H24 - 100/s_TD_1
AZ31B-H24 - 100/s_TD_2
AZ31B-H24 - 100/s_TD_3

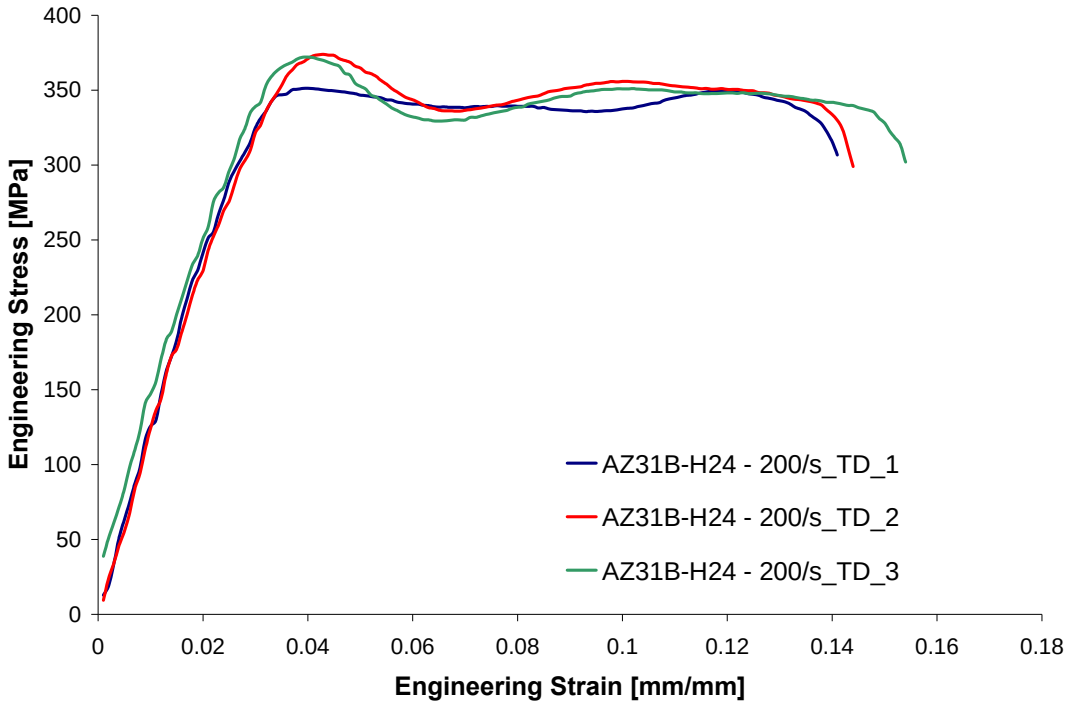
Engineering Stress [MPa]
400
350
300
250
200
150
100
50
0
0
0.02
0.04
0.06
0.08
0.1
0.12
0.14
0.16
0.18
Engineering Strain [mm/mm]
AZ31B-H24 - 200/s_TD_1
AZ31B-H24 - 200/s_TD_2
AZ31B-H24 - 200/s_TD_3

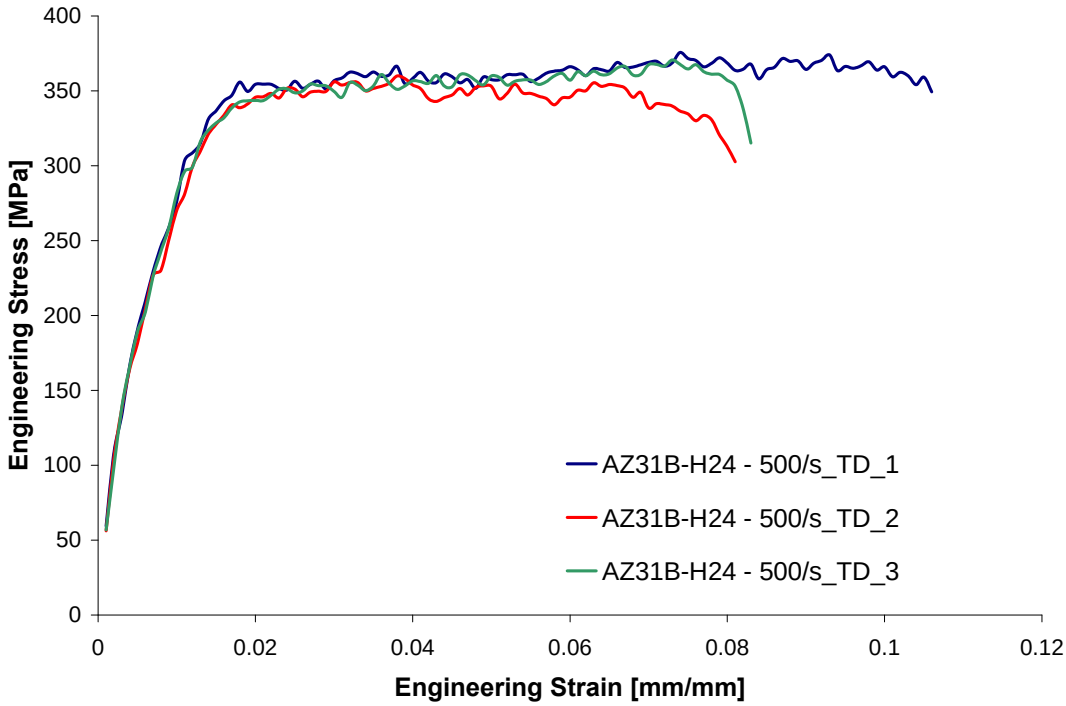
Engineering Stress [MPa]
400
350
300
250
200
150
100
50
0
0
0.02
0.04
0.06
0.08
0.1
0.12
Engineering Strain [mm/mm]
AZ31B-H24 - 500/s_TD_1
AZ31B-H24 - 500/s_TD_2
AZ31B-H24 - 500/s_TD_3

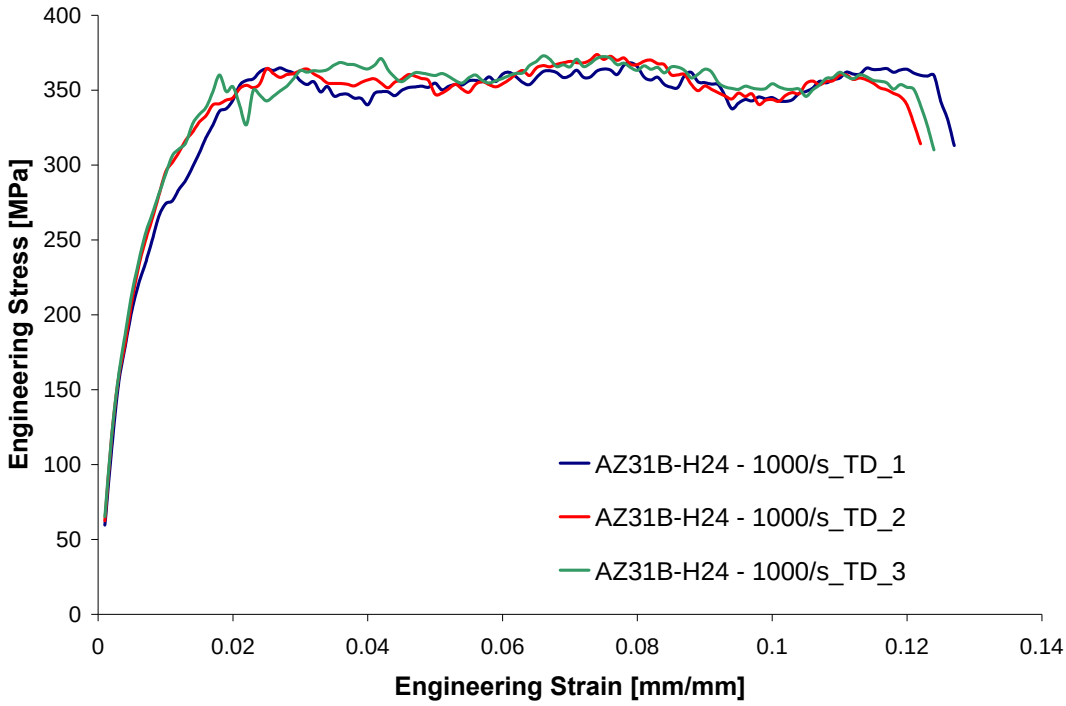
Engineering Stress [MPa]
400
350
300
250
200
150
100
50
0
0
0.02
0.04
0.06
0.08
0.1
0.12
0.14
Engineering Strain [mm/mm]
AZ31B-H24 - 1000/s_TD_1
AZ31B-H24 - 1000/s_TD_2
AZ31B-H24 - 1000/s_TD_3

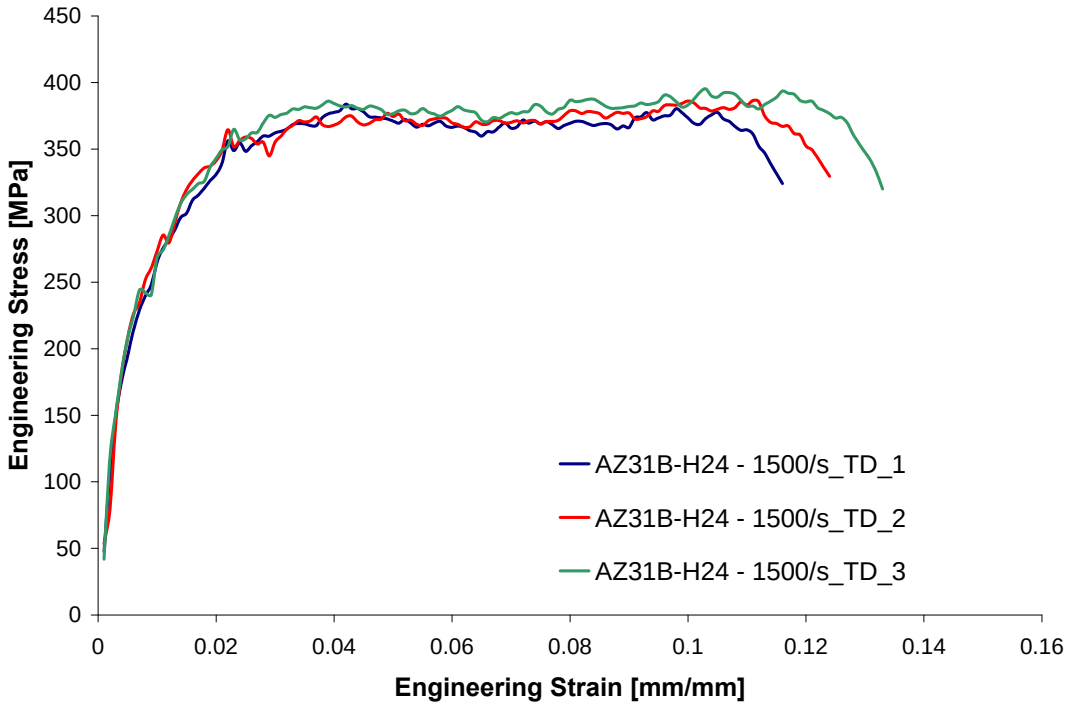
Engineering Stress [MPa]
450
400
350
300
250
200
150
100
50
0
0
0.02
0.04
0.06
0.08
0.1
0.12
0.14
0.16
Engineering Strain [mm/mm]
AZ31B-H24 - 1500/s_TD_1
AZ31B-H24 - 1500/s_TD_2
AZ31B-H24 - 1500/s_TD_3

AZ31B-H24, Transverse Direction, elevated temperatures

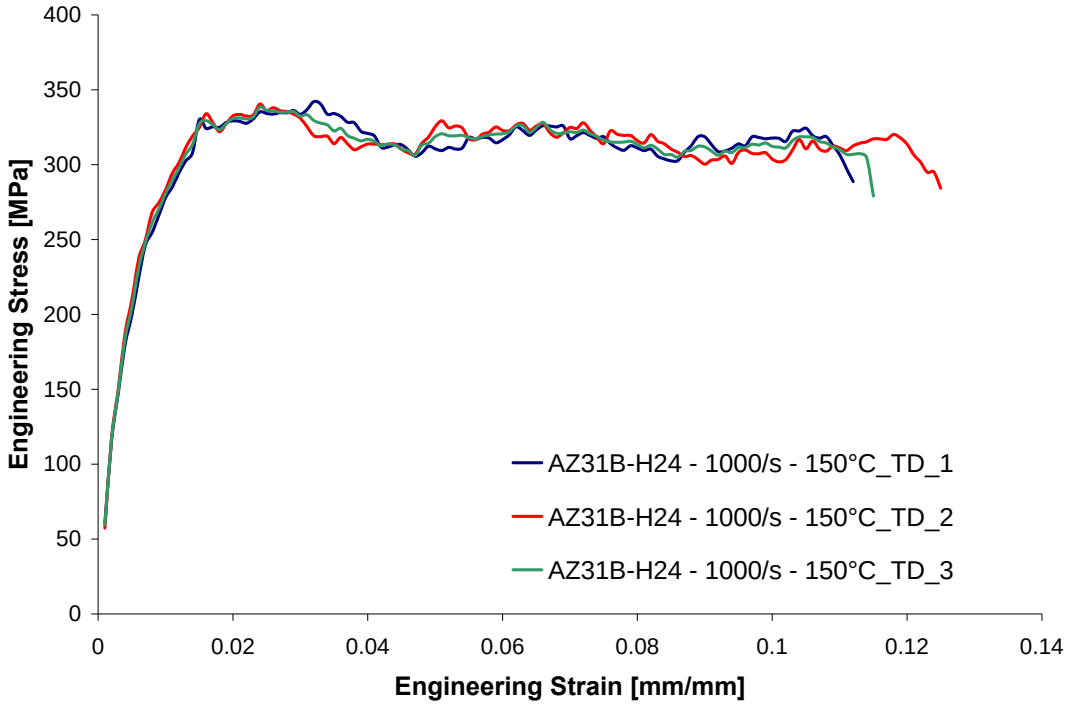

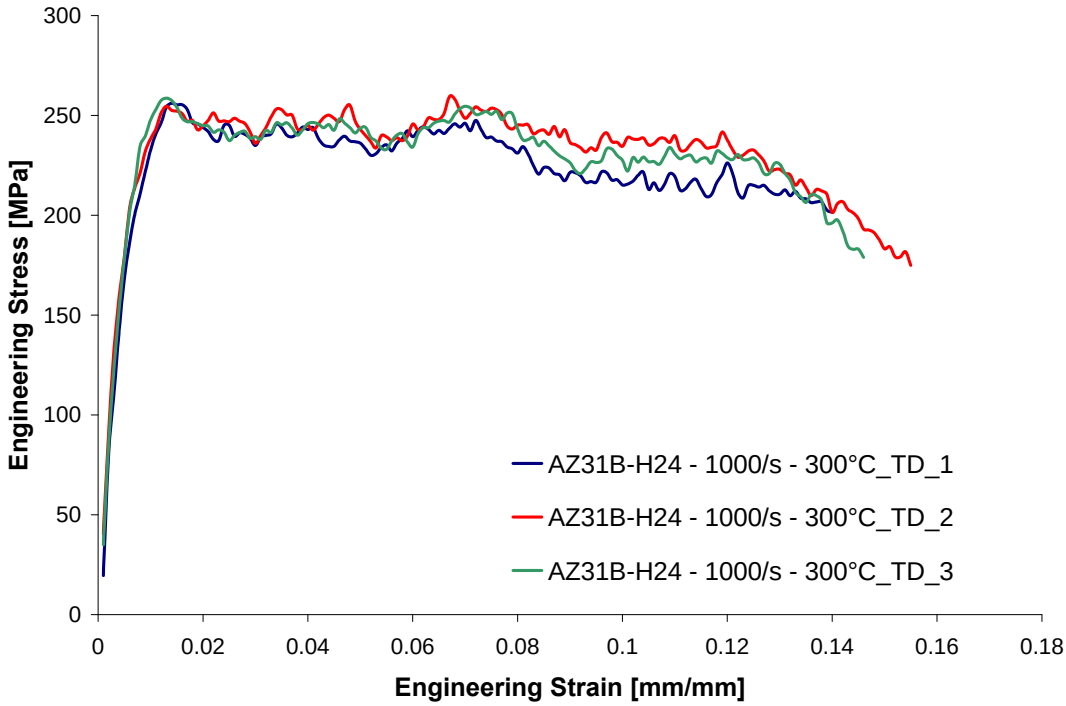

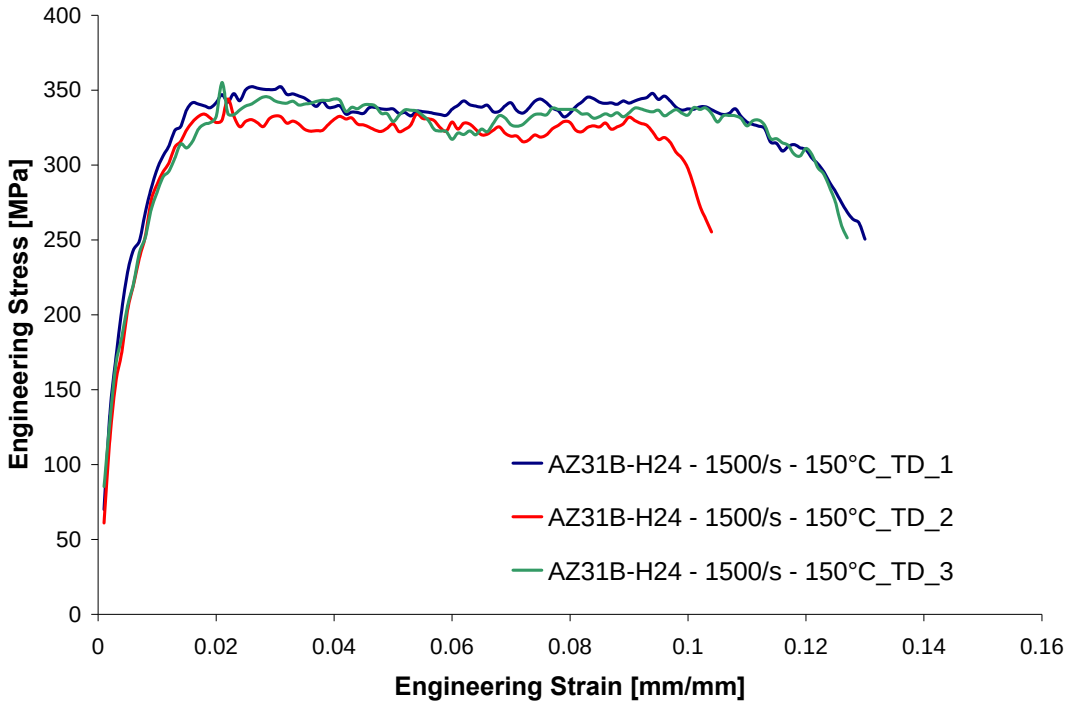
Engineering Stress [MPa]
400
350
300
250
200
150
100
50
0
0
0.02
0.04
0.06
0.08
0.1
0.12
0.14
0.16
Engineering Strain [mm/mm]
AZ31B-H24 - 1500/s - 150°C_TD_1
AZ31B-H24 - 1500/s - 150°C_TD_2
AZ31B-H24 - 1500/s - 150°C_TD_3

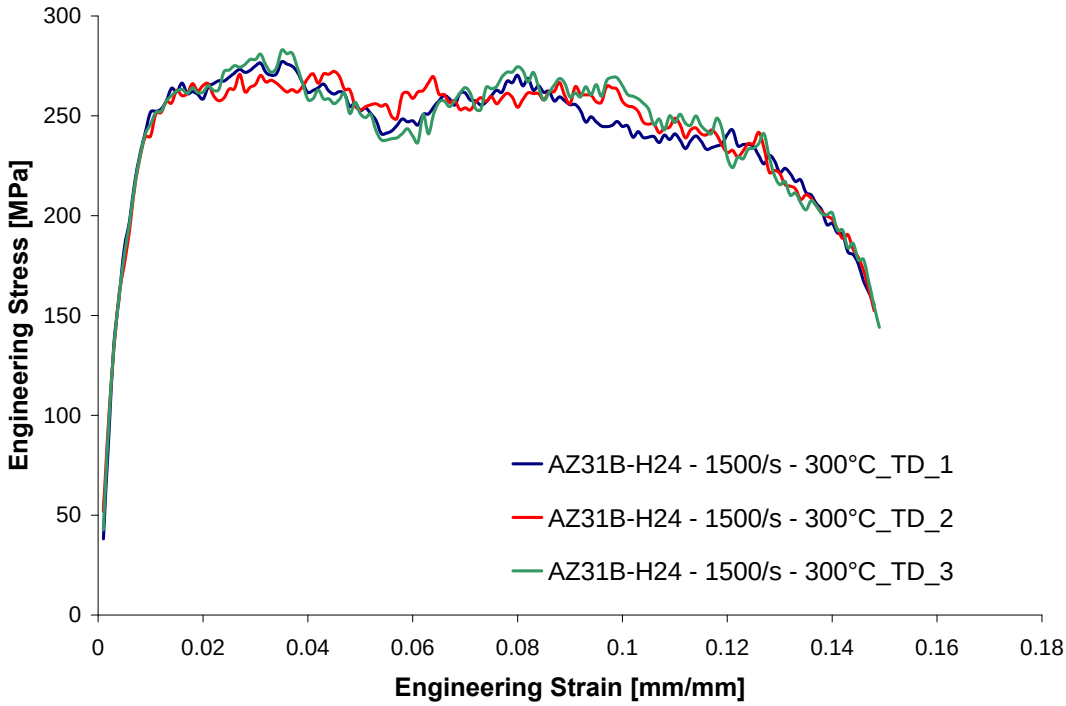
Engineering Stress [MPa]
300
250
200
150
100
50
0
0
0.02
0.04
0.06
0.08
0.1
0.12
0.14
0.16
0.18
Engineering Strain [mm/mm]
AZ31B-H24 - 1500/s - 300°C_TD_1
AZ31B-H24 - 1500/s - 300°C_TD_2
AZ31B-H24 - 1500/s - 300°C_TD_3

Appendix B2:

AZ31B-O, 1.6mm, Rolling Direction, room temperature

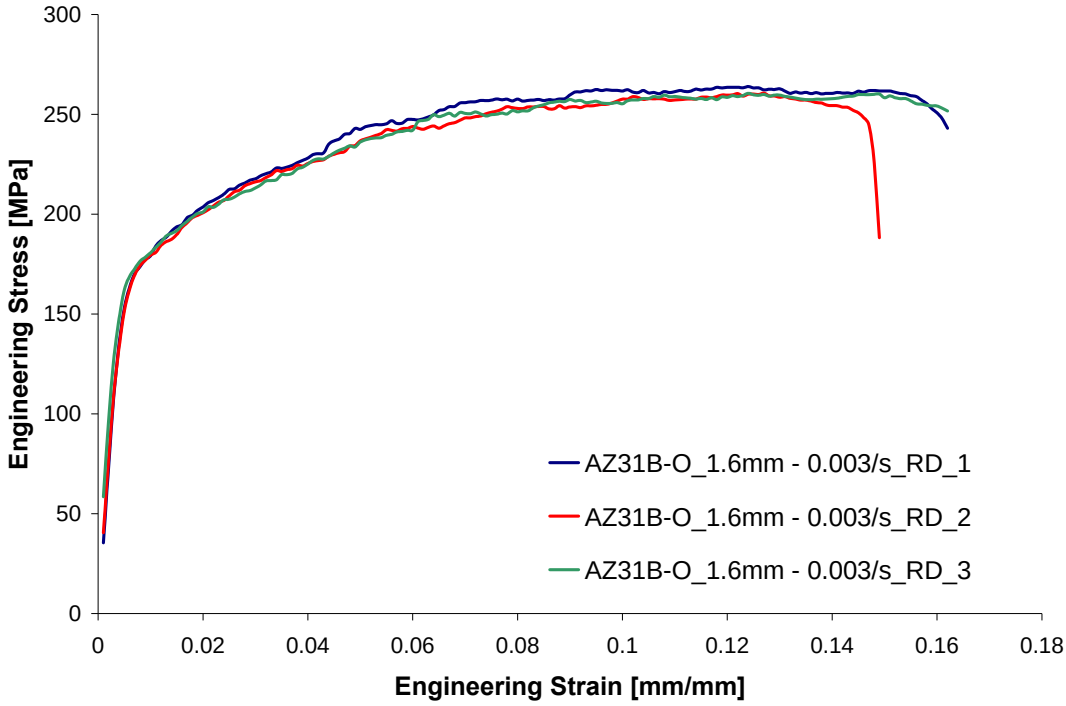

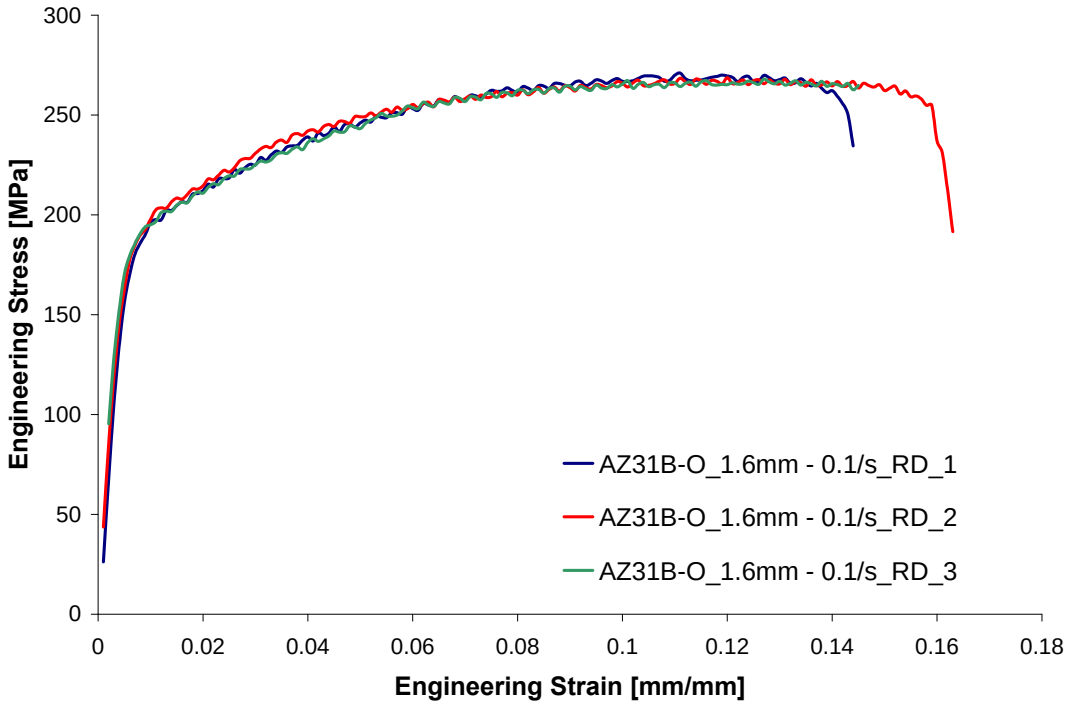

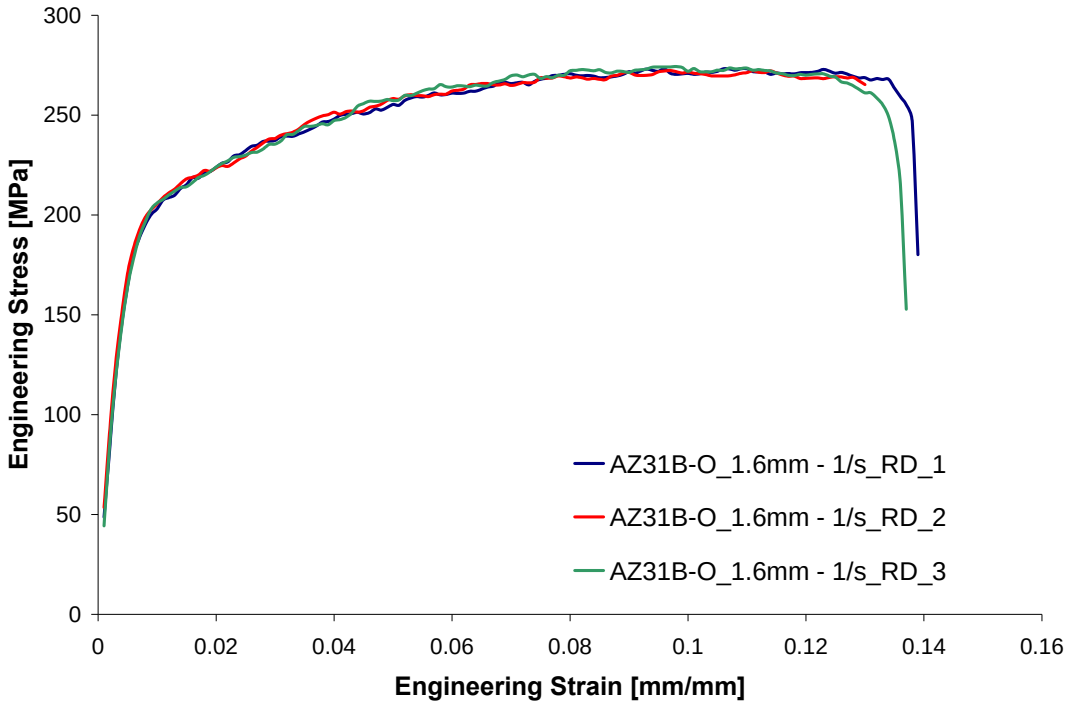
300
250
200
150
100
50
0
Engineering Stress [MPa]
0
0.02
0.04
0.06
0.08
0.1
0.12
0.14
0.16
Engineering Strain [mm/mm]
AZ31B-O_1.6mm - 1/s_RD_1
AZ31B-O_1.6mm - 1/s_RD_2
AZ31B-O_1.6mm - 1/s_RD_3

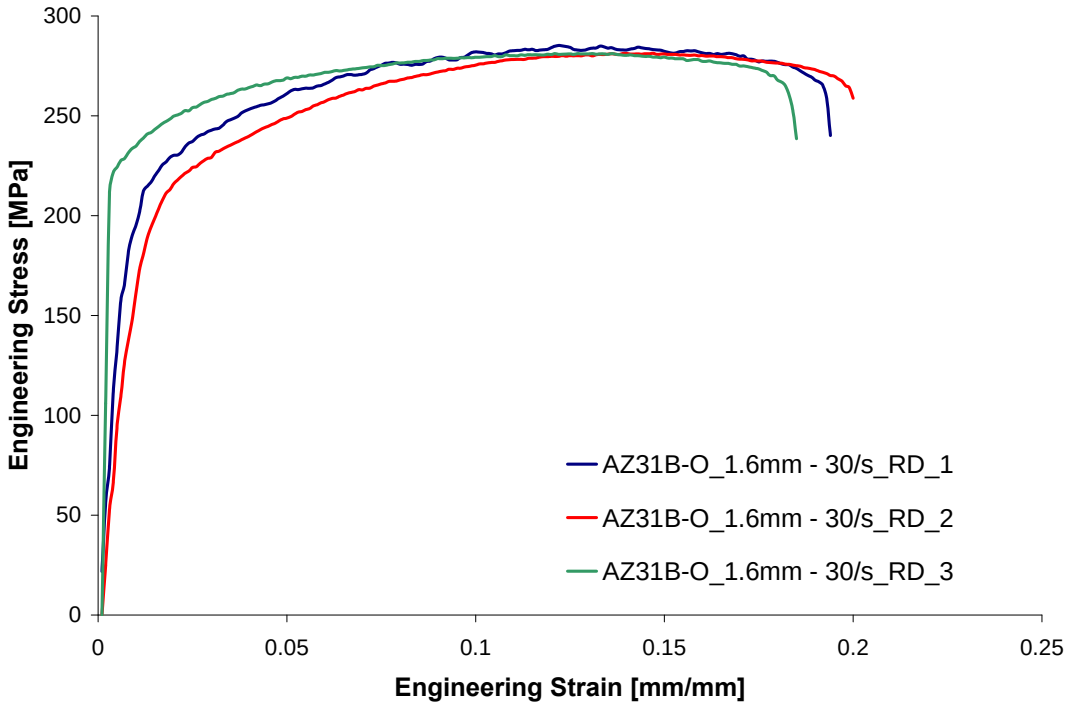
300
250
200
150
100
50
0
Engineering Stress [MPa]
0
0.05
0.1
0.15
0.2
0.25
Engineering Strain [mm/mm]
AZ31B-O_1.6mm - 30/s_RD_1
AZ31B-O_1.6mm - 30/s_RD_2
AZ31B-O_1.6mm - 30/s_RD_3

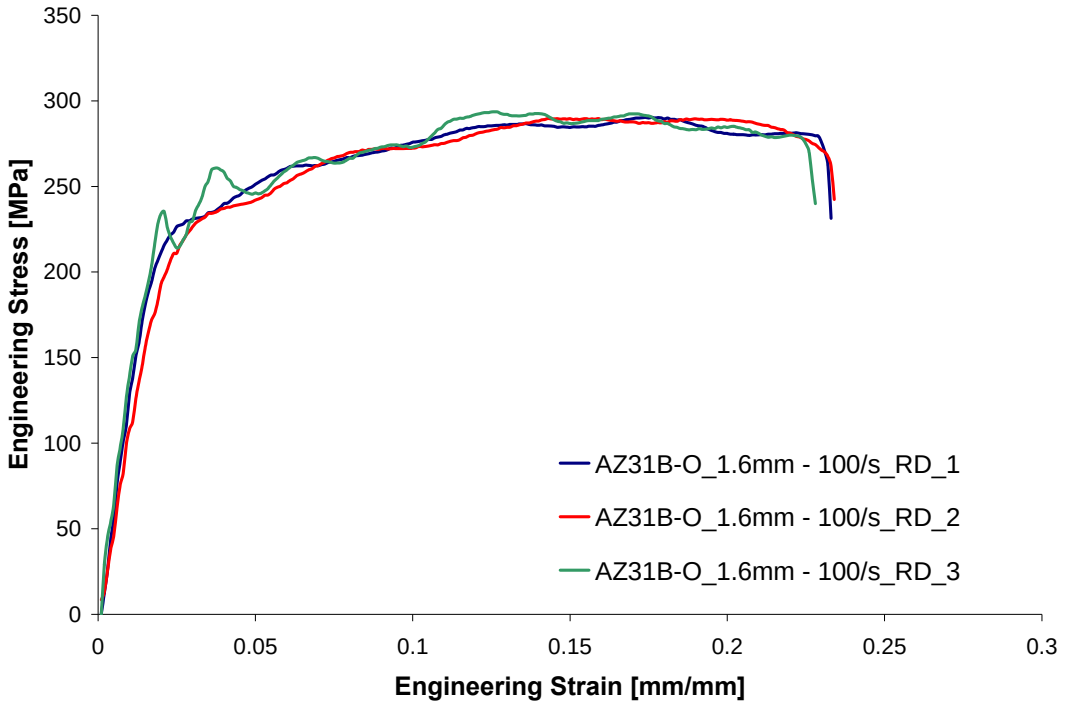
Engineering Stress [MPa]
350
300
250
200
150
100
50
0
0
0.05
0.1
0.15
0.2
0.25
0.3
Engineering Strain [mm/mm]
AZ31B-O_1.6mm - 100/s_RD_1
AZ31B-O_1.6mm - 100/s_RD_2
AZ31B-O_1.6mm - 100/s_RD_3

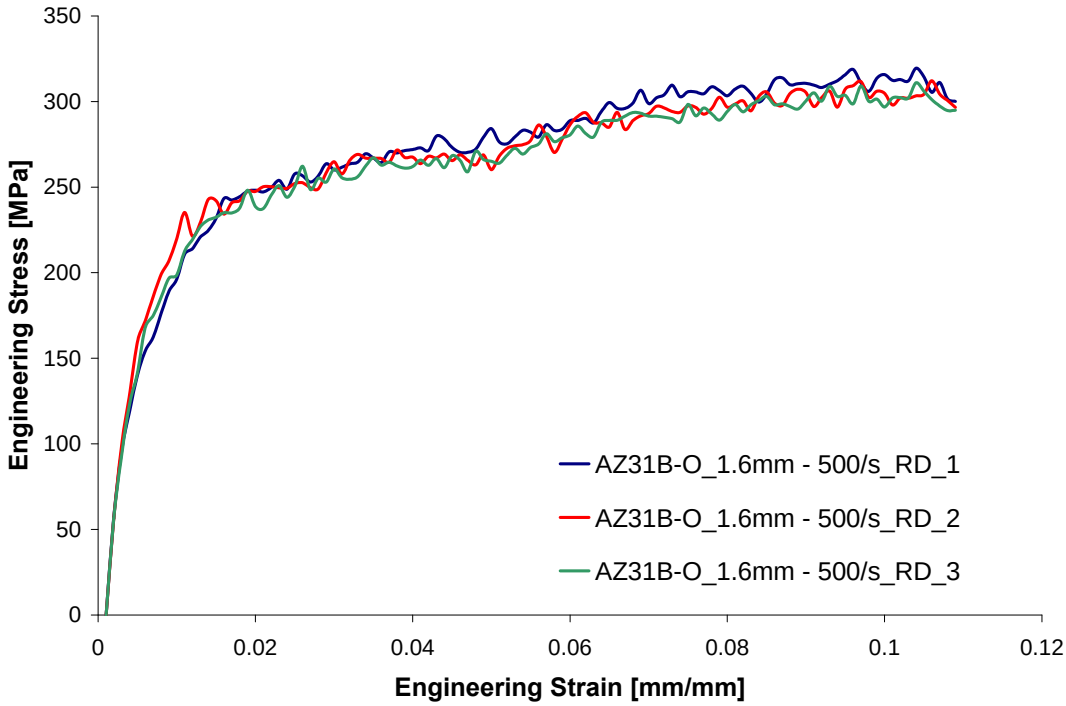
Engineering Stress [MPa]
350
300
250
200
150
100
50
0
0
0.02
0.04
0.06
0.08
0.1
0.12
Engineering Strain [mm/mm]
AZ31B-O_1.6mm - 500/s_RD_1
AZ31B-O_1.6mm - 500/s_RD_2
AZ31B-O_1.6mm - 500/s_RD_3

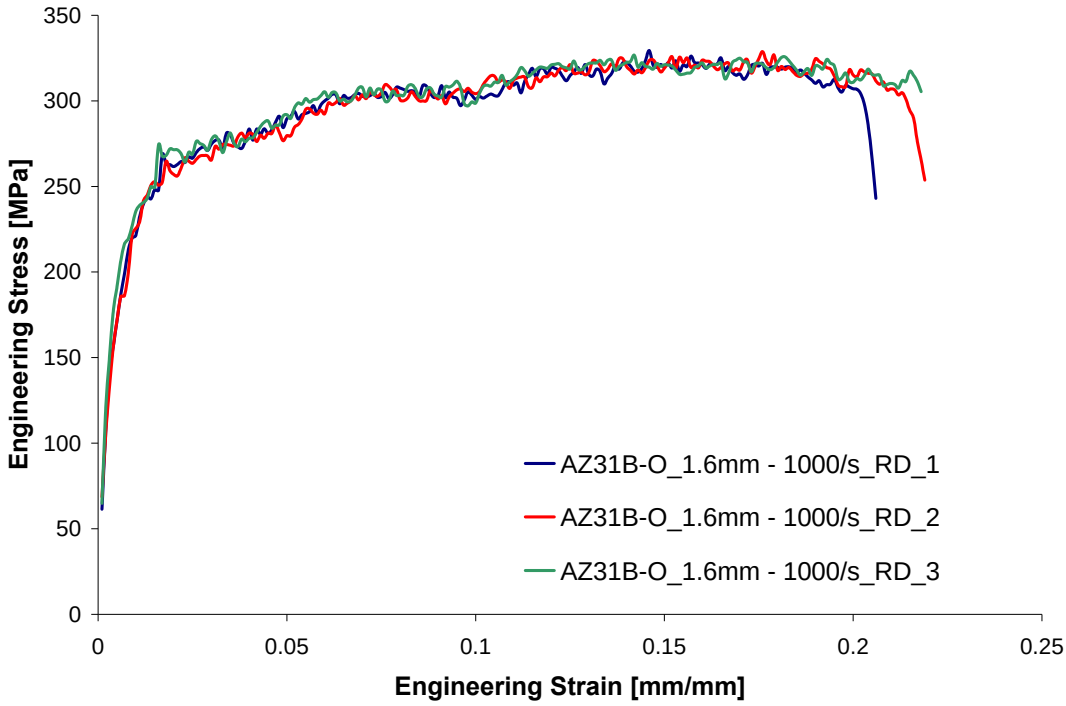
Engineering Stress [MPa]
350
300
250
200
150
100
50
0
0
0.05
0.1
0.15
0.2
0.25
Engineering Strain [mm/mm]
AZ31B-O_1.6mm - 1000/s_RD_1
AZ31B-O_1.6mm - 1000/s_RD_2
AZ31B-O_1.6mm - 1000/s_RD_3

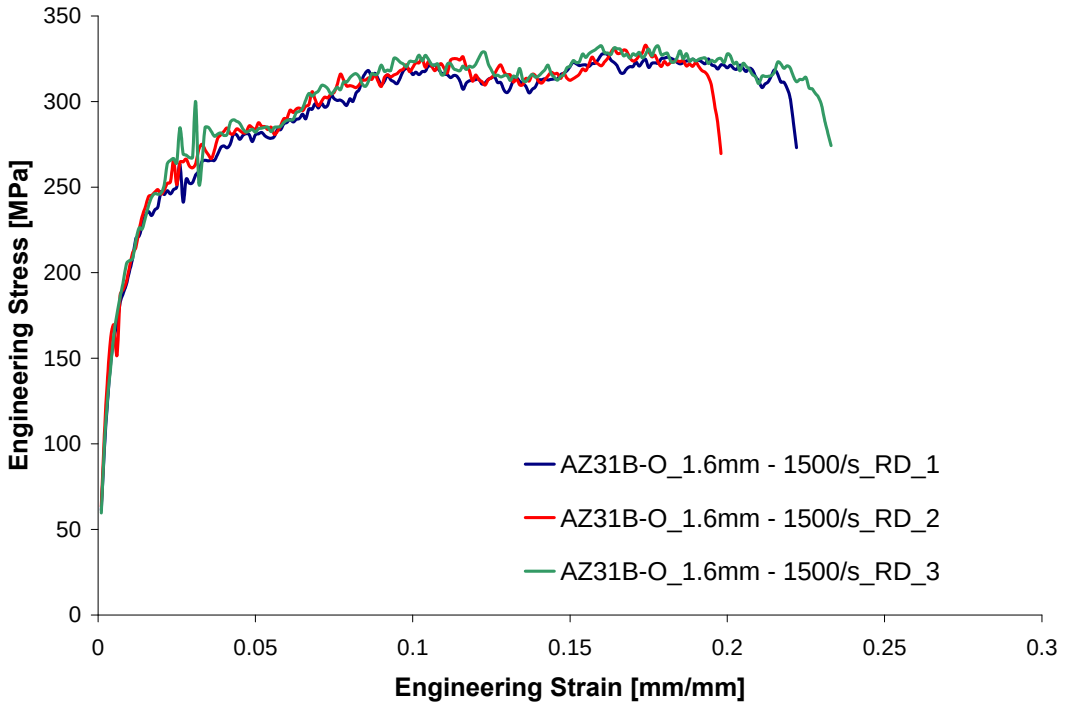
Engineering Stress [MPa]
350
300
250
200
150
100
50
0
0
0.05
0.1
0.15
0.2
0.25
0.3
Engineering Strain [mm/mm]
AZ31B-O_1.6mm - 1500/s_RD_1
AZ31B-O_1.6mm - 1500/s_RD_2
AZ31B-O_1.6mm - 1500/s_RD_3

AZ31B-O, 1.6mm, Rolling Direction, elevated temperatures

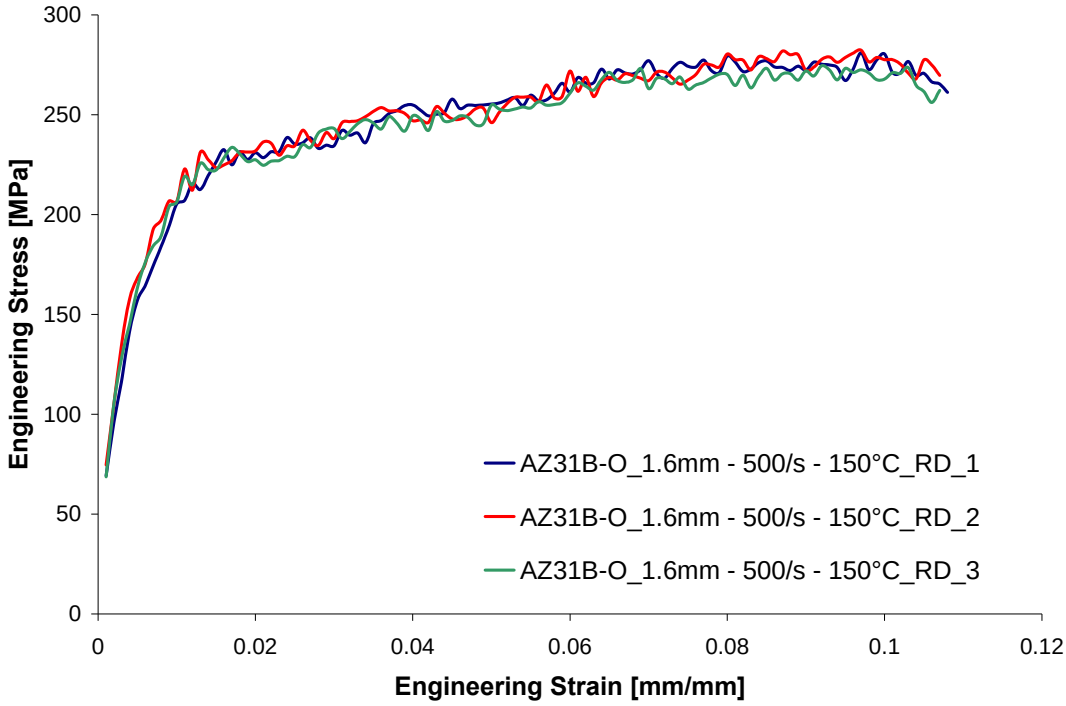

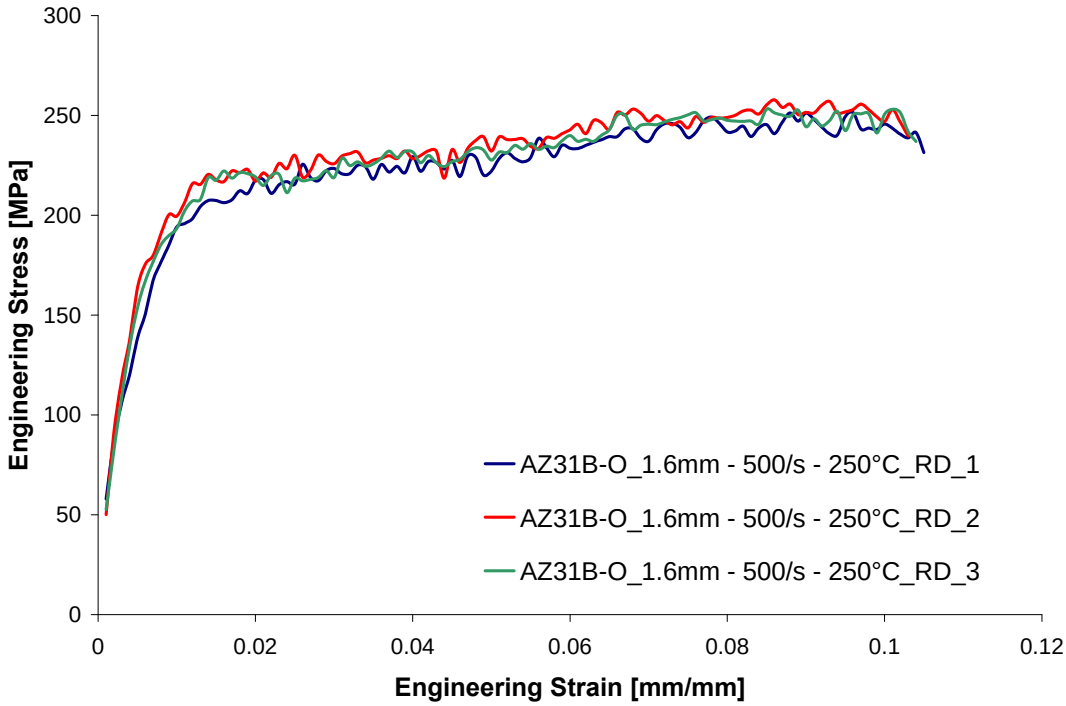

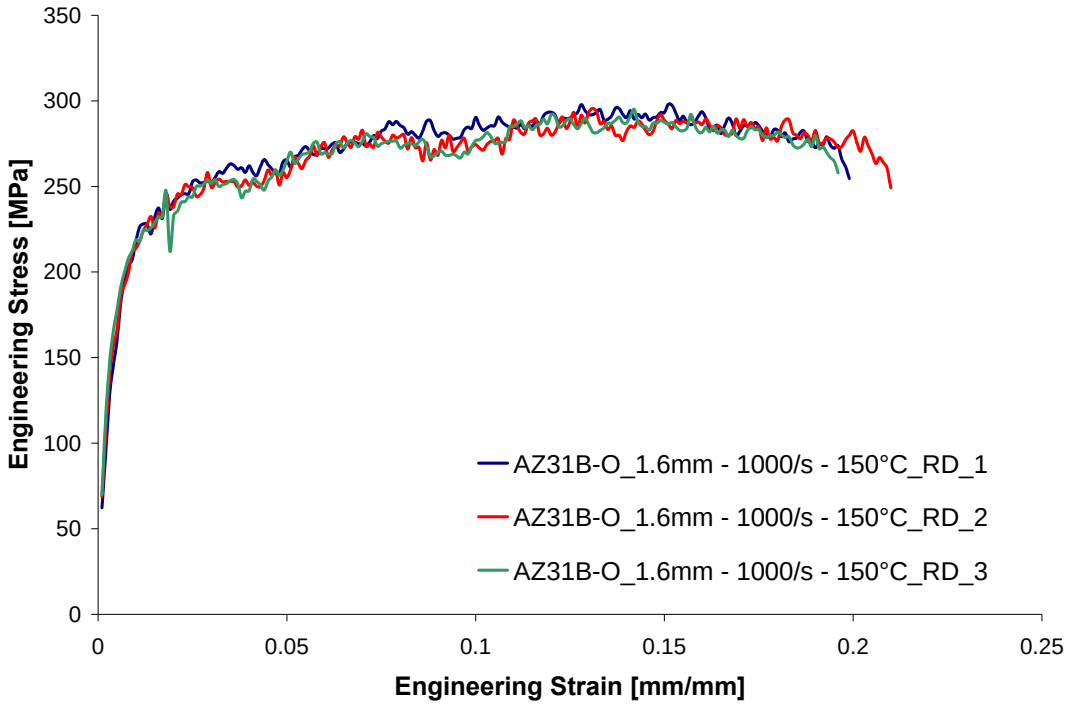
Engineering Stress [MPa]
350
300
250
200
150
100
50
0
0
0.05
0.1
0.15
0.2
0.25
Engineering Strain [mm/mm]
AZ31B-O_1.6mm - 1000/s - 150°C_RD_1
AZ31B-O_1.6mm - 1000/s - 150°C_RD_2
AZ31B-O_1.6mm - 1000/s - 150°C_RD_3

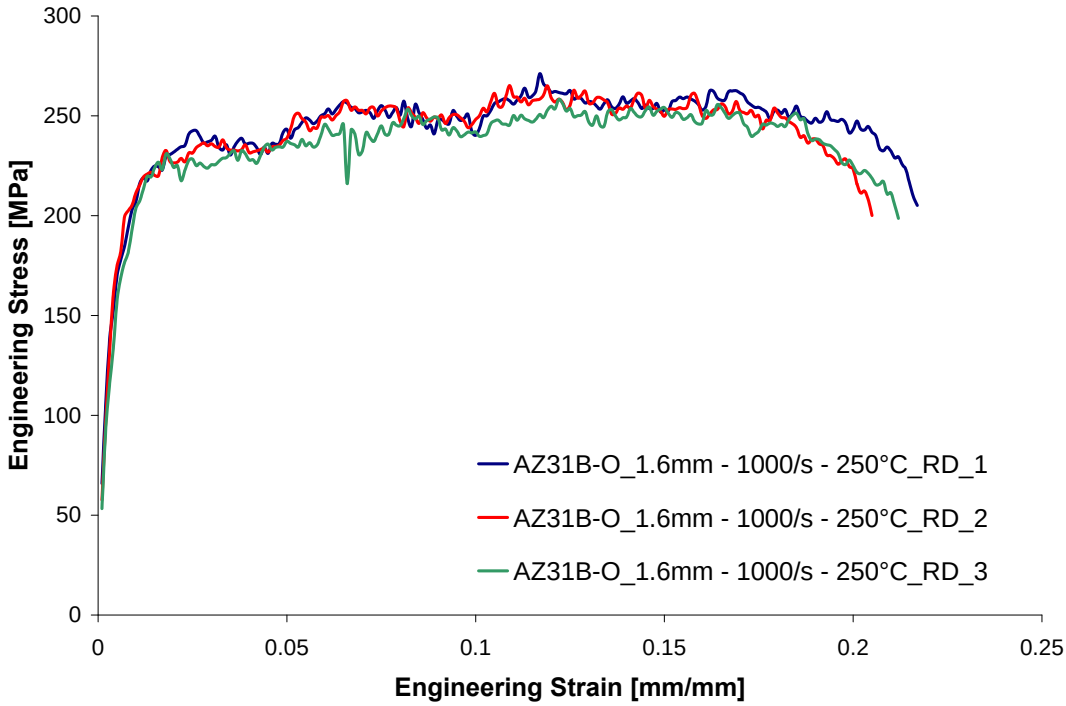
Engineering Stress [MPa]
300
250
200
150
100
50
0
0
0.05
0.1
0.15
0.2
0.25
Engineering Strain [mm/mm]
AZ31B-O_1.6mm - 1000/s - 250°C_RD_1
AZ31B-O_1.6mm - 1000/s - 250°C_RD_2
AZ31B-O_1.6mm - 1000/s - 250°C_RD_3

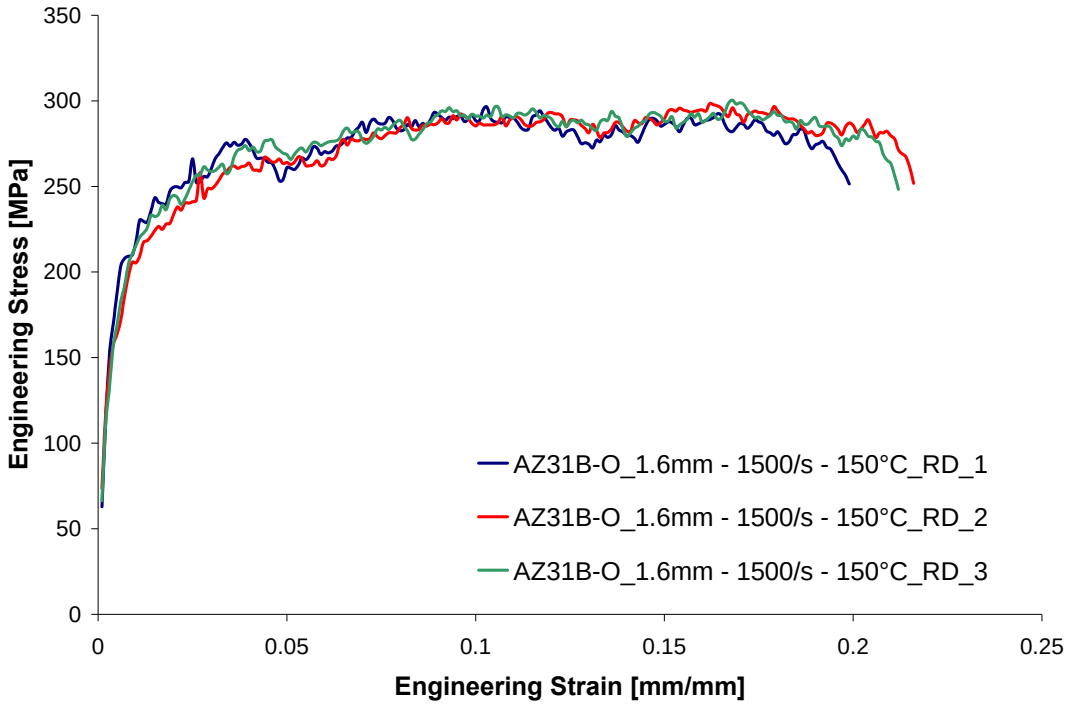
Engineering Stress [MPa]
350
300
250
200
150
100
50
0
0
0.05
0.1
0.15
0.2
0.25
Engineering Strain [mm/mm]
AZ31B-O_1.6mm - 1500/s - 150°C_RD_1
AZ31B-O_1.6mm - 1500/s - 150°C_RD_2
AZ31B-O_1.6mm - 1500/s - 150°C_RD_3

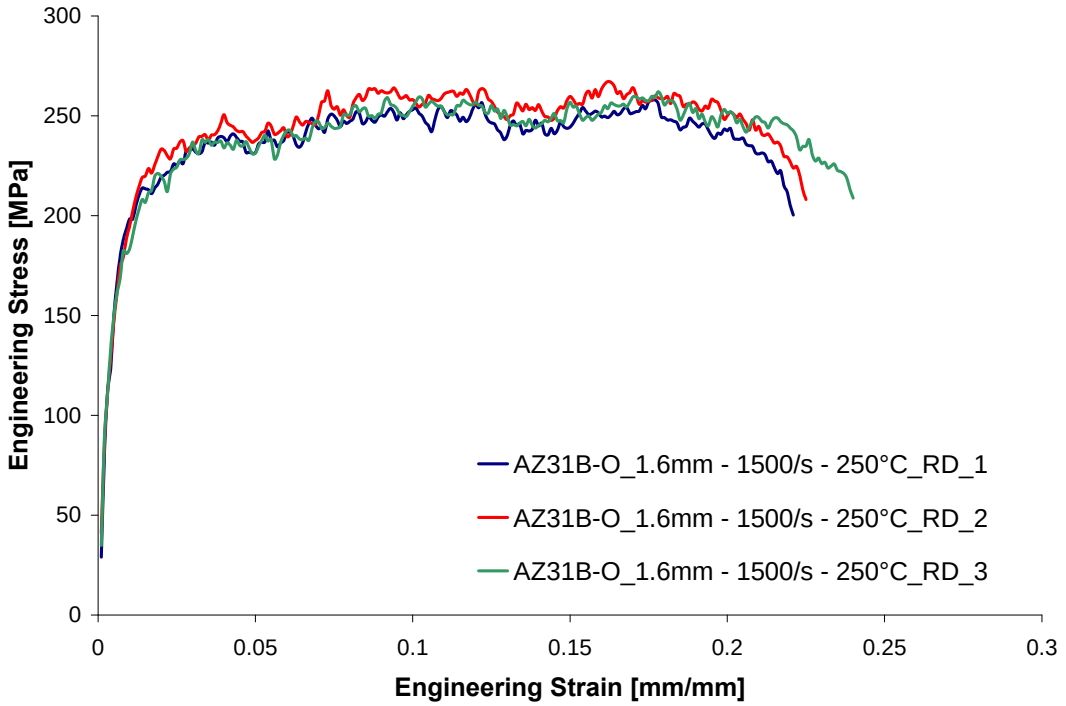
Engineering Stress [MPa]
300
250
200
150
100
50
0
0
0.05
0.1
0.15
0.2
0.25
0.3
Engineering Strain [mm/mm]
AZ31B-O_1.6mm - 1500/s - 250°C_RD_1
AZ31B-O_1.6mm - 1500/s - 250°C_RD_2
AZ31B-O_1.6mm - 1500/s - 250°C_RD_3

AZ31B-O, 1.6mm, Transverse Direction, room temperature

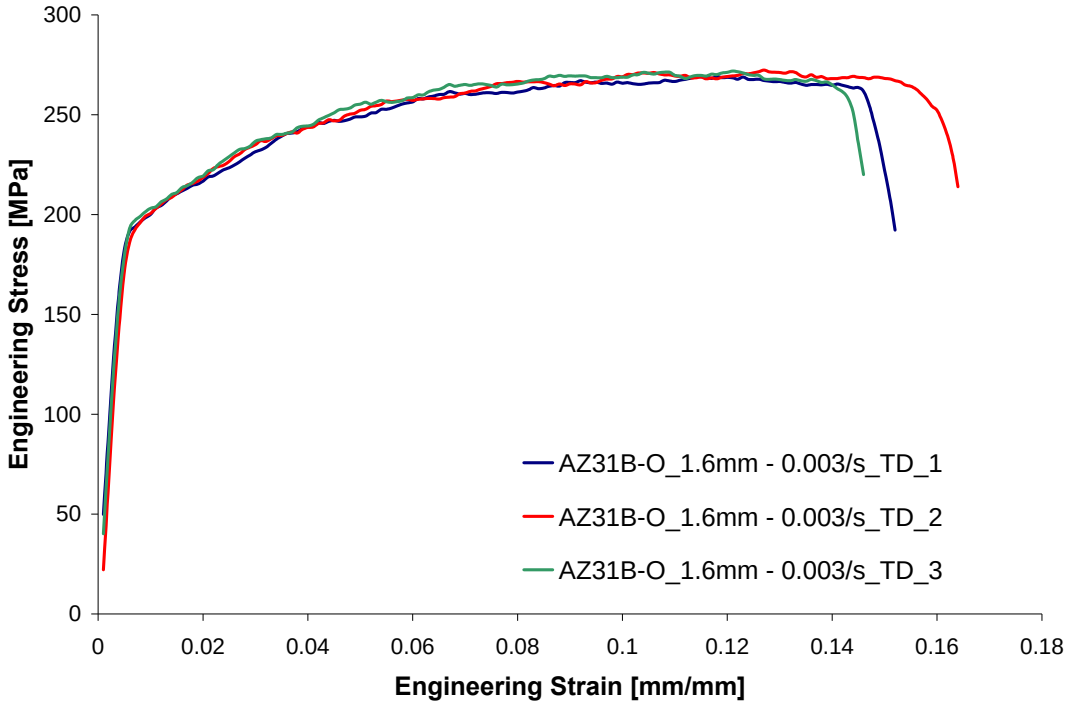

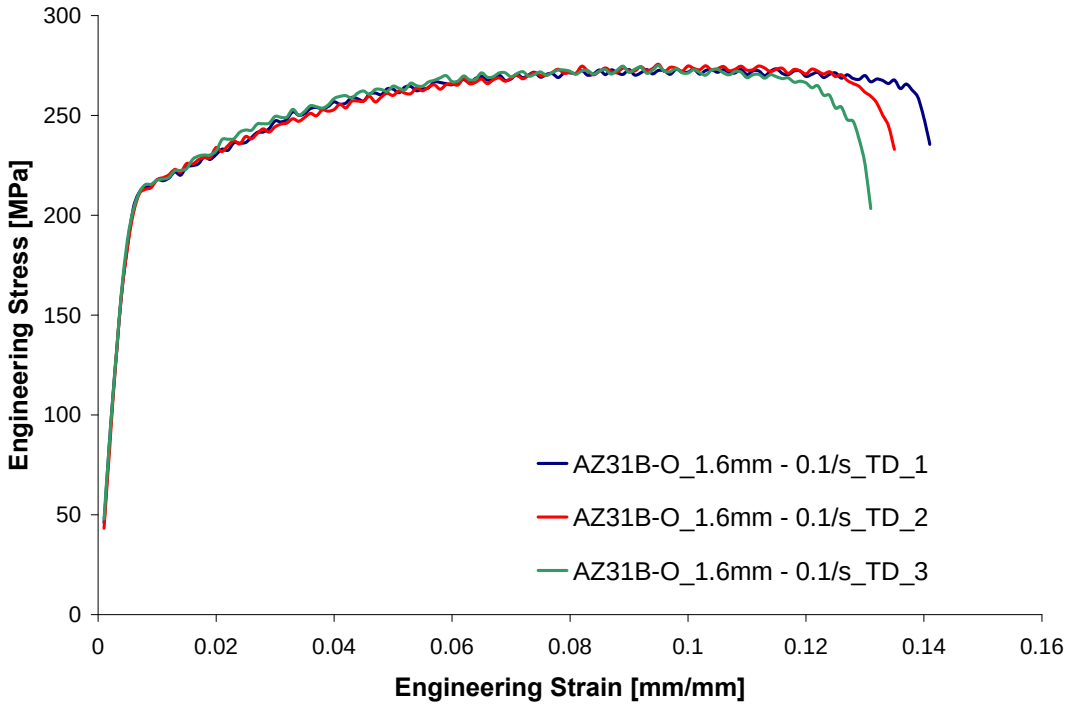

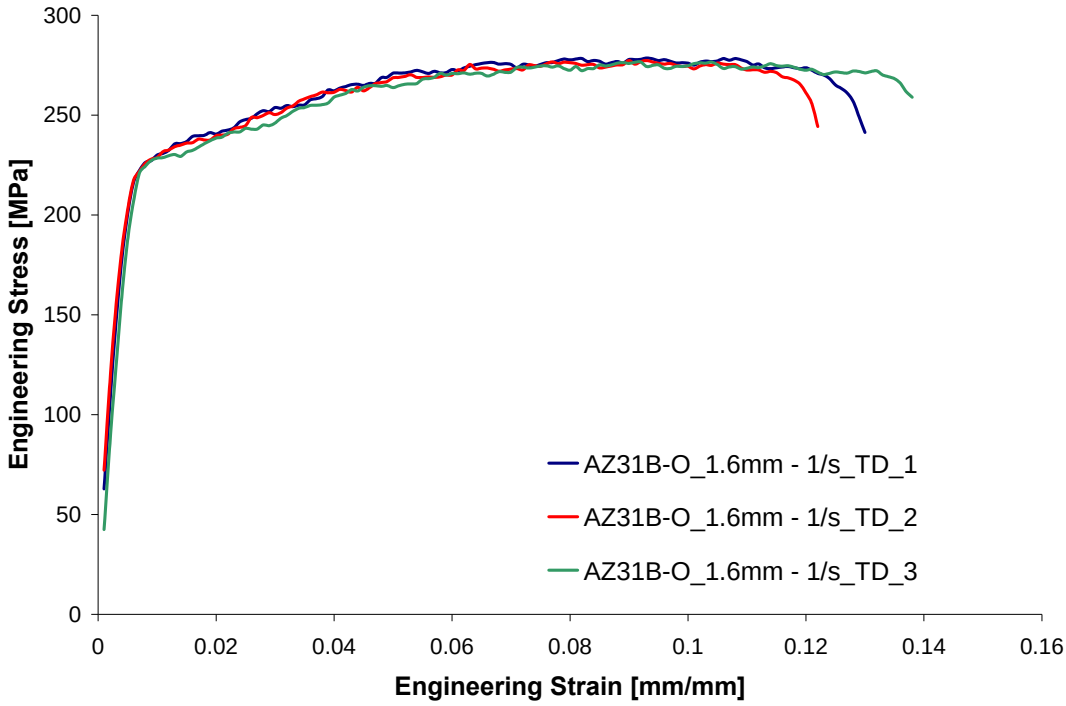
300
250
200
150
100
50
0
Engineering Stress [MPa]
0
0.02
0.04
0.06
0.08
0.1
0.12
0.14
0.16
Engineering Strain [mm/mm]
AZ31B-O_1.6mm - 1/s_TD_1
AZ31B-O_1.6mm - 1/s_TD_2
AZ31B-O_1.6mm - 1/s_TD_3

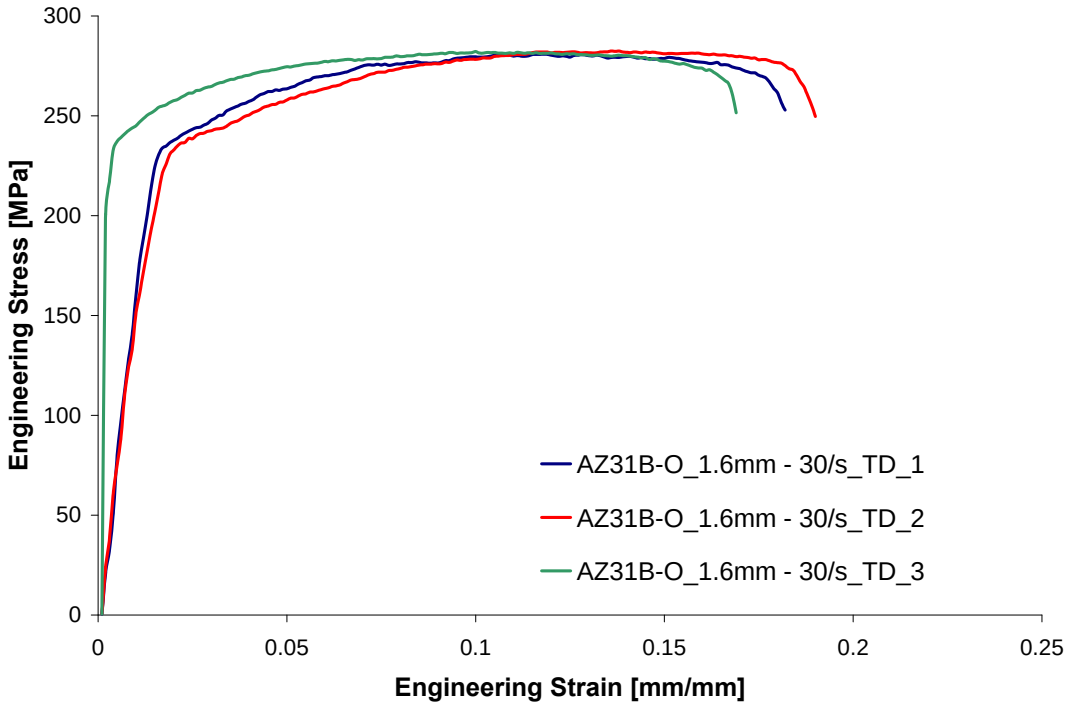
300
250
200
150
100
50
0
Engineering Stress [MPa]
0
0.05
0.1
0.15
0.2
0.25
Engineering Strain [mm/mm]
AZ31B-O_1.6mm - 30/s_TD_1
AZ31B-O_1.6mm - 30/s_TD_2
AZ31B-O_1.6mm - 30/s_TD_3

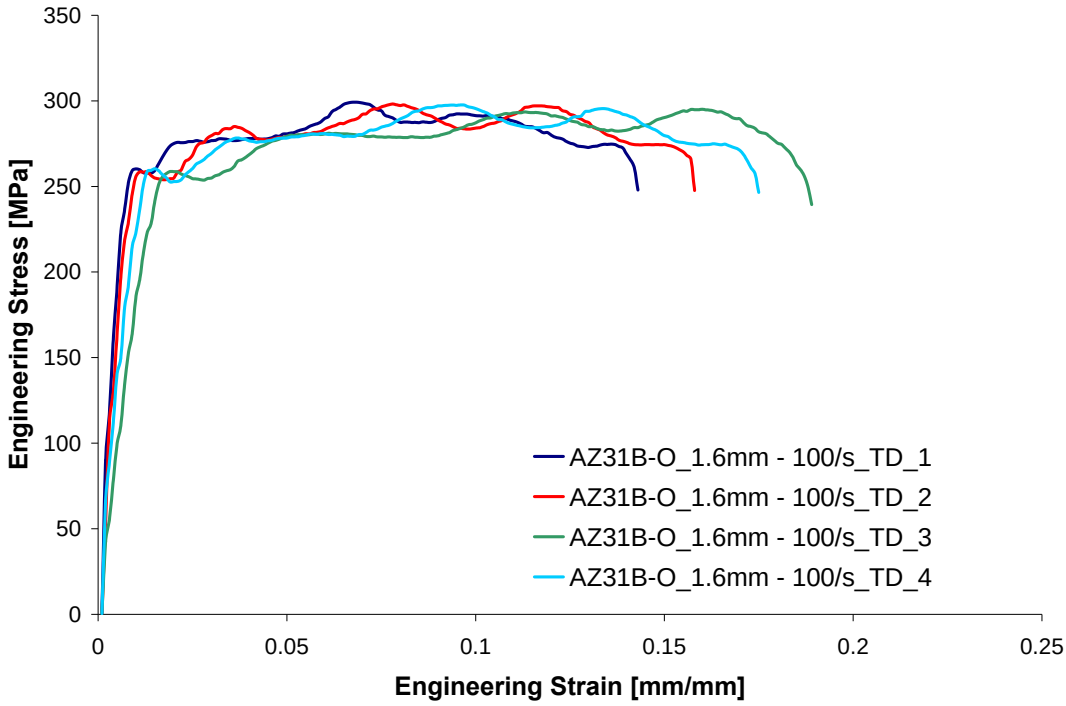
Engineering Stress [MPa]
350
300
250
200
150
100
50
0
0
0.05
0.1
0.15
0.2
0.25
Engineering Strain [mm/mm]
AZ31B-O_1.6mm - 100/s_TD_1
AZ31B-O_1.6mm - 100/s_TD_2
AZ31B-O_1.6mm - 100/s_TD_3
AZ31B-O_1.6mm - 100/s_TD_4

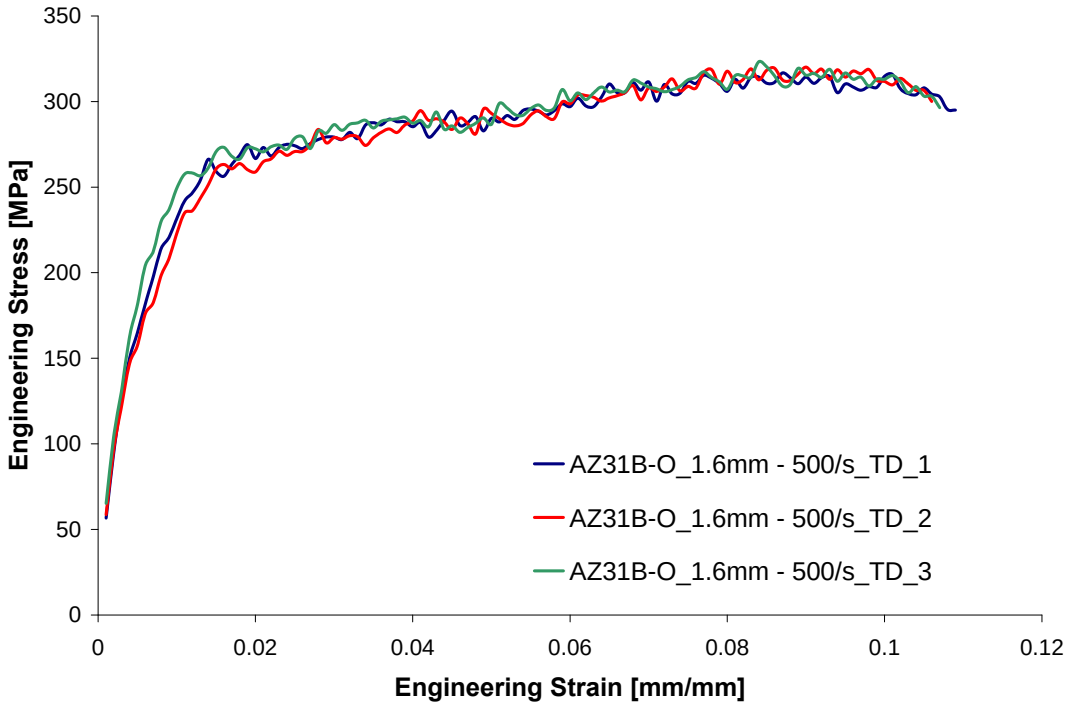
Engineering Stress [MPa]
350
300
250
200
150
100
50
0
0
0.02
0.04
0.06
0.08
0.1
0.12
Engineering Strain [mm/mm]
AZ31B-O_1.6mm - 500/s_TD_1
AZ31B-O_1.6mm - 500/s_TD_2
AZ31B-O_1.6mm - 500/s_TD_3

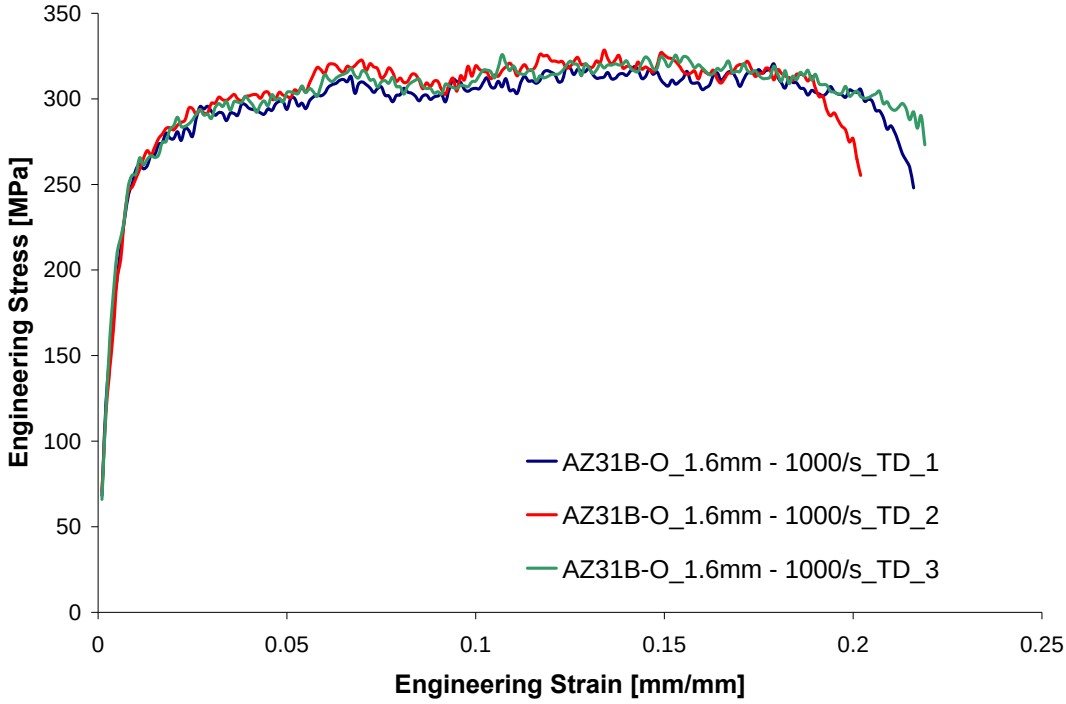
Engineering Stress [MPa]
Engineering Strain [mm/mm]
AZ31B-O_1.6mm - 1000/s_TD_1
AZ31B-O_1.6mm - 1000/s_TD_2
AZ31B-O_1.6mm - 1000/s_TD_3

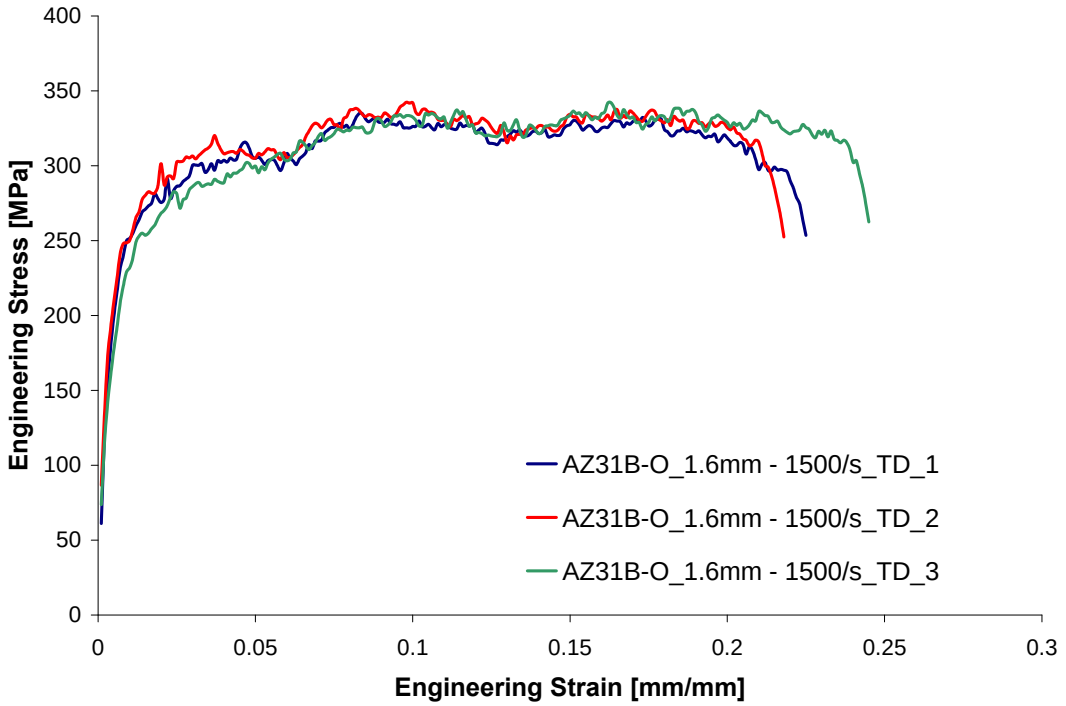
Engineering Stress [MPa]
Engineering Strain [mm/mm]
AZ31B-O_1.6mm - 1500/s_TD_1
AZ31B-O_1.6mm - 1500/s_TD_2
AZ31B-O_1.6mm - 1500/s_TD_3

AZ31B-O, 1.6mm, Transverse Direction, elevated temperatures

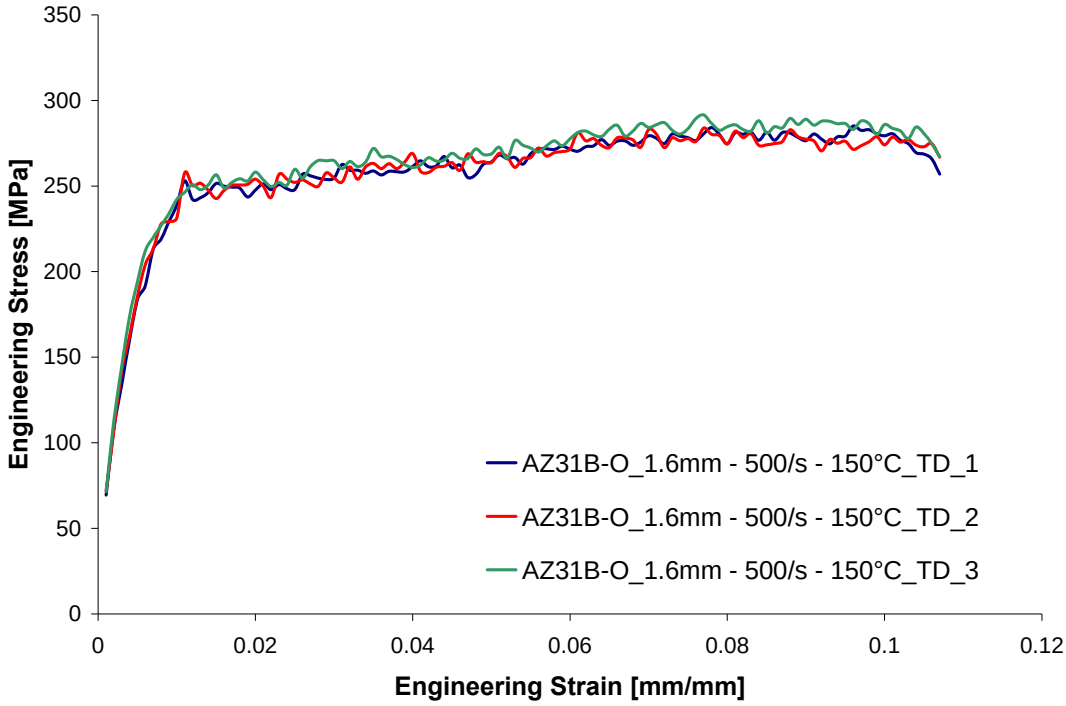

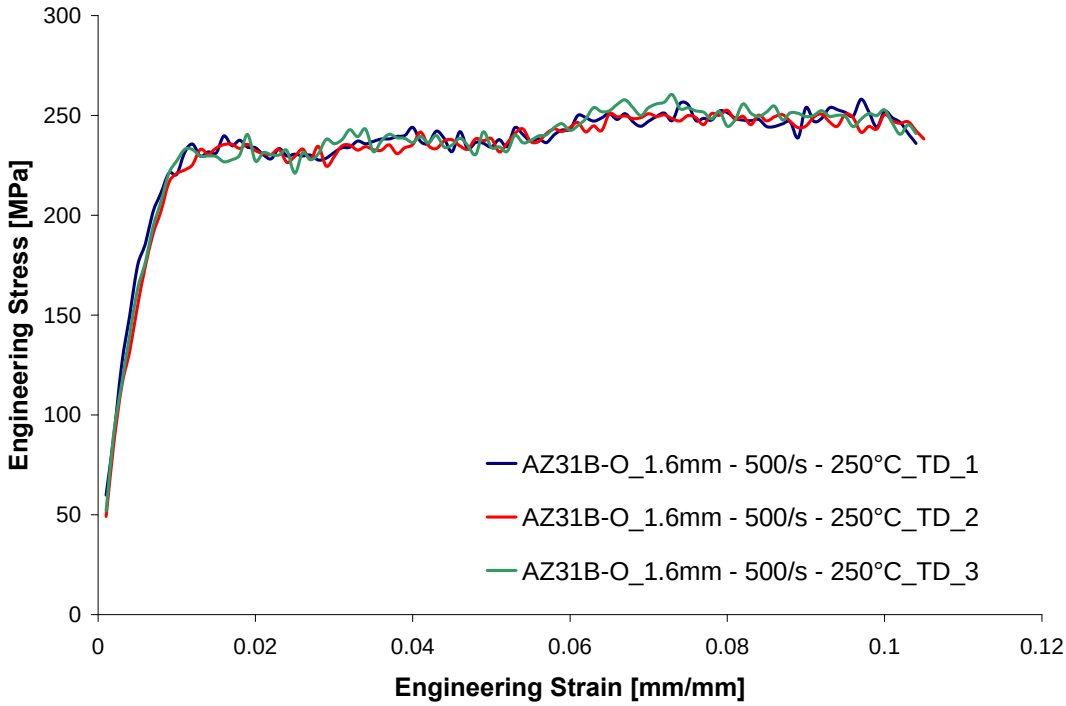

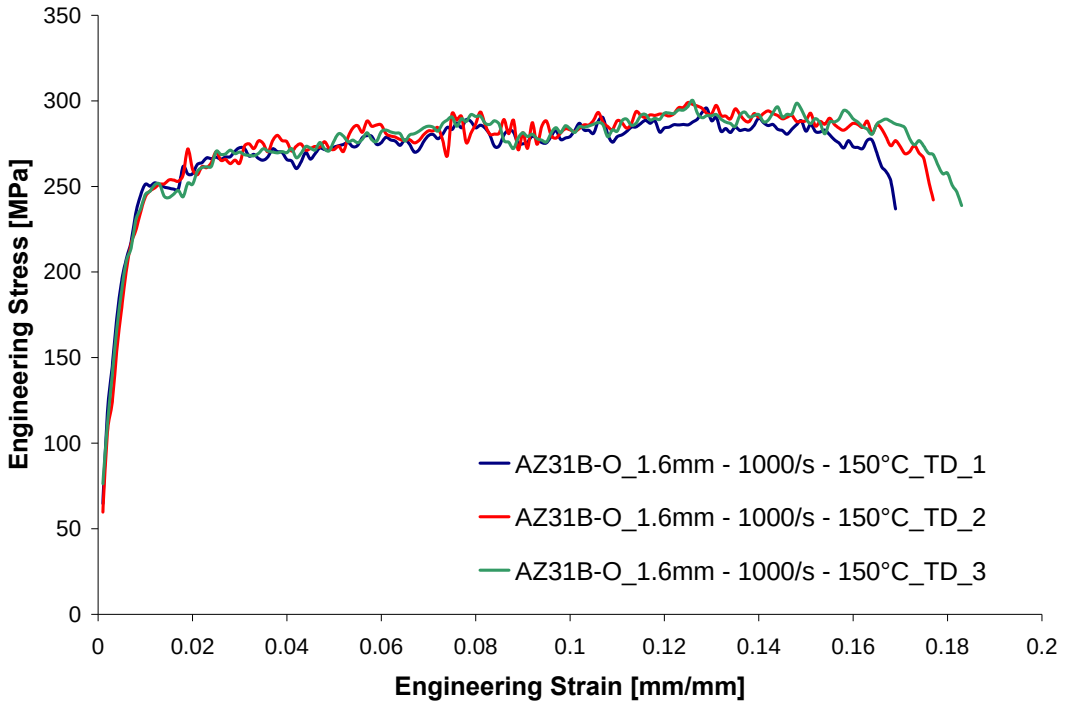
Engineering Stress [MPa]
350
300
250
200
150
100
50
0
0
0.02
0.04
0.06
0.08
0.1
0.12
0.14
0.16
0.18
0.2
Engineering Strain [mm/mm]
AZ31B-O_1.6mm - 1000/s - 150°C_TD_1
AZ31B-O_1.6mm - 1000/s - 150°C_TD_2
AZ31B-O_1.6mm - 1000/s - 150°C_TD_3

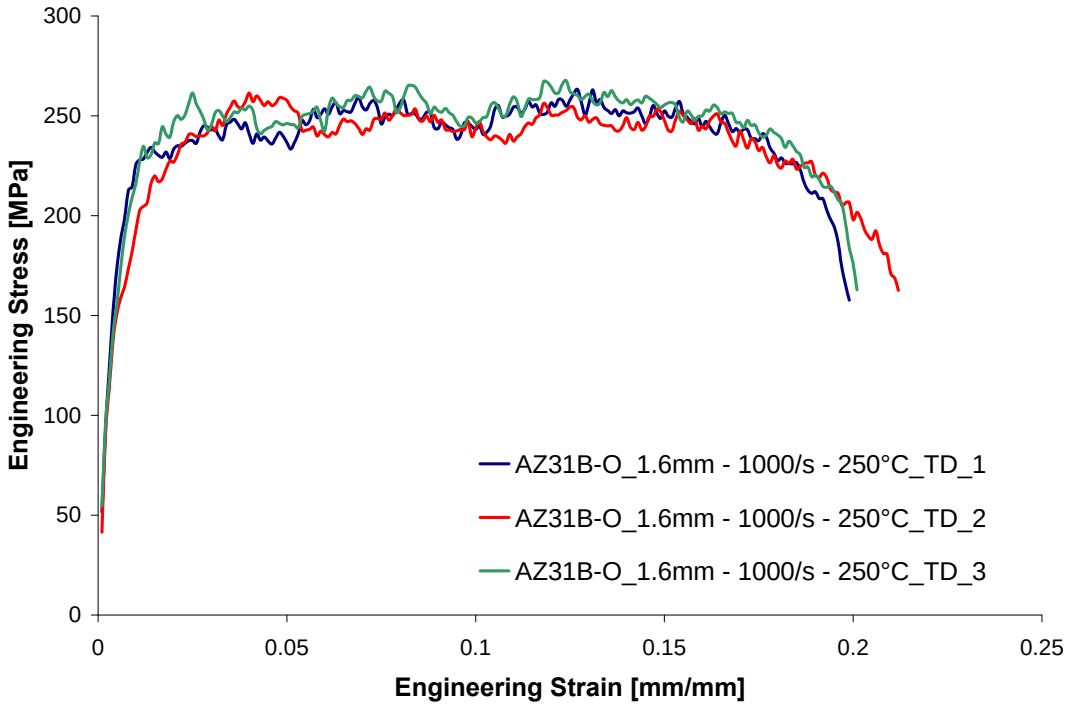
Engineering Stress [MPa]
300
250
200
150
100
50
0
0
0.05
0.1
0.15
0.2
0.25
Engineering Strain [mm/mm]
AZ31B-O_1.6mm - 1000/s - 250°C_TD_1
AZ31B-O_1.6mm - 1000/s - 250°C_TD_2
AZ31B-O_1.6mm - 1000/s - 250°C_TD_3

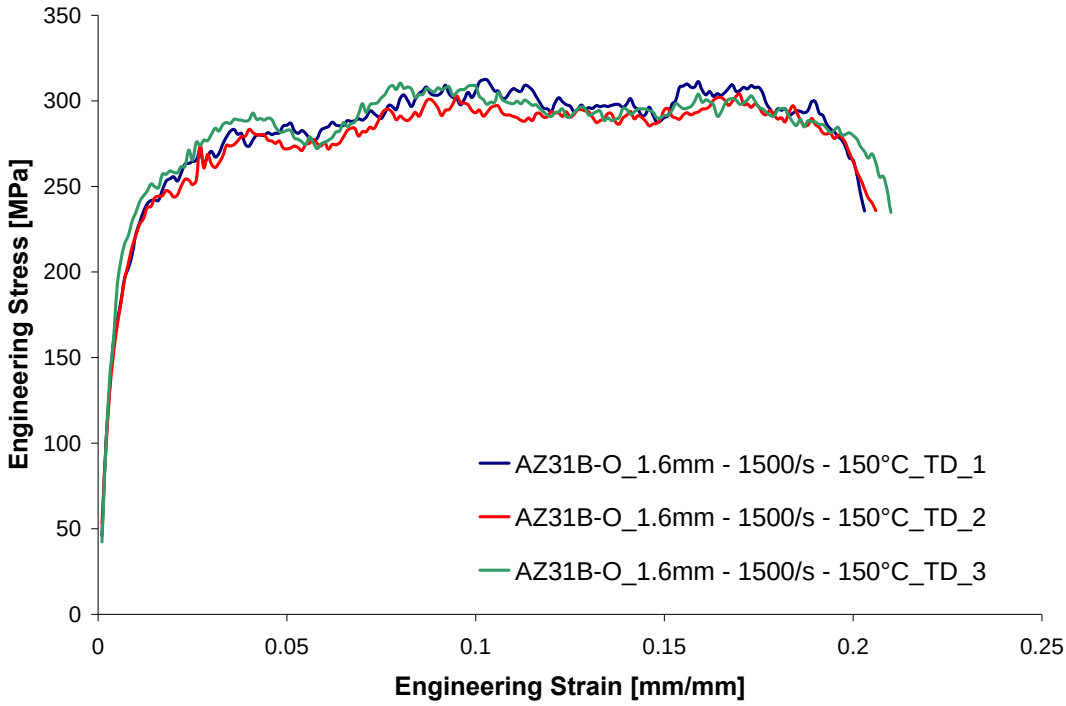
Engineering Stress [MPa]
350
300
250
200
150
100
50
0
0
0.05
0.1
0.15
0.2
0.25
Engineering Strain [mm/mm]
AZ31B-O_1.6mm - 1500/s - 150°C_TD_1
AZ31B-O_1.6mm - 1500/s - 150°C_TD_2
AZ31B-O_1.6mm - 1500/s - 150°C_TD_3

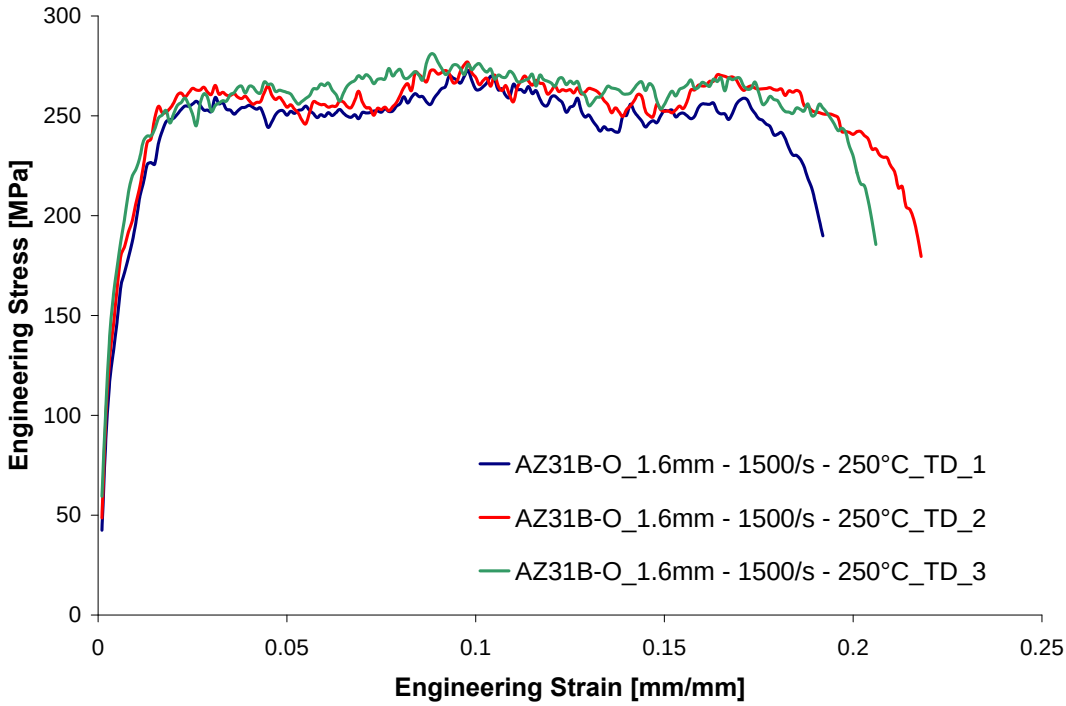
Engineering Stress [MPa]
300
250
200
150
100
50
0
0
0.05
0.1
0.15
0.2
0.25
Engineering Strain [mm/mm]
AZ31B-O_1.6mm - 1500/s - 250°C_TD_1
AZ31B-O_1.6mm - 1500/s - 250°C_TD_2
AZ31B-O_1.6mm - 1500/s - 250°C_TD_3

Appendix B3:

AZ31B-O, 2.5mm, Rolling Direction, room temperature

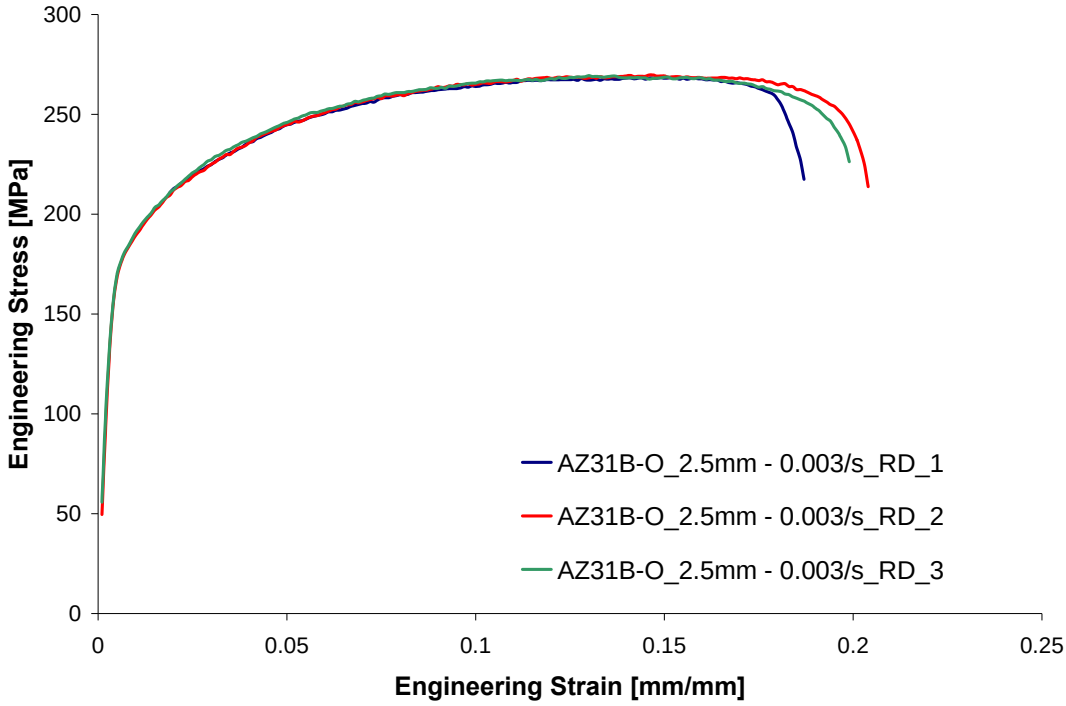

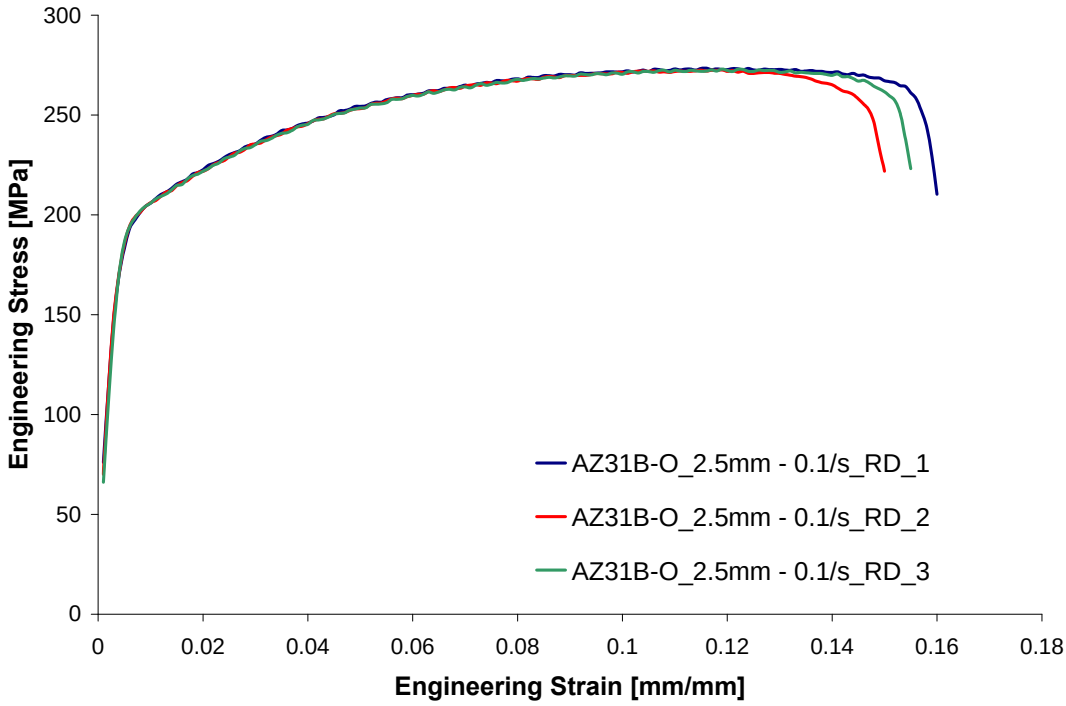

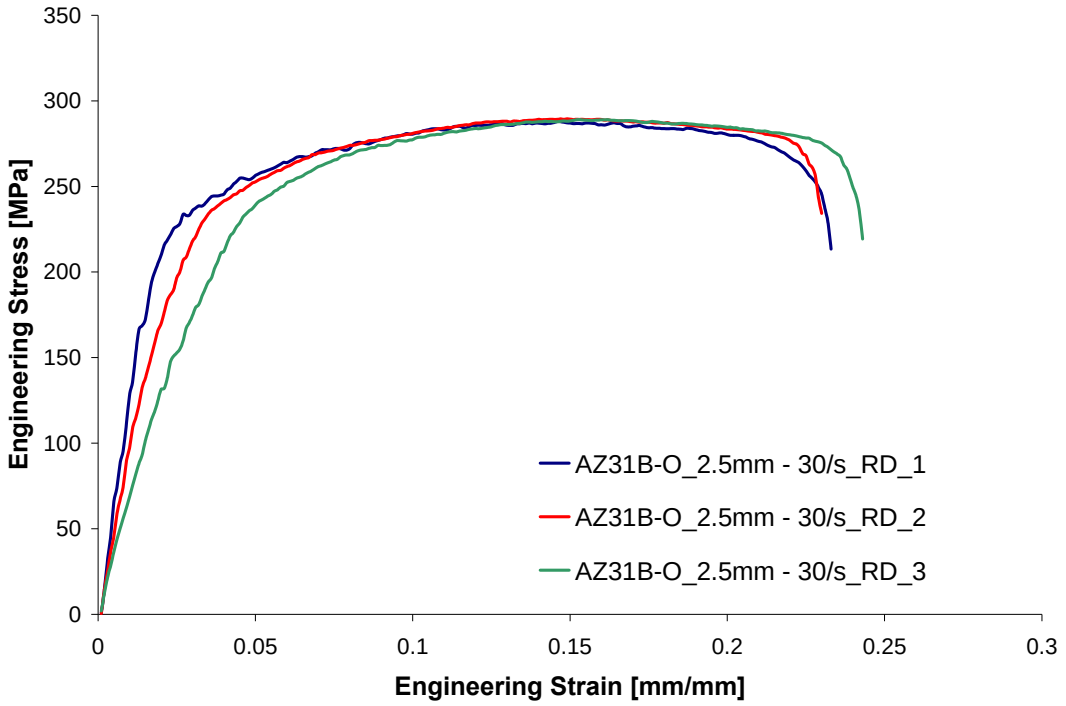
Engineering Stress [MPa]
350
300
250
200
150
100
50
0
0
0.05
0.1
0.15
0.2
0.25
0.3
Engineering Strain [mm/mm]
AZ31B-O_2.5mm - 30/s_RD_1
AZ31B-O_2.5mm - 30/s_RD_2
AZ31B-O_2.5mm - 30/s_RD_3

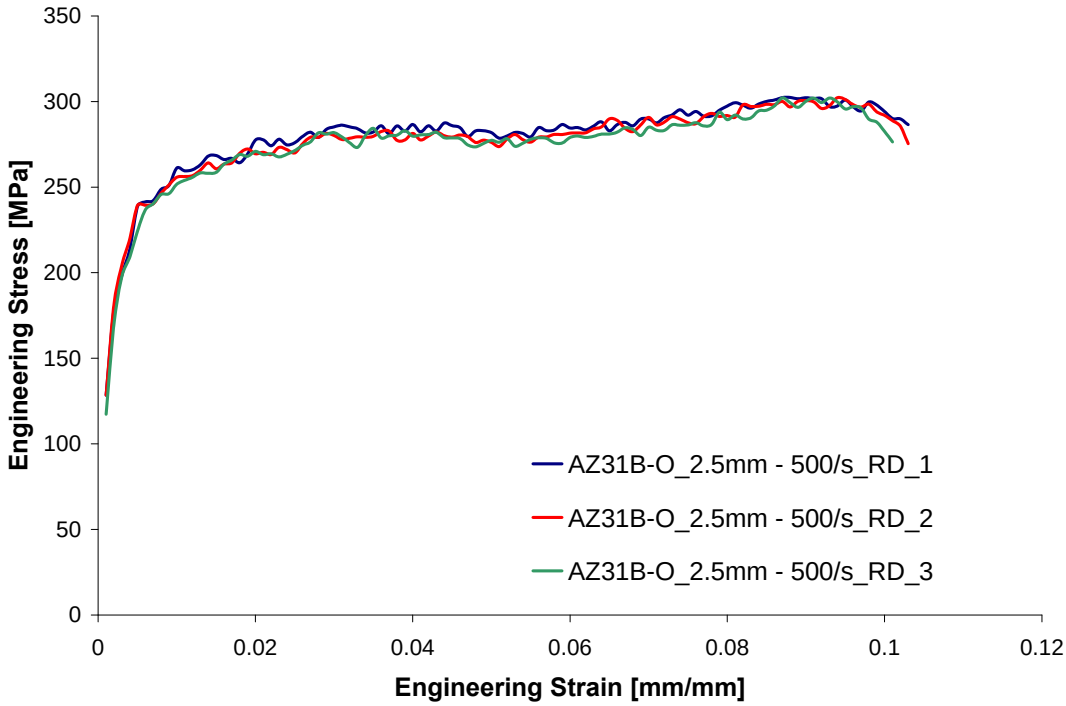
Engineering Stress [MPa]
350
300
250
200
150
100
50
0
0
0.02
0.04
0.06
0.08
0.1
0.12
Engineering Strain [mm/mm]
AZ31B-O_2.5mm - 500/s_RD_1
AZ31B-O_2.5mm - 500/s_RD_2
AZ31B-O_2.5mm - 500/s_RD_3

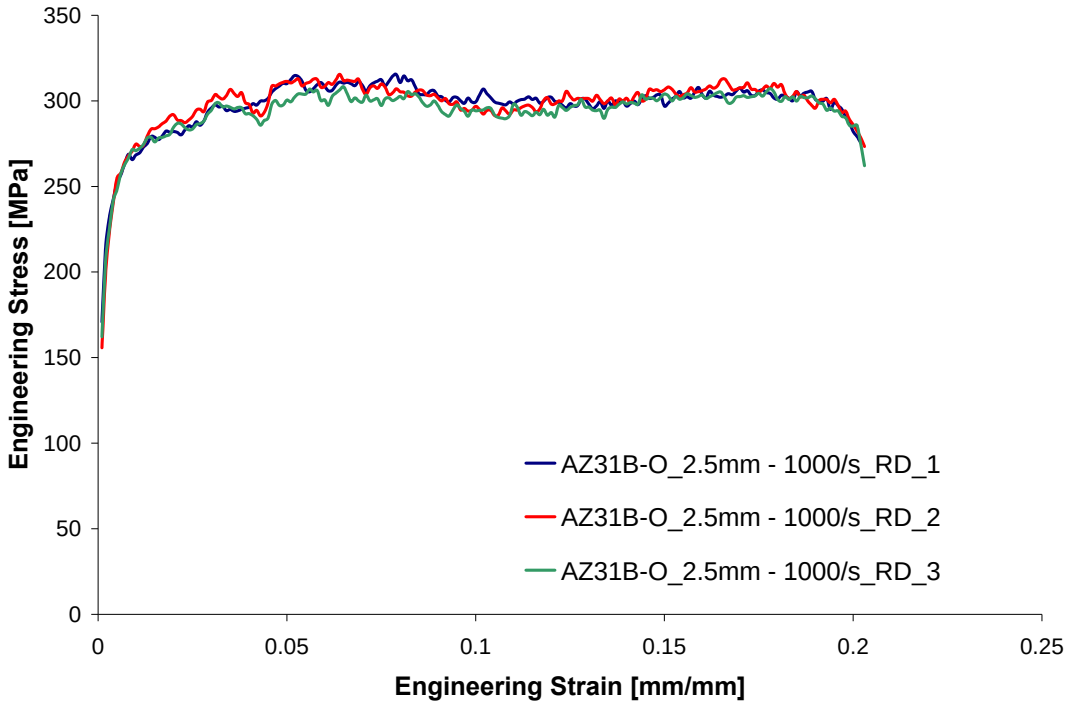

AZ31B-O, 2.5mm, Transverse Direction, room temperature

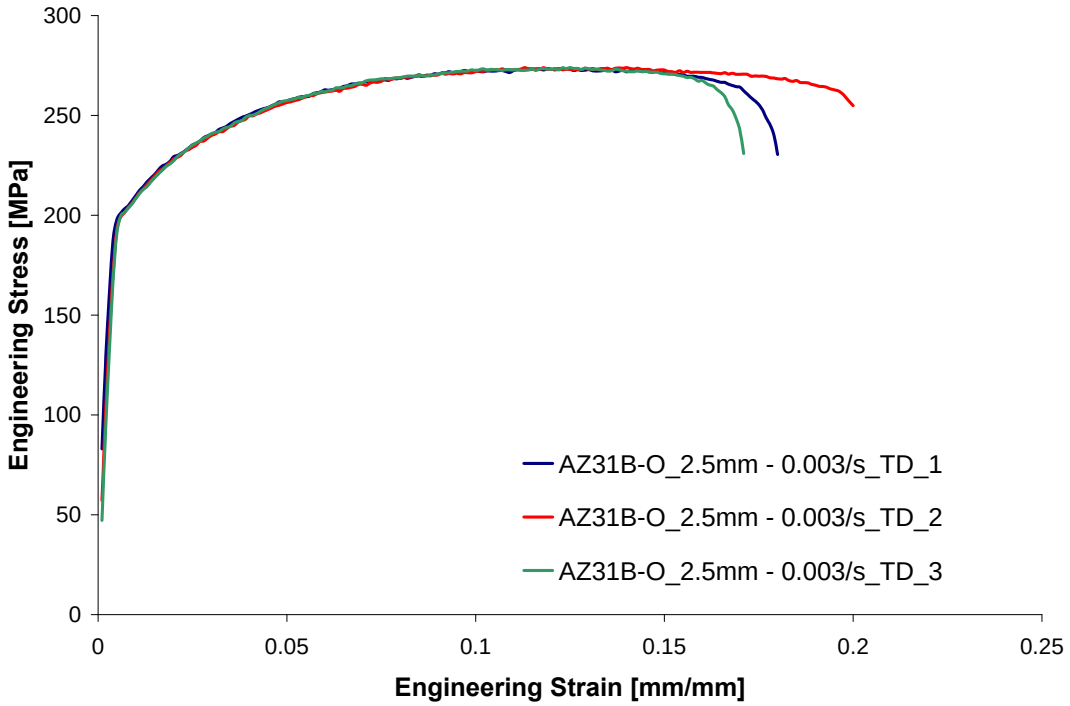

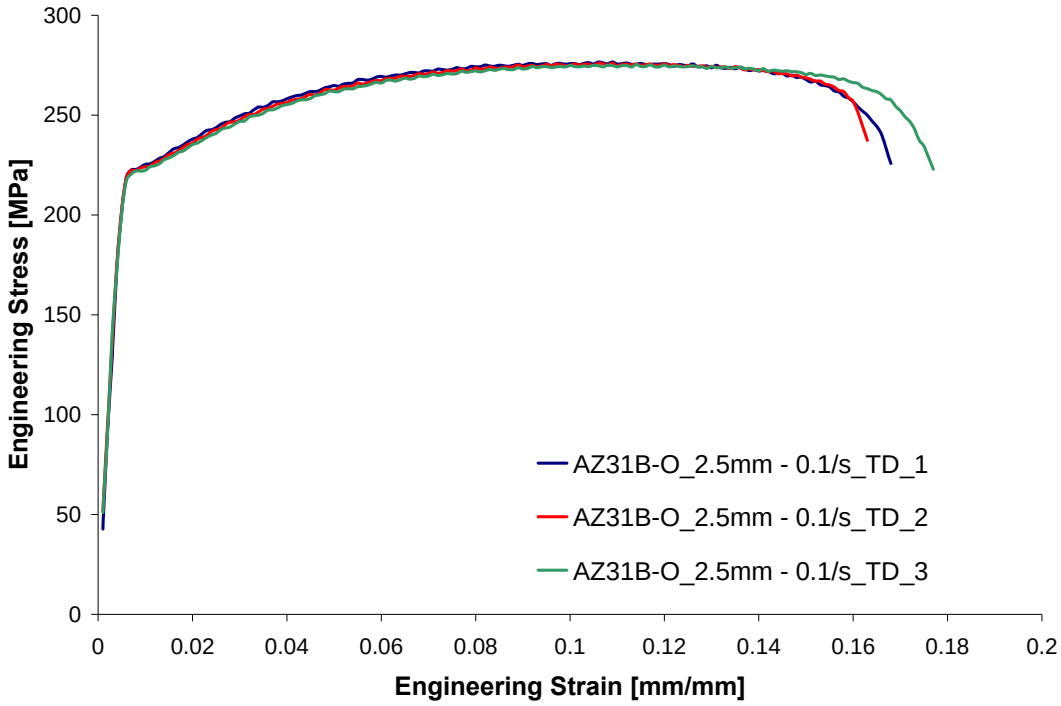
300
250
200
150
100
50
0
Engineering Stress [MPa]
0
0.02
0.04
0.06
0.08
0.1
0.12
0.14
0.16
0.18
0.2
Engineering Strain [mm/mm]
AZ31B-O_2.5mm - 0.1/s_TD_1
AZ31B-O_2.5mm - 0.1/s_TD_2
AZ31B-O_2.5mm - 0.1/s_TD_3

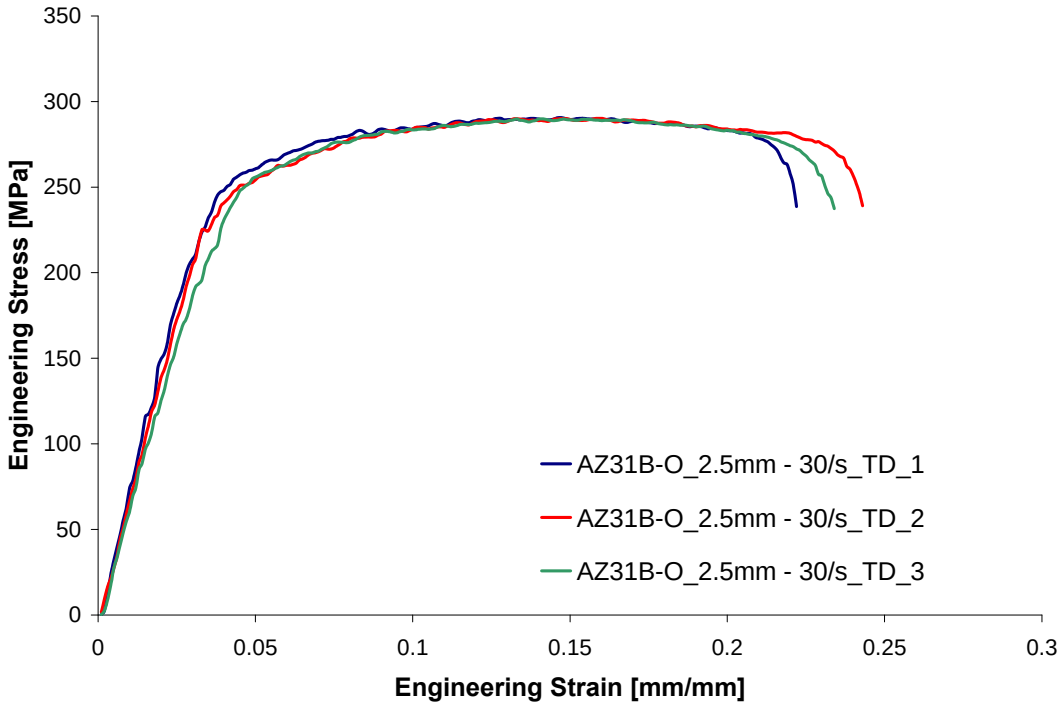
350
300
250
200
150
100
50
0
Engineering Stress [MPa]
0
0.05
0.1
0.15
0.2
0.25
0.3
Engineering Strain [mm/mm]
AZ31B-O_2.5mm - 30/s_TD_1
AZ31B-O_2.5mm - 30/s_TD_2
AZ31B-O_2.5mm - 30/s_TD_3

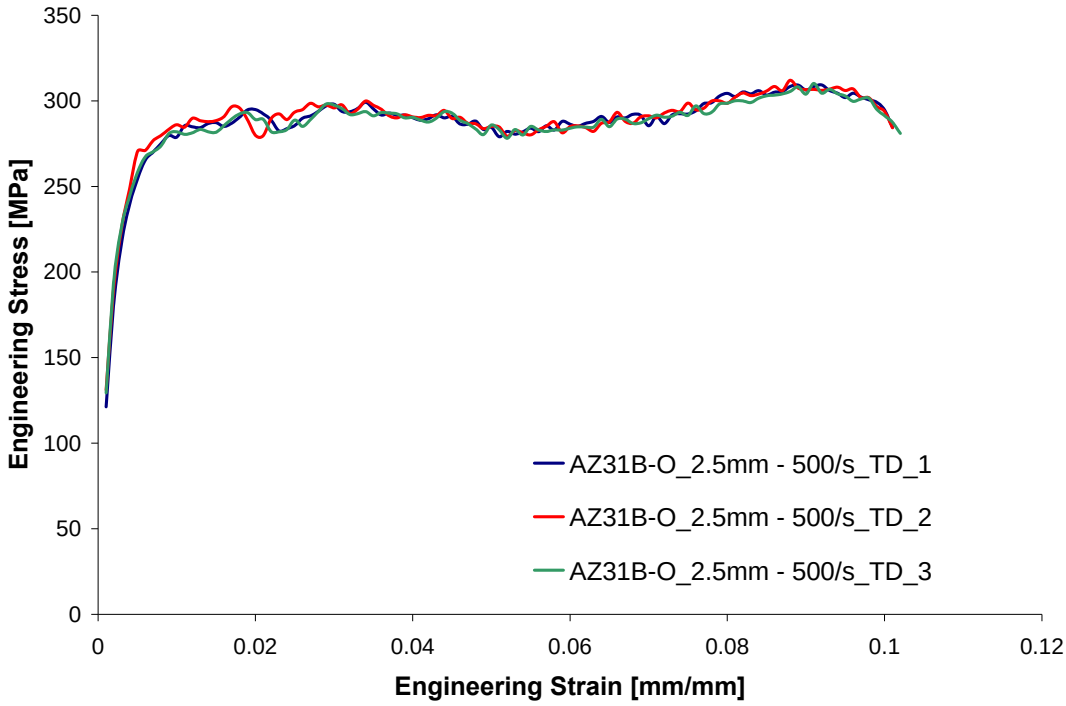
Engineering Stress [MPa]
350
300
250
200
150
100
50
0
0
0.02
0.04
0.06
0.08
0.1
0.12
Engineering Strain [mm/mm]
AZ31B-O_2.5mm - 500/s_TD_1
AZ31B-O_2.5mm - 500/s_TD_2
AZ31B-O_2.5mm - 500/s_TD_3

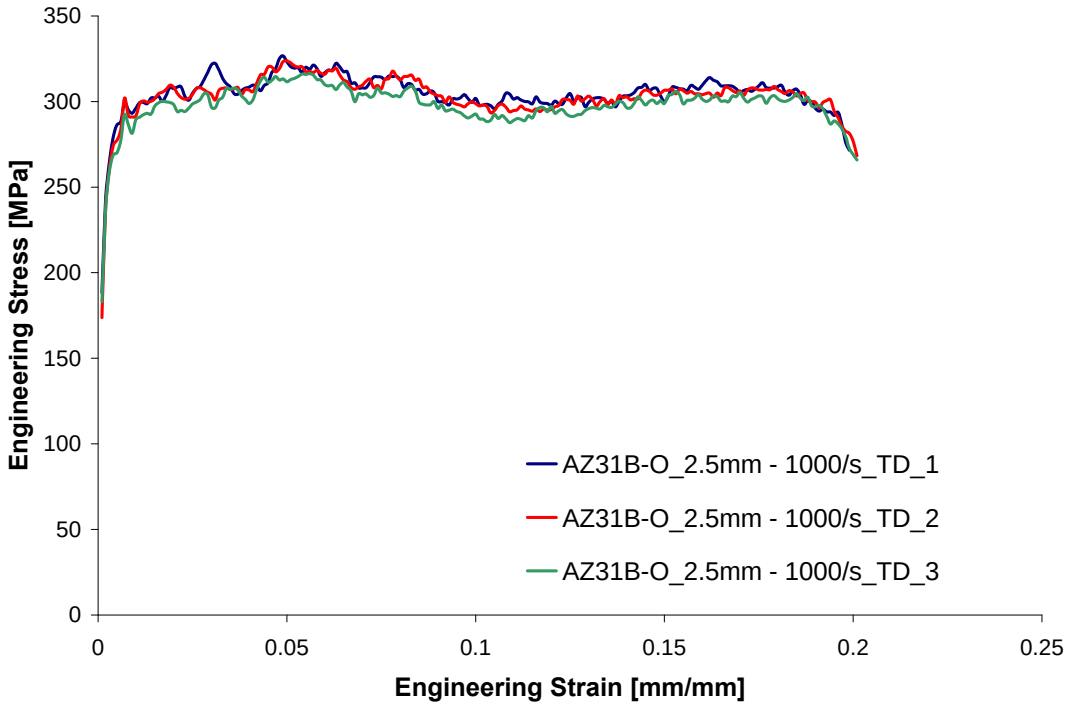
Engineering Stress [MPa]
350
300
250
200
150
100
50
0
0
0.05
0.1
0.15
0.2
0.25
Engineering Strain [mm/mm]
AZ31B-O_2.5mm - 1000/s_TD_1
AZ31B-O_2.5mm - 1000/s_TD_2
AZ31B-O_2.5mm - 1000/s_TD_3

Appendix B4:

AZ31B-O, 1.0mm, Rolling Direction, room temperature

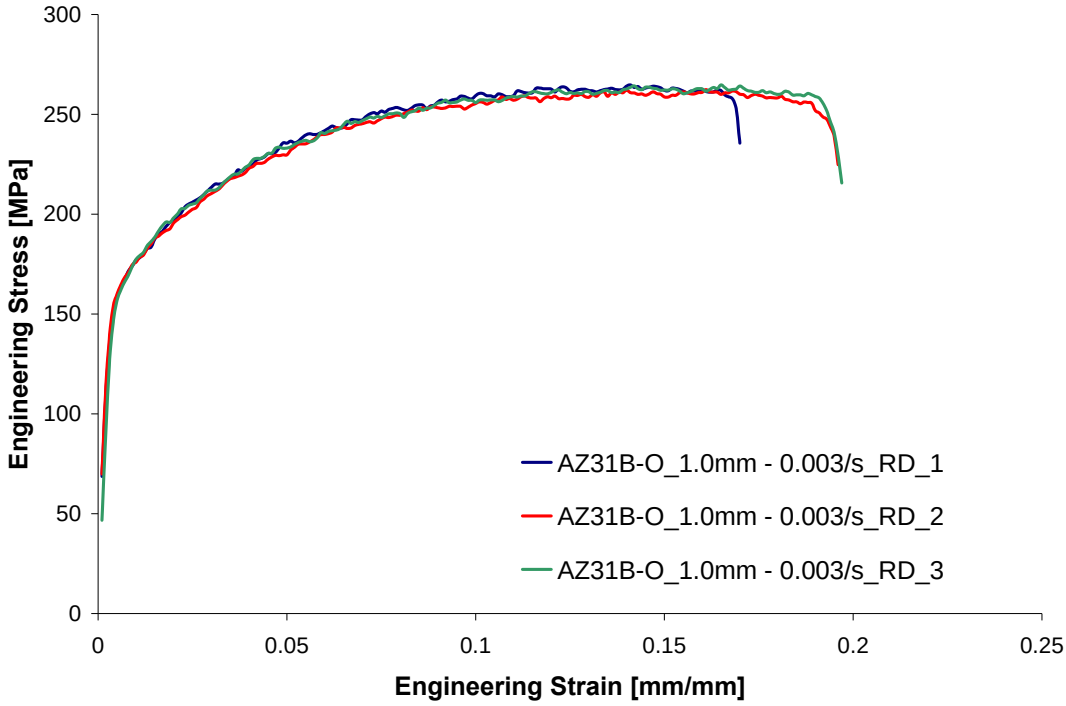

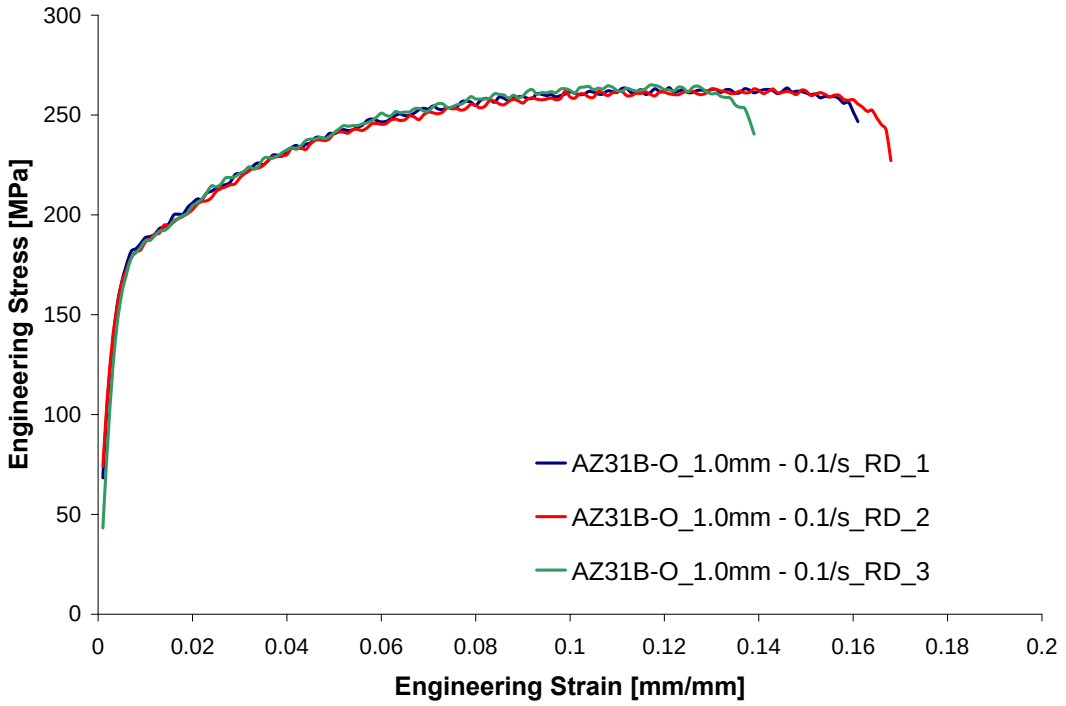

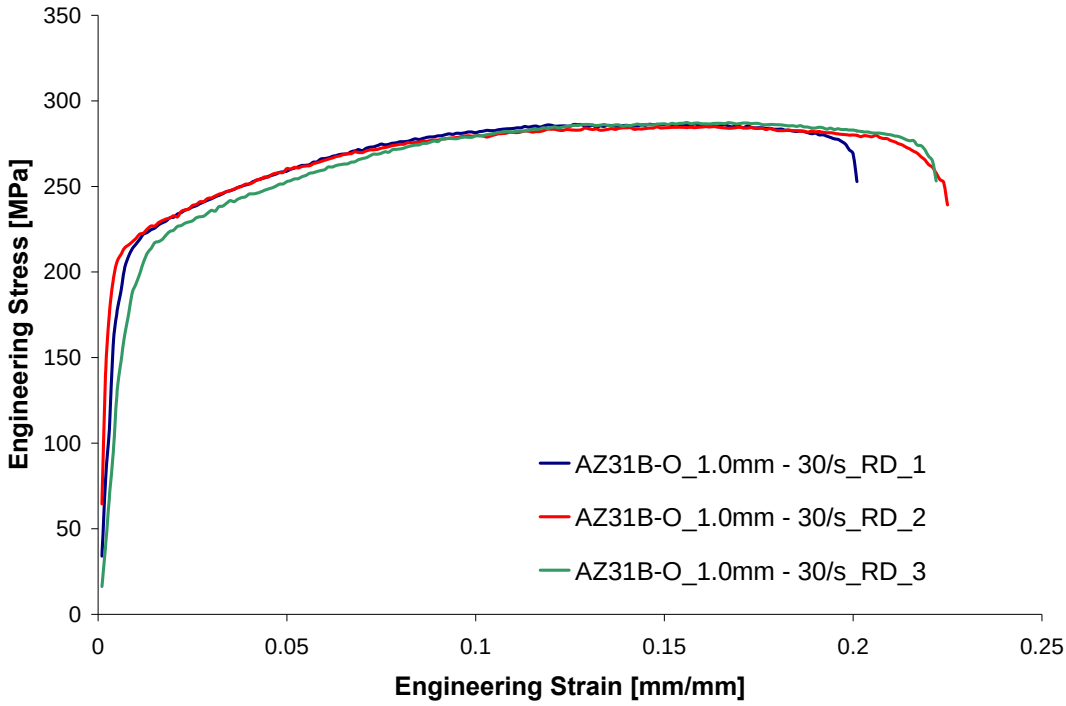
Engineering Stress [MPa]
350
300
250
200
150
100
50
0
0
0.05
0.1
0.15
0.2
0.25
Engineering Strain [mm/mm]
AZ31B-O_1.0mm - 30/s_RD_1
AZ31B-O_1.0mm - 30/s_RD_2
AZ31B-O_1.0mm - 30/s_RD_3

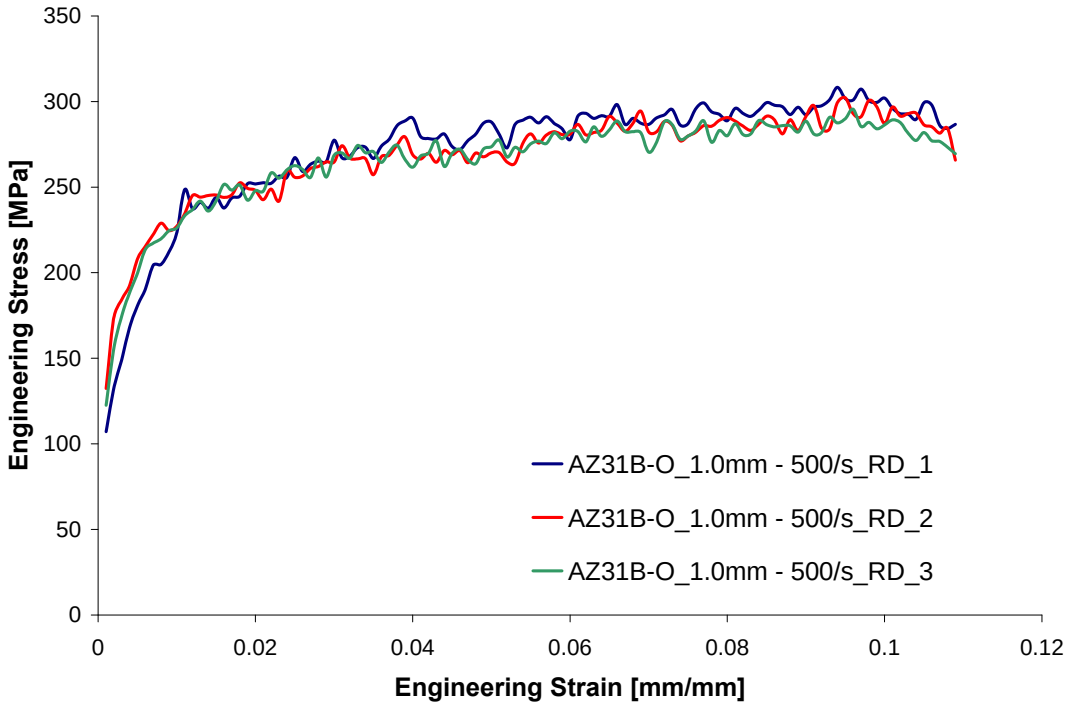
Engineering Stress [MPa]
350
300
250
200
150
100
50
0
0
0.02
0.04
0.06
0.08
0.1
0.12
Engineering Strain [mm/mm]
AZ31B-O_1.0mm - 500/s_RD_1
AZ31B-O_1.0mm - 500/s_RD_2
AZ31B-O_1.0mm - 500/s_RD_3

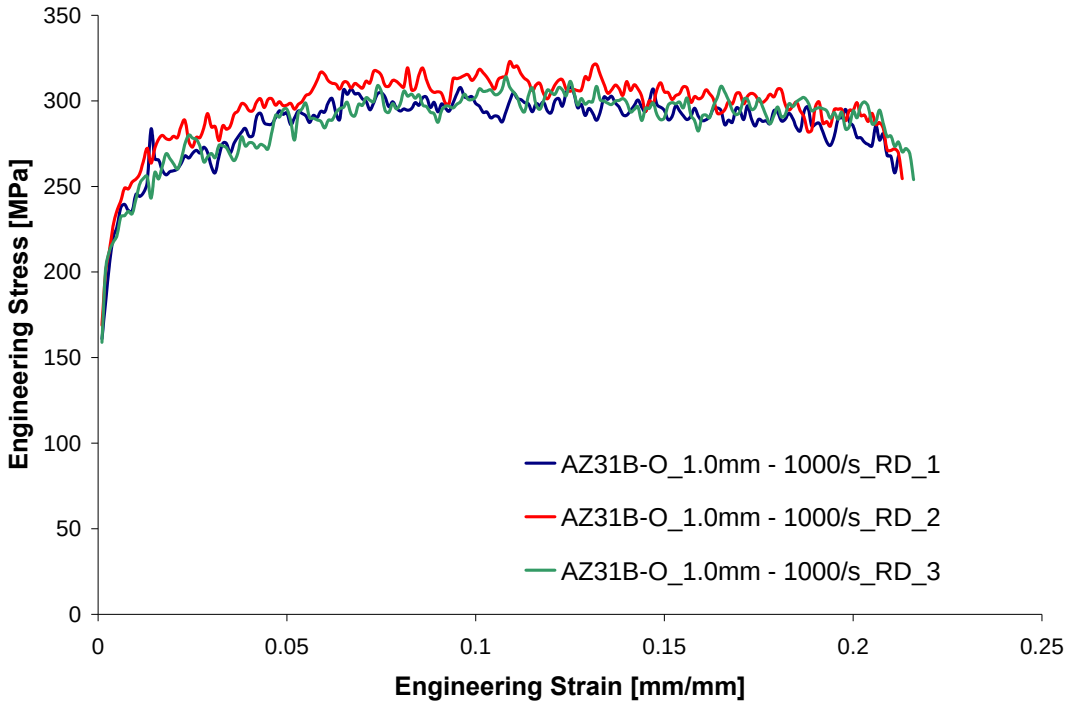
Engineering Stress [MPa]
Engineering Strain [mm/mm]
AZ31B-O_1.0mm - 1000/s_RD_1
AZ31B-O_1.0mm - 1000/s_RD_2
AZ31B-O_1.0mm - 1000/s_RD_3

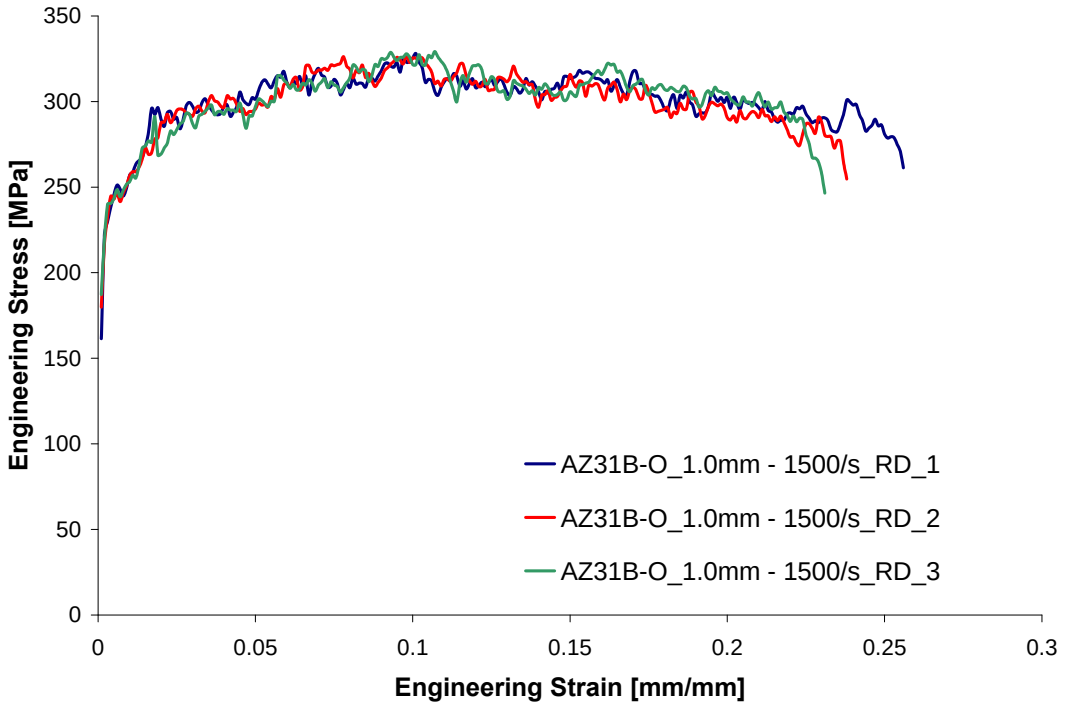
Engineering Stress [MPa]
Engineering Strain [mm/mm]
AZ31B-O_1.0mm - 1500/s_RD_1
AZ31B-O_1.0mm - 1500/s_RD_2
AZ31B-O_1.0mm - 1500/s_RD_3

AZ31B-O, 1.0mm, Transverse Direction, room temperature

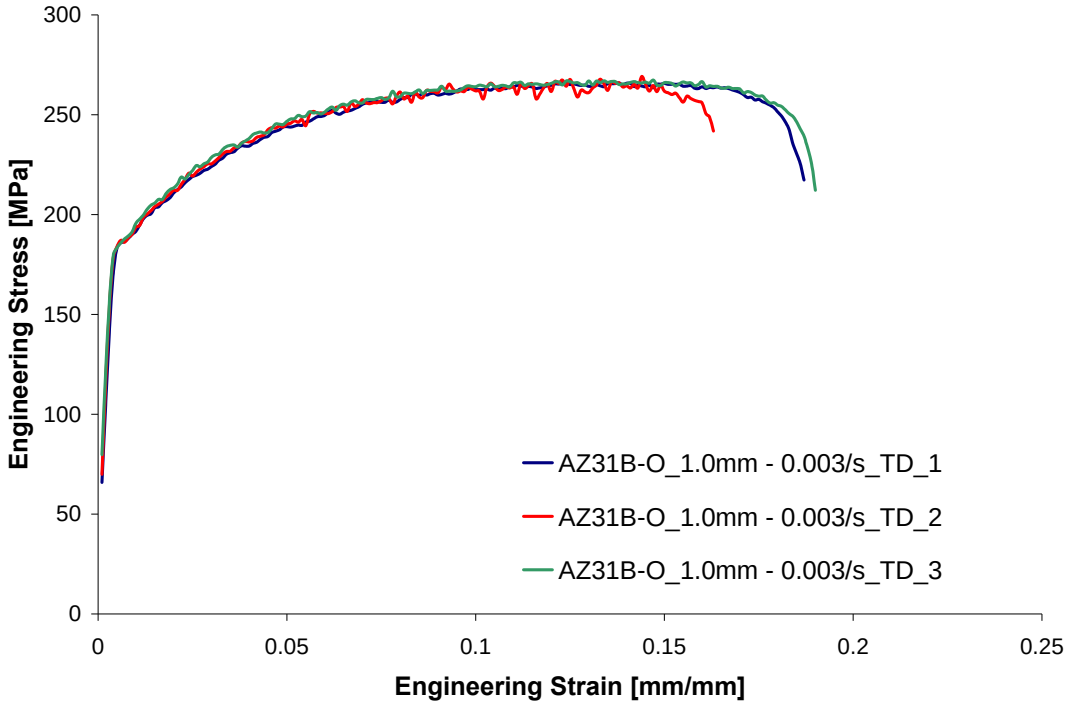

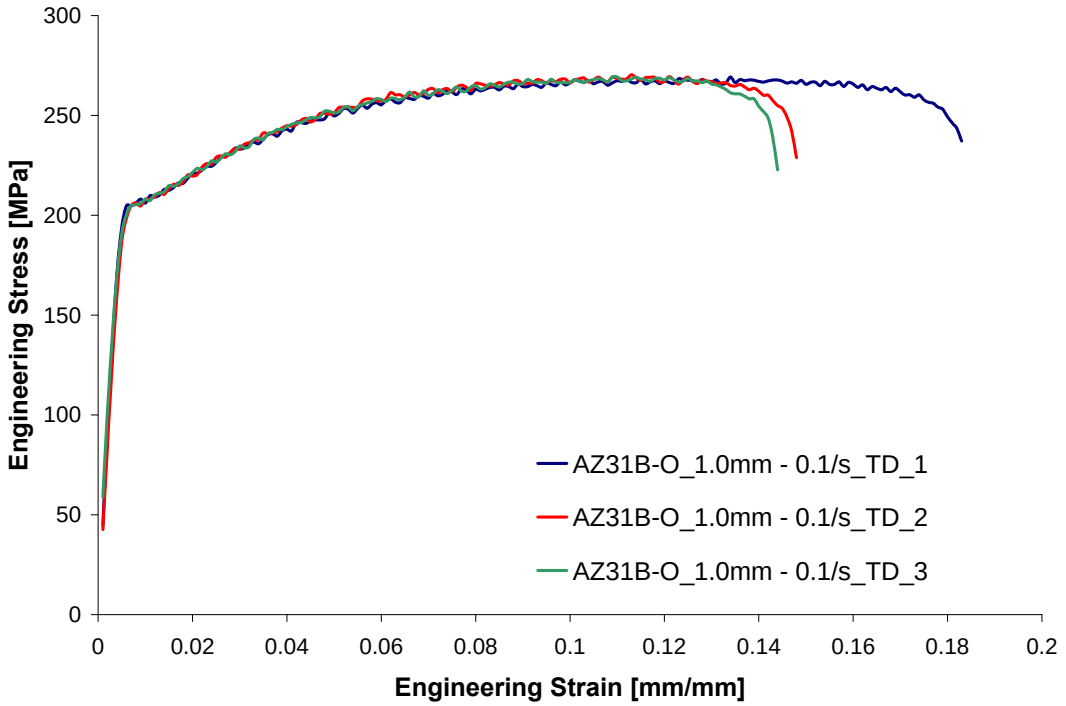

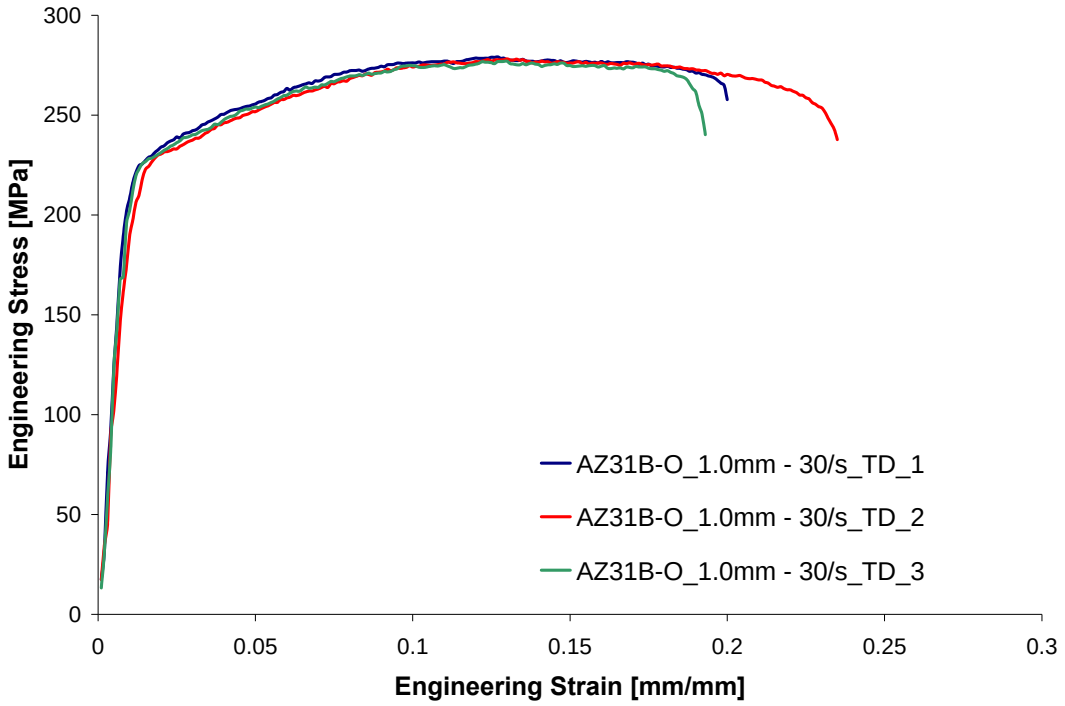
300
250
200
150
100
50
0
Engineering Stress [MPa]
0
0.05
0.1
0.15
0.2
0.25
0.3
Engineering Strain [mm/mm]
AZ31B-O_1.0mm - 30/s_TD_1
AZ31B-O_1.0mm - 30/s_TD_2
AZ31B-O_1.0mm - 30/s_TD_3

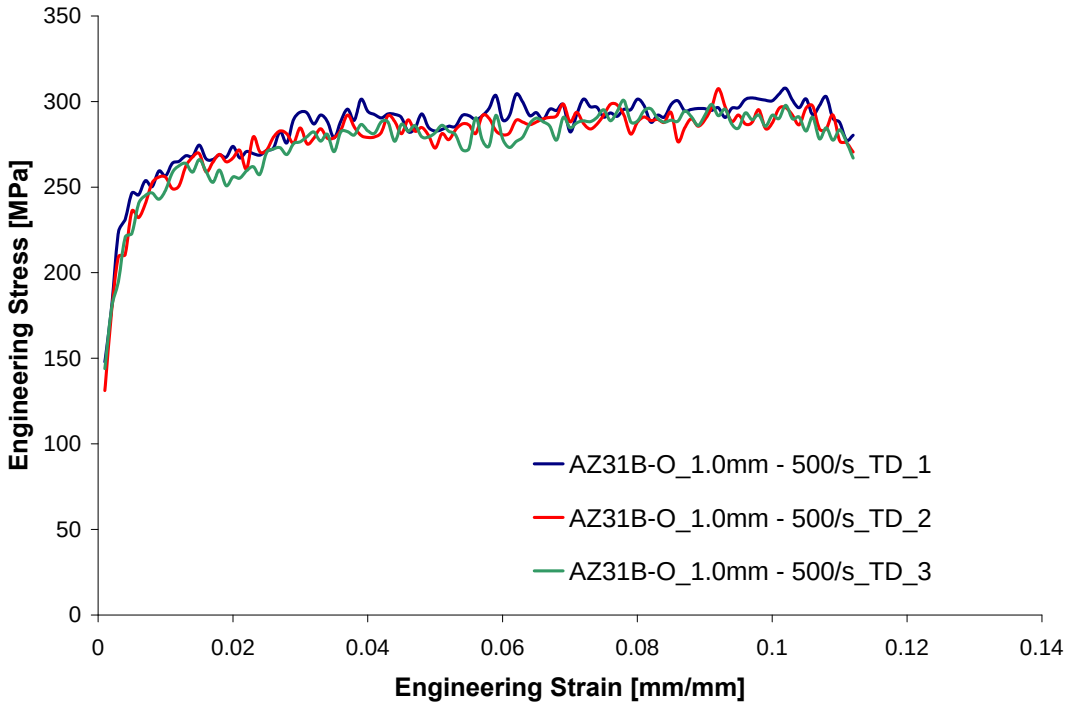
350
300
250
200
150
100
50
0
Engineering Stress [MPa]
0
0.02
0.04
0.06
0.08
0.1
0.12
0.14
Engineering Strain [mm/mm]
AZ31B-O_1.0mm - 500/s_TD_1
AZ31B-O_1.0mm - 500/s_TD_2
AZ31B-O_1.0mm - 500/s_TD_3

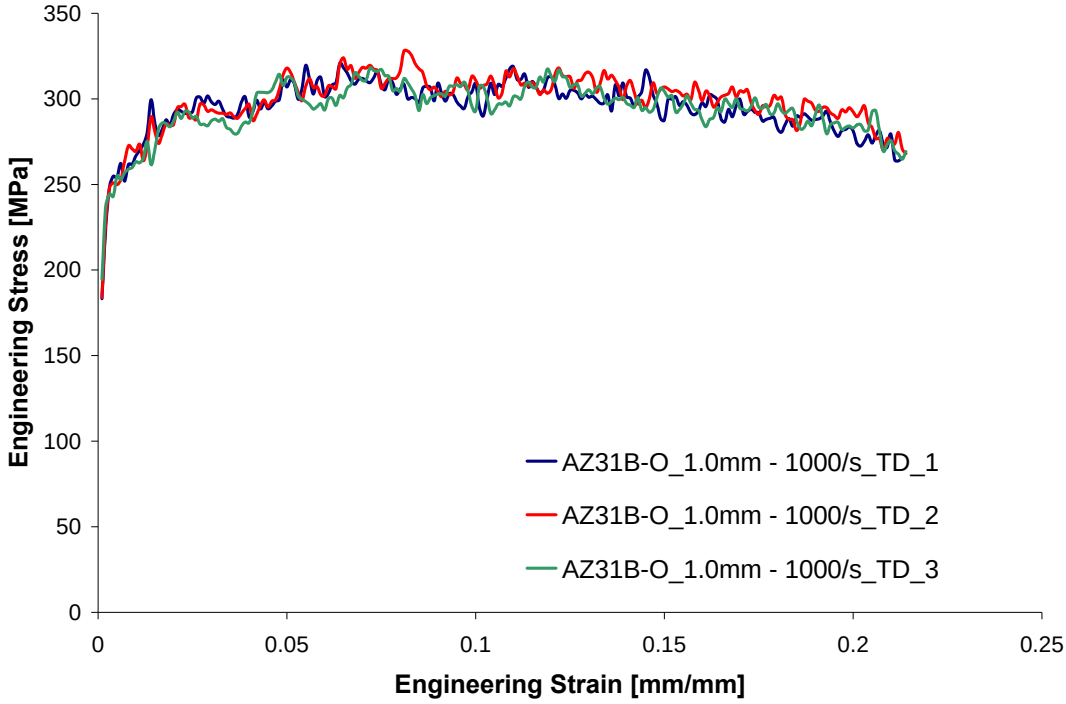
Engineering Stress [MPa]
350
300
250
200
150
100
50
0
0
0.05
0.1
0.15
0.2
0.25
Engineering Strain [mm/mm]
AZ31B-O_1.0mm - 1000/s_TD_1
AZ31B-O_1.0mm - 1000/s_TD_2
AZ31B-O_1.0mm - 1000/s_TD_3

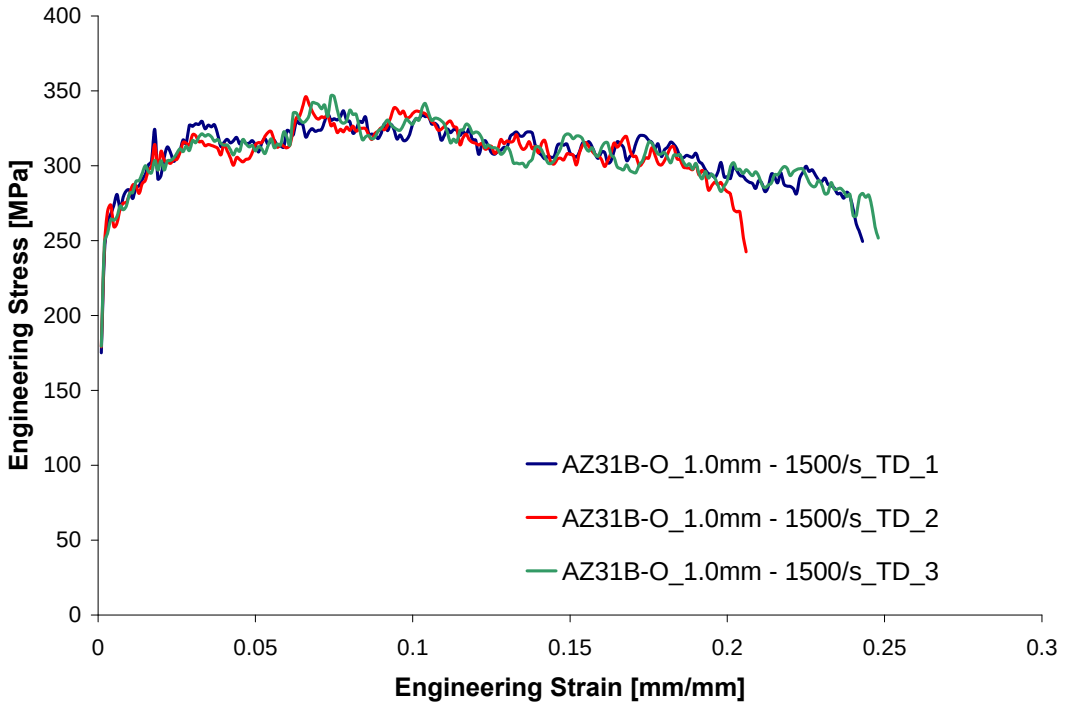
Engineering Stress [MPa]
400
350
300
250
200
150
100
50
0
0
0.05
0.1
0.15
0.2
0.25
0.3
Engineering Strain [mm/mm]
AZ31B-O_1.0mm - 1500/s_TD_1
AZ31B-O_1.0mm - 1500/s_TD_2
AZ31B-O_1.0mm - 1500/s_TD_3

APPENDIX C: LS-DYNA INPUT DECKS

Appendix C1:

TSHB finite element input deck for LS-DYNA

```
$ Units: N-mm-ms-g-MPa
$
*KEYWORD
*TITLE
TSHB Simulation
*CONTROL_ENERGY
$         HGEN        RWEN      SLNTEN       RYLEN
               2           2           2           1
*CONTROL_HOURGLASS
$          IHQ          QH
               3         0.1
*CONTROL_TERMINATION
$      ENDTIM     ENDCYC       DTMIN     ENDNEG     ENDMAS
            0.75
$
*CONTROL_SOLUTION
$         SOLN         NLQ       ISNAN       LCINT
               0
$
*DATABASE_NODFOR
$           DT      BINARY        LCUR       IOOPT
            0.001
*DATABASE_NODOUT
$           DT      BINARY        LCUR       IOOPT        DTHF       BINHF
            0.001
$
*DATABASE_BINARY_D3PLOT
$     DT/CYCL        LCDT     NOBEAM
            0.01
$        IOOPT
               0
$
*DATABASE_GLSTAT
$           DT      BINARY        LCUR       IOOPT        DTHF       BINHF
            0.001
$
*DATABASE_NODAL_FORCE_GROUP
$          SID         CID
               1
*DATABASE_EXTENT_BINARY
$        NEIPH       NEIPS      MAXINT     STRFLG     SIGFLG     EPSFLG     RLTFLG     ENGFLG
               1
$     CMPFLG      IEVERP      BEAMIP      DCOMP       SHGE       STSSZ     N3THDT    IALEMAT
```

```
                0
$      NINTSLD     PKP_SEN          SCLP                    MSSCL       THERM
                0
$
*DATABASE_HISTORY_SOLID_SET
$           IDS1           IDS2           IDS3
                4              5              6
$
*DATABASE_RCFORC
$             DT
          0.001
$
*DATABASE_ELOUT
$             DT
          0.001
$
$ --+----1----+----2----+----3----+----4----+----5----+----6----+----7----+----8
$
$ Part and Section Definitions
$
$ --+----1----+----2----+----3----+----4----+----5----+----6----+----7----+----8
$
*PART
$                        TITLE
SPECIMEN
$            PID        SECID          MID       EOSID        HGID        GRAV    ADPOPT        TMID
                1              1              1              1
$
*PART
$                        TITLE
INCIDENT_BAR
$            PID        SECID          MID       EOSID        HGID        GRAV    ADPOPT        TMID
                2              1              2
$
*PART
$                        TITLE
TRANSMITTED_BAR
$            PID        SECID          MID       EOSID        HGID        GRAV    ADPOPT        TMID
                3              1              2
$
*SECTION_SOLID
$         SECID      ELFORM          AET
                1              1
$
$ --+----1----+----2----+----3----+----4----+----5----+----6----+----7----+----8
$
$ Boundry Conditions
$
$ --+----1----+----2----+----3----+----4----+----5----+----6----+----7----+----8
$
```

```
$ Imposed Velocity (curve 99)
*BOUNDARY_PRESCRIBED_MOTION_SET
$             SID             DOF             VAD            LCID              SF             VID           DEATH           BIRTH
                1               1               0              99               1                            0.25
$
$ Include curve 99
*INCLUDE
Velocity_TSHB_1000s-1.k
$
$ Symmetry BC (normal to Z)
*BOUNDARY_SPC_SET
$             NSID             CID            DOFX            DOFY            DOFZ           DOFRX           DOFRY           DOFRZ
                2               0               0               0               1               1               1               0
$
$ Symmetry BC (normal to Y)
*BOUNDARY_SPC_SET
$             NSID             CID            DOFX            DOFY            DOFZ           DOFRX           DOFRY           DOFRZ
                3               0               0               1               0               1               0               1
$
$ --+----1----+----2----+----3----+----4----+----5----+----6----+----7----+----8
$
$ Contact Definitions
$
$ --+----1----+----2----+----3----+----4----+----5----+----6----+----7----+----8
$
$ Specimen - Incident Bar
*CONTACT_TIED_SURFACE_TO_SURFACE
$             SSID            MSID           SSTYP           MSTYP          SBOXID          MBOXID             SPR             MPR
                2               1               3               3
$               FS              FD              DC              VC             VDC         PENCHK              BT              DT
              0.0               0
$              SFS             SFM             SST             MST            SFST            SFMT             FSF             VSF
                0
$
$ Specimen - Transmitted Bar
*CONTACT_TIED_SURFACE_TO_SURFACE
$             SSID            MSID           SSTYP           MSTYP          SBOXID          MBOXID             SPR             MPR
                3               1               3               3
$               FS              FD              DC              VC             VDC         PENCHK              BT              DT
              0.0               0
$              SFS             SFM             SST             MST            SFST            SFMT             FSF             VSF

$
$ --+----1----+----2----+----3----+----4----+----5----+----6----+----7----+----8
$
$ Material Properties
$
$ --+----1----+----2----+----3----+----4----+----5----+----6----+----7----+----8
$
*INCLUDE
```

```
Materials_TSHB_1.6mm.k
$
$ --+----1----+----2----+----3----+----4----+----5----+----6----+----7----+----8
$
$ Mesh
$
$ --+----1----+----2----+----3----+----4----+----5----+----6----+----7----+----8
$
*INCLUDE
Mesh_Quarter_1.6mm.k
$
*END
```

Appendix C2:

Johnson-Cook input deck for LS-DYNA

```
*KEYWORD
$ Units: N-mm-ms-g-MPa
$ --+----1----+----2----+----3----+----4----+----5----+----6----+----7----+----8
$
$ Material Properties
$
$ --+----1----+----2----+----3----+----4----+----5----+----6----+----7----+----8
$
$ SPECIMEN - AZ31B-O 1.6mm fit Johnson-Cook (RD)
*MAT_JOHNSON_COOK
$ MAT 15
$        MID          RO           G           E          PR         DTF      VP    RATEOP
             1    1.77E-03    1.70E+04    4.50E+04        0.35                  1         0
$          A           B           N           C           M          TM      TR      EPSO
       133.082     345.821       0.293       0.016       1.849         905     298  1.00E-03
$         CP          PC       SPALL          IT          D1          D2      D3        D4
         1040                                    1
$         D5       C2/P

$
*EOS_LINEAR_POLYNOMIAL
$      EOSID          C0          C1          C2          C3          C4      C5        C6
             1           0    5.00E+04
$         E0          V0
             0           1
$ Note: E0= RO*CP*T0  -> fix initial Temp = (Troom + T0)
$ 25°C -> E0 = 0.0; 150°C -> E0=230.1; 250°C -> E0=414.18; 300°C -> E0=506.22
$
*MAT_THERMAL_ISOTROPIC
$       TMID         TRO        TGRLC     TGMULT        TLAT        HLAT
             1           0           0          0         905    3.39E+05
$         HC          TC
         1040    7.69E-02
$
$ Bars properties
*MAT_ELASTIC
$ MAT 001
$        MID          RO           E          PR          DA          DB       K
             2    2.70E-03    6.89E+04        0.35
$
*END
```

Appendix C3:

Cowper-Symonds input deck for LS-DYNA

```
*KEYWORD
$ Units: N-mm-ms-g-MPa
$ --+----1----+----2----+----3----+----4----+----5----+----6----+----7----+----8
$
$ Material Properties
$
$ --+----1----+----2----+----3----+----4----+----5----+----6----+----7----+----8
$
$ SPECIMEN- AZ31B-O 1.6mm fit J-C with Cowper-Symonds (RD)
*MAT_JOHNSON_COOK
$ MAT 15
$         MID          RO           G           E          PR         DTF      VP     RATEOP
            1    1.77E-03    1.70E+04    4.50E+04        0.35                  1          3
$           A           B           N           C           M          TM      TR       EPSO
      105.698     313.947       0.256    7.00E+03       1.787         905     298          1
$          CP          PC       SPALL          IT          D1          D2      D3         D4
        1040                                     1
$          D5       C2/P
       6.028
$
*EOS_LINEAR_POLYNOMIAL
$       EOSID          C0          C1          C2          C3          C4      C5         C6
            1           0    5.00E+04
$          E0          V0
            0           1
$ Note: E0= RO*CP*T0 -> fix initial Temp = (Troom + T0)
$ 25°C -> E0 = 0.0; 150°C -> E0=230.1; 250°C -> E0=414.18; 300°C -> E0=506.22
$
*MAT_THERMAL_ISOTROPIC
$        TMID         TRO       TGRLC     TGMULT        TLAT        HLAT
            1           0           0          0         905    3.39E+05
$          HC          TC
        1040    7.69E-02
$
$ Bars properties
*MAT_ELASTIC
$ MAT 001
$         MID          RO           E          PR          DA          DB       K
            2    2.70E-03    6.89E+04        0.35
$
*END
```

Appendix C4:

Zerilli-Armstrong input deck for LS-DYNA

```
*KEYWORD
$ Units: N-mm-ms-g-MPa
$ --+----1----+----2----+----3----+----4----+----5----+----6----+----7----+----8
$
$ Material Properties
$
$ --+----1----+----2----+----3----+----4----+----5----+----6----+----7----+----8
$
$ SPECIMEN- AZ31B-O 1.6mm fit Zerilli-Armstrong BCC (RD)
*MAT_MODIFIED_ZERILLI_ARMSTRONG
$ MAT 65
$              MID               RO                G               E0                N            TROOM               PC            SPALL
                 1         1.77E-03         1.70E+04         1.00E-03              0.4              298
$               C1               C2                C3               C4               C5               C6            EFAIL               VP
                 0            57.42                 0         2.30E-04          413.083           95.247                                    1
$               B1               B2                B3               G1               G2               G3               G4             BULK
              1.105         3.84E-04         -2.66E-06         1.37E+03           -2.256         4.53E-03         -2.20E-06
$
*EOS_LINEAR_POLYNOMIAL
$            EOSID               C0               C1               C2               C3               C4               C5               C6
                 1                0         5.00E+04
$               E0               V0
                 0                1
$ Note: E0= RO*CP*T0 -> fix initial Temp = (Troom + T0)
$ 25°C -> E0 = 0.0; 150°C -> E0=230.1; 250°C -> E0=414.18; 300°C -> E0=506.22
$
*MAT_THERMAL_ISOTROPIC
$             TMID              TRO             TGRLC            TGMULT              TLAT              HLAT
                 1                0                 0                 0               632         3.39E+05
$               HC               TC
              1040         7.69E-02
$
$ Bars properties
*MAT_ELASTIC
$ MAT 001
$              MID               RO                E               PR               DA               DB                K
                 2         2.70E-03         6.89E+04             0.35
$
*END
```